

DISS. ETH NO. 25280

**DEVELOPMENT OF IRON AND COPPER OXIDE BASED OXYGEN  
CARRIERS FOR CHEMICAL LOOPING APPLICATIONS:  
STRUCTURAL INSIGHT AND PERFORMANCE ASSESSMENT**

A thesis submitted to attain the degree of  
DOCTOR OF SCIENCES of ETH ZURICH  
(Dr. sc. ETH Zurich)

presented by  
NUR SENA YÜZBASİ

M.Sc. Chemical Engineering, Middle East Technical University, Turkey

born on 14.12.1987  
citizen of Turkey

accepted on the recommendation of  
Prof. Christoph R. Müller, examiner  
Prof. Henrik Leion, co-examiner  
Dr. Paula M. Abdala, co-examiner

2018



*"Science is the most reliable guide for civilization, for life, for success in the world."*

***Mustafa Kemal Atatürk***

***To my family and knowledge***

## Acknowledgements

I would like to express my gratitude to everyone who supported me throughout this study. First and foremost, I am deeply grateful to my supervisor, Prof. Dr. Christoph Müller for providing me the opportunity to be a part of the Laboratory of Energy Science and Engineering (LESE) and to do my PhD studies in one of the world's leading universities, ETH Zürich, and for his continuous guidance and scientific advices throughout my research period. It was a privilege to work with Dr. Paula M. Abdala, who has been an academic inspiration for me with her wise, fair, kind and professional approach. Thanks to her, I have acquired invaluable knowledge regarding advanced characterization techniques and applications. Her guidance and contributions to each paper published throughout this study improved the quality of the work substantially. Also, I was very fortunate to have the chance to work with Dr. Andac Armutlulu in the second half of my PhD, who was always kind and supportive in both technical and non-technical issues. His characterization skills, scientific advises, approaches in discussions and passion for new ideas were always encouraging. I am also thankful to our lab manager Dr. Agnieszka Kierzkowska for helping me to gain experience in the lab, material synthesis techniques and for the coffee sessions. I am grateful to Dr. Felix Donat for proofreading the abstract, introduction and conclusion of this Dissertation. I would like to show my appreciation to the current members of LESE, Dr. A. Federov. and Dr. E. Deeva, and PhD students; Davood (my dear office mate), Sung Min, Alexey K (a), Awais, Manu (the poet), Pedro (the freedom fighter), Nancy (mou), Margarita (the supporter), Giancarlo (Giankie mou), Alex, Chris (Mr. Energy), Niki, Sergey, Meng, and former members Dr. Qasim Imtiaz (a fair mentor), Max, Guang, Yong, Marcin and Abera. Now, I have very good friends, valuable memories and experience in new cultures by being involved in this international group. I gratefully acknowledge the support of my dear friends, Onur, Utku, Yunus, Büsra, Ekin and Swiss Alps, whom I consider as my family in Switzerland. I would like to thank Yunus, for translating my abstract to German and his “exaggerated” approach. I am very grateful for the precious friendship of Didem, who always believed in me and never let me feel lonely. I am thankful to the Yüzbasi family; my father Unal from whom I learned determination and dedication, and my mother Yildiz from whom I learned patience and unconditional love, my dear brother Sinan, my dear sister in-law Esra and my lovely niece Zeynep Ada.



## Abstract

The increasing atmospheric CO<sub>2</sub> concentration is most likely the major contributor to global warming. The growing concern about climate change and more restrictive legislations to reduce CO<sub>2</sub> emissions, necessitate the implementation of low-carbon technologies for electricity generation and the production of fuels for transportation. Hydrogen (H<sub>2</sub>) is considered a clean and promising energy carrier since its combustion yields only water. For H<sub>2</sub> to become an important energy carrier, it must be produced in an efficient and, ideally, CO<sub>2</sub>-neutral manner. In this context, the distributed production of high purity H<sub>2</sub> with the simultaneous capture of CO<sub>2</sub> can be achieved through a chemical looping (CL) cycle relying on an Fe<sub>2</sub>O<sub>3</sub>-based oxygen carrier. In this process, a carbonaceous fuel is first gasified to produce a synthesis gas (H<sub>2</sub> and CO) that is used to reduce Fe<sub>2</sub>O<sub>3</sub> to a lower oxidation state. Subsequent re-oxidation of the reduced iron (oxide) with steam yields high-purity H<sub>2</sub>. For the practical implementation of this technology, the availability of highly reactive Fe<sub>2</sub>O<sub>3</sub>-based oxygen carriers that can withstand multiple redox cycles is a key requirement.

In this study, Fe<sub>2</sub>O<sub>3</sub>-based oxygen carriers were developed using a co-precipitation technique. It was found that pure Fe<sub>2</sub>O<sub>3</sub> deactivates after only a few redox cycles when Fe<sub>2</sub>O<sub>3</sub> is reduced completely to Fe. By stabilizing Fe<sub>2</sub>O<sub>3</sub> with e.g. aluminum oxide (Al<sub>2</sub>O<sub>3</sub>) or zirconium oxide (ZrO<sub>2</sub>) the extent of detrimental morphological changes occurring over repeated redox cycles could be mitigated. Stabilizing Fe<sub>2</sub>O<sub>3</sub> with Al<sub>2</sub>O<sub>3</sub> improved the cyclic redox stability, however, the H<sub>2</sub> yield was lowered owing to the formation of unreactive FeAl<sub>2</sub>O<sub>4</sub>. On the other hand, ZrO<sub>2</sub>-supported oxygen carriers displayed a very high and stable H<sub>2</sub> yield over 15 redox cycles. Electrical conductivity measurements showed that the addition of ZrO<sub>2</sub> decreased the activation energy for charge transport when compared to pure Fe<sub>2</sub>O<sub>3</sub>, indicating an enhanced solid-state ionic diffusion through the material. In addition, it was observed that the pH value at which precipitation was performed, affected appreciably the morphological properties, local structure, and redox stability.

To improve the reaction kinetics of the Fe<sub>2</sub>O<sub>3</sub>-ZrO<sub>2</sub> system, copper was introduced to the oxygen carrier formulation (via sol-gel technique) and its effect on the reaction rate, reaction pathways and redox characteristics was probed. After calcination the material was composed Fe<sub>2</sub>O<sub>3</sub> and CuFe<sub>2</sub>O<sub>4</sub> distributed within the ZrO<sub>2</sub> matrix. Fe K-

edge X-ray absorption near edge structure (XANES) experiments revealed that the reduction of both  $\text{Fe}_2\text{O}_3$  and  $\text{CuFe}_2\text{O}_4$  proceeded *via* a  $\text{Fe}^{2+}$  intermediate, viz.  $\text{Fe}_2\text{O}_3$  ( $\text{CuFe}_2\text{O}_4$ ) -  $\text{Fe}_3\text{O}_4$  ( $\text{Cu}^0$ ) -  $\text{FeO}$  ( $\text{Cu}^0$ ) -  $\text{Fe}^0$  ( $\text{Cu}^0$ ). It was found that metallic Cu, leaving the spinel structure in the first reduction step, increased the rate of reduction of iron oxides.

Turning to  $\text{Al}_2\text{O}_3$  stabilized  $\text{Fe}_2\text{O}_3$ , a  $\text{Na}^+$  doping strategy was developed to avoid the formation of the unreactive  $\text{FeAl}_2\text{O}_4$  spinel phase. The addition of sodium to the  $\text{Fe}_2\text{O}_3$ - $\text{Al}_2\text{O}_3$  system prevented the formation of  $\text{FeAl}_2\text{O}_4$  under CL-relevant reaction conditions and yielded an inexpensive material with a high redox stability and  $\text{H}_2$  yield (close to theoretically expected values) over 15 redox cycles. *Ex situ* X-ray diffraction (XRD) complemented by XAS (Fe, Al and Na K-edge) confirmed the formation of a mixed oxide,  $\text{NaAl}_{11}\text{O}_{17}$  (also known as Na- $\beta$ - $\text{Al}_2\text{O}_3$ ), which is considered to prevent the interaction between iron oxide and  $\text{Al}_2\text{O}_3$ .

Finally, highly effective, CuO-based oxygen carriers were developed for a chemical looping combustion (CLC) scheme. To avoid a sintering-induced deactivation of the material, electrodeposited Cu foams were coated with a thin film of  $\text{Al}_2\text{O}_3$  using atomic layer deposition. The  $\text{Al}_2\text{O}_3$ -coated Cu foams exhibited an excellent redox stability and high oxygen carrying capacity over 10 redox cycles, outperforming their co-precipitated counterpart (with an equal content of  $\text{Al}_2\text{O}_3$ ) and pointing out the importance of a compositional homogeneity in an oxygen carrier to yield a stable redox performance.

## Zusammenfassung

Die zunehmende CO<sub>2</sub>-Konzentration in der Atmosphäre ist mit hoher Wahrscheinlichkeit die Hauptursache für die globale Erwärmung. Das wachsende Bewusstsein bezüglich des Klimawandels und restriktivere Rechtsvorschriften zur Senkung der CO<sub>2</sub>-Emissionen erfordern die Einführung von CO<sub>2</sub>-armen Technologien für die Stromerzeugung und die Produktion von Kraftstoffen für das Transportwesen. Wasserstoff (H<sub>2</sub>) gilt als ein sauberer und vielversprechender Energieträger, da durch seine Verbrennung nur Wasser produziert wird. Damit H<sub>2</sub> ein wichtiger Energieträger werden kann, muss der Stoff effizient und idealerweise CO<sub>2</sub>-neutral hergestellt werden. In diesem Zusammenhang kann die dezentrale Produktion von hochreinem H<sub>2</sub> bei gleichzeitigem Binden von CO<sub>2</sub> durch einen Chemical Looping (CL) -Zyklus erreicht werden, in welchem Sauerstoffträger auf Fe<sub>2</sub>O<sub>3</sub>-Basis verwendet werden. Bei diesem Verfahren wird ein kohlenstoffhaltiger Brennstoff zuerst vergast um ein Synthesegas (H<sub>2</sub> und CO) zu erzeugen und damit das Fe<sub>2</sub>O<sub>3</sub> in einen niedrigeren Oxidationszustand zu reduzieren. Die anschließende Reoxidation des reduzierten Eisens (bzw. des Eisenoxids) mit Wasserdampf ergibt hochreines H<sub>2</sub>. Für die praktische Umsetzung dieser Technologie ist die Verfügbarkeit von hochreaktiven Fe<sub>2</sub>O<sub>3</sub>-basierten Sauerstoffträgern, die mehreren Redoxzyklen standhalten können, eine zentrale Voraussetzung.

In dieser Dissertation wurden Fe<sub>2</sub>O<sub>3</sub>-basierte Sauerstoffträger mittels eines Cofällungsverfahrens entwickelt. Es stellte sich heraus, dass reines Fe<sub>2</sub>O<sub>3</sub> nach nur wenigen Redoxzyklen deaktiviert wenn Fe<sub>2</sub>O<sub>3</sub> vollständig zu Fe reduziert wird. Durch das Stabilisieren von Fe<sub>2</sub>O<sub>3</sub> mit z.B. Aluminiumoxid (Al<sub>2</sub>O<sub>3</sub>) oder Zirkoniumoxid (ZrO<sub>2</sub>) konnten unvorteilhafte morphologische Veränderungen, die über wiederholte Redoxzyklen auftreten, deutlich vermindert werden. Die Stabilisierung von Fe<sub>2</sub>O<sub>3</sub> mit Al<sub>2</sub>O<sub>3</sub> verbesserte die zyklische Redoxstabilität, verringerte jedoch die H<sub>2</sub>-Ausbeute aufgrund der Bildung von nicht reaktivem FeAl<sub>2</sub>O<sub>4</sub>. Andererseits zeigten die durch ZrO<sub>2</sub>-stabilisierten Sauerstoffträger eine sehr hohe und stabile H<sub>2</sub>-Ausbeute über 15 Redoxzyklen. Elektrische Leitfähigkeitsmessungen zeigten, dass die Zugabe von ZrO<sub>2</sub> die Aktivierungsenergie für den Ladungstransport im Vergleich zu reinem Fe<sub>2</sub>O<sub>3</sub> verringerte, was auf eine verbesserte ionische Diffusion durch das Material hinweist. Zusätzlich wurde beobachtet, dass der pH-Wert, bei welchem die Fällungsreaktion

durchgeführt wurde, merklich die morphologischen Eigenschaften, die lokale Kristallstruktur, sowie die Redoxstabilität beeinflusste.

Um die Reaktionskinetik des  $\text{Fe}_2\text{O}_3\text{-ZrO}_2$ -Systems zu verbessern wurde Kupfer (Cu) zur Sauerstoffträgerzusammensetzung hinzugefügt (mittels Sol-Gel-Technik) und seine Wirkung auf die Reaktionsgeschwindigkeit, Reaktionswege und Redox Eigenschaften untersucht. Fe K-Kanten-Röntgenabsorptionsspektroskopie-Experimente (XANES) zeigten, dass die Reduktion sowohl von  $\text{Fe}_2\text{O}_3$  als auch von  $\text{CuFe}_2\text{O}_4$  über ein  $\text{Fe}^{2+}$ -Zwischenprodukt erfolgte, d.h.  $\text{Fe}_2\text{O}_3$  ( $\text{CuFe}_2\text{O}_4$ )  $\rightarrow$   $\text{Fe}_3\text{O}_4$  ( $\text{Cu}^0$ )  $\rightarrow$   $\text{FeO}$  ( $\text{Cu}^0$ )  $\rightarrow$   $\text{Fe}^0$  ( $\text{Cu}^0$ ). Es wurde festgestellt, dass metallisches Cu die Spinellstruktur im ersten Reduktionsschritt verliess, was die Reduktionsgeschwindigkeit der Eisenoxide erhöhte.

Mit  $\text{Al}_2\text{O}_3$ -stabilisiertem  $\text{Fe}_2\text{O}_3$  wurde eine  $\text{Na}^+$ -Dotierungsstrategie entwickelt um die Entstehung der unreaktiven  $\text{FeAl}_2\text{O}_4$ -Spinellphase zu vermeiden. Die Beimischung von Natrium zum  $\text{Fe}_2\text{O}_3\text{-Al}_2\text{O}_3$ -System verhinderte die Bildung von  $\text{FeAl}_2\text{O}_4$  unter CL-relevanten Reaktionsbedingungen und ergab ein kostengünstiges Material mit einer hohen Redoxstabilität und  $\text{H}_2$ -Ausbeute (nahe an den theoretisch erwarteten Werten) über 15 Redoxzyklen. Die durch XAS (Fe, Al und Na K-Kante) ergänzte ex-situ Röntgenbeugung (XRD) bestätigte die Bildung des Mischoxids  $\text{NaAl}_{11}\text{O}_{17}$  (auch bekannt als  $\text{Na-}\beta\text{-Al}_2\text{O}_3$ ), von welchem angenommen wird, dass es die Wechselwirkung zwischen Eisenoxid und  $\text{Al}_2\text{O}_3$  verhindert.

Schliesslich wurden hochwirksame, CuO-basierte Sauerstoffträger für ein Chemical-Looping-Combustion (CLC) Schema entwickelt. Um eine durch Sinterprozesse hervorgerufene Deaktivierung des Materials zu vermeiden, wurden galvanisierte Cu-Schäume mit einem dünnen  $\text{Al}_2\text{O}_3$ -Film mittels Atomlagenabscheidung beschichtet. Die mit  $\text{Al}_2\text{O}_3$  beschichteten Cu-Schäume zeigten eine ausgezeichnete Redoxstabilität und eine hohe Sauerstofftragfähigkeit über 10 Redoxzyklen. Damit übertrafen die beschichteten Cu-Schäume ihr mittels Cofällung hergestelltes Gegenstück (mit gleichem  $\text{Al}_2\text{O}_3$  Gehalt) und lieferten einen Hinweis auf die Bedeutung der Homogenität des Kompositionsgefüges in Sauerstoffträgern um eine zyklisch stabile Redoxleistung zu erzielen.

## Table of Contents

<b>Chapter 1: Introduction.....</b>	<b>2</b>
1.1 Dissertation Background and Objectives .....	2
1.1.1 Problem overview .....	2
1.1.2 Low carbon technologies and hydrogen as an energy carrier .....	3
1.1.3 Chemical looping process.....	5
1.1.4 Oxygen carriers used in CLC applications.....	6
1.1.5 Chemical looping based H <sub>2</sub> production (steam-iron process) .....	8
1.1.6 Development of Fe <sub>2</sub> O <sub>3</sub> -based oxygen carriers for CL-based H <sub>2</sub> production	10
1.2 Objectives and structure of this dissertation.....	12
1.3 References.....	13
<b>Chapter 2: ZrO<sub>2</sub>-Supported Fe<sub>2</sub>O<sub>3</sub> for Chemical-Looping-Based Hydrogen Production: Effect of pH on Its Structure and Performance as Probed by X-ray Absorption Spectroscopy and Electrical Conductivity Measurements.....</b>	<b>16</b>
2.1 Abstract.....	17
2.2 Introduction .....	17
2.3 Experimental .....	19
2.4 Results and Discussion.....	20
2.4.1 Morphological and structural characterization of the oxygen carriers ...	20
2.4.2 Temperature-programmed reduction.....	25
2.4.3 Redox performance and H <sub>2</sub> production capacity of the synthesized oxygen carriers .....	27
2.4.4 Purity of hydrogen .....	34
2.5 Conclusions.....	35
2.6 References.....	36
2.7 Supporting Information.....	38
<b>Chapter 3: The Effect of Copper on the Redox Behaviour of Iron Oxide for Chemical-Looping Hydrogen Production Probed by <i>in situ</i> X-Ray Absorption Spectroscopy .....</b>	<b>51</b>
3.1 Abstract.....	52
3.2 Introduction .....	52
3.3 Experimental .....	54
3.3.1 Synthesis of oxygen carriers.....	54
3.3.2 Characterization of the oxygen carriers .....	54
3.3.3 Cyclic redox tests .....	55

3.4	Results and discussion .....	57
3.4.1	Structure and morphology of the as-synthesized oxygen carriers .....	57
3.4.2	CLC performance of the oxygen carriers .....	59
3.4.3	Reduction behaviour of the oxygen carriers .....	60
3.4.4	Reduction pathways probed by <i>in situ</i> XANES .....	62
3.4.5	H <sub>2</sub> -temperature programmed desorption (TPD) .....	66
3.5	Conclusions.....	68
3.6	Supporting Information.....	69
3.7	References.....	78
<b>Chapter 4: Sodium Promotion of Fe<sub>2</sub>O<sub>3</sub>-Al<sub>2</sub>O<sub>3</sub>: Effect on Phase and Redox Stability .....</b>		<b>80</b>
4.1	Abstract.....	81
4.2	Introduction .....	82
4.3	Experimental .....	84
4.3.1	Synthesis of the oxygen carriers.....	84
4.3.2	Characterization of the oxygen carriers .....	85
4.3.3	Cycling redox tests .....	87
4.4	Results and Discussion.....	88
4.4.1	Structure and microstructure of the calcined materials.....	88
4.4.2	Cyclic redox performance .....	94
4.4.3	Structural evolution over multiple redox cycles.....	96
4.4.4	Microstructural changes on redox cycles.....	99
4.5	Conclusions.....	101
4.6	References.....	102
4.7	Supporting Information.....	105
<b>Chapter 5: Atomic Layer Deposition of a Film of Al<sub>2</sub>O<sub>3</sub> on Electrodeposited Copper Foams to Yield Highly Effective Oxygen Carriers for Chemical Looping Combustion-Based CO<sub>2</sub> Capture .....</b>		<b>113</b>
5.1	Abstract.....	114
5.2	Introduction .....	114
5.3	Experimental .....	116
5.4	Results and Discussion.....	120
5.4.1	Structural and morphological characterization of the as-synthesized and calcined materials .....	120
5.4.2	Cyclic redox performance of the oxygen carriers.....	123
5.4.3	Redox pathways as determined by <i>in situ</i> XRD.....	126

5.4.4	Structural and morphological evolution of the oxygen carriers during redox cycles.....	129
5.4.5	Probing solid-state diffusion and phase interaction in model films.....	133
5.5	Conclusions.....	136
5.6	References.....	137
5.7	Supporting Information.....	139
<b>6.</b>	<b>Conclusions and Future Work .....</b>	<b>151</b>
6.1	Conclusions.....	151
6.2	Future Work .....	152
	<b>Curriculum Vitae.....</b>	<b>155</b>

# Chapter 1: Introduction

---

## 1.1 Dissertation Background and Objectives

### 1.1.1 Problem overview

The global energy demand continues to increase, driven largely by economic and population growth. According to the International Energy Outlook 2017 <sup>1</sup>, the global energy consumption is expected to increase from 168 PWh in 2015 to 215 PWh by 2040, a 28 % increase compared to the current state (Figure 1.1). Currently, 83 % of the world's energy demand is supplied by fossil fuels and they are predicted to remain the dominant energy source with only a marginal decline by 2040 <sup>1</sup>. CO<sub>2</sub> emissions from the combustion of fossil fuels and industrial processes contribute by ~ 78 % to the total, global greenhouse gas (GHG) emissions <sup>2</sup>. As a result of the continuing anthropogenic CO<sub>2</sub> emissions, its concentration in the atmosphere has increased from ~ 280 ppm in pre-industrial times to ~ 407 ppm in 2017 <sup>3</sup>. The increasing concentration of atmospheric CO<sub>2</sub> is considered to be the dominant cause of global warming that has been recorded since the mid-20<sup>th</sup> century <sup>2, 4, 5</sup>. The period from 1983 to 2012 was most likely the warmest 30-year period of the last 1400 years in the Northern Hemisphere <sup>2</sup>.

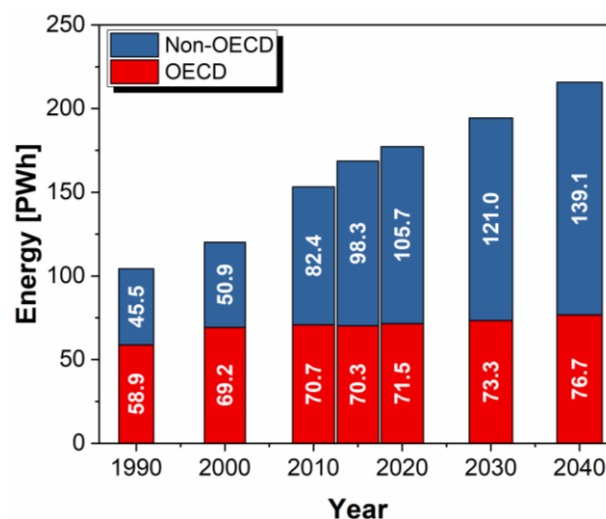


**Figure 1.1:** Global energy consumption (adapted from International Energy Outlook of the IEA, 2017) <sup>1</sup>.



It seems reasonable to assume that unless immediate action is taken to reduce or halt global CO<sub>2</sub> emissions, dramatic consequences such as rising global temperature and sea levels, flooding risks or the destruction of the ecosystem will continue to intensify. Hence, increasingly restrictive climate and environmental policies to curb emissions from combustion processes are being introduced globally. According to the “450 Scenario” published by the International Energy Agency (IEA), the rise in the average global temperature can be limited to 2 °C relative to pre-industrial levels if the total CO<sub>2</sub> emissions are restricted to 18.5 billion metric tons/year by 2040 – about half of what is emitted currently <sup>6,7</sup>.

Strategies proposed to achieve this aim typically involve efficiency improvements in energy systems, increasing the use of renewable energy technologies and the sustainable utilization of biomass instead of fossil fuels, as it has the potential to result in negative CO<sub>2</sub> emissions <sup>7,8</sup>. Although the complete substitution of fossil fuels with low carbon footprint alternatives is the ultimate goal, to meet the continuously growing energy demand in the near- to mid-term, the utilization of fossil fuels in an efficient and “environmentally friendly” manner (e.g., involving the capture of the CO<sub>2</sub>) is required <sup>4,5,7</sup>.

### **1.1.2 Low carbon technologies and hydrogen as an energy carrier**

As a consequence of the increasing public awareness of climate change and more restrictive legislations to reduce CO<sub>2</sub> emissions, there is a growing interest in low carbon technologies for electricity generation including renewable energy sources such as wind, solar, geothermal, biomass and biofuels <sup>2,6,9</sup>. Despite the continuing rise of the share of renewables (carbon free energy sources) in the global energy market, as provided in Figure 1.2, a substantial part of the global primary energy consumption is supplied by fossil fuels.

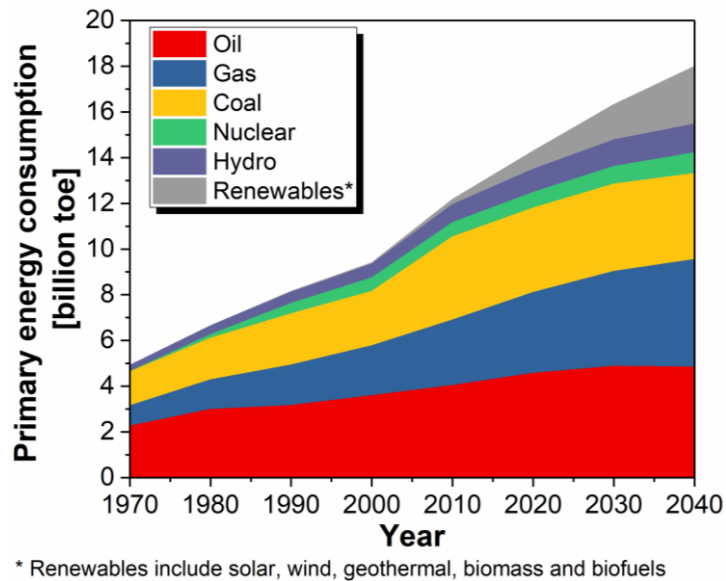


**Figure 1.2:** Global total primary energy consumption by energy carrier (adapted from the reported of BP) <sup>10</sup>.

A potentially emerging energy carrier is hydrogen ( $H_2$ ) with potential applications in the transport, industry and power sectors <sup>9, 11-13</sup>. Hydrogen is a clean-burning fuel yielding water vapour as the only combustion product. Hence, if produced sustainably, hydrogen has the potential as a near-zero emission energy carrier, hence reducing energy-related  $CO_2$  emissions <sup>9, 12, 13</sup>. Also, recent progress in  $H_2$ -powered fuel cell technology has opened up the opportunity to decarbonize the transportation sector. In a recent technology roadmap published by the IEA on  $H_2$  and fuel cells, it has been reported that transport-related  $CO_2$  emissions could be reduced by 10 % (depending on the region) if the share of fuel cell vehicles in road transportation is increased to 25 % by 2050, contributing to meeting the targets of the 2 °C scenario <sup>11</sup>.

Currently, ~ 48 % of the hydrogen is produced from natural gas via steam methane reforming (SMR) without carbon capture, ~ 30 % from refinery/chemical off-gases, ~ 18 % from coal gasification, and the balance (~ 4 %) is produced via the electrolysis of water <sup>11</sup>. However, these production processes are energy intensive and emit a significant amount of  $CO_2$  (specifically the SMR) <sup>9, 11</sup>. Moreover, for  $H_2$  to be used in proton exchange membrane (PEM) fuel cells it has to contain less than 50 ppmv  $CO$  to prevent poisoning of the Pt anode <sup>14</sup>. Therefore, in order for  $H_2$  to become an energy carrier in the future, it must be produced in an efficient and sustainable manner with high purity, and the by-product  $CO_2$  has to be captured and stored to meet long-term climate targets.

### 1.1.3 Chemical looping process

Chemical looping combustion (CLC) is a combustion technique (introduced by Richter and Knoche<sup>15</sup> and developed further by Ishida and Jin<sup>16</sup>) that relies on a redox process and utilizes oxygen of a solid oxygen carrier for the combustion of a carbonaceous fuel such as methane<sup>5, 17-22</sup>. CLC, which is illustrated schematically in Figure 1.3, contains two separate reaction steps: (a) reduction executed in the so-called fuel reactor and (b) a re-oxidation, performed in the air reactor. In the first reaction step, a carbonaceous fuel (e.g., natural gas, coal or syngas) is oxidized via lattice oxygen (instead of air) provided by a solid oxygen carrier, typically a transition metal oxide ( $\text{Me}_x\text{O}_y$ ). The combustion reaction yields a mixture of  $\text{CO}_2$  and  $\text{H}_2\text{O}$ , which can be separated via condensation. In the second reaction step, the reduced oxygen carrier is re-oxidized (*i.e.*, oxidized back to its original oxidation state) with air<sup>5, 17-20</sup>. CLC has been demonstrated using gaseous fuels, such as methane or a synthesis gas<sup>5, 22</sup>. As the solid-solid reaction between an oxygen carrier and a solid fuel, e.g. coal, is extremely slow, solid fuels would have to undergo first a gasification step to produce a synthesis gas, the main components of which are  $\text{CO}$ ,  $\text{H}_2$ ,  $\text{CO}_2$  and  $\text{H}_2\text{O}$ <sup>5, 22</sup>. An alternative to the pre-gasification step is the so-called chemical looping with oxygen uncoupling (CLOU)<sup>5, 23</sup>. In CLOU, a suitable oxygen carrier, releases molecular oxygen, e.g.  $2\text{Me}_x\text{O}_y \rightarrow 2\text{Me}_x\text{O}_{y-1} + \text{O}_2$  that oxidizes subsequently the solid fuel at a high rate.

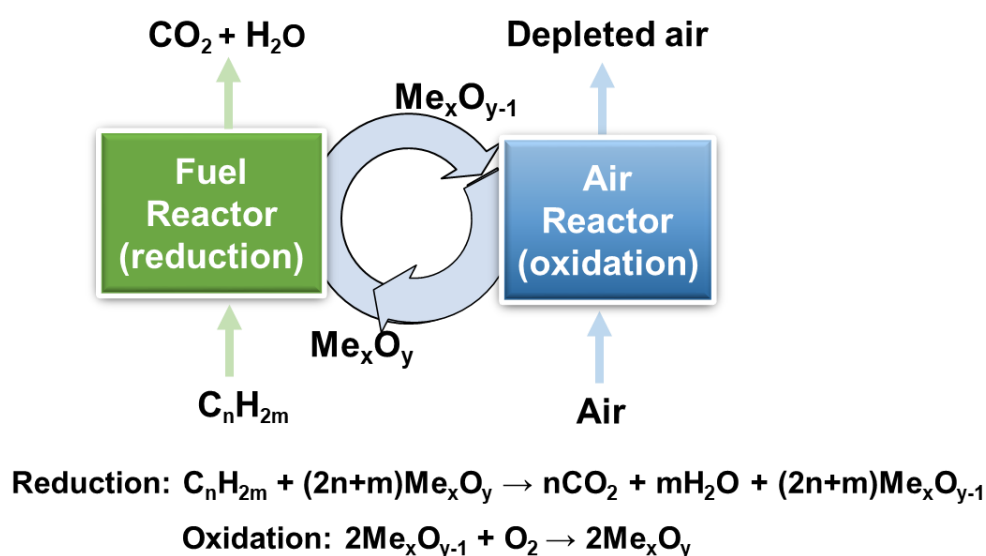


**Figure 1.3:** Schematic diagram of the CLC process.

An important advantage of CLC is that air and the fuel do not mix in the combustion chamber and thus, CO<sub>2</sub> capture (after the condensation of steam) is achieved inherently. Hence, energy intensive steps for the separation of CO<sub>2</sub> from e.g. N<sub>2</sub> are avoided<sup>5, 17, 22</sup>. This advantage makes CLC an economically attractive CCS technology. For example, Adanez *et al.*<sup>24</sup> estimated the costs for CO<sub>2</sub> capture by CLC as 20 USD/t CO<sub>2</sub> comparing favourable to the cost of other technical solutions, such as amine scrubbing-based systems in pulverised coal and natural gas combined cycle plants (~ 36–53 USD/t CO<sub>2</sub>), sorbent-based systems at integrated coal gasification combined cycle (IGCC) plants (~ 28–41 USD/t CO<sub>2</sub>), or the capture of CO<sub>2</sub> via oxy-combustion in pulverised coal plants (~ 36–67 USD/t CO<sub>2</sub>)<sup>25</sup>.

Over the past two decades, research on CLC has focused mostly on the development of suitable oxygen carriers and the reactor design to scale up the process. Currently, chemical looping combustors in the range 300 W – 3 MW have been designed and operated successfully in several units worldwide with an operational experience exceeding 7000 h<sup>22, 24, 26</sup>.

#### **1.1.4 Oxygen carriers used in CLC applications**

A key aspect of CLC is the availability of suitable oxygen carriers. Important criteria that oxygen carriers are expected to fulfil are:

- i. Favourable thermodynamic and kinetic properties at the relevant operating conditions of CLC, *i.e.*, high reactivity and conversion for both the oxidation and reduction reactions.
- ii. Thermal stability.
- iii. Resistance against attrition.
- iv. Feasibility for large-scale production with low production costs.
- v. No health and environmental concerns.

Since the early 2000s, advances in material development have focused mostly on the oxides of the first row transition metals such as Ni, Cu, Mn, Co and Fe<sup>5, 14, 17, 18, 22, 23, 27</sup>. These metal oxides are often supported on an inert material to provide a high surface area, enhanced mechanical strength and attrition resistance, and in some cases to increase the conductivity of charge carriers in the solid<sup>17</sup>.

NiO-based oxygen carriers stand out due to their high reactivity with gaseous fuels such as methane and also have a high oxygen carrying capacity ( $0.21 \text{ g O}_2/\text{g NiO}$ )<sup>23, 28-31</sup>. However, metallic Ni, forming in the reduction step, is prone to carbon deposition<sup>29</sup>. Carbon deposition reduces the  $\text{CO}_2$  capture efficiency of a CLC process, as the combustion of the deposited carbon in the air oxidation step forms CO and  $\text{CO}_2$ , which are emitted to the atmosphere. Moreover, the carcinogenic nature of nickel and its oxides, as well as its high costs (when compared to CuO and  $\text{Fe}_2\text{O}_3$ ), are key drawbacks<sup>32</sup>.

CuO-based oxygen carriers are attractive candidates for CLC owing to their high oxygen carrying capacity, *i.e.*,  $0.2 \text{ g O}_2/\text{g CuO}$ <sup>5, 27, 28, 30, 33-36</sup>. Moreover, for the Cu-CuO couple both the reduction and the oxidation reactions are exothermic. Compared to Ni, metallic Cu has also a lower tendency for carbon formation and is less toxic. The main drawback of Cu is its low melting point ( $1083 \text{ }^\circ\text{C}$ ), which can lead to significant agglomeration and sintering problems. However, by stabilizing CuO with high Tammann temperature ( $T_m$ , indicates the onset of sintering) supports such as  $\text{Al}_2\text{O}_3$  and  $\text{ZrO}_2$ , this issue can be mitigated<sup>34, 35</sup>.

$\text{Fe}_2\text{O}_3$  is among the cheapest metal oxides available<sup>14</sup>. Moreover, it is non-toxic and does not cause severe environmental or health problems. The reduction of  $\text{Fe}_2\text{O}_3$ -based oxygen carriers typically proceeds via different oxidation states:  $\text{Fe}_2\text{O}_3 \rightarrow \text{Fe}_3\text{O}_4$ ,  $\text{Fe}_3\text{O}_4 \rightarrow \text{FeO}$ , and  $\text{FeO} \rightarrow \text{Fe}$ <sup>14</sup>. The  $\text{Fe}_2\text{O}_3$ -Fe transition possesses the highest oxygen carrying capacity of  $0.30 \text{ g O}_2/\text{g Fe}_2\text{O}_3$ . For practical reasons (*i.e.*, achieving the complete conversion of the fuel to  $\text{CO}_2$  and  $\text{H}_2\text{O}$ ) the  $\text{Fe}_2\text{O}_3/\text{Fe}_3\text{O}_4$  couple is favoured<sup>14</sup>. Thermodynamics predict that when using lower oxidation states, the complete conversion of the fuel is not possible. The oxygen carrying capacity for the  $\text{Fe}_2\text{O}_3 \rightarrow \text{Fe}_3\text{O}_4$  transition is  $0.034 \text{ g O}_2/\text{g Fe}_2\text{O}_3$ , which is much lower than that of NiO and CuO. Because of the thermodynamic properties of the lower oxidation states,  $\text{Fe}_2\text{O}_3$ -based oxygen carriers are interesting candidates for chemical-looping based schemes for hydrogen production<sup>37, 38</sup>. This aspect is discussed in more detail further below.

$\text{Mn}_2\text{O}_3$ - and  $\text{Co}_3\text{O}_4$ -based oxygen carriers are somewhat less attractive oxygen carriers when compared to the oxides of Ni and Cu due to their low oxygen carrying capacities (the  $\text{Mn}_2\text{O}_3 - \text{Mn}_3\text{O}_4$  and  $\text{Co}_3\text{O}_4 - \text{CoO}$  redox pairs possess

0.034 O<sub>2</sub>/g Mn<sub>2</sub>O<sub>3</sub> and 0.066 O<sub>2</sub>/g Co<sub>3</sub>O<sub>4</sub>, respectively). Similar to CuO, both materials are capable of releasing gas-phase oxygen at high temperature and, thus, they have been investigated mostly in the context of CLOU<sup>5, 23, 27, 39</sup>. One important drawback is their relatively poor reactivity in the re-oxidation reaction with air<sup>5, 23, 27, 39</sup>. Therefore, Mn<sub>2</sub>O<sub>3</sub>- and Co<sub>3</sub>O<sub>4</sub>-based oxygen carriers have often been combined with other active or inert materials<sup>5</sup>, such as the oxides of Fe<sup>32, 40, 41</sup>, Ni<sup>23</sup>, Mg<sup>39</sup>, or Si<sup>41</sup> to improve both their reactivity and thermodynamic properties (through the formation of solid solutions such as Ni<sub>1-x</sub>Mn<sub>2+x</sub>O<sub>4</sub>, (Fe<sub>x</sub>Mn<sub>1-x</sub>)<sub>2</sub>O<sub>3</sub> or Mn<sub>7</sub>SiO<sub>12</sub>).

As an alternative to transition metal oxide-based oxygen carriers, perovskite-type materials have been suggested recently as suitable oxygen carriers for CLC. Favourable characteristics of this class of materials include high lattice oxygen mobility and high thermal resistance<sup>32</sup>. Perovskites are represented of the formula ABO<sub>3</sub>, in which A is typically a large alkaline earth or rare earth metal and B is a smaller transition metal cation<sup>42, 43</sup>. One of the main advantages of perovskite-type oxygen carriers is the possibility to incorporate dopants, increasing the rate of oxygen transport through the creation of oxygen vacancies. To obtain materials with a good cyclic stability, phase transitions have to be avoided<sup>32, 43</sup>. Therefore, the extent of the reduction reaction must be limited to ensure that the perovskite structure is preserved, this limits, however, the oxygen capacity of the material<sup>43</sup>.

### **1.1.5 Chemical looping based H<sub>2</sub> production (steam-iron process)**

One potential modification of chemical looping combustion is the chemical looping (CL) based production of hydrogen. The key modification of this process compared to classic CLC is that the re-oxidation of the reduced oxygen carrier is performed with steam (instead of air) yielding hydrogen. CL-based H<sub>2</sub> production is based on the “steam-iron process” which was proposed originally by Howard Lane<sup>44</sup> in 1903 and patented by Messerschmitt<sup>45</sup> in 1911. It was the first large scale H<sub>2</sub> production process. However, the steam-iron process was replaced by the SMR due to the wide availability of inexpensive methane. However, SMR followed by a high- and low-temperature water-gas shift reaction is a highly endothermic process that requires multiple unit operations to produce high purity hydrogen<sup>14</sup>. Additionally, the SMR releases large quantities of CO<sub>2</sub> into the atmosphere. A further challenge concerning hydrogen is its distribution and transportation. Conventional steam methane reforming

plants have large production capacities, *i.e.*, 50 PJ H<sub>2</sub>/year<sup>46</sup>. The scale-down of SMR units, allowing the distributed production of hydrogen on the small and distributed scale is currently probably prohibitively expensive.

Instead, the distributed production of high-purity H<sub>2</sub> from a carbonaceous fuel (with simultaneous CO<sub>2</sub> capture) on a small scale might be achieved by a chemical looping system based on a cyclic steam-iron process, *i.e.*, the reduction of an iron oxide-based oxygen carrier and its subsequent re-oxidation with steam (illustrated in Figure 1.4). This CL-based H<sub>2</sub> production process is the main focus of this Dissertation.

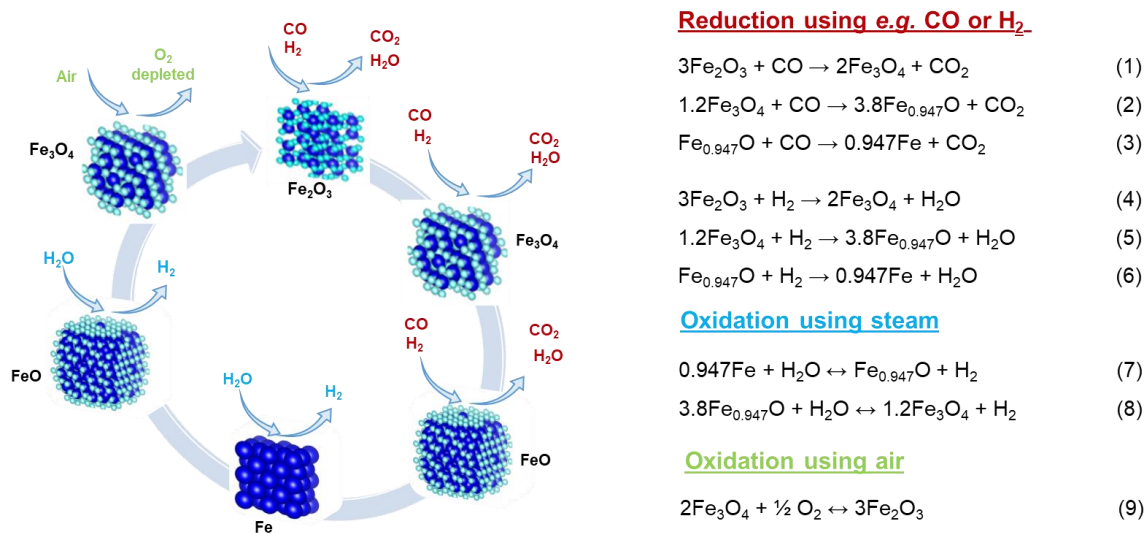


**Figure 1.4:** Schematic representation of the chemical looping-based process for the production of H<sub>2</sub> using synthesis gas (H<sub>2</sub> and CO) as the fuel.

In a CL-based H<sub>2</sub> production process, a solid fuel, *e.g.* coal or biomass, is first gasified to produce a synthesis gas, *i.e.*, a mixture of predominantly CO and H<sub>2</sub>. Subsequently, the following cyclic redox process is operated. Each cycle is comprised of the following three main steps:

**Reduction:** The synthesis gas reduces iron oxides to metallic Fe yielding CO<sub>2</sub> and H<sub>2</sub>O. According to the equilibrium phase diagrams of the Fe-CO-CO<sub>2</sub> (solid lines) and Fe-H<sub>2</sub>-H<sub>2</sub>O (dashed lines) systems, Figure 1.5, it is feasible to reduce Fe<sub>2</sub>O<sub>3</sub> to Fe for partial pressure ratios of  $p_{\text{CO}_2}/p_{\text{CO}}$  and  $p_{\text{H}_2\text{O}}/p_{\text{H}_2}$  below 0.5 (at 800 °C).

**Steam Oxidation:** The thermodynamic equilibrium, Figure 1.5, predicts that steam can be used to oxidized Fe and Fe<sub>0.947</sub>O back to Fe<sub>0.947</sub>O and Fe<sub>3</sub>O<sub>4</sub>, respectively. In the oxidation step H<sub>2</sub> is produced according to reactions 7 – 8.

However, re-oxidation with steam to  $\text{Fe}_2\text{O}_3$  (reaction 9 in Figure 1.4) is thermodynamically limited, as already a very small amount of  $\text{H}_2$  ( $p_{\text{H}_2\text{O}}/p_{\text{H}_2} < 50\,000$ ) prevents the further oxidation to  $\text{Fe}_2\text{O}_3$ .

**Air Oxidation:** Oxidation to  $\text{Fe}_2\text{O}_3$  (reaction 9 in Figure 1.4) is achieved by air (required to close the cycle). The oxidation of  $\text{Fe}_3\text{O}_4$  to  $\text{Fe}_2\text{O}_3$  is highly exothermic ( $\Delta H_{298}^0 = -472\text{ kJ/mol}$ ) and can be used for power generation.

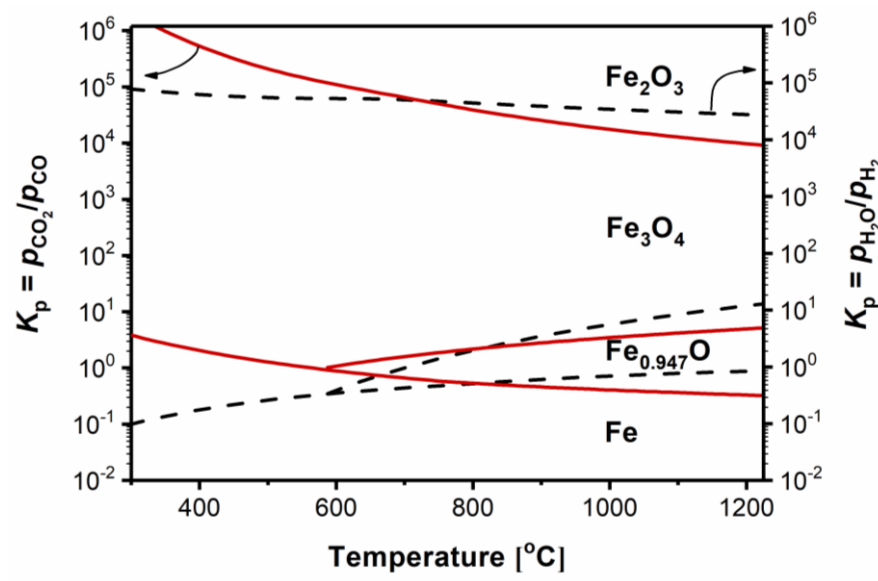


**Figure 1.5:** The phase diagram of the oxides of Fe in a mixture of CO and  $\text{CO}_2$  (solid lines) and in a mixture of  $\text{H}_2$  and  $\text{H}_2\text{O}$  (dashed lines) as a function of temperature.

### 1.1.6 Development of $\text{Fe}_2\text{O}_3$ -based oxygen carriers for CL-based $\text{H}_2$ production

The CL-based production of  $\text{H}_2$  relies on the availability of suitable  $\text{Fe}_2\text{O}_3$ -based oxygen carriers that show excellent stability over multiple redox cycles. Bohn *et al.*<sup>14</sup> demonstrated that the reduction of unsupported  $\text{Fe}_2\text{O}_3$  to metallic Fe and its subsequent oxidation with steam at 600, 750 and 900 °C, resulted in a dramatic loss of its surface area and a significant decay in the  $\text{H}_2$  yield at all temperatures. When the reduction of  $\text{Fe}_2\text{O}_3$  was limited to FeO, the  $\text{H}_2$  yield in the subsequent steam oxidation step was stable but significantly reduced (the steam oxidation of FeO yields only a quarter of the amount of  $\text{H}_2$  (4.2 mmol  $\text{H}_2/\text{g Fe}_2\text{O}_3$ ) that the steam oxidation of Fe yields (16.8 mmol  $\text{H}_2/\text{g Fe}_2\text{O}_3$ ))<sup>14, 47</sup>.



To improve the stability of Fe<sub>2</sub>O<sub>3</sub>-based oxygen carriers, attempts have been made to stabilize it on high Tammann temperature supports<sup>47</sup>. Here, alumina (Al<sub>2</sub>O<sub>3</sub>)<sup>37</sup>, magnesium aluminium spinel (MgAl<sub>2</sub>O<sub>4</sub>)<sup>48, 49</sup>, titania (TiO<sub>2</sub>)<sup>50, 51</sup>, silica (SiO<sub>2</sub>)<sup>52</sup> and zirconia (ZrO<sub>2</sub>)<sup>38</sup> are arguably the most widely studied supports for Fe<sub>2</sub>O<sub>3</sub>-based oxygen carriers. According to Bohn *et al.*<sup>53</sup> the best improvement (with respect to unsupported Fe<sub>2</sub>O<sub>3</sub>) was achieved by stabilizing Fe<sub>2</sub>O<sub>3</sub> with 10 mol % Al<sub>2</sub>O<sub>3</sub> (prepared via wet impregnation) when compared to SiO<sub>2</sub>, MgO and Cr<sub>2</sub>O<sub>3</sub>. Similarly, Kierzkowska *et al.*<sup>37</sup> developed cyclically stable, Al<sub>2</sub>O<sub>3</sub>-supported Fe<sub>2</sub>O<sub>3</sub> (containing 40 wt. % of the support material) using a sol-gel technique. However, the H<sub>2</sub> yield, 7.5 mmol H<sub>2</sub>/g oxygen carrier, was less than the theoretically expected value of 10 mmol H<sub>2</sub>/g oxygen carrier due to the formation of hercynite (FeAl<sub>2</sub>O<sub>4</sub>), which is unreactive with steam. Besides Al<sub>2</sub>O<sub>3</sub>, also MgAl<sub>2</sub>O<sub>4</sub> does not seem to be a fully inert support, as Imtiaz *et al.* observed the formation of the spinel phase MgFe<sub>1.4</sub>Al<sub>0.6</sub>O<sub>4</sub> during cyclic redox experiments<sup>49</sup>. On the other hand, Liu *et al.*<sup>38</sup> demonstrated that ZrO<sub>2</sub> is chemically inert and does not react with Fe<sub>2</sub>O<sub>3</sub> under cyclic redox conditions, which makes ZrO<sub>2</sub> an attractive support material for the CL-based production of H<sub>2</sub>. However, ZrO<sub>2</sub> is more expensive when compared to Al<sub>2</sub>O<sub>3</sub>.

Apart from the phase stability of the oxygen carriers, also the synthesis technique chosen and the synthesis parameters can affect strongly the performance of the oxygen carriers<sup>34, 54</sup>. So far a series of synthesis techniques, including mechanical mixing, freeze granulation, impregnation and co-precipitation, have been used to manufacture Fe<sub>2</sub>O<sub>3</sub>-based oxygen carriers<sup>53, 55, 56</sup>. However, common limitations of these methods listed above are (i) the low surface area of the material prepared and (ii) the fact that mixing between the active component (Fe<sub>2</sub>O<sub>3</sub>) and the support occurs on a macroscopic level only (resulting often in a poor homogeneity of the materials synthesized)<sup>34, 37</sup>. On the other hand, sol-gel synthesis offers the possibility to obtain a homogeneous mixture of the components on the microscopic level (nanometer or even atom-scale)<sup>57</sup>. In addition, the use of atomic layer deposition (ALD) provides the opportunity to deposit films of the support material with thickness control on the atomic level and high conformity<sup>58</sup>. These two synthesis techniques are used more routinely in the area of catalysis and are linked to higher production costs, yet they yield arguably more “defined” materials, making their characterization easier. Such

techniques will, however, allow to formulate structure-performance relationships, which is one of the objectives of this Dissertation.

## 1.2 Objectives and structure of this dissertation

The overall goal of this Dissertation is to develop and study novel Fe<sub>2</sub>O<sub>3</sub>-based materials for the CL-based production of H<sub>2</sub> elucidating structure-performance relationships.

In particular, the following objectives are formulated:

- Synthesis of Fe<sub>2</sub>O<sub>3</sub>-based materials with improved cyclic stability and high H<sub>2</sub> yield by supporting them on ZrO<sub>2</sub> and Al<sub>2</sub>O<sub>3</sub>, and investigate the effect of the synthesis parameters on the structure and performance of the synthesized oxygen carriers.
- Assessment of the effect of the addition of a metal promoter (Cu) on the reaction rate, reaction pathways and redox characteristics of Fe<sub>2</sub>O<sub>3</sub>-based oxygen carriers.
- Probing the interaction between Fe<sub>2</sub>O<sub>3</sub> and Al<sub>2</sub>O<sub>3</sub> under CL relevant conditions and assessing the effect of alkali (sodium) addition on this interaction.
- Development of alternative synthesis protocols to achieve highly effective, CuO-based oxygen carriers for CLC by means of an improved compositional homogeneity.

Specifically, Chapter 1 of this Dissertation provides a short introduction into chemical looping and its potential application for the production of high-purity H<sub>2</sub>. In Chapter 2, the effect of key synthesis parameters (e.g., pH) on the cyclic redox performance of Al<sub>2</sub>O<sub>3</sub> or ZrO<sub>2</sub> stabilized Fe<sub>2</sub>O<sub>3</sub> was critically assessed by means of X-ray Absorption Spectroscopy (XAS) and electrical conductivity measurements. In Chapter 3, the promotion of ZrO<sub>2</sub>-supported Fe<sub>2</sub>O<sub>3</sub> with Cu was probed. *In situ* pulsed-H<sub>2</sub> XANES (Fe K-edge) combined with thermogravimetric and X-ray diffraction (XRD) measurement experiments were used to assess the reduction pathways in these materials. Chapter 4 reports on the development of highly reactive and cyclically stable Al<sub>2</sub>O<sub>3</sub>-supported Fe<sub>2</sub>O<sub>3</sub> oxygen carriers using sol-gel synthesis. Addition of sodium was employed to prevent the formation of a solid solution between Fe<sub>2</sub>O<sub>3</sub> and Al<sub>2</sub>O<sub>3</sub>. Chapter 5 reports on the synthesis of CuO-based, Al<sub>2</sub>O<sub>3</sub>-stabilized oxygen carriers for

chemical looping combustion. Here, an ALD approach was utilized to improve the compositional homogeneity of the oxygen carriers. Finally, this work is concluded with Chapter 6, which contains also suggestions for future work.

### 1.3 References

1. EIA, International Energy Outlook, 2017.
2. IPCC, Climate Change 2014 Synthesis Report, 2017.
3. NOAA, Trends in atmospheric carbon dioxide, <https://www.esrl.noaa.gov/gmd/ccgg/trends/graph.html>, 2018.
4. A. Abad, T. Mendiara, P. Gayán, F. García-Labiano, L. F. de Diego, J. A. Bueno, R. Pérez-Vega and J. Adánez, *Energy Procedia*, 2017, **114**, 285-301.
5. Q. Imtiaz, D. Hosseini and C. R. Müller, *Energy Technology*, 2013, **1**, 633-647.
6. IEA, 2017.
7. A. Otto, T. Grube, S. Schiebahn and D. Stolten, *Energy & environmental science*, 2015, **8**, 3283-3297.
8. R. E. H. Sims, H.-H. Rogner and K. Gregory, *Energy Policy*, 2003, **31**, 1315-1326.
9. M. Zerta, P. R. Schmidt, C. Stiller and H. Landinger, *International journal of hydrogen energy*, 2008, **33**, 3021-3025.
10. BP, Energy Outlook 2017.
11. IEA, Technology Roadmap: Hydrogen and Fuel Cells, 2015.
12. J. D. Holladay, J. Hu, D. L. King and Y. Wang, *Catalysis Today*, 2009, **139**, 244-260.
13. J. A. Turner, *Science*, 2004, **305**, 972-974.
14. C. D. Bohn, C. R. Müller, J. P. Cleeton, A. N. Hayhurst, J. F. Davidson, S. A. Scott and J. S. Dennis, *Industrial & Engineering Chemistry Research*, 2008, **47**, 7623-7630.
15. H. J. Richter and K. F. Knoche, ACS Publications, 1983.
16. M. Ishida and H. Jin, *Journal of Chemical Engineering of Japan*, 1994, **27**, 296-301.
17. J. d. Adánez, L. F. de Diego, F. García-Labiano, P. Gayán, A. Abad and J. Palacios, *Energy & Fuels*, 2004, **18**, 371-377.
18. M. M. Hossain and H. I. de Lasa, *Chemical Engineering Science*, 2008, **63**, 4433-4451.
19. A. Lyngfelt, *Applied Energy*, 2014, **113**, 1869-1873.
20. H. Yang, Z. Xu, M. Fan, R. Gupta, R. B. Slimane, A. E. Bland and I. Wright, *Journal of environmental sciences*, 2008, **20**, 14-27.
21. H. Leion, T. Mattisson and A. Lyngfelt, *International Journal of Greenhouse Gas Control*, 2008, **2**, 180-193.

22. T. Mattisson, M. Keller, C. Linderholm, P. Moldenhauer, M. Rydén, H. Leion and A. Lyngfelt, *Fuel Processing Technology*, 2018, **172**, 1-12.
23. A. Shulman, E. Cleverstam, T. Mattisson and A. Lyngfelt, *Energy & Fuels*, 2009, **23**, 5269-5275.
24. J. Adánez, A. Abad, T. Mendiara, P. Gayán, L. de Diego and F. García-Labiano, *Progress in Energy and Combustion Science*, 2017.
25. E. S. Rubin, J. E. Davison and H. J. Herzog, *International Journal of Greenhouse Gas Control*, 2015, **40**, 378-400.
26. J. Abanades, B. Arias, A. Lyngfelt, T. Mattisson, D. Wiley, H. Li, M. Ho, E. Mangano and S. Brandani, *International Journal of Greenhouse Gas Control*, 2015, **40**, 126-166.
27. H. Song, K. Shah, E. Doroodchi, T. Wall and B. Moghtaderi, *Energy & Fuels*, 2014, **28**, 1284-1294.
28. P. Cho, T. Mattisson and A. Lyngfelt, *Fuel*, 2004, **83**, 1215-1225.
29. P. Cho, T. Mattisson and A. Lyngfelt, *Industrial & Engineering Chemistry Research*, 2005, **44**, 668-676.
30. F. Garcia-Labiano, J. Adánez, L. F. de Diego, P. Gayán and A. Abad, *Energy & Fuels*, 2006, **20**, 26-33.
31. J. Wolf, M. Anheden and J. Yan, *Fuel*, 2005, **84**, 993-1006.
32. D. Jing, T. Mattisson, H. Leion, M. Rydén and A. Lyngfelt, *International Journal of Chemical Engineering*, 2013, **2013**.
33. Q. Imtiaz, A. Kurlov, J. L. M. Rupp and C. R. Müller, *ChemSusChem*, 2015, **8**, 2055-2065.
34. Q. Imtiaz, A. M. Kierzkowska, M. Broda and C. R. Müller, *Environmental science & technology*, 2012, **46**, 3561-3566.
35. Q. Imtiaz, M. Broda and C. R. Müller, *Applied energy*, 2014, **119**, 557-565.
36. Q. Imtiaz, P. M. Abdala, A. M. Kierzkowska, W. Van Beek, S. Schweiger, J. L. Rupp and C. R. Müller, *Physical Chemistry Chemical Physics*, 2016, **18**, 12278-12288.
37. A. Kierzkowska, C. Bohn, S. Scott, J. Cleeton, J. Dennis and C. Muller, *Industrial & Engineering Chemistry Research*, 2010, **49**, 5383-5391.
38. W. Liu, J. S. Dennis and S. A. Scott, *Industrial & Engineering Chemistry Research*, 2012, **51**, 16597-16609.
39. A. Shulman, E. Cleverstam, T. Mattisson and A. Lyngfelt, *Fuel*, 2011, **90**, 941-950.
40. D. Hosseini, F. Donat, S. M. Kim, L. Bernard, A. M. Kierzkowska and C. R. Müller, *ACS Applied Energy Materials*, 2018.
41. M. Rydén, H. Leion, T. Mattisson and A. Lyngfelt, *Applied Energy*, 2014, **113**, 1924-1932.
42. M. Pishahang, Y. Larring, M. Sunding, M. Jacobs and F. Snijkers, *Energy Technology*, 2016, **4**, 1305-1316.
43. J. E. Readman, A. Olafsen, Y. Larring and R. Blom, *Journal of Materials Chemistry*, 2005, **15**, 1931-1937.
44. S. Hurst, *Oil & Soap*, 1939, **16**, 29-35.

45. A. Messerschmitt, *Patent*, 1910.
46. IEA, Hydrogen Production & Distribution, <http://www.iea.org/publications/freepublications/publication/essentials5.pdf>, 2018 ).
47. A. Thursfield, A. Murugan, R. Franca and I. S. Metcalfe, *Energy & Environmental Science*, 2012, **5**, 7421-7459.
48. M. Johansson, T. Mattisson and A. Lyngfelt, *Industrial & Engineering Chemistry Research*, 2004, **43**, 6978-6987.
49. Q. Imtiaz, N. S. Yüzbaşı, P. M. Abdala, A. M. Kierzkowska, W. van Beek, M. Broda and C. R. Müller, *Journal of Materials Chemistry A*, 2016, **4**, 113-123.
50. N. L. Galinsky, Y. Huang, A. Shafieifarhood and F. Li, *ACS Sustainable Chemistry & Engineering*, 2013, **1**, 364-373.
51. T. Pröll, K. Mayer, J. Bolhàr-Nordenkampf, P. Kolbitsch, T. Mattisson, A. Lyngfelt and H. Hofbauer, *Energy Procedia*, 2009, **1**, 27-34.
52. Q. Zafar, T. Mattisson and B. Gevert, *Industrial & engineering chemistry research*, 2005, **44**, 3485-3496.
53. C. Bohn, J. Cleeton, C. Muller, S. Chuang, S. Scott and J. Dennis, *Energy & Fuels*, 2010, **24**, 4025-4033.
54. S. Chuang, J. Dennis, A. Hayhurst and S. Scott, *Combustion and Flame*, 2008, **154**, 109-121.
55. M. Ishida, K. Takeshita, K. Suzuki and T. Ohba, *Energy & Fuels*, 2005, **19**, 2514-2518.
56. T. Mattisson, M. Johansson and A. Lyngfelt, *Energy & Fuels*, 2004, **18**, 628-637.
57. J. D. Wright and N. A. Sommerdijk, *Sol-gel materials: chemistry and applications*, CRC press, 2014.
58. A. Armutlulu, M. A. Naeem, H. J. Liu, S. M. Kim, A. Kierzkowska, A. Fedorov and C. R. Müller, *Advanced Materials*, 2017, **29**, 1702896 .

## Chapter 2: ZrO<sub>2</sub>-Supported Fe<sub>2</sub>O<sub>3</sub> for Chemical-Looping-Based Hydrogen Production: Effect of pH on Its Structure and Performance as Probed by X-ray Absorption Spectroscopy and Electrical Conductivity Measurements

---

This section contains a reprint of the article: Yüzbaşı, N.S., Kierzkowska, A.M., Imtiaz, Q., Abdala, P.M., Kurlov, A., Rupp, J.L. and Müller, C.R., 2016, *J. Phys. Chem. C*, 120 (34), pp.18977-18985. **DOI:** 10.1021/acs.jpcc.6b05276

The author of this Dissertation carried out the synthesis of the oxygen carriers, TGA, XRD, BET, FTIR, XAS and cyclic performance tests. SEM/EDX analysis was conducted by A. Kurlov. Conductivity measurements were implemented with Dr. Q. Imtiaz in Prof. J. L. Rupp's laboratory. Dr. P. M. Abdala performed Rietveld refinement, provided guidance in developing models for EXAFS fittings and overall discussion of the paper. Additionally, Dr. Q. Imtiaz, Dr. A. M. Kierzkowska, Prof. J. L. Rupp and Prof. C. R. Müller assisted with discussion and proof-reading of the paper.

## 2.1 Abstract

Chemical looping is a promising process to produce high purity H<sub>2</sub> while simultaneously capturing CO<sub>2</sub>. The key requirement for this process is the availability of oxygen carriers that possess a high cyclic redox stability, resistance to carbon deposition, and thermal sintering. In this study, ZrO<sub>2</sub>-supported Fe<sub>2</sub>O<sub>3</sub>-based oxygen carriers were developed using a co-precipitation technique. We assess in detail the influence of the key synthesis parameter, *i.e.*, the pH value at which the precipitation was performed, on the morphological properties, chemical composition, local structure, and cyclic redox stability. The performance of the new oxygen carriers was compared to unsupported Fe<sub>2</sub>O<sub>3</sub> and Al<sub>2</sub>O<sub>3</sub>-supported Fe<sub>2</sub>O<sub>3</sub>. A higher degree of disorder in the local structure of oxygen carriers precipitated at low pH values was confirmed by X-ray absorption spectroscopy (XAS) measurements. Electrical conductivity measurements showed that supporting Fe<sub>2</sub>O<sub>3</sub> on ZrO<sub>2</sub> lowered significantly the activation energy for charge transport when compared to pure Fe<sub>2</sub>O<sub>3</sub>. In line with this observation, ZrO<sub>2</sub>-supported oxygen carriers displayed a very high and stable H<sub>2</sub> yield over 15 redox cycles when precipitation was performed at pH > 5.

## 2.2 Introduction

Hydrogen is a clean energy carrier since its combustion yields only water, and the recent progress in hydrogen powered fuel cell technology has opened up the opportunity to decarbonize the transportation sector <sup>1, 2</sup>. However, for hydrogen to become a promising energy carrier in the future, it must be produced in an efficient and sustainable manner, *e.g.*, from renewable energy sources, such as biomass, or by solar-derived processes. If hydrogen is derived from fossil fuels, the by-product CO<sub>2</sub> has to be captured and stored <sup>3-6</sup>.

Steam methane reforming (SMR) followed by a high- and low-temperature water-gas shift reaction is currently the dominating process for the industrial production of hydrogen. However, SMR is a highly endothermic process that requires multiple unit operations to produce high purity hydrogen. Additionally, the SMR releases large quantities of CO<sub>2</sub> into the atmosphere. A further challenge concerning hydrogen is its distribution and transportation. Conventional steam methane reforming plants have large production capacities, *i.e.*, 50 PJ H<sub>2</sub>/year <sup>7</sup>. The scale-down of SMR units,

allowing the distributed production of hydrogen on the small and distributed scale, which is critical if biomass is used as a feedstock, is currently probably prohibitively expensive <sup>1, 8</sup>.

To produce high purity hydrogen from biomass (with the simultaneous capture of CO<sub>2</sub>) on a small and distributed scale, a modification of an iron oxide-based chemical looping combustion scheme has been proposed, which was originated from steam-iron process derived by Messerschmitt <sup>9</sup>. In this process, biomass is first gasified to produce a synthesis gas, *i.e.*, a mixture of predominantly CO and H<sub>2</sub>. The synthesis gas is subsequently used to reduce iron oxide to metallic iron, producing thereby a mixture of CO<sub>2</sub> and H<sub>2</sub>O. A pure stream of CO<sub>2</sub> is obtained after the condensation of steam. Subsequent re-oxidation of metallic iron with steam yields hydrogen of high purity. To close the cycle, the final oxidation step, *i.e.*, from Fe<sub>3</sub>O<sub>4</sub> to Fe<sub>2</sub>O<sub>3</sub>, is performed in air owing to thermodynamic constraints <sup>1, 8, 10-15</sup>. A key requirement of the above-described process is the development of iron oxide-based oxygen carriers that possess (i) a high reactivity at typical operation temperatures, (ii) cyclic redox stability, and (iii) a high resistance to attrition and synthesis gas impurities. Unsupported iron oxide is not suitable for the above-described process since it deactivates after only a single cycle if reduced completely down to metallic iron, Fe <sup>8, 10, 12, 16</sup>.

A common attempt to increase the reactivity and cyclability of iron oxide is the addition of a support. The most commonly used supports are alumina (Al<sub>2</sub>O<sub>3</sub>), magnesium aluminium spinel (MgAl<sub>2</sub>O<sub>4</sub>), and zirconia (ZrO<sub>2</sub>) <sup>10-12, 16-20</sup>. For example, Bohn *et al.* <sup>1</sup> prepared Fe-based oxygen carriers supported on oxides of aluminium, chromium, magnesium, or silicon using wet impregnation (1, 10, or 30 mol % support). Cyclic redox experiments using CO as the reducing gas (850 °C) showed that Fe<sub>2</sub>O<sub>3</sub>-supported on Al<sub>2</sub>O<sub>3</sub> (10 mol %) gives stable and high yields of hydrogen. Kierzkowska *et al.* <sup>10</sup>, using a sol-gel technique, prepared several Al<sub>2</sub>O<sub>3</sub>-supported oxygen carriers containing different weight ratios of Fe<sub>2</sub>O<sub>3</sub> to Al<sub>2</sub>O<sub>3</sub> (0.6-0.9). The oxygen carriers containing 60 wt % Fe<sub>2</sub>O<sub>3</sub> showed a stable hydrogen production of 7.5 mmol/g for over 40 cycles which is, however, lower than the theoretically expected value of 10.0 mmol/g. Kierzkowska *et al.* <sup>10</sup> attributed the stability of this particular oxygen carrier to the formation of the spinel structure FeAl<sub>2</sub>O<sub>4</sub> (hercynite). The thermodynamically limited re-oxidation of FeAl<sub>2</sub>O<sub>4</sub> with steam explained the lower than expected hydrogen



yield. However, oxidation in air re-oxidized  $\text{FeAl}_2\text{O}_4$  back to  $\text{Fe}_2\text{O}_3$  and  $\text{Al}_2\text{O}_3$ . In a further study Imtiaz *et al.*<sup>18</sup> showed that also  $\text{MgAl}_2\text{O}_4$  cannot be considered as a fully inert support as the formation of the  $\text{MgFe}_{1.4}\text{Al}_{0.6}\text{O}_4$  spinel phase was observed during cyclic redox experiments. On the other hand,  $\text{ZrO}_2$  does not seem to form a solid solution with  $\text{Fe}_2\text{O}_3$ <sup>13, 21</sup>.

Besides the phase stability of the oxygen carriers, also the synthesis parameters can affect strongly the performance of the oxygen carriers. Indeed, previous studies that utilized co-precipitation to synthesize CuO-based oxygen carriers for chemical looping reported that the pH value at which the precipitation reaction was performed influenced strongly the redox performance of the oxygen carriers<sup>22, 23</sup>. Owing to its chemical inertness and very low cationic solubility in the Fe–O–Zr system,  $\text{ZrO}_2$  appears to be an attractive support for  $\text{Fe}_2\text{O}_3$ . However, the influence of the (co-precipitation) synthesis parameters on the morphological and redox characteristics of the oxygen carriers has not been studied in detail for the  $\text{Fe}_2\text{O}_3$ – $\text{ZrO}_2$  system yet. Thus, the objective of this study is to assess systematically the effect of the pH value at which precipitation is performed on the structural and redox properties for  $\text{ZrO}_2$ -stabilized  $\text{Fe}_2\text{O}_3$  for chemical looping combustion.

## 2.3 Experimental

$\text{ZrO}_2$ -supported,  $\text{Fe}_2\text{O}_3$ -based oxygen carriers were prepared using co-precipitation. Co-precipitation was performed at four different pH values, *i.e.*, pH 5, pH 7, pH 11, and pH 13, identified from a previously acquired titration curve (Figure S2.1). Additionally, pure  $\text{Fe}_2\text{O}_3$  and  $\text{Al}_2\text{O}_3$ -stabilized  $\text{Fe}_2\text{O}_3$  were synthesized as reference materials. The following nomenclature is used to describe the oxygen carriers: the symbol Fe is followed by an abbreviation for the support (Zr or Al) and the pH value at which precipitation was performed. For example, FeZr-pH 5 refers to an oxygen carrier that was precipitated at pH 5 and is supported on  $\text{ZrO}_2$ . The synthesized oxygen carriers were characterized by X-ray diffraction (XRD), scanning electron microscopy (SEM) equipped with an energy dispersive spectrometer (EDX),  $\text{N}_2$  adsorption, attenuated total reflection Fourier-transformed infrared (ATR-FTIR) spectroscopy, X-ray absorption spectroscopy (XAS), and  $\text{H}_2$ -temperature-programmed reduction (TPR). The electrical conductivity was determined by four-point conductivity measurements. The cyclic redox stability and  $\text{H}_2$  yield were assessed in the fixed bed

reactor over 15 cycles at 800 °C. The synthesized oxygen carriers were reduced by CO and re-oxidized first by steam, followed by re-oxidation in air. Details about the synthesis protocol, material characterization, and cyclic redox tests can be found in the supporting information.

## 2.4 Results and Discussion

### 2.4.1 Morphological and structural characterization of the oxygen carriers

ATR-FTIR spectroscopy was used to characterize the precipitated compounds. The IR spectra acquired are plotted in Figure S2.2. The IR spectra show that precipitation with NaOH leads to the formation of hydrous ferric oxides and hydrous zirconium oxides<sup>24–28</sup>. The hydrous ferric oxide further transformed slowly to goethite ( $\alpha$ -FeOOH), at room temperature. The bands located at 882 and 788  $\text{cm}^{-1}$  are representative of asymmetric Fe–O–H bending vibrations in goethite<sup>26–28</sup>. However, peaks due to Fe–O–H vibrations were only observed for oxygen carriers precipitated at pH 13. This was attributed to (i) an increased crystallinity and (ii) the formation of high molecular weight polycations ( $(\text{Fe}_n(\text{OH})_m^{z+})$ ) under strongly basic conditions. Indeed, Woude *et al.*<sup>26</sup> reported that peaks due to Fe–O–H vibrations cannot be observed in amorphous precipitates. The broad peak in the range 1280–1520  $\text{cm}^{-1}$  is due to asymmetric stretching vibrations of nitrate ions ( $\text{NO}_3^-$ ). This peak is particularly strong for oxygen carriers precipitated at pH 5 and 7 (when compared to pH 11 and pH 13), indicating the incomplete removal of  $\text{NO}_3^-$  during washing for these materials<sup>28</sup>. The crystalline phases in the calcined oxygen carriers were determined using X-ray diffraction (XRD). The diffractograms of the calcined oxygen carriers (Figure 2.1) indicate the presence of hematite ( $\text{Fe}_2\text{O}_3$ ) and two polymorphs of zirconium oxide ( $\text{ZrO}_2$ ), *i.e.*, monoclinic and tetragonal  $\text{ZrO}_2$ , independent of the pH value at which precipitation was performed. It is to be noted that monoclinic  $\text{ZrO}_2$  is the thermodynamically more stable phase whereas tetragonal  $\text{ZrO}_2$  is metastable. The presence of both polymorphs in co-precipitated  $\text{Fe}_2\text{O}_3$ – $\text{ZrO}_2$  has been reported in previous studies<sup>11, 29</sup>. In the diffractogram of  $\text{Al}_2\text{O}_3$ -stabilized  $\text{Fe}_2\text{O}_3$ , weak peaks due to  $\text{Al}_2\text{O}_3$  were detected. Using the Scherrer equation, the average crystallite size of  $\text{Fe}_2\text{O}_3$  was determined as  $\sim 40$  nm (Table S2.1). The crystallite size of  $\text{Fe}_2\text{O}_3$  did not

change significantly with the pH value. It is important to note that the width of a diffraction peak can be affected by inhomogeneous stain and crystal imperfections together with instrumental effects. Therefore, the values calculated for the average crystallite are lower estimates.

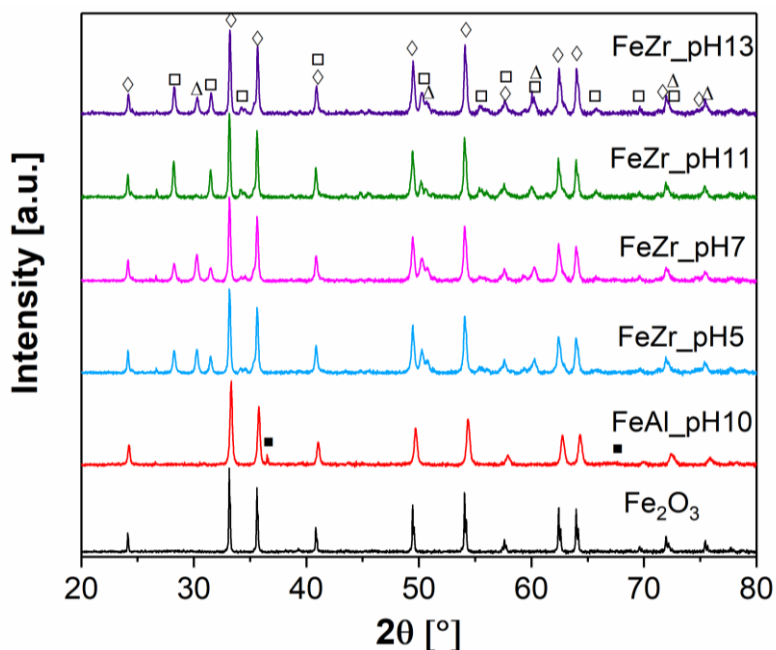


**Figure 2.1:** XRD patterns of unsupported  $\text{Fe}_2\text{O}_3$ ,  $\text{Fe}_2\text{O}_3\text{-ZrO}_2$  precipitated at pH 5, 7, 11, 13, and  $\text{Fe}_2\text{O}_3\text{-Al}_2\text{O}_3$  calcined at  $900^\circ\text{C}$  for 2 h. The following compounds were identified: ( $\diamond$ ) hematite,  $\text{Fe}_2\text{O}_3$ , ( $\square$ ) baddeleyite, m- $\text{ZrO}_2$ , ( $\Delta$ ) t- $\text{ZrO}_2$ , ( $\blacksquare$ ) aluminum oxide,  $\text{Al}_2\text{O}_3$ .

To quantify the phases present in the oxygen carriers and to obtain the cell parameters of the different phases, Rietveld refinement was performed on the acquired XRD data (Table S2.2) of the calcined materials. Rietveld refinement confirms that the quantity of  $\text{Fe}_2\text{O}_3$  is very similar in the oxygen carriers synthesized, *i.e.*, in the range 70–73 wt %. Nonetheless, we observe an increasing fraction of t- $\text{ZrO}_2$  with decreasing pH values. Furthermore, the tetragonal cell volume in FeZr-pH 5 and FeZr-pH 7 is smaller than in FeZr-pH 13. Importantly, when we compare the unit cell volumes of m- $\text{ZrO}_2$  in the synthesized  $\text{Fe}_2\text{O}_3\text{-ZrO}_2$  with pure m- $\text{ZrO}_2$  (synthesized as a reference material), we can conclude that the addition of  $\text{Fe}_2\text{O}_3$  increases the unit cell volume of m- $\text{ZrO}_2$  (Table S2.2). Moreover, the unit cell volume of m- $\text{ZrO}_2$  in  $\text{Fe}_2\text{O}_3\text{-ZrO}_2$  decreases slightly with decreasing pH value. These observations can be explained by the incorporation of  $\text{Fe}^{3+}$  cations in the zirconia structure, substituting

Zr<sup>4+</sup> cations. It has been reported that the incorporation of Fe<sup>3+</sup> in the ZrO<sub>2</sub> lattice stabilizes the metastable t-ZrO<sub>2</sub> phase<sup>21, 30-33</sup>. It should be noted that the mutual cationic solubility in the Fe–O–Zr system is very low, with an equilibrium solubility of Fe<sub>2</sub>O<sub>3</sub> in ZrO<sub>2</sub> of 2 mol % and ZrO<sub>2</sub> in Fe<sub>2</sub>O<sub>3</sub> of 1 mol % at 1373 K<sup>11</sup>.

The local structure around Fe in the synthesized oxygen carriers was probed by XAS. Fe K-edge XANES spectra of the calcined oxygen carriers are shown in Figure 2.2. For comparison, the XANES spectrum of the reference  $\alpha$ -Fe<sub>2</sub>O<sub>3</sub> is also provided. The XANES spectrum of the  $\alpha$ -Fe<sub>2</sub>O<sub>3</sub> reference shows a main absorption edge position at ~7120 eV (corresponding to the 1s  $\rightarrow$  4p electronic transition) and a very intense peak (white line) at ~7132 eV. In addition, a pre-edge peak is observed at ~7112 eV corresponding to the 1s  $\rightarrow$  3d electronic transition. This transition is normally dipole-forbidden in a centrosymmetric site such as a regular octahedron, but it is possible in structures in which the Fe atom is in the symmetrically distorted centre<sup>34-36</sup>. A change in the pre-edge intensity can be an indicator for a distortion around the central atom, *e.g.*, a change in the local oxygen coordination around a Fe atom<sup>35</sup>. Qualitatively, all the oxygen carriers synthesized exhibit similar XANES features as  $\alpha$ -Fe<sub>2</sub>O<sub>3</sub>. This is in agreement with the XRD results. However, the XANES spectra of ZrO<sub>2</sub>-supported Fe<sub>2</sub>O<sub>3</sub> exhibit differences in the relative intensities of the characteristic  $\alpha$ -Fe<sub>2</sub>O<sub>3</sub> features, such as a lower white line intensity and a higher pre-edge peak intensity. The higher intensity of the pre-edge peak indicates that the octahedral environment of the Fe atom is more distorted in ZrO<sub>2</sub>-supported Fe<sub>2</sub>O<sub>3</sub> when compared to (pure)  $\alpha$ -Fe<sub>2</sub>O<sub>3</sub>. It is worth noting that these differences are more evident for oxygen carriers synthesized at lower pH values.

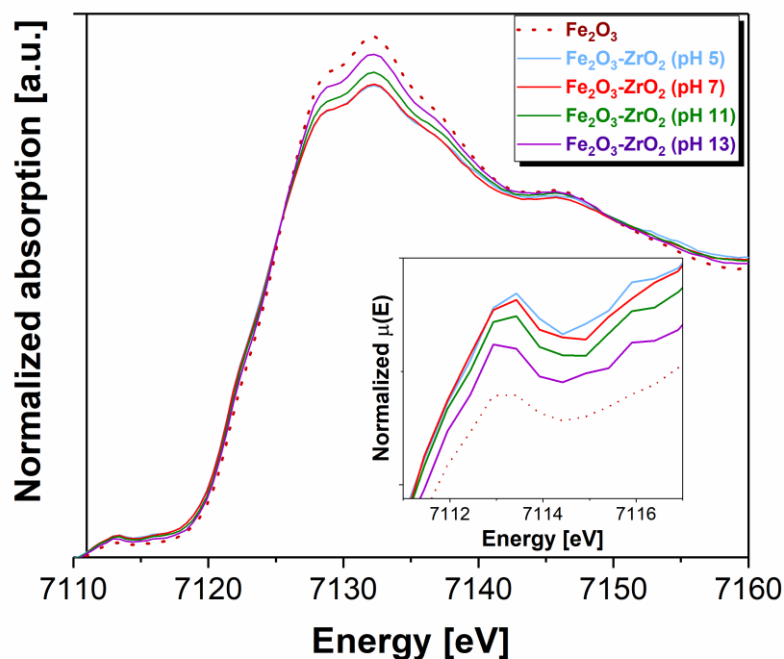


**Figure 2.2:** XANES spectra of calcined oxygen carriers.

The Fourier-transformed (FT) EXAFS functions ( $k^2$ -weighted) of the synthesized oxygen carriers (and the reference  $\alpha$ - $\text{Fe}_2\text{O}_3$ ) are shown in Figure S2.3. In agreement with the XANES and XRD data, all samples exhibit a similar local atomic distribution as the  $\alpha$ - $\text{Fe}_2\text{O}_3$  reference. The peaks located in the range 1–2 Å correspond to Fe–O bonds, and those in the range 2–4 Å are dominated by Fe–Fe next-nearest-neighbour distances. In spite of the similarities with the  $\alpha$ - $\text{Fe}_2\text{O}_3$  reference, a reduction of the amplitude of the first and second peaks can be observed in the synthesized materials. This observation is indicative of a higher degree of disorder in the local structure of these materials. Quantitative structural information was obtained by nonlinear least-squares fitting of the acquired EXAFS functions. A detailed description of the fitting model is given in the supporting information and the structural parameters obtained are reported in Table S2.3. All experimental EXAFS data could be fitted well using the crystallographic structure of  $\alpha$ - $\text{Fe}_2\text{O}_3$ , yielding R-factors in the range 0.011–0.022. Table S2.3 shows that larger values for the Debye–Waller factors ( $\sigma^2$ ) for Fe–O and Fe–Fe spheres were obtained for  $\text{ZrO}_2$ -supported  $\text{Fe}_2\text{O}_3$  when compared to the  $\alpha$ - $\text{Fe}_2\text{O}_3$  reference. In particular,  $\text{Fe}_2\text{O}_3$ – $\text{ZrO}_2$  precipitated at lower pH values exhibit higher  $\sigma^2$  values. The  $\sigma^2$  value for the second Fe–O sphere decreases in the following order:  $\sigma^2_{\text{FeZr-pH 5}} > \sigma^2_{\text{FeZr-pH 7}} > \sigma^2_{\text{FeZr-pH 11}} > \sigma^2_{\text{FeZr-pH 13}} > \sigma^2_{\alpha\text{-Fe}_2\text{O}_3}$ . A higher value of

$\sigma^2$  can be interpreted as a higher disorder in the local environment around a Fe atom. A possible explanation for the increasing disorder and changes in the relative intensity of the pre-edge peak and the white line peak with decreasing pH could be the incorporation of  $\text{Fe}^{3+}$  into  $\text{ZrO}_2$ . However, it is also clear that the majority of Fe is in an  $\alpha\text{-Fe}_2\text{O}_3$  type environment since the observed differences between  $\text{Fe}_2\text{O}_3\text{-ZrO}_2$  and  $\alpha\text{-Fe}_2\text{O}_3$  are relatively small.

We have compared the results of our XAS measurements of  $\text{ZrO}_2$  supported  $\text{Fe}_2\text{O}_3$  to previous literature reports. The shapes of our XANES spectra including pre-edge and post-edge features, the edge positions, and shapes are in close resemblance to  $\text{Fe}_2\text{O}_3\text{-ZrO}_2$  systems reported previously<sup>32, 37, 38</sup>. For example, in the study of Yamamoto *et al.*,<sup>38</sup> an increase in the intensity of the pre-edge peak was also attributed to distortions around the local structure of Fe (due to the formation of a solid solution between zirconia and iron oxide). Similarly, Li *et al.*<sup>32</sup> and Ji *et al.*<sup>38</sup> also observed two distinct peaks at 1.6 and 3 Å in the Fourier transformed EXAFS spectra of  $\text{Fe}_2\text{O}_3\text{-ZrO}_2$ . The first and second peaks were attributed to Fe–O and Fe–Fe scatters, respectively. However, somewhat contradictory, Mastelaro *et al.*<sup>39</sup> and Yamamoto *et al.*<sup>38</sup> assigned the second peak to Fe–Zr scatters.

The surface morphology of the oxygen carriers was characterized with high-resolution scanning electron microscopy (HR-SEM) and is shown in Figure 2.3a–d. For comparison, a HR-SEM image of unsupported  $\text{Fe}_2\text{O}_3$  is given in Figure 2.3e. The surface of the freshly calcined, unsupported  $\text{Fe}_2\text{O}_3$  is composed of nanosized grains. The morphology of the freshly calcined  $\text{ZrO}_2$ -supported  $\text{Fe}_2\text{O}_3$  is affected only marginally by the pH value at which the precipitation was performed. Based on the analysis of 20 grains, the average grain size of  $\text{ZrO}_2$ -supported  $\text{Fe}_2\text{O}_3$  was determined as  $120 \pm 10$  nm, independent of the pH at which precipitation was performed.

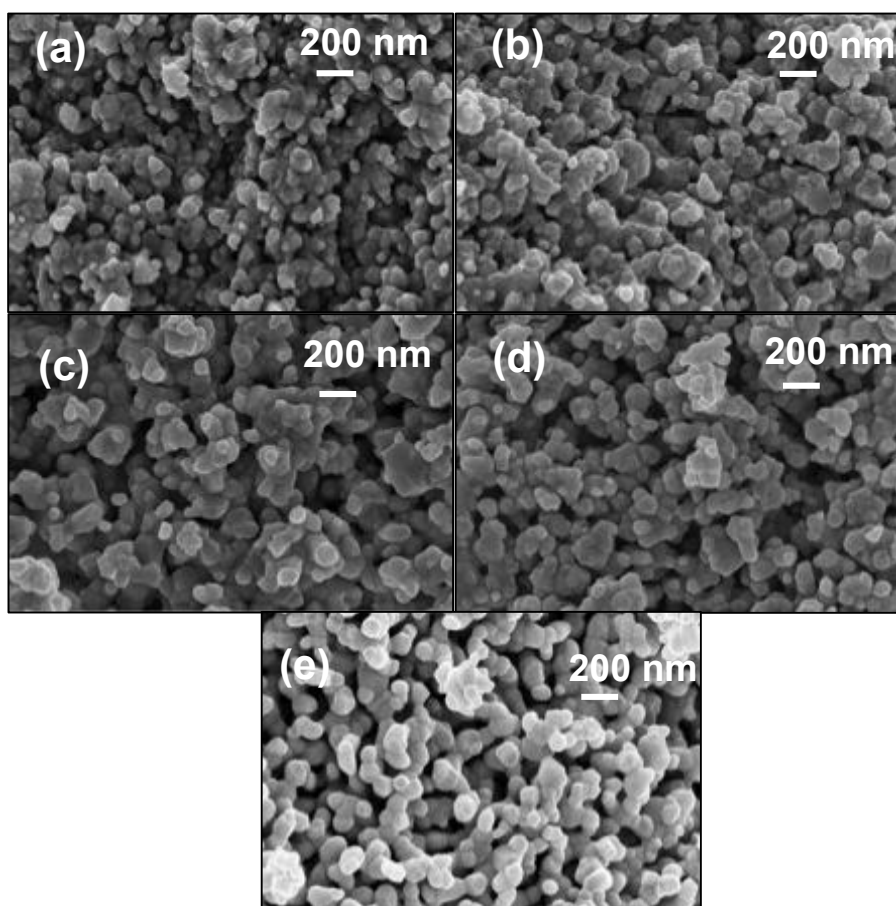


**Figure 2.3:** Electron micrographs of the calcined oxygen carriers (a) FeZr-pH5, (b) FeZr-pH7, (c) FeZr-pH11, (d) FeZr-pH13 and (e) unsupported Fe<sub>2</sub>O<sub>3</sub>.

The BET surface area and BJH pore volume of the calcined oxygen carriers are summarized in Table S2.1. The measurements show that the pH value at which the precipitation was performed did not influence significantly the surface area and pore volume of the calcined oxygen carriers. The lowest surface area of 4 m<sup>2</sup>/g was measured for FeZr-pH 5. The oxygen carriers that were precipitated at pH 7, 11, and 13 had slightly larger surface areas, *i.e.*, 7 m<sup>2</sup>/g. Unsupported Fe<sub>2</sub>O<sub>3</sub> had a very low surface area of 1 m<sup>2</sup>/g, whereas Al<sub>2</sub>O<sub>3</sub>-supported Fe<sub>2</sub>O<sub>3</sub> possessed a comparatively high surface area of 19 m<sup>2</sup>/g, which is in agreement with previous studies<sup>10, 40</sup>.

### 2.4.2 Temperature-programmed reduction

The mass fraction of Fe<sub>2</sub>O<sub>3</sub> in the calcined oxygen carriers was determined using H<sub>2</sub>-temperature-programmed reduction (TPR), shown in Figure S2.4. All oxygen carriers were completely reduced during H<sub>2</sub>-TPR. This was confirmed by XRD analysis

of the reduced samples. Using the TPR profiles, Fe<sub>2</sub>O<sub>3</sub> contents of 73.1, 73.1, 72, and 72.2 wt % were calculated for FeZr-pH 5, FeZr-pH 7, FeZr-pH 11, and FeZr-pH 13, respectively. The iron oxide content determined by H<sub>2</sub>-TPR is substantially higher than the theoretically expected value of 60 wt % Fe<sub>2</sub>O<sub>3</sub>, which can be explained by the partial dissolution of Zr<sup>4+</sup> in aqueous media via Zr(OH)<sub>n</sub>(4-n)<sup>+</sup> (n = 1–5) formation<sup>25, 41</sup>. During washing, soluble polymeric zirconium hydrous oxide species are washed out resulting in an Fe<sub>2</sub>O<sub>3</sub>-rich material. The Fe<sub>2</sub>O<sub>3</sub> content in FeAl-pH 10 was determined as 77 wt %, in good agreement with the theoretically expected value of 73 wt % Fe<sub>2</sub>O<sub>3</sub>.

Figure 2.4 plots the hydrogen consumption during the TPR experiments as a function of temperature. ZrO<sub>2</sub>-supported Fe<sub>2</sub>O<sub>3</sub> showed a three-step reduction mechanism, independent of the pH value at which precipitation was performed. During the first, relatively sharp peak located around ~350 °C, hematite is reduced to magnetite. For FeZr-pH 11 and FeZr-pH 13, the first reduction step was shifted to higher temperatures, *i.e.*, ~400 °C. The reduction peaks for the transitions from magnetite to wüstite and wüstite to metallic iron overlap, leading to a second relatively broad feature in the TPR profile. Deconvolution of the H<sub>2</sub> consumption profiles indicate that the Fe<sub>3</sub>O<sub>4</sub> → FeO and FeO → Fe transitions proceed simultaneously and not sequentially. These results are consistent with the work of Galvita *et al.*<sup>42</sup>, who reported an (apparent) two-step reduction mechanism from Fe<sub>2</sub>O<sub>3</sub> to metallic iron. The peak temperatures of the second and third (fitted) peaks shift to lower temperatures for increasing pH values, indicating a poorer reducibility of FeZr-pH 5 than FeZr-pH 13. The poorer reducibility of FeZr-pH 5 can be attributed to an increased interaction between the oxides of iron and zirconia as confirmed previously by EXAFS modelling (Table S2.3).



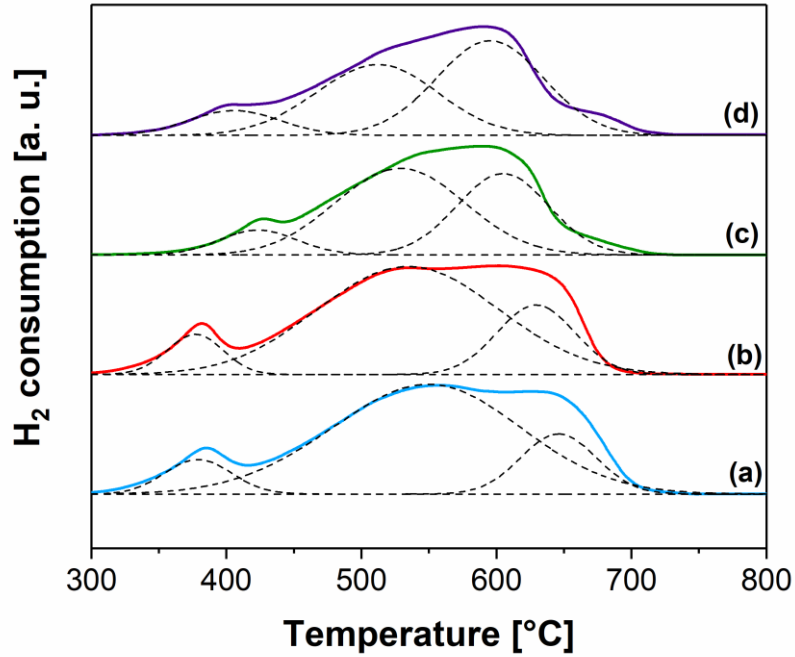


**Figure 2.4:** H<sub>2</sub> consumption during TPR of ZrO<sub>2</sub>-stabilized Fe<sub>2</sub>O<sub>3</sub>. Precipitation was performed at the following pH values: (a) FeZr-pH5, (b) FeZr-pH7, (c) FeZr-pH11 and (d) FeZr-pH13.

### 2.4.3 Redox performance and H<sub>2</sub> production capacity of the synthesized oxygen carriers

The redox characteristics of the synthesized oxygen carriers were evaluated over 15 cycles at 800 °C in a fixed bed reactor. For each cycle, the hydrogen yield was calculated according to

$$N_{H_2} = \dot{N}_{N_2} \times \int \frac{y_{H_2}}{1 - y_{H_2}} dt$$

where  $N_{H_2}$  is the number of moles of H<sub>2</sub> produced,  $\dot{N}_{N_2}$  is the molar flow rate of N<sub>2</sub>, and  $y_{H_2}$  is mole fraction of hydrogen in the gas leaving the fixed bed. Figure 2.5 plots the quantity of hydrogen produced, expressed as mmol H<sub>2</sub>/g oxygen carrier, as a function of the cycle number. For unsupported iron oxide the hydrogen yield decreased rapidly over 15 cycles, viz. from 13 mmol H<sub>2</sub>/g in the first to only 4.1 mmol H<sub>2</sub>/g in the 15<sup>th</sup> cycle. The theoretically expected value is 16.7 mmol H<sub>2</sub>/g Fe<sub>2</sub>O<sub>3</sub>. The rapidly

decreasing hydrogen yield of unsupported  $\text{Fe}_2\text{O}_3$  has been observed previously by Bohn *et al.*<sup>8</sup> and was attributed to severe sintering. Severe sintering and substantial morphological changes of unsupported iron oxide over multiple redox cycles are confirmed by HR-SEM (Figure 2.6e). Bohn *et al.*<sup>8</sup> reported that for unsupported  $\text{Fe}_2\text{O}_3$  stable  $\text{H}_2$  yields could be obtained only when the reduction was limited to  $\text{FeO}$ . However, since the oxidation of  $\text{Fe}$  to  $\text{Fe}_3\text{O}_4$  provides 4 times more hydrogen when compared to the  $\text{FeO}$ – $\text{Fe}_3\text{O}_4$  transition, oxygen carriers that allow the full reduction to  $\text{Fe}$  are highly desirable.

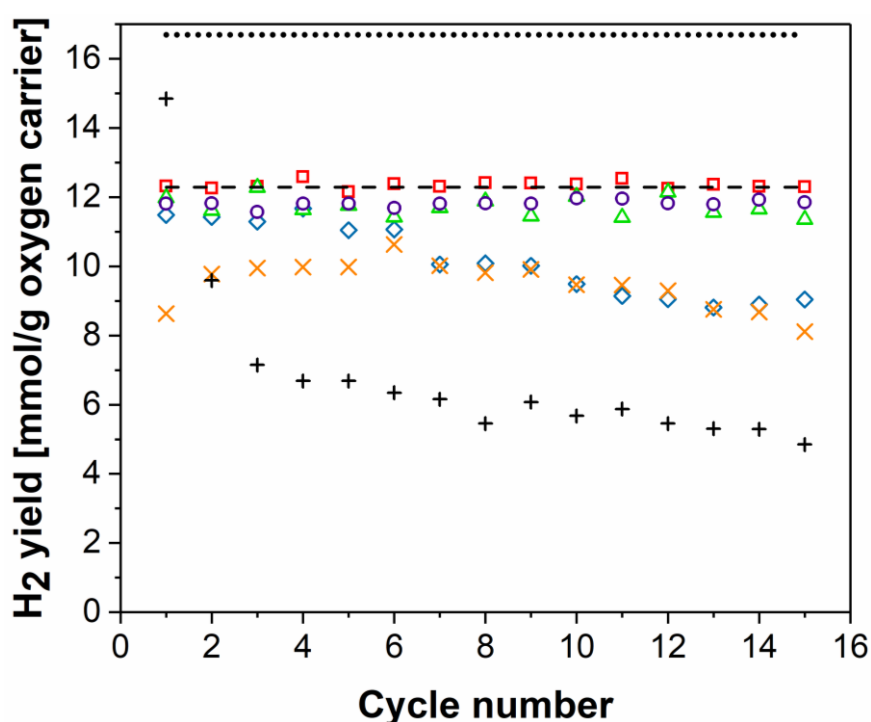


**Figure 2.5:**  $\text{H}_2$  yield as a function of cycle number: (◇) FeZr-pH5, (□) FeZr-pH7, (△) FeZr-pH11, (○) FeZr-pH13, (×) FeAl-pH10, (+) unsupported  $\text{Fe}_2\text{O}_3$ . The dashed and dotted horizontal lines give the theoretically expected quantities of hydrogen, *i.e.* 12.3 mmol  $\text{H}_2/\text{g}$  and 16.7 mmol  $\text{H}_2/\text{g}$  for oxygen carriers containing 73.6 and 100 wt. %  $\text{Fe}_2\text{O}_3$ , respectively (assuming a full reduction to  $\text{Fe}$ ).

It is believed that material sintering causes an appreciable decrease in the rate of reduction, leading in turn to incomplete reduction and low  $\text{H}_2$  yields during re-oxidation. Indeed, the presence of  $\text{Fe}_3\text{O}_4$  and  $\text{FeO}$  in the diffractogram of cycled and reduced  $\text{Fe}_2\text{O}_3$  (Figure S2.5a) supports this hypothesis. Similarly, the diffractogram of cycled (oxidized), unsupported  $\text{Fe}_2\text{O}_3$  showed peaks due to  $\text{Fe}_2\text{O}_3$ ,  $\text{Fe}_3\text{O}_4$ , and  $\text{FeO}$  indicating that  $\text{Fe}_2\text{O}_3$  was not re-oxidized fully (Figure S2.5b). Supporting iron oxide on  $\text{Al}_2\text{O}_3$

resulted in an improved redox performance when compared to unsupported Fe<sub>2</sub>O<sub>3</sub>. However, the H<sub>2</sub> yield after 15 cycles (9 mmol H<sub>2</sub>/g) is still substantially below the theoretically expected value of 12.3 mmol H<sub>2</sub>/g. The low H<sub>2</sub> yield is due to the formation of hercynite (FeAl<sub>2</sub>O<sub>4</sub>), as verified by XRD (Figure S2.5a); the formation of hercynite is thermodynamically favoured for  $8 \times 10^{-2} < p_{CO_2}/p_{CO} < 1.8 \times 10^5$  and  $1 \times 10^{-2} < p_{H_2O}/p_{H_2} < 2.1 \times 10^5$ ,<sup>10</sup> but undesirable since re-oxidation of FeAl<sub>2</sub>O<sub>4</sub> with steam is thermodynamically limited. In comparison to Al<sub>2</sub>O<sub>3</sub>-supported Fe<sub>2</sub>O<sub>3</sub>, ZrO<sub>2</sub>-stabilized Fe<sub>2</sub>O<sub>3</sub> precipitated at pH 7, 11, or 13 showed very high and stable hydrogen yields close to the theoretically expected value of 12.3 mmol H<sub>2</sub>/g oxygen carrier. The only unstable ZrO<sub>2</sub>-supported Fe<sub>2</sub>O<sub>3</sub> is FeZr-pH 5 that starts to deactivate from the sixth cycle onward.

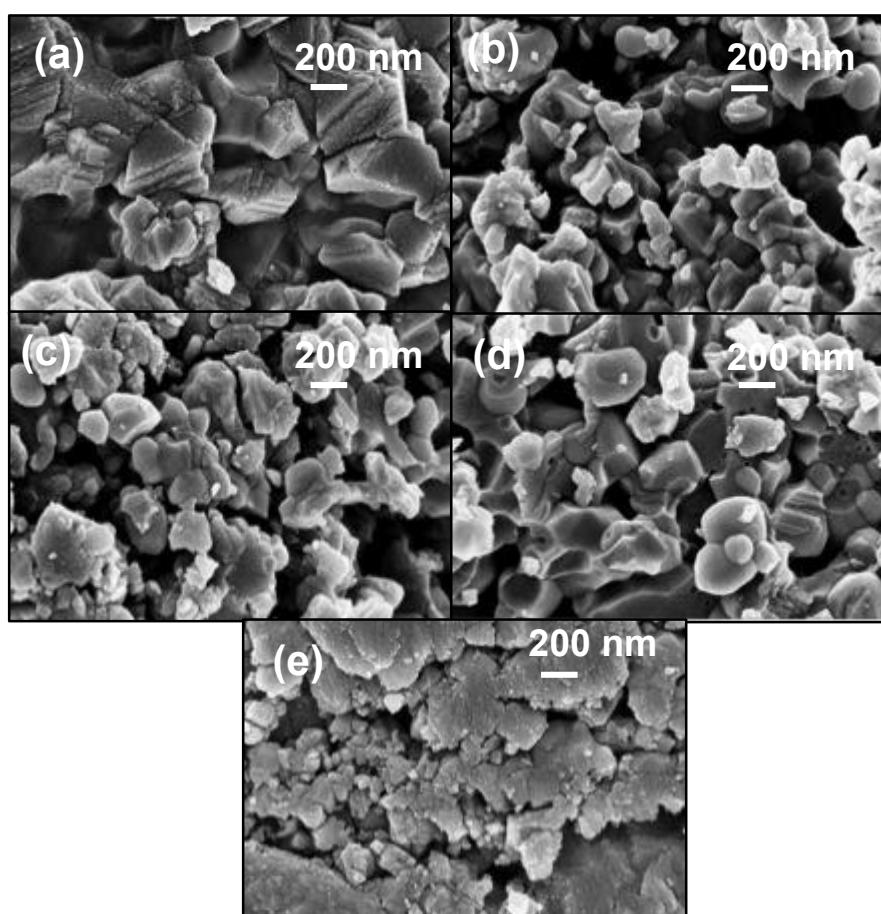


**Figure 2.6:** Electron micrographs of oxygen carriers that have undergone 15 redox cycles (oxidized state): (a) FeZr-pH 5, (b) FeZr-pH 7, (c) FeZr-pH 11, (d) FeZr-pH 13 and (e) unsupported Fe<sub>2</sub>O<sub>3</sub>.

The improved performance of supported Fe<sub>2</sub>O<sub>3</sub> (when compared to pure Fe<sub>2</sub>O<sub>3</sub>) was attributed previously to a higher porosity and an increased sintering resistance,

leading to higher surface area materials <sup>43</sup>. However, the ZrO<sub>2</sub>-stabilized iron oxide reported here has a very low surface area of <1 m<sup>2</sup>/g after 15 redox cycles (Table S2.4). Thus, the high and stable hydrogen yield of ZrO<sub>2</sub>-supported Fe<sub>2</sub>O<sub>3</sub> precipitated at pH 7, 11, or 13 cannot be attributed to surface area effects. Instead, we speculate that the redox characteristics of the oxygen carriers are more affected by solid-state ionic diffusion than by intraparticle gaseous diffusion. This hypothesis was also put forward by Li *et al.* <sup>43</sup> and Tan *et al.* <sup>44</sup> For example, Li *et al.* <sup>43</sup> probed the oxidation mechanism of unsupported and TiO<sub>2</sub>-supported iron (oxides) using inert marker experiments. It was argued that the transport of oxygen ions through distortions and oxygen vacancies (*i.e.*, ionic diffusivity) rather than porosity is the controlling mechanism during oxidation. These vacancies are formed as a result of substitutional defects that form at the interfaces between iron- and TiO<sub>2</sub>-rich zones in the crystal structure <sup>43,45</sup>. Using DFT calculations and molecular dynamic simulations, Tan *et al.* <sup>44</sup> investigated the influence of ZrO<sub>2</sub> on the electronic structure of Fe<sub>2</sub>O<sub>3</sub> and its reaction with CO. The calculations showed that (i) compared to pure Fe<sub>2</sub>O<sub>3</sub>, ZrO<sub>2</sub> increased the adsorption energy of CO on Fe<sub>2</sub>O<sub>3</sub> from 0.533 to 2.134 eV, promoting in turn the chemisorption of CO on Fe sites, and (ii) the activation energy of the reaction between chemisorbed CO and lattice oxygen of Fe<sub>2</sub>O<sub>3</sub> decreased from 2.59 to 0.826 eV. While these theories can explain the favourable redox performance of FeZr-pH 7, FeZr-pH 11, and FeZr-pH 13, it fails to explain the deactivation of FeZr-pH 5. Therefore, the electrical conduction and charge transport properties of the freshly calcined oxygen carriers were analysed in more detail using four-point conductivity measurements (Figure 2.7).

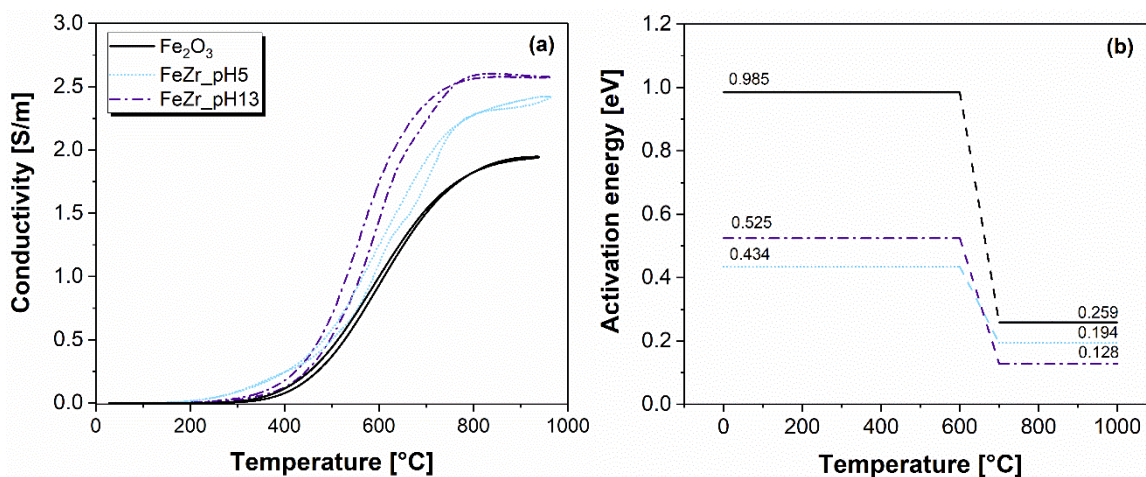


**Figure 2.7:** (a) Conductivity as a function of temperature and (b) activation energy for charge transport. The charge transport characteristics of the following oxygen carriers were assessed: (—) Fe<sub>2</sub>O<sub>3</sub>, (.....) FeZr-pH5 and (-·-·-) FeZr-pH13.

XRD pattern and energy-dispersive X-ray spectroscopy (EDX) maps of the FeZr-pH 5 and FeZr-pH13 pellets that were used for the conductivity measurements are presented in Figures S2.6 and S2.7, respectively. The XRD spectra confirmed that both of the pellets were composed of Fe<sub>2</sub>O<sub>3</sub> and m-ZrO<sub>2</sub>. We could not observe the metastable tetragonal zirconia phase in the pellets. Our measurements show that ZrO<sub>2</sub>-supported Fe<sub>2</sub>O<sub>3</sub> possessed a higher total conductivity when compared to unsupported Fe<sub>2</sub>O<sub>3</sub>. The total conductivity increases in the following order Fe<sub>2</sub>O<sub>3</sub> < FeZr-pH 5 < FeZr-pH 13. The activation energy for charge transport was determined using an Arrhenius relationship (Figure 2.7b). In Figure 2.7b, two regions, *i.e.*, a low- and a high-temperature regime (below and above 600 °C, respectively), can be identified. In the high-temperature region, *i.e.*, the region relevant for CLC, the activation energies were 0.259, 0.194, and 0.128 eV for unsupported Fe<sub>2</sub>O<sub>3</sub>, FeZr-pH 5, and FeZr-pH 13, respectively (Figure 2.7). The lower activation energy for charge transport for Fe<sub>2</sub>O<sub>3</sub>-ZrO<sub>2</sub> when compared to unsupported Fe<sub>2</sub>O<sub>3</sub> suggests that the presence of ZrO<sub>2</sub> enhances the solid-state diffusion of oxygen anions and electrons in Fe<sub>2</sub>O<sub>3</sub>. This is in agreement with the DFT calculations and inert marker experiments of Li *et al.*<sup>43</sup> From Figure 2.7b, we can also observe that an increasing pH value during precipitation results in a decreasing activation energy for charge transport. We believe that the faster transport of ionic and electronic carriers leads to a higher reduction (and oxidation) rate and, thus, explains the high cyclic oxygen carrying capacity of FeZr-pH 13 when compared to FeZr-pH 5 and Fe<sub>2</sub>O<sub>3</sub>.

In order to compare quantitatively the reduction rates of FeZr-pH 5 (deactivating) and FeZr-pH 13 (cyclically stable), the conversion of the oxygen carrier is plotted as a function of time in Figure 2.8. During a redox cycle the reduction time was fixed to 15 min. Already in the first reduction cycle, the conversion of FeZr-pH 5 is appreciably slower than that of FeZr-pH 13, in agreement with the H<sub>2</sub>-TPR experiments. With cycle number the apparent reduction rate decreased dramatically for FeZr-pH 5, whereas the overall reduction duration of FeZr-pH 13 is fairly unaffected by the cycle number. Thus, owing to the decreasing reduction rates of FeZr-pH 5 with cycle number, FeZr-pH 5 is not fully reduced within 15 min from cycle number six onward, explaining the decreasing H<sub>2</sub> yields of this material. Furthermore, the diffractograms of the cycled (oxidized) FeZr-pH 5 showed the presence of Fe<sub>2</sub>O<sub>3</sub>, Fe<sub>3</sub>O<sub>4</sub>, and FeO, indicating that FeZr-pH 5 could not re-oxidized fully in the fixed bed reactor due to a decrease in the rate of oxidation (Figure S2.5b).

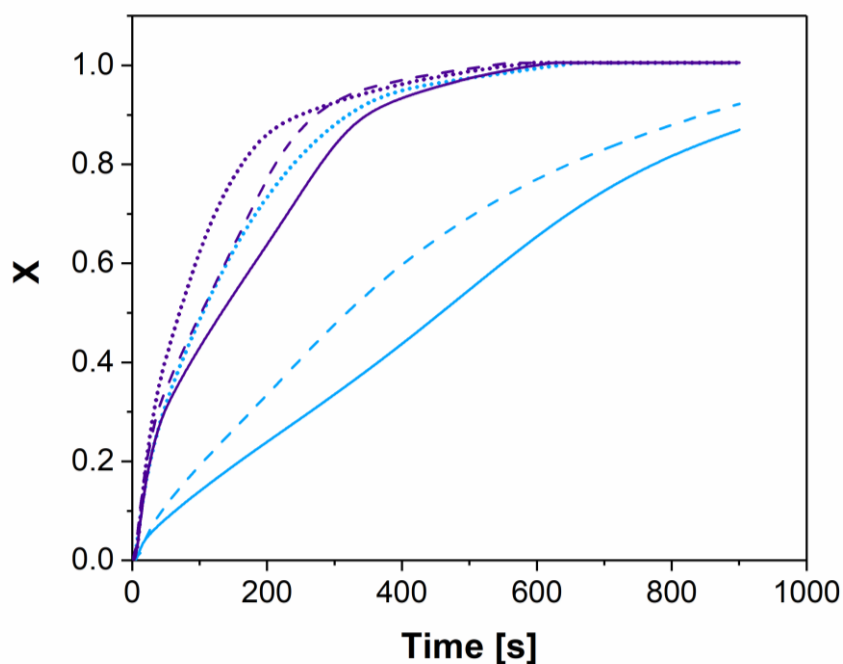


**Figure 2.8:** Effect of cycle number [(.....) 1<sup>st</sup> cycle, (- - -) 6<sup>th</sup> cycle and (—) 10<sup>th</sup> cycle] on fractional conversion for FeZr-pH5 (blue) and FeZr-pH13 (purple).

To explain in more detail, the decreasing reduction kinetics of FeZr-pH 5, energy-dispersive X-ray spectroscopy (EDX) was used to determine the surface composition and the distribution of the different phases in FeZr-pH 5 and FeZr-pH 13 (freshly calcined and after 15 redox cycles, oxidized state). EDX mapping of the freshly



calcined oxygen carriers (Figure 2.9a, b) revealed that in FeZr-pH 13 the two phases  $\text{Fe}_2\text{O}_3$  and  $\text{ZrO}_2$ , were distributed more homogeneously than in FeZr-pH 5. After cycling appreciable difference appeared in the surface composition of FeZr-pH 5 and FeZr-pH 13 in both reduced (Figure S2.8a, b) and oxidized (Figure 2.9c, d) states. For FeZr-pH 13, some phase separation occurred; however,  $\text{Fe}_2\text{O}_3$  and  $\text{ZrO}_2$  were still distributed fairly homogeneously. On the other hand, EDX mapping of FeZr-pH 5 revealed a very heterogeneous distribution of the two metal oxides with big clusters of iron oxide and  $\text{ZrO}_2$  forming after 15 redox cycles.

The titration curves of pure iron(III) nitrate and zirconium-(IV) oxynitrate solutions with NaOH (Figure S2.9) show that iron and zirconium precursors do not precipitate at the same pH. Thus, it is conceivable that the pH value at which precipitation is performed influences crucially the degree of mixing between the different phases. Indeed, EDX mapping of the freshly calcined oxygen carriers (Figure 2.9) indicates that the degree of mixing between the iron and zirconium containing phases are affected by the pH, leading in turn to very different conductivity and redox behaviour. In addition, the heterogeneous distribution of the  $\text{Fe}_2\text{O}_3$  and  $\text{ZrO}_2$  phases in FeZr-pH 5 affects negatively charge carrier transport. Thus, we attribute the decreasing rate of reduction and redox stability of FeZr-pH 5 to large-scale phase separation.

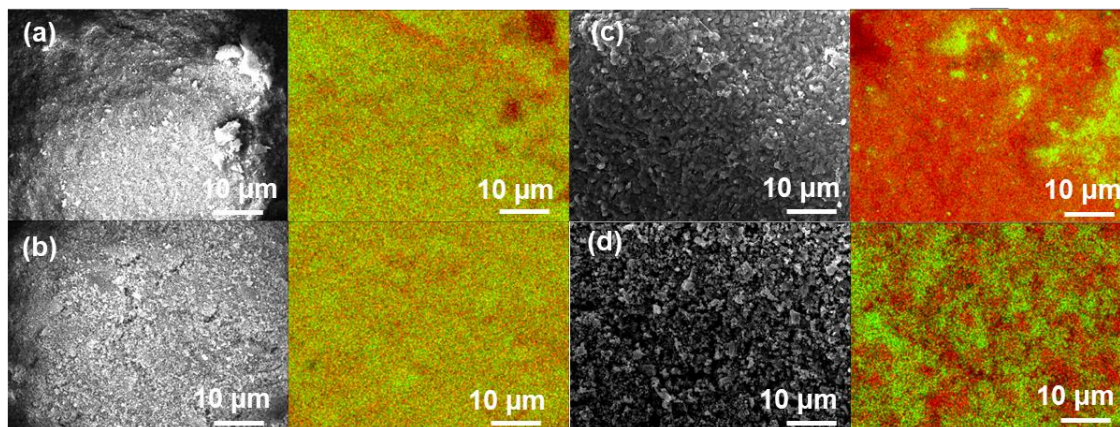


**Figure 2.9:** EDX maps of (a) calcined FeZr-pH5 and (b) calcined FeZr-pH13 (c) cycled and oxidized FeZr-pH5 and (d) cycled FeZr-pH13. The green colour represents Zr and the red colour Fe.

## 2.4.4 Purity of hydrogen

The Boudouard reaction,  $2\text{CO} \leftrightarrow \text{CO}_2 + \text{C(s)}$ , a side reaction in the proposed process, would lead to  $\text{CO}_x$ -contaminated hydrogen during re-oxidation. Indeed, during steam oxidation CO formation was observed at the start of the reaction, suggesting that some carbon deposition occurred. The average CO contamination of the hydrogen produced, *i.e.*,  $[\text{CO}]/([\text{H}_2] + [\text{CO}])$ , for FeZr-pH 5 and FeZr-pH 13, as a function of the duration of the  $\text{N}_2$  purge between the reduction and oxidation steps is tabulated in Table 2.1. Purging with  $\text{N}_2$  for 1 min before the oxidation step gave CO levels of <1000 ppm.

Another interesting finding of this study was that after 15 redox cycles for FeZr-pH 5 the CO contamination of hydrogen was notably lower than for FeZr-pH 13. This observation would support the hypothesis that metallic iron catalyses the Boudouard reaction. For FeZr-pH 13, CO contamination of the hydrogen produced could be avoided completely when the hydrogen yield was limited to 88% (by decreasing the reduction time from 15 to 8 min). A decrease of the reduction time implies an only partial reduction of FeO to metallic iron, thus inhibiting effectively the Boudouard reaction.

**Table 2.1:** Carbon deposition as a function of cycle number, duration of reduction and  $\text{N}_2$  purge.

	1 min purging			
	1 <sup>st</sup> cycle		15 <sup>th</sup> cycle	
		H <sub>2</sub> yield		H <sub>2</sub> yield
	CO (ppm)	(%)	CO (ppm)	(%)
FeZr-pH13	862	97	907	97
FeZr-pH 5	839	95	135	75
	30 min purging			
	15 min reduction		8 min reduction	
		H <sub>2</sub> yield		H <sub>2</sub> yield
	CO (ppm)	(%)	CO (ppm)	(%)
FeZr-pH13	27	97	-	88
FeZr-pH 5	32	95	5	88



## 2.5 Conclusions

In this study, we have investigated in detail the effect of the key synthesis parameter (*i.e.*, the pH value) on the morphological properties, phase changes, chemical composition, local structure, and redox characteristics of ZrO<sub>2</sub>-supported Fe<sub>2</sub>O<sub>3</sub>. Here, unsupported Fe<sub>2</sub>O<sub>3</sub> and Fe<sub>2</sub>O<sub>3</sub>-Al<sub>2</sub>O<sub>3</sub> were used as reference materials. XAS measurements revealed that the static disorder of the local environment around Fe increased with decreasing pH value at which precipitation was performed. Also, the unit cell volume of m-ZrO<sub>2</sub> obtained through Rietveld refinement was smaller for the oxygen carriers precipitated at low pH values when compared to pure m-ZrO<sub>2</sub>. These two observations can be explained by the substitution of Zr<sup>4+</sup> by Fe<sup>3+</sup>. H<sub>2</sub>-TPR experiments showed that the interaction between the oxides of iron and zirconia influenced the reduction characteristics, leading to a slower rate of reduction for the oxygen carriers that were precipitated at low pH values. Cyclic redox tests demonstrated that unsupported Fe<sub>2</sub>O<sub>3</sub> deactivated rapidly when fully reduced to Fe. Supporting iron oxide on Al<sub>2</sub>O<sub>3</sub> resulted in an improved redox stability although the H<sub>2</sub> yield was lower than the theoretically expected value due to the formation of unreactive FeAl<sub>2</sub>O<sub>4</sub>. On the other hand, zirconia supported Fe<sub>2</sub>O<sub>3</sub> (precipitated at pH 7, 11, and 13) demonstrated excellent redox characteristics, *i.e.*, a very high and stable H<sub>2</sub> yield over 15 redox cycles. Only the oxygen carrier precipitated at pH 5 was found to deactivate with cycle number. The deactivation of FeZr-pH 5 was attributed to a “demixing” of the Fe<sub>2</sub>O<sub>3</sub> and ZrO<sub>2</sub> phases with cycle number, thus reducing the materials conductivity and reduction rate.

## 2.6 References

1. C. D. Bohn, J. P. Cleeton, C. R. Müller, S. Y. Chuang, S. A. Scott, J. S. Dennis, *Energy Fuels*, 2010, **24**, 4025–4033.
2. Y. U. Shi, A. H. Bork, S. Schweiger, J. L. Rupp, *M. Nat. Mater.* 2015, **14**, 721–727.
3. A. H. Bork, M. Kubicek, M. Struzik, J. L. Rupp, *M. J. Mater. Chem. A*, 2015, **3**, 15546–15557.
4. M. Broda, A. M. Kierzkowska, D. Baudouin, Q. Imtiaz, C. Coperet, C. R. Müller, *ACS Catal.*, 2012, **2**, 1635–1646.
5. W. C. Chueh, C. Falter, M. Abbott, D. Scipio, P. Furler, S. M. Haile, A. Steinfeld, *Science*, 2010, 330, 1797–1801.
6. C. Jarrett, W. Chueh, C. Yuan, Y. Kawajiri, K. H. Sandhage, A. Henry, *Sol. Energy* 2016, **123**, 57–73.
7. Hydrogen Production & Distribution, *IEA Energy Technology Essentials*, 2007 pp 1–4 <http://www.iea.org/publications/freepublications/publication/essentials5.pdf> Date of access: 06.08.2016.
8. C. D. Bohn, C. R. Müller, J. P. Cleeton, A. N. Hayhurst, J. F. Davidson, S. A. Scott, J. S. Dennis, *Ind. Eng. Chem. Res.* 2008, **47**, 7623–7630.
9. Messerschmitt, A. Process of Producing Hydrogen. Google Patents: 1910.
10. A. M. Kierzkowska, C. D. Bohn, S. A. Scott, J. P. Cleeton, J. S. Dennis, C. R. Müller, *Ind. Eng. Chem. Res.* 2010, **49**, 5383–5391.
11. W. Liu, J. S. Denis, S. A. Scott, *Ind. Eng. Chem. Res.* 2012, **51**, 16597–16609.
12. A. Thursfield, A. Murugan, R. Franca, I. S. Metcalfe, *Energy Environ. Sci.* 2012, **5**, 7421–7459.
13. M. Keller, H. Leion, T. Mattisson, H. Thunman, *Energy Fuels* 2014, **28**, 3833–3840.
14. M. Rydén, M. Arjmand, *Int. J. Hydrogen Energy* 2012, **37**, 4843–4854.
15. D. Mei, A. Abad, H. Zhao, J. Adánez, C. Zheng, *Energy Fuels* 2014, **28**, 7043–7052.
16. J. Adanez, A. Abad, F. Garcia-Labiano, P. Gayan, L. F. de Diego, *Prog. Energy Combust. Sci.* 2012, **38**, 215–282.
17. V. Galvita, K. Sundmacher, *Chem. Eng. J.* 2007, **134**, 168–174.
18. Q. Imtiaz, N. S. Yuzbasi, P. M. Abdala, A. M. Kierzkowska, W. van Beek, M. Broda, C. R. Müller, *J. Mater. Chem. A* 2016, **4**, 113–123.
19. K. Otsuka, T. Kaburagi, C. Yamada, S. Takenaka, *J. Power Sources* 2003, **122**, 111–121.
20. S. Takenaka, T. Kaburagi, C. Yamada, K. Nomura, K. Otsuka, *J. Catal.* 2004, **228**, 66–74.
21. S. Saha, A. Nandy, A. K. Meikap, S. K. Pradhan, *Mater. Res. Bull.* 2015, **68**, 66–74.
22. S. Y. Chuang, J. S. Dennis, A. N. Hayhurst, S. A. Scott, *Combust. Flame* 2008, **154**, 109–121.

23. Q. Imtiaz, A. M. Kierzkowska, C. R. Müller, *ChemSusChem* 2012, **5**, 1610–1618.
24. G. Y. Guo, Y. L. Chen, W. J. Ying, Thermal, *Mater. Chem. Phys.* 2004, **84**, 308–314.
25. T. Kobayashi, T. Sasaki, I. Takagi, H. Moriyama, *J. Nucl. Sci. Technol.* 2007, **44**, 90–94.
26. J. H. A. Van Der Woude, P. L. De Bruyn, *Colloids Surf.* 1983, **8**, 55–78.
27. X. F. Wang, L. J. Andrews, *Phys. Chem. A* 2006, **110**, 10035–10045.
28. M. Zic, M. Ristic, Music, S. *J. Mol. Struct.* 2011, **993**, 115–119.
29. S. N. Basahel, T. T. Ali, K. Narasimharao, A. A. Bagabas, M. Mokhtar, *Mater. Res. Bull.* 2012, **47**, 3463–3472.
30. B. A. Boukamp, T. P. Raming, A. J. A. Winnubst, H. Verweij, *Solid State Ionics* 2003, **158**, 381–394.
31. A. Lamperti, E. Cianci, R. Ciprian, D. Sangalli, A. Debernardi, *Thin Solid Films* 2013, **533**, 83–87.
32. P. Li, I. W. Chen, J. E. Penner-Hahn, *J. Am. Ceram. Soc.* 1994, **77**, 118–128.
33. Popović, S. Grzeta, B. Czako-Nagy, I. Musić, S. *J. Alloys Compd.* 1996, **241**, 10–15.
34. E. de Smit, A. M. Beale, S. Nikitenko, B. M. Weckhuysen, *J. Catal.* 2009, **262**, 244–256.
35. M. Holzapfel, O. Proux, P. Strobel, C. Darie, M. Borowski, M. Morcrette, *J. Mater. Chem.* 2004, **14**, 102–110.
36. I. Moog, C. Feral-Martin, M. Duttine, A. Wattiaux, C. Prestipino, S. Figueroa, J. Majimel, A. Demourgues, *J. Mater. Chem. A* 2014, **2**, 20402–20414.
37. W. Ji, Y. Kuo, S. Shen, S. Li, H. Wang, *Stud. Surf. Sci. Catal.* 1993, **75**, 2059–2062.
38. T. Yamamoto, T. Tanaka, S. Takenaka, S. Yoshida, T. Onari, Y. Takahashi, T. Kosaka, S. Hasegawa, M. Kudo, *J. Phys. Chem. B* 1999, **103**, 2385–2393.
39. V. R. Mastelaro, V. Briois, D. P. de Souza, C. L. Silva, *J. Eur. Ceram. Soc.* 2003, **23**, 273–282.
40. P. R. Kidambi, J. P. Cleeton, S. A. Scott, J. S. Dennis, C. D. Bohn, *Energy Fuels* 2011, **26**, 603–617.
41. A. Veyland, L. Dupont, J.-C. Pierrard, J. Rimbault, M. Aplincourt, *Eur. J. Inorg. Chem.* 1998, **1998**, 1765–1770.
42. V. Galvita, K. Sundmacher, *J. Mater. Sci.* 2007, **42**, 9300–9307.
43. F. Li, Z. Sun, S. Luo, L. S. Fan, *Energy Environ. Sci.* 2011, **4**, 876–880.
44. Q. W. Tan, Q. Qin, C. Chen, W. Dong, Li, Y. Yang, *Appl. Surf. Sci.* 2012, **258**, 10022–10027.
45. L. Qin, Cheng, Z. Fan, J. A. Kopechek, D. Xu, D. Deshpande, N. Fan, L. S. J. *Mater. Chem. A* 2015, **3**, 11302–11312.

## 2.7 Supporting Information

### Experimental details

#### *Synthesis of the oxygen carriers*

Fe<sub>2</sub>O<sub>3</sub>-based, ZrO<sub>2</sub>-supported oxygen carriers were synthesized using co-precipitation. Co-precipitation was performed at four different pH values identified from a previously acquired titration curve (Figure S2.1) using a 1 M solution of iron (III) nitrate (Fe(NO<sub>3</sub>)<sub>3</sub>·9H<sub>2</sub>O, Acros Organics) and zirconium (IV) oxynitrate hydrate (ZrO(NO<sub>3</sub>)<sub>2</sub>·xH<sub>2</sub>O, Sigma Aldrich). Titration was performed with a 2 M solution of sodium hydroxide (NaOH, Fisher Scientific). The following pH values were chosen for precipitation: (i) pH 5: Acidic region before the equivalence point, (ii) pH 7: Equivalence point, (iii) pH 11: Slightly alkaline medium after the equivalence point and (iv) pH 13: Highly alkaline region.

In a typical experiment, 1 M aqueous solutions of iron nitrate and zirconium oxynitrate were prepared. The ratio of the quantity of iron nitrate to zirconium oxynitrate was chosen such that the final material contained 60 wt. % Fe<sub>2</sub>O<sub>3</sub> (assuming full precipitation). Precipitation was performed by adding NaOH dropwise under magnetic stirring to the solution containing the metal nitrates until the desired pH value was reached. The stirring rate was adjusted according to the viscosity of the slurry. The resulting precipitate was aged for 2 hours at room temperature. Subsequently, the slurry was washed with deionized water until the conductivity of the filtrate was below 50 μS/cm. The filtered precipitate was dried in an oven at 100 °C over night and calcined in a muffle furnace at 900 °C for two hours. The calcined material was crushed and sieved into the size range of 300 – 425 μm.

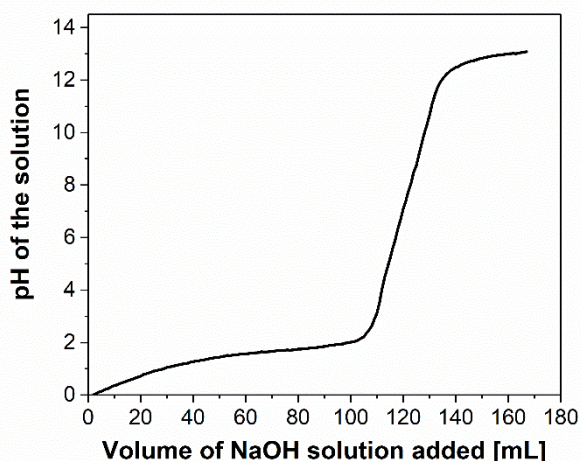


**Figure S2.1:** Titration curve of 1 M mixed nitrate solution with 2 M NaOH solution.

For the synthesis of  $\text{Al}_2\text{O}_3$ -stabilized  $\text{Fe}_2\text{O}_3$ , ammonia (aqueous solution, 28–30 %  $\text{NH}_3$ , Fisher Scientific) was used as the precipitating base to avoid the introduction of  $\text{Na}^+$  ions which affect the formation of a solid solution between iron oxide and alumina. For  $\text{Al}_2\text{O}_3$ -stabilized  $\text{Fe}_2\text{O}_3$  precipitation was performed at pH 10. Unsupported  $\text{Fe}_2\text{O}_3$  was precipitated at pH 13 using NaOH as the precipitation agent.

### ***Characterization of the oxygen carriers***

The chemical composition of the calcined oxygen carriers was characterized by X-ray diffraction (XRD) using a Bruker AXS D8 Advance X-ray diffractometer mounted with a Lynxeye superspeed detector, operated at 40 kV and 40 mA ( $\text{CuK}\alpha$  radiation). The step size was  $0.275^\circ/\text{s}$  and diffraction patterns were recorded in the range of  $2\theta = 20\text{--}80^\circ$ . The surface morphology of the fresh and cycled oxygen carriers was assessed using scanning electron microscopy (Zeiss Gemini 1530 FEG). Prior to imaging, the materials were sputter-coated (MED 010) with an approximately 5 nm-thick layer of platinum. Additionally, a Leo Gemini 1530 scanning electron microscope (SEM) equipped with an energy dispersive spectrometer (EDX) was used to probe the elemental composition of the surface of the materials before and after redox cycles. The surface area and pore size distribution of the calcined oxygen carriers were determined using a Quantochrome NOVA 4000e  $\text{N}_2$  adsorption analyzer. Prior to the acquisition of the  $\text{N}_2$  isotherms, the samples were degassed at  $300^\circ\text{C}$  for two hours. BET<sup>1</sup> and BJH<sup>2</sup> models were used to calculate, respectively, the surface area and

the pore size distribution of the materials. The precipitated products were analyzed by attenuated total reflection Fourier-transformed infrared (ATR-FTIR) spectroscopy (Thermo Scientific Nicolet iS10). The ATR-FTIR spectra were collected with a resolution of  $4\text{ cm}^{-1}$  (32 scan average).

The electrical conductivity was determined by 4-point conductivity measurement on sintered pellets of the cermet zirconia-alumina structures in an own constructed furnace set-up. Prior to the experiments, the synthesized materials were pelletized *via* uniaxial (40 kN for 2 min) and isostatic (1000 kN for 2 min) pressing. The pellets were sintered for 24 h at 1000 °C at a 2 °C/min heating rate. Platinum electrodes were applied in a 4-point electrode arrangement on both sides of the pellets (Heraeus 3605).

The resistance of each pellet was measured in air as a function of temperature up to 950 °C at 3 °C/min heating/cooling rate by applying a DC voltage of 1 V and measuring the current (Keithley 2601B multimeter). To ensure reproducibility, three heating and cooling cycles were performed. The set-up and sample arrangement for electrical conductivity measurements is described in further detail in Afyon *et al.* <sup>3</sup>

X-ray absorption spectroscopy (XAS) measurements were performed at the Swiss-Norwegian beamline (BM01B) at the European Synchrotron Radiation Facility (ESRF), Grenoble, France. The measurements were performed at the Fe K-edge in transmission mode using a Si (111) double crystal monochromator. For *ex situ* XAS measurements, the oxygen carriers were ground, mixed with cellulose (ratio 1:8) and pelletized. EXAFS (extended X-ray absorption fine structure) data processing and analysis were performed using the Athena and Artemis software packages (Demeter 0.9.20) <sup>4</sup>. The structural parameters, *i.e.* the inter-atomic distances, coordination numbers and the Debye-Waller factors were obtained by nonlinear least-squares fitting of the  $k^2$  and  $k^3$ -weighted EXAFS functions in the  $k$ -range of 3 - 12 Å<sup>-1</sup>.

H<sub>2</sub>-temperature programmed reduction (TPR) was performed in a thermogravimetric analyzer (TGA, Mettler Toledo TGA/DSC 1). In a typical experiment ~ 30 mg of the oxygen carrier was placed in an alumina crucible. The flow rate of hydrogen (10 vol. % H<sub>2</sub> in N<sub>2</sub>) and the purge stream over the micro-balance (N<sub>2</sub>) were 100 ml/min and 25 ml/min, respectively. The sample was heated from 25 to 1050 °C using a temperature ramp of 10 °C/min. Subsequently, the sample was held at 1050 °C for 30 minutes. Additional TPR tests were conducted in a BELCAT-M (equipped

with a thermal conductivity detector). In a typical experiment, 10 mg of the calcined material was loaded in a quartz reactor and pre-treated to 300 °C under N<sub>2</sub> for 30 min. The temperature of the reactor was subsequently increased to 1000 °C (temperature ramp of 10 °C/min). The quantity of H<sub>2</sub> consumed was recorded with a TCD detector.

### ***Cycling redox test***

In a typical TGA redox experiment, ~20 mg of an oxygen carrier were used and 10 redox cycles were conducted at 800 °C. At the beginning of the experiment, the sample was heated from room temperature to 800 °C under a flow of N<sub>2</sub>. The subsequent reduction step was performed in 10 vol. % H<sub>2</sub> in N<sub>2</sub> for 45 min. Re-oxidation was carried out in 10 vol. % CO<sub>2</sub> in N<sub>2</sub> (25 min), followed by 5 vol. % O<sub>2</sub> in N<sub>2</sub> (10 min).

The fixed bed reactor used for the cyclic redox experiments was made of recrystallized Al<sub>2</sub>O<sub>3</sub> and had an internal diameter of 20 mm (length 590 mm). A frit containing 5 holes (diameter 1.5 mm) was located 200 mm above the bottom of the reactor. In a typical experiment, the bed was first loaded with 3.5 g of coarse Al<sub>2</sub>O<sub>3</sub> (1400-1700 μm), followed by an approximately 10 mm long plug of quartz wool. Subsequently, 0.5 g of the oxygen carrier, mixed with 5 g of Al<sub>2</sub>O<sub>3</sub> (300-425 μm), were placed on top of the quartz wool plug. Finally, 10 g of coarse alumina (1400-1700 μm) were added. The layer of coarse alumina and the quartz wool plug in the bottom section of the bed prevented oxygen carriers from falling through the holes of the frit. The top layer of coarse alumina effectively preheated the gas entering the bed. The reactor was placed in a tubular furnace. The temperature of the bed was controlled *via* an N-type thermocouple placed inside the layer of the oxygen carrier. The flow rate of CO was metered with a calibrated rotameter whereas the flowrates of CO<sub>2</sub>, N<sub>2</sub> and air were recorded *via* calibrated mass flow meters (AWM5101VN, Honeywell). The switching between the different gas atmospheres was performed using a computer-controlled setup comprising six solenoid valves. Water was fed *via* a syringe pump (0.3 ml/min) to an electrically heated vaporizer maintained at 210 °C. In a typical redox cycle, the following steps were performed: (i) reduction in CO (10 % CO in N<sub>2</sub>) for 15 minutes (1.5 L/min), (ii) purging with N<sub>2</sub> (1.5 L/min) for 1 minute, (iii) oxidation of the reduced oxygen carrier with steam (23 % H<sub>2</sub>O in N<sub>2</sub>) for 7 minutes (1.94 L/min), (iv) purge with N<sub>2</sub> (1.5 L/min) for 1 minute, and (v) oxidation with 5% O<sub>2</sub> in N<sub>2</sub> (2 L/min) for

5 minutes. The gas stream leaving the fixed bed reactor was passed first through three impinger tubes, immersed in an ice bath, followed by a CaCl<sub>2</sub> drying tube, to remove unreacted steam. The composition of the gas stream was determined using the following analyzers: (i) non-dispersive infrared analyzer for CO, CH<sub>4</sub> and CO<sub>2</sub> (ABB, Uras 26), (ii) non-dispersive infrared analyzer for CO in the range 0 – 5000 ppmv (ABB, Uras 26), (iii) paramagnetic analyzer for O<sub>2</sub> (ABB, Magnos 206) and (iv) thermal conductivity analyzer for H<sub>2</sub> (ABB, Caldos 27). Our gas analyzers are calibrated after each experiment using calibration gas cylinders.

1. Brunauer, S.; Emmett, P. H.; Teller, E., *J. Am. Chem. Soc.* 1938, 60, 309-319.
2. Barrett, E. P.; Joyner, L. G.; Halenda, P. P., *J. Am. Chem. Soc.* 1951, 73, 373-380.
3. Afyon, S.; Krumeich, F.; Rupp, J. L. M., *J. Mater. Chem. A* 2015, 3, 18636-18648.
4. Ravel, B.; Newville, M., *J. Synchrotron Radiat.* 2005, 12, 537-541.

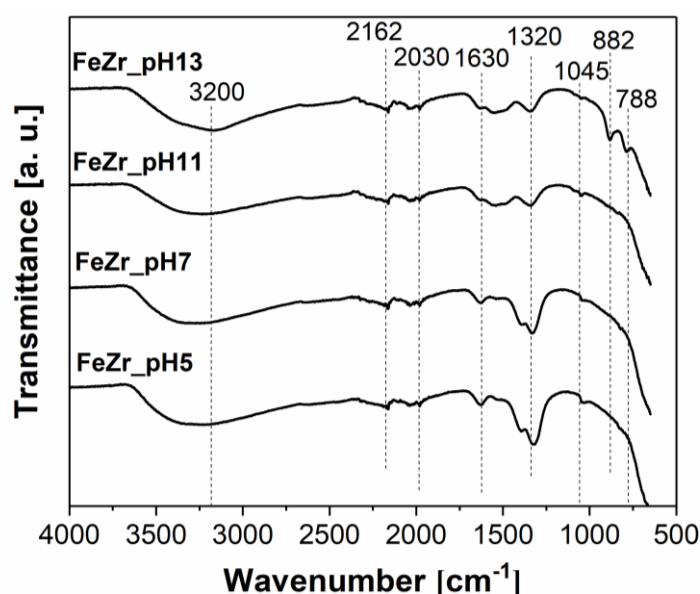


**Figure S2.2:** ATR- FTIR spectra of the dried oxygen carriers precipitated at pH 5, 7, 11, and 13.

The gelatinous nature of low pH value precipitates (*i.e.* pH <7) made washing very difficult. The vibrations of hydrous zirconium oxides are typically found at < 500 cm<sup>-1</sup> *i.e.* below the limit of our equipment. Nonetheless, it is commonly agreed on that positively charged Zr<sub>3</sub>(OH)<sub>4</sub><sup>8+</sup> or Zr<sub>4</sub>(OH)<sub>8</sub><sup>8+</sup> are formed under acidic conditions while negatively charged hydrous zirconia (Zr(OH)<sub>5</sub><sup>-</sup>) is formed under basic conditions <sup>5</sup>. The broad peak in the range 3000 – 3500 cm<sup>-1</sup> is due to the O–H stretching vibrations that would be expected for goethite and hydrous zirconia, whereas the absorption band at 1630 cm<sup>-1</sup> is due to the bending vibration of adsorbed water <sup>6</sup>. The broad peak in the



range 1280-1520  $\text{cm}^{-1}$  corresponds to asymmetric stretching vibrations of nitrate ions ( $\text{NO}_3^-$ ), indicating their incomplete removal during washing <sup>7</sup>. From the IR spectra of the oxygen carriers precipitated at pH 5 and 7, a double peak can be observed in the range 1280-1520  $\text{cm}^{-1}$ , whereas materials precipitated at pH 11 and 13 show only a single peak. Goebbert *et al.* argued that the shape of the nitrate absorption band depends on the number of water molecules in the  $\text{NO}_3^-(\text{H}_2\text{O})_n$  clusters <sup>8</sup>. Single peaks were observed for  $n = 3$  or 4, whereas a double peak occurred for  $n = 1, 2, 5$  and 6.

5. Kobayashi, T.; Sasaki, T.; Takagi, I.; Moriyama, H., *J. Nucl. Sci. Technol.* 2007, 44, 90-94.

6. Monroy-Guzman, F.; Díaz-Archundia, L.; Ramírez, *Appl. Radiat. Isot.* 2003, 59, 27-34.

7. Zic, M.; Ristic, M.; Music, S., *J. Mol. Struct.* 2011, 993, 115-119.

8. Goebbert, D. J.; Garand, E.; Wende, T.; Bergmann, R.; Meijer, G.; Asmis, K. R.; Neumark, D. M., *J. Phys. Chem. A* 2009, 113, 7584-7592.

**Table S2.1:** BET surface area, BJH pore volume and average crystallite size of  $\text{Fe}_2\text{O}_3$  in the calcined oxygen carriers.

	Surface area [ $\text{m}^2/\text{g}$ ]	Pore volume [ $\text{cm}^3/\text{g}$ ]	Crystallite size of $\text{Fe}_2\text{O}_3$ [nm]
<b>FeZr-pH 5</b>	4	0.07	39
<b>FeZr-pH 7</b>	7	0.09	39
<b>FeZr-pH 11</b>	7	0.05	44
<b>FeZr-pH 13</b>	7	0.07	39
<b><math>\text{Fe}_2\text{O}_3</math></b>	8	0.2	44
<b>FeAl-pH10</b>	19	0.2	33

**Table S2.2:** Phase composition and cell volumes determined by Rietveld refinement of the XRD data of the calcined oxygen carriers (the errors represent the statistical standard deviation).

	Composition [wt. %]			Unit cell volume [ $\text{\AA}^3$ ]		
	$\text{Fe}_2\text{O}_3$	t- $\text{ZrO}_2$	m- $\text{ZrO}_2$	$\text{Fe}_2\text{O}_3$	t- $\text{ZrO}_2$	m- $\text{ZrO}_2$
<b>FeZr-pH5</b>	70 $\pm$ 1	13 $\pm$ 1	17 $\pm$ 1	301.98 $\pm$ 0.03	66.90 $\pm$ 0.02	140.23 $\pm$ 0.04
<b>FeZr-pH7</b>	70 $\pm$ 1	15 $\pm$ 1	15 $\pm$ 1	302.10 $\pm$ 0.03	66.92 $\pm$ 0.02	140.27 $\pm$ 0.04
<b>FeZr-pH11</b>	73 $\pm$ 1	-	27 $\pm$ 1	302.13 $\pm$ 0.03	-	140.45 $\pm$ 0.04
<b>FeZr-pH13</b>	72 $\pm$ 1	6 $\pm$ 1	23 $\pm$ 1	302.12 $\pm$ 0.03	67.00 $\pm$ 0.05	140.48 $\pm$ 0.04
<b>m-<math>\text{ZrO}_2</math></b>	-	-	100	-	-	140.59 $\pm$ 0.04
<b><math>\text{Fe}_2\text{O}_3</math></b>	100	-	-	301.98 $\pm$ 0.01	-	-

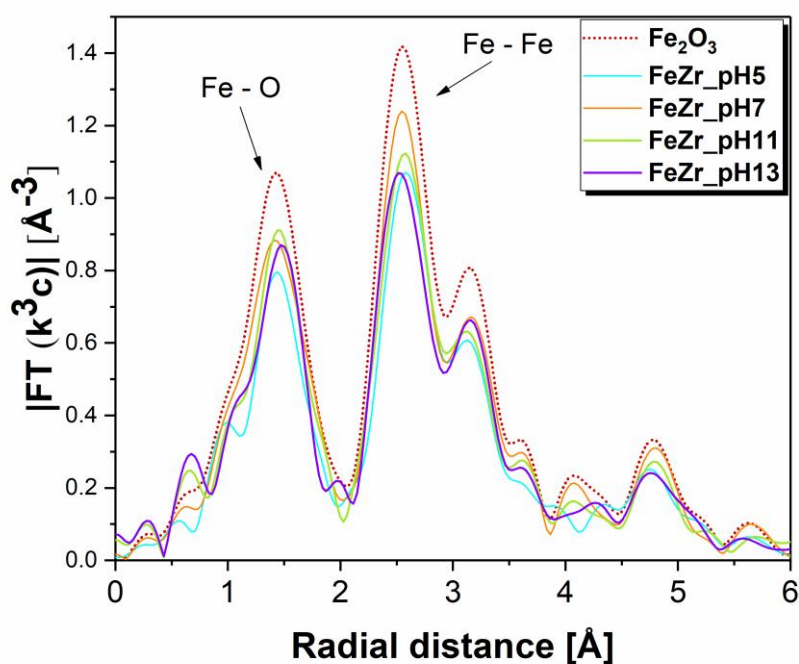


**Figure S2.3:** Fourier-transformed EXAFS functions ( $k^2$ -weighted) calcined oxygen carriers.

The EXAFS data was fitted using a model based on the  $\alpha$ -Fe<sub>2</sub>O<sub>3</sub> crystal structure, containing two Fe-O oxygen shells for the first peak and three Fe-Fe paths for the second peak. The coordination numbers (N) were kept constant (set to the crystallographic data reported in the literature <sup>9</sup>), while the Debye-Waller factors ( $\sigma^2$ ), the zero energy shift ( $E_0$ ) and interatomic distances (R) were obtained from the fitted EXAFS data.

**Table S2.3:** Structural parameters of the calcined oxygen carriers and the  $\alpha$ -Fe<sub>2</sub>O<sub>3</sub> reference.

	Bonding	CN	R [Å]	$\sigma^2$ [Å <sup>2</sup> ]
<b>Fe<sub>2</sub>O<sub>3</sub></b>	Fe-O	3	1.93 ± 0.01	0.0017 ± 0.0016
	Fe-O	3	2.09 ± 0.01	0.0034 ± 0.0016
	Fe-Fe	4	2.95 ± 0.004	0.0038 ± 0.0004
	Fe-Fe	3	3.38 ± 0.01	0.0019 ± 0.0007
	Fe-Fe	6	3.68 ± 0.01	0.0084 ± 0.0013
<b>Amp = 0.72, E<sub>0</sub> = -2.3, R-factor = 0.011</b>				
<b>FeZr-pH5</b>	Fe-O	3	1.95 ± 0.01	0.0034 ± 0.0015
	Fe-O	3	2.12 ± 0.02	0.012 ± 0.0086
	Fe-Fe	4	2.95 ± 0.01	0.0052 ± 0.0007
	Fe-Fe	3	3.39 ± 0.01	0.0035 ± 0.0012
	Fe-Fe	6	3.68 ± 0.01	0.0081 ± 0.0017
<b>Amp = 0.72, E<sub>0</sub> = -2.3, R-factor = 0.017</b>				
<b>FeZr-pH7</b>	Fe-O	3	1.94 ± 0.01	0.0038 ± 0.0013
	Fe-O	3	2.11 ± 0.01	0.0086 ± 0.0031
	Fe-Fe	4	2.95 ± 0.01	0.0059 ± 0.0006
	Fe-Fe	3	3.38 ± 0.01	0.0030 ± 0.0008
	Fe-Fe	6	3.69 ± 0.01	0.01 ± 0.0015
<b>Amp = 0.72, E<sub>0</sub> = -2.3, R-factor = 0.022</b>				
<b>FeZr-pH11</b>	Fe-O	3	1.93 ± 0.01	0.0031 ± 0.0009
	Fe-O	3	2.10 ± 0.01	0.0062 ± 0.0018
	Fe-Fe	4	2.95 ± 0.003	0.0046 ± 0.0004
	Fe-Fe	3	3.39 ± 0.01	0.003 ± 0.0006
	Fe-Fe	6	3.69 ± 0.01	0.009 ± 0.0011
<b>Amp = 0.72, E<sub>0</sub> = -2.3, R-factor = 0.011</b>				
<b>FeZr-pH13</b>	Fe-O	3	1.94 ± 0.01	0.0023 ± 0.0012
	Fe-O	3	2.09 ± 0.02	0.007 ± 0.0032
	Fe-Fe	4	2.95 ± 0.05	0.0044 ± 0.0005
	Fe-Fe	3	3.38 ± 0.02	0.0029 ± 0.0009
	Fe-Fe	6	3.68 ± 0.02	0.009 ± 0.0015
<b>Amp = 0.72, E<sub>0</sub> = -2.3, R-factor = 0.016</b>				

9. Maslen, E.; Streltsov, V.; Streltsova, N.; Ishizawa, N., *Sect. B: Struct. Sci.* 1994, 50, 435-441.

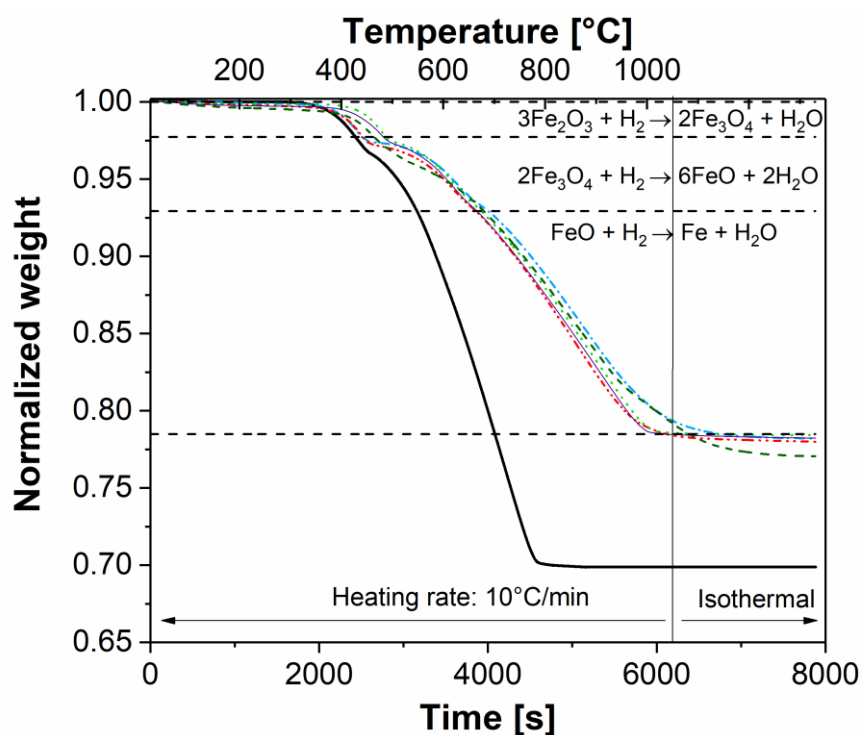


**Figure S2.4:** H<sub>2</sub>-temperature programmed reduction of ZrO<sub>2</sub>-stabilized Fe<sub>2</sub>O<sub>3</sub>. Precipitation was performed at the following pH values: (---) FeZr-pH5, (-.-.-) FeZr-pH7, (.....) FeZr-pH11 and (—) FeZr-pH13. H<sub>2</sub>-TPR profiles of FeAl-pH10 (----) and unsupported Fe<sub>2</sub>O<sub>3</sub> (—) are also plotted. The dashed horizontal lines represent the theoretically expected weight for the different oxidation states of iron.

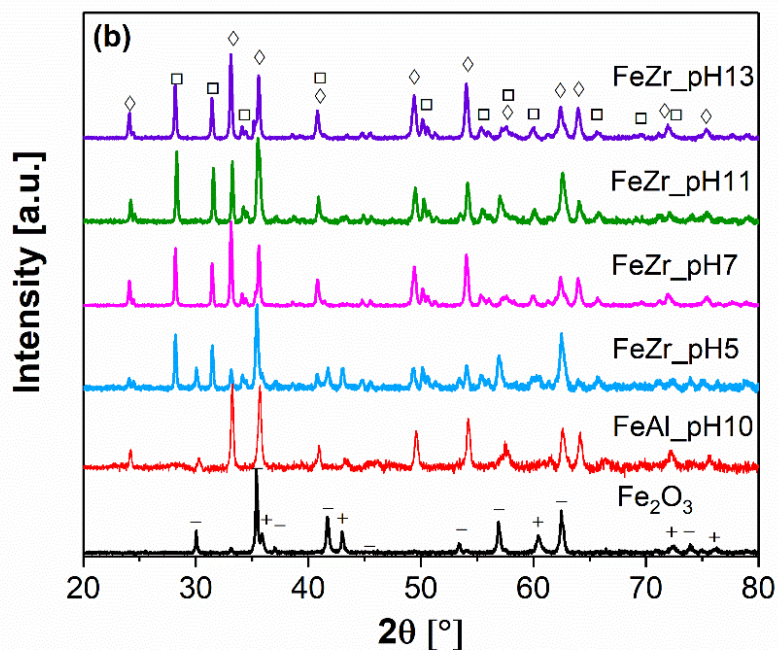
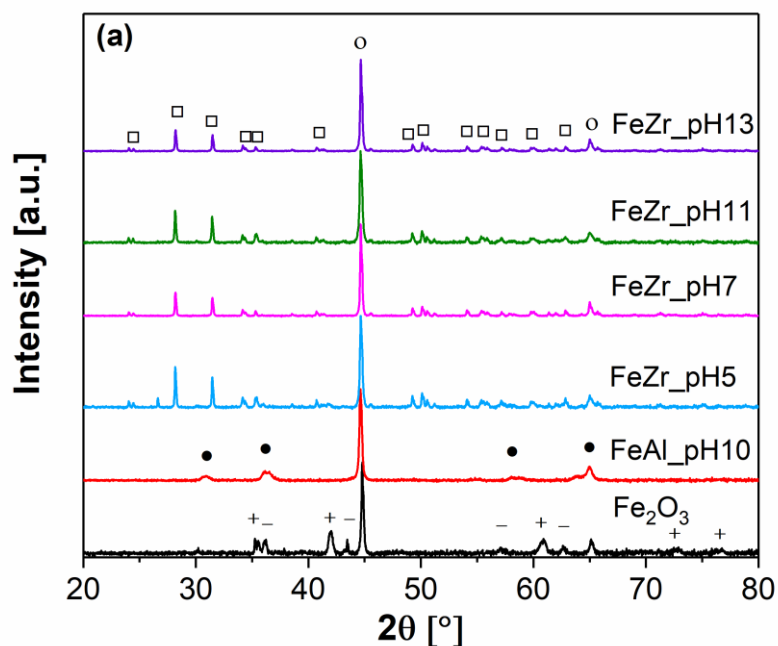


**Figure S2.5:** XRD of unsupported  $\text{Fe}_2\text{O}_3$ ,  $\text{Fe}_2\text{O}_3\text{-ZrO}_2$  precipitated at pH 5, 7, 11, 13, and  $\text{Fe}_2\text{O}_3\text{-Al}_2\text{O}_3$  in their (a) reduced and (b) oxidized state after being subjected to 15 redox cycles. The following compounds were identified: ( $\diamond$ ) hematite,  $\text{Fe}_2\text{O}_3$ , ( $\square$ ) baddeleyite, m- $\text{ZrO}_2$ , ( $\circ$ ) iron, Fe, (+) wüstite,  $\text{FeO}$ , (-) magnetite,  $\text{Fe}_3\text{O}_4$ , and ( $\bullet$ ) herycnite,  $\text{FeAl}_2\text{O}_4$ .

**Table S2.4:** BET surface area, BJH pore volume and crystallite size of the cycled oxygen carriers.

	Surface area [m <sup>2</sup> /g]	Pore volume [cm <sup>3</sup> /g]	Crystallite size [nm]
FeZr-pH 5	2	<0.01	49
FeZr-pH 7	4	<0.01	42
FeZr-pH 11	4	<0.01	44
FeZr-pH 13	4	<0.01	39
Fe <sub>2</sub> O <sub>3</sub>	2	<0.01	56
FeAl-pH10	<1	0.01	32

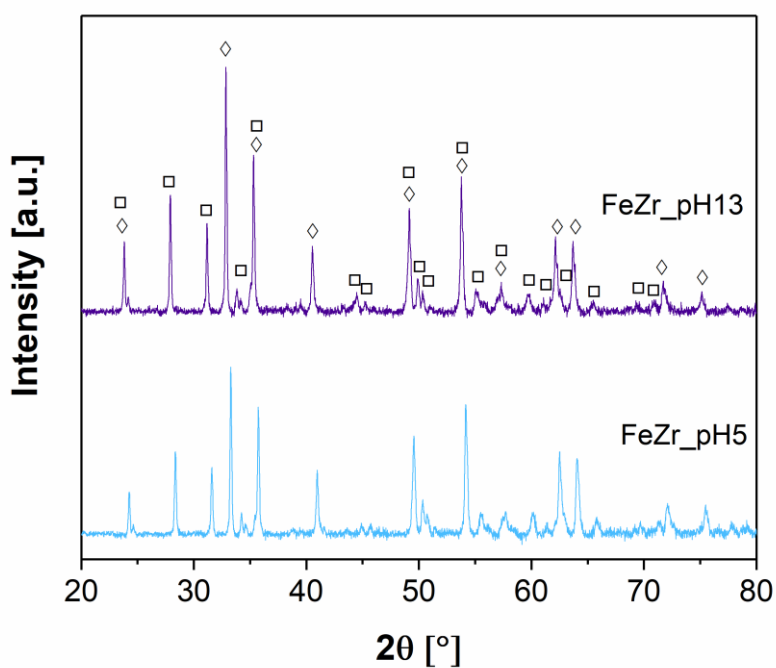


**Figure S2.6:** XRD of FeZr\_pH5 and FeZr\_pH13 pellets used in the conductivity measurements. The following compounds were identified: (□) baddeleyite, m-ZrO<sub>2</sub> and (◇) hematite, Fe<sub>2</sub>O<sub>3</sub>.

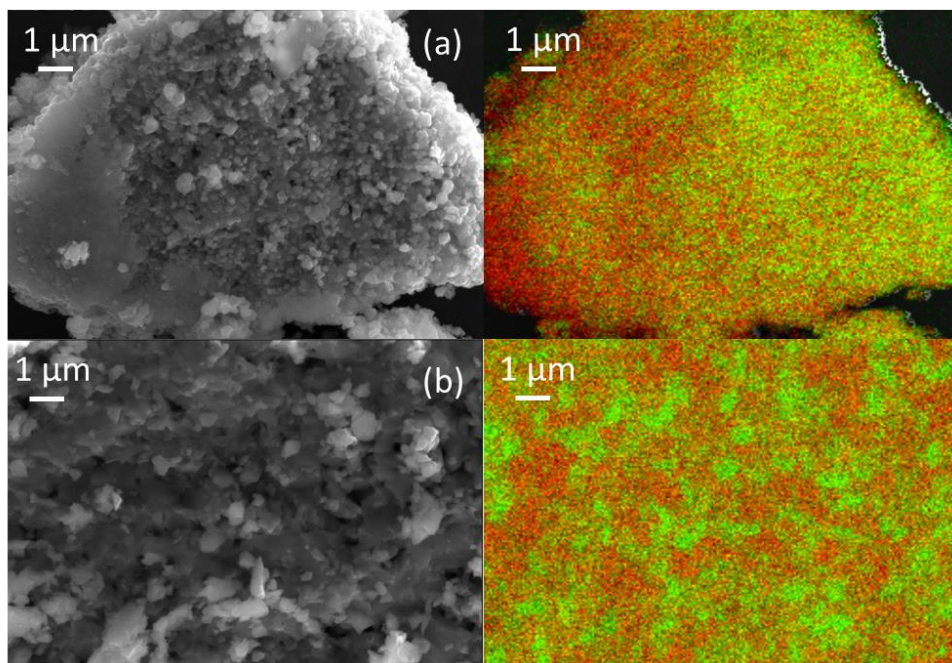


**Figure S2.7:** EDX maps of (a) FeZr-pH 5 pellet and (b) FeZr-pH 13 pellet. The green colour represents Zr and the red colour Fe.

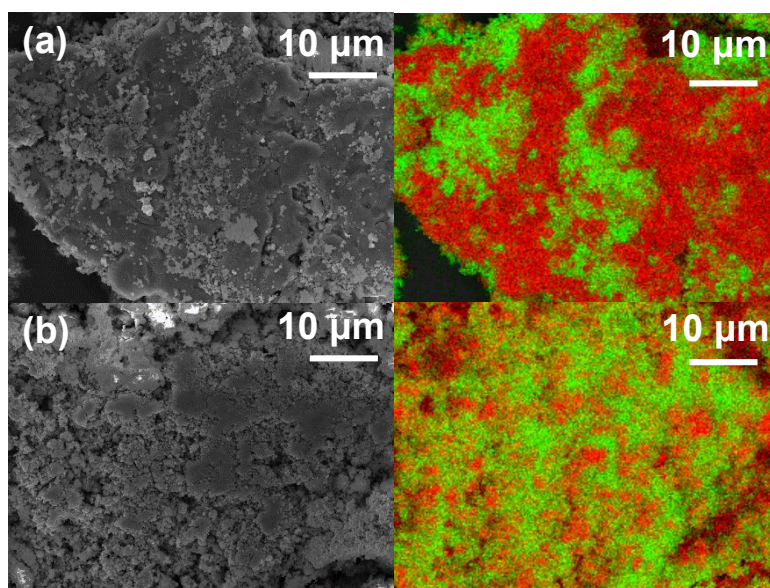


**Figure S2.8:** EDX maps of (a) cycled FeZr-pH 5 and (b) cycled FeZr-pH 13 in their reduced state after being subjected to 15 redox cycles. The green colour represents Zr and the red colour Fe.

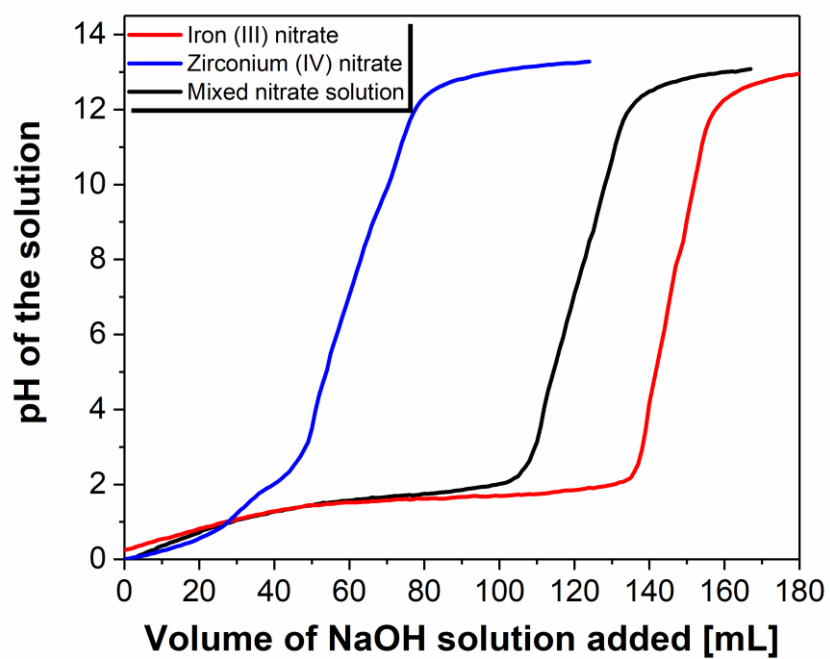


**Figure S2.9:** Titration curves of 1 M iron (III) nitrate, 1 M zirconium (IV) nitrate and mixed nitrate solution with 2 M NaOH solution.



## Chapter 3: The Effect of Copper on the Redox Behaviour of Iron Oxide for Chemical-Looping Hydrogen Production Probed by *in situ* X-Ray Absorption Spectroscopy

---

This section contains a reprint of the article: Yüzbaşı, N.S., Abdala, P.M., Imtiaz, Q., Kim, S.M., Kierzkowska, A.M., Armutlulu, A., van Beek, W. And Müller, C.R., 2018. The effect of copper on the redox behaviour of iron oxide for chemical-looping hydrogen production probed by *in situ* X-ray absorption spectroscopy. *Physical Chemistry Chemical Physics*, 20(18), pp.12736-12745. **DOI:** 10.1039/c8cp01309h

The author of this thesis carried out TGA, XRD, BET, XAS and cyclic performance tests. The oxygen carriers were synthesized together with Dr. A.M. Kierzkowska. SEM/EDX measurements were conducted by Dr. A. Armutlulu. S. M. Kim contributed to H<sub>2</sub>-TPD measurements. Dr. W. van Beek got involved in *in situ* XAS set-up design and measurements in ESRF synchrotron facility. Dr. P. M. Abdala provided guidance *in situ* XAS data analysis and interpretation of the H<sub>2</sub>-TPD data and general structuring of the study. Additionally, Dr. Q. Imtiaz, Dr. P. M. Abdala and Prof. C. R. Müller assisted with discussion and proof-reading of the paper.

### 3.1 Abstract

The production of high purity hydrogen with the simultaneous capture of CO<sub>2</sub>, can be achieved through a chemical looping (CL) cycle relying on an iron oxide-based oxygen carrier. Indeed, the availability of active and cyclically stable oxygen carriers is a key criterion for the practical implementation of this technology. In this regard, improving our understanding of the reduction pathway(s) of iron-based oxygen carriers and the development of concepts to increase the reduction kinetics are important aspects. The aim of this work is to evaluate the effect of the addition of copper on the redox behaviour of iron oxide based oxygen carriers stabilized on ZrO<sub>2</sub>. *In situ* pulsed-H<sub>2</sub> XANES (Fe K-edge) experiments allowed for the determination of the reduction pathways in these materials, viz. the reduction of both Fe<sub>2</sub>O<sub>3</sub> and CuFe<sub>2</sub>O<sub>4</sub> proceeded via a Fe<sup>2+</sup> intermediate: Fe<sub>2</sub>O<sub>3</sub> (CuFe<sub>2</sub>O<sub>4</sub>) - Fe<sub>3</sub>O<sub>4</sub> (Cu<sup>0</sup>) - FeO (Cu<sup>0</sup>) - Fe<sup>0</sup> (Cu<sup>0</sup>). In the first step CuFe<sub>2</sub>O<sub>4</sub> is reduced to Cu<sup>0</sup> and Fe<sub>3</sub>O<sub>4</sub>, whereby Cu<sup>0</sup> promotes the further reduction of iron oxide, increasing their rate of formation. In particular, the rate of reduction of FeO - Fe<sup>0</sup> is accelerated most dramatically by Cu<sup>0</sup>. This is an encouraging result as the FeO - Fe<sup>0</sup> transition is the slowest reduction reaction.

### 3.2 Introduction

For hydrogen to become an important energy carrier, it must be produced in an efficient and sustainable manner, e.g. from renewable energy sources<sup>1,2</sup>. In this context, a modified chemical looping process for the production of high-purity hydrogen has been proposed. In the first step, biomass is gasified to produce a synthesis gas, *i.e.* a mixture containing largely CO, H<sub>2</sub>, CO<sub>2</sub>, H<sub>2</sub>O. Subsequently, the synthesis gas reduces Fe<sub>2</sub>O<sub>3</sub> to metallic Fe yielding a mixture of CO<sub>2</sub> and H<sub>2</sub>O. A pure stream of CO<sub>2</sub> is readily obtained through the condensation of steam. Re-oxidation of Fe to Fe<sub>3</sub>O<sub>4</sub> with steam yields high-purity H<sub>2</sub><sup>1,3</sup>. The cycle is closed by re-oxidizing Fe<sub>3</sub>O<sub>4</sub> back to Fe<sub>2</sub>O<sub>3</sub> with air. An important aspect of this process is the development of Fe<sub>2</sub>O<sub>3</sub>-based oxygen carriers that possess fast reduction and re-oxidation kinetics with a high recyclability, as pure Fe<sub>2</sub>O<sub>3</sub> deactivates after a very small number of redox cycles<sup>1,4,5</sup>. To stabilize Fe<sub>2</sub>O<sub>3</sub> over several redox cycles it is often supported on a high Tammann temperature metal oxide, e.g. Al<sub>2</sub>O<sub>3</sub>, ZrO<sub>2</sub>, MgAl<sub>2</sub>O<sub>4</sub> or TiO<sub>2</sub><sup>3,4,6-10</sup>. For instance, Fe<sub>2</sub>O<sub>3</sub> supported on ZrO<sub>2</sub> was found to be a suitable oxygen carrier yielding

high H<sub>2</sub> yields over multiple redox cycles<sup>5,8</sup>. It was argued that ZrO<sub>2</sub> not only provides sintering resistance without forming a solid solution, but also enhances solid-state ionic diffusion through the material<sup>5</sup>.

With regards to improving the rate of the redox reactions, the incorporation of a second metal has been proposed<sup>3,11–13</sup>. For example, it has been demonstrated that the reactivity of Fe<sub>2</sub>O<sub>3</sub>-based oxygen carriers could be improved by using a bimetallic oxygen carrier containing both Fe and Cu<sup>6,11,14–18</sup>. Kang *et al.*<sup>14</sup> reduced CuFe<sub>2</sub>O<sub>4</sub> in methane at 900 °C for 50 min and re-oxidized it in steam at 800 °C for 120 min in a TGA. It was reported that CuFe<sub>2</sub>O<sub>4</sub> possessed faster reduction kinetics, a lower tendency to form iron carbide and graphite and a higher methane conversion when compared to pure Fe<sub>3</sub>O<sub>4</sub>. However, the conversion of CH<sub>4</sub> during reduction and the yield of H<sub>2</sub> in the steam oxidation step were not stable over repeated redox cycles. In a further study Cu-modified Fe<sub>2</sub>O<sub>3</sub>, stabilized on MgAl<sub>2</sub>O<sub>4</sub> exhibited a high reactivity towards CH<sub>4</sub> and low rates of carbon deposition<sup>6</sup>. The high resistance to carbon deposition was attributed to the (partial) coverage of surface Fe with Cu. The studies summarized above demonstrated the potentially beneficial effects of adding Cu to iron oxides such as enhancing the rate of reduction, high fuel conversion and low rates of carbon deposition, however, the influence of Cu on the characteristics of the redox process, *e.g.* the reaction pathways or the interaction between Cu(O) and Fe<sub>2</sub>O<sub>3</sub> has not been probed in detail.

Hence, in this work, we study in detail the effect of the addition of copper on the redox behaviour and, in particular, the reduction of ZrO<sub>2</sub>-supported Fe<sub>2</sub>O<sub>3</sub> at an operating temperature of 700 °C. ZrO<sub>2</sub> was selected as a support due to its inert nature and low cationic solubility of the Fe–O–Zr system. To achieve a homogeneous distribution of the three compounds, a sol–gel technique was utilized. *In situ* pulsed-H<sub>2</sub> XANES measurements, combined with TPR, XRD and SEM/EDX were applied to provide insight into the reduction pathways of these oxygen carriers.

## 3.3 Experimental

### 3.3.1 Synthesis of oxygen carriers

Two different Fe<sub>2</sub>O<sub>3</sub>–ZrO<sub>2</sub> oxygen carriers (with and without the addition of copper) were prepared via a sol–gel technique using a modification of the method reported by Martinez *et al.*<sup>19</sup> The quantity of Fe<sub>2</sub>O<sub>3</sub> was fixed to 30 wt. % in both oxygen carriers. In the copper modified oxygen carrier, the molar ratio between Fe<sup>3+</sup> and Cu<sup>2+</sup> was equal to 3:1. In a typical synthesis, first, a solution was prepared by mixing zirconium propoxide and 1-propanol at room temperature. Subsequently, HNO<sub>3</sub> was added to catalyse the condensation reaction. The molar ratio between Zr<sup>4+</sup>, alcohol and H<sup>+</sup> was equal to 1:20:0.6. A second solution was prepared which contained appropriate amounts of iron nitrate, copper nitrate, H<sub>2</sub>O, 1-propanol and was fed dropwise to condensed zirconium propoxide. The solution was aged for 3 days until gelation occurred. Finally, the oxygen carriers were dried at 100 °C for 24 h and subsequently calcined in a muffle furnace at 900 °C for 2 h using a temperature ramp of 5 °C min<sup>-1</sup>. The calcined oxygen carriers were crushed and sieved into the size range of 110–212 μm. To describe the two oxygen carriers, the following nomenclature is used throughout this paper: Fe<sub>30</sub>Zr<sub>70</sub> and Fe<sub>30</sub>Cu<sub>10</sub>Zr<sub>60</sub>.

### 3.3.2 Characterization of the oxygen carriers

The crystalline phases of the fresh and cycled oxygen carriers were characterized by X-ray diffraction (XRD) using a PANalytical Empyrean X-ray Powder Diffractometer equipped with a X'Celerator Scientific ultra-fast line detector and Bragg–Brentano HD incident beam optics using Cu K<sub>α</sub> radiation (45 kV and 40 mA). A diffracted beam monochromator was used to suppress unwanted fluorescence originated from iron in the samples. The scans were collected in the 2θ range of 10°–90° with a step size of 0.02° and a scanning speed of 0.0111 s<sup>-1</sup>.

The morphology of the fresh and cycled oxygen carriers was assessed using scanning electron microscopy (Zeiss Gemini 1530 FEG). Prior to imaging, the materials were sputter-coated (MED 010) with a ~5 nm-thick layer of platinum. Additionally, the elemental composition of the surface of the materials before and after redox cycles was analysed using a Leo Gemini 1530 scanning electron microscope

(SEM) equipped with an energy dispersive (EDX) spectrometer. A Quantachrome NOVA 4000e N<sub>2</sub> adsorption analyser was used to determine the surface area and pore size distribution of the oxygen carriers. Each sample was degassed at 300 °C for two hours prior to the measurements. BET and BJH models were used to calculate the surface area and the pore size distribution of the materials, respectively <sup>20,21</sup>.

Temperature programmed reduction (TPR) was conducted in a BELCAT-M (equipped with a thermal conductivity detector). In a typical experiment, 10 mg of the calcined material was loaded in a quartz reactor and pre-treated at 300 °C under N<sub>2</sub> for 30 min. The sample was subsequently heated to 1000 °C with a temperature ramp of 10 °C min<sup>-1</sup> under 5 vol. % H<sub>2</sub>. H<sub>2</sub>-temperature programmed desorption (TPD) was carried out in an Autochem 2920 apparatus with a TCD detector coupled with a Cirrus 2 Quadrupole Mass Spectrometer. Here, 200 mg of the calcined material was pre-treated at 300 °C under N<sub>2</sub> for 30 min. Prior to H<sub>2</sub> adsorption, the oxygen carriers were first reduced at different temperatures *i.e.* 200 °C, 250 °C, 400 °C and 800 °C. Subsequently, the sample was cooled down to 40 °C using a temperature ramp of 90 °C min<sup>-1</sup>. Hydrogen adsorption was conducted by flowing 5% H<sub>2</sub>–95% Ar (50 mL min<sup>-1</sup>) for 0.5 h. A TPD experiment was performed using high-purity Ar (50 mL min<sup>-1</sup>) and a temperature ramp of 5 °C min<sup>-1</sup> up to 800 °C.

### 3.3.3 Cyclic redox tests

Cyclic redox experiments were performed in a fixed bed reactor made of recrystallized Al<sub>2</sub>O<sub>3</sub>. The internal diameter of the reactor was 20 mm and the length was 590 mm. The reactor was loaded in the following order: (i) 3.5 grams of coarse Al<sub>2</sub>O<sub>3</sub> (1400–1700 μm), (ii) ~10 mm long plug of quartz wool, (iii) 0.5 grams of the oxygen carrier mixed with 5 grams of Al<sub>2</sub>O<sub>3</sub> (300–425 μm) on a wool plug, and (iv) 10 grams of coarse alumina (1400–1700 μm). A tubular furnace controlled via a N-type thermocouple was used to heat the reactor. The flow rates of the gases were controlled by mass flow meters (AWM5101VN, Honeywell). The gas switching between the reducing, inert and oxidizing atmospheres was computer-controlled using a setup comprising 6 solenoid valves. In a typical redox cycle, the oxygen carriers were first reduced in H<sub>2</sub> (2.5 vol. % in N<sub>2</sub>, 1.5 L min<sup>-1</sup>) for 6 min. Subsequently; the reactor was purged with N<sub>2</sub> (1.5 L min<sup>-1</sup>) for 1 min and oxidized with steam (23 vol. % H<sub>2</sub>O in N<sub>2</sub>, 1.94 L min<sup>-1</sup>) for 7 min. In the oxidation step, steam was generated by feeding water

via a syringe pump at a rate of  $0.3 \text{ mL min}^{-1}$  into an electrically heated vaporizer maintained at  $210 \text{ }^\circ\text{C}$ . In the last step, after purging the reactor with  $\text{N}_2$  ( $1.5 \text{ L min}^{-1}$ ) for 1 min, the oxygen carrier was oxidized with 5 vol. %  $\text{O}_2$  in  $\text{N}_2$  ( $1.5 \text{ L min}^{-1}$ ) for 5 min. Three impinger tubes immersed in an ice bath, followed by a  $\text{CaCl}_2$  drying tube, were used to remove moisture prior to gas analysis. The composition of the gas stream was determined using the following analysers: (i) paramagnetic analyser for  $\text{O}_2$  (ABB, Magnos 206) and (ii) thermal conductivity analyser for  $\text{H}_2$  (ABB, Caldos 27). The cyclic redox reactions were performed at  $700 \text{ }^\circ\text{C}$ .

X-ray absorption spectroscopy (XAS) measurements were performed at the Swiss-Norwegian beamline (BM01B) at the European Synchrotron Radiation Facility (ESRF), Grenoble, France. The measurements were performed at the Fe K-edge in transmission mode using a Si (111) double crystal monochromator. The reduction pathways of the oxygen carriers were determined via *in situ* X-ray absorption near edge structure (XANES) spectroscopy. The cyclic redox reactions were performed at  $700 \text{ }^\circ\text{C}$  using a quartz capillary tube (outer diameter of 1 mm and wall thickness of 0.1 mm) as the reactor. The oxygen carriers were diluted with boron nitride (BN), (mass ratio of 1:2) and pelletized to optimize the transmission of X-rays. The pelletized mixture was then crushed and sieved to below  $100 \text{ }\mu\text{m}$ . Approximately 2 mg of the sieved material was placed between two plugs of quartz wool in the capillary tube. The reduction and oxidation reactions were performed using 5 vol. %  $\text{H}_2$  in He and 5 vol. %  $\text{O}_2$  in He, respectively. Three redox cycles were conducted for each material. In order to probe the reduction pathways, each spectrum was collected in He after a small amount of  $\text{H}_2$  was released into the bed instead of using a continuous flow of the reactant gas. In the first cycle, initially 50 pulses of  $\text{H}_2$  (duration 5 s) were sent to the reactor. This was followed by 50 pulses of 10 s duration, 25 pulses of 20 s duration, 10 pulses of 50 s duration and finally 10 pulses of 100 s duration. Pulses of duration 5 s, 10 s, 20 s, 50 s and 100 s correspond to 0.1 mL, 0.2 mL, 0.4 mL, 1 mL and 2 mL of  $\text{H}_2$ , respectively. The duration of the pulses was optimized experimentally in order to resolve the intermediates<sup>22</sup>. In order to reduce the total acquisition time (due to limited beam time) the pulse sequence was changed in the second and third cycles, *i.e.* the number of pulses was reduced and the pulse length was increased instead. Therefore, in the second and third cycle the following sequence was used: 50 pulses of 5 s duration, followed by 25 pulses of 10 s duration,

5 pulses of 50 s duration, 5 pulses of 100 s duration, 10 pulses of 100 s duration and 1 pulse of 500 s duration. Gas switching was performed using computer-controlled valves. The total gas flow rate for all *in situ* experiments was 25 mL min<sup>-1</sup>. The off-gases were monitored using an on-line mass spectrometer (MS). XAS data processing and analysis was performed using Athena software (Demeter 0.9.20 software package)<sup>23</sup>.

For *ex situ* XAS measurements, the oxygen carriers were ground, mixed with cellulose (ratio 1 : 8) and pelletized. The pellets were measured in transmission mode to acquire Fe and Cu K-edge XAS data.

## 3.4 Results and discussion

### 3.4.1 Structure and morphology of the as-synthesized oxygen carriers

The XRD data of Fe<sub>30</sub>Zr<sub>70</sub> show the presence of hematite (Fe<sub>2</sub>O<sub>3</sub>) and two phases of zirconium oxide, *i.e.* monoclinic(m) and tetragonal (t) ZrO<sub>2</sub>. Fe<sub>30</sub>Cu<sub>10</sub>Zr<sub>60</sub> exhibits peaks corresponding to a tetragonal copper ferrite spinel phase (t-CuFe<sub>2</sub>O<sub>4</sub>) in addition to α-Fe<sub>2</sub>O<sub>3</sub> and monoclinic ZrO<sub>2</sub> (Figure 3.1a). The presence of bulk CuO was not detected. Phase quantification by Rietveld refinement gave 26 wt. % Fe<sub>2</sub>O<sub>3</sub>, 57 wt. % m-ZrO<sub>2</sub> and 17 wt. % t-ZrO<sub>2</sub> for Fe<sub>30</sub>Zr<sub>70</sub>. In the case of Fe<sub>30</sub>Cu<sub>10</sub>Zr<sub>60</sub> the phase composition was determined as: 10 wt. % Fe<sub>2</sub>O<sub>3</sub>, 29 wt. % CuFe<sub>2</sub>O<sub>4</sub> and 61 wt. % m-ZrO<sub>2</sub> (standard deviation 1 wt. %). This is in good agreement with the expected composition according to the synthesis protocol. The addition of copper resulted in a larger average crystallite size of Fe<sub>2</sub>O<sub>3</sub> in Fe<sub>30</sub>Cu<sub>10</sub>Zr<sub>60</sub> (150 nm) when compared to Fe<sub>30</sub>Zr<sub>70</sub> (70 nm), as estimated using the Scherrer equation<sup>24</sup>.

Fe and Cu K-edge XANES spectra of the synthesized oxygen carriers together with reference materials are given in Figure 3.1b and c. The Fe K-edge XANES spectrum of Fe<sub>30</sub>Zr<sub>70</sub> shows characteristic features of α-Fe<sub>2</sub>O<sub>3</sub> while the spectrum of Fe<sub>30</sub>Cu<sub>10</sub>Zr<sub>60</sub> shows a closer resemblance to CuFe<sub>2</sub>O<sub>4</sub> than to α-Fe<sub>2</sub>O<sub>3</sub> (Figure 3.1b), in agreement with XRD. The Cu K-edge spectrum of Fe<sub>30</sub>Cu<sub>10</sub>Zr<sub>60</sub> (Figure 3.1c) confirms the absence of Cu<sub>2</sub>O or CuO due to the lack of a pre-edge feature that is characteristic for these oxides. Indeed, all the copper is present as a spinel CuFe<sub>2</sub>O<sub>4</sub> and no amorphous phases are present.

Figure S3.1 shows scanning electron micrographs of freshly calcined Fe<sub>30</sub>Zr<sub>70</sub> and Fe<sub>30</sub>Cu<sub>10</sub>Zr<sub>60</sub>. The calcined oxygen carriers were composed of particles with an average size of  $150 \pm 30$  nm and  $260 \pm 50$  nm (based on the analysis of 30 grains) for Fe<sub>30</sub>Zr<sub>70</sub> and Fe<sub>30</sub>Cu<sub>10</sub>Zr<sub>60</sub>, respectively. The micrograph of the Cu-containing oxygen carrier shows a comparatively dense microstructure with larger particles. The larger average grain size of Fe<sub>30</sub>Cu<sub>10</sub>Zr<sub>60</sub>, as determined by SEM, might be linked to the relatively low Tammann temperature of CuFe<sub>2</sub>O<sub>4</sub> (~400 °C) leading to rapid grain growth at high calcination temperatures (900 °C in this study)<sup>25</sup>. The BET surface area and BJH pore volume of the calcined oxygen carriers are given in Table 3.1. As expected from the electron micrograph images, Fe<sub>30</sub>Cu<sub>10</sub>Zr<sub>70</sub> possessed a lower surface area and pore volume than Fe<sub>30</sub>Zr<sub>70</sub>, most likely due to thermal sintering during calcination. Energy dispersive X-ray spectroscopy (EDX) was performed to visualize the distribution of the different phases in freshly calcined Fe<sub>30</sub>Zr<sub>70</sub> and Fe<sub>30</sub>Cu<sub>10</sub>Zr<sub>60</sub>. The different phases, *i.e.* Fe<sub>2</sub>O<sub>3</sub>, CuFe<sub>2</sub>O<sub>4</sub> and ZrO<sub>2</sub>, were distributed homogeneously after calcination as confirmed by the EDX maps shown in Figure S3.2

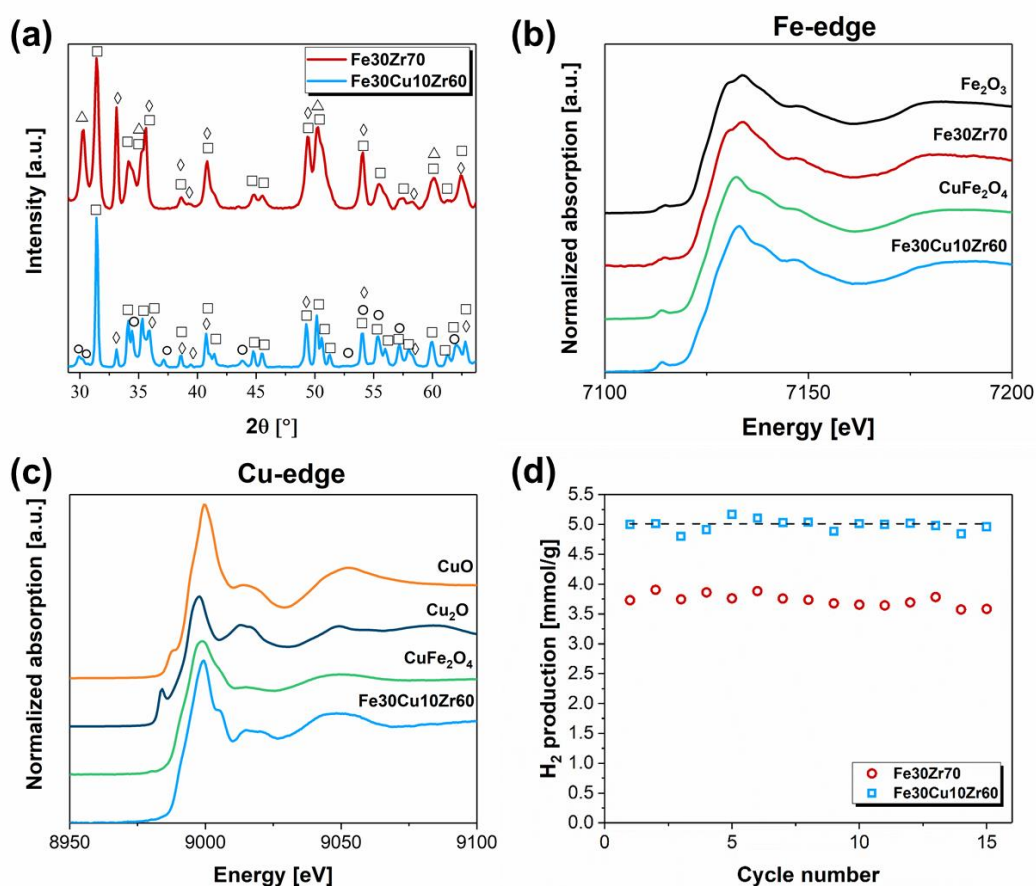




**Figure 3.1:** (a) XRD patterns of Fe<sub>30</sub>Zr<sub>70</sub> and Fe<sub>30</sub>Cu<sub>10</sub>Zr<sub>60</sub> calcined at 900 °C for 2 h. The following phases were identified: (◇) Fe<sub>2</sub>O<sub>3</sub>, (□) m-ZrO<sub>2</sub>, (Δ) t-ZrO<sub>2</sub>, (○) t-CuFe<sub>2</sub>O<sub>4</sub>, (b) Fe K-edge and (c) Cu K-edge XANES spectra of (—) Fe<sub>30</sub>Zr<sub>70</sub>, (—) Fe<sub>30</sub>Cu<sub>10</sub>Zr<sub>60</sub>, (—) α-Fe<sub>2</sub>O<sub>3</sub> reference, (—) CuFe<sub>2</sub>O<sub>4</sub> reference, (—) CuO reference and (—) Cu<sub>2</sub>O reference and (d) H<sub>2</sub> yield during re-oxidation as a function of cycle number (reduction in 2.5 vol. % H<sub>2</sub> in N<sub>2</sub> for 6 min at 700 °C): (□) Fe<sub>30</sub>Zr<sub>70</sub> and (○) Fe<sub>30</sub>Cu<sub>10</sub>Zr<sub>60</sub>. The dashed line gives the theoretically expected quantities of hydrogen, *i.e.* 5 mmol H<sub>2</sub>/g for an oxygen carrier containing 30 wt. % Fe<sub>2</sub>O<sub>3</sub> (assuming its full reduction to Fe).

**Table 3.1:** Textural characteristics of the oxygen carriers: BET surface area, BJH pore volume and average particle size of Fe<sub>2</sub>O<sub>3</sub> in calcined Fe<sub>30</sub>Zr<sub>70</sub> and Fe<sub>30</sub>Cu<sub>10</sub>Zr<sub>60</sub>.

	Surface Area [m <sup>2</sup> /g]	Pore Volume [cm <sup>3</sup> /g]	Average particle size (nm)
Fe <sub>30</sub> Zr <sub>70</sub>	4	0.04	150 ± 30
Fe <sub>30</sub> Cu <sub>10</sub> Zr <sub>60</sub>	1	< 0.01	260 ± 50

### 3.4.2 CLC performance of the oxygen carriers

The cyclic CLC performance of the oxygen carriers was determined in a fixed bed reactor at 700 °C, with each cycle comprising three steps. First, a reduction step was carried out using 2.5 vol. % H<sub>2</sub> in N<sub>2</sub>. Here, H<sub>2</sub> was selected as a model gas as it is one of the main components of a synthesis gas. The reduction was followed by oxidation using 23 vol. % H<sub>2</sub>O in N<sub>2</sub>, yielding high-purity H<sub>2</sub>. The quantity of H<sub>2</sub> produced during the oxidation with steam (mmol H<sub>2</sub> per g oxygen carrier; 3Fe + 4H<sub>2</sub>O → Fe<sub>3</sub>O<sub>4</sub> + 4H<sub>2</sub>) is plotted as a function of the cycle number in Figure 3.1d. Subsequently, an oxidation step in 5 vol. % O<sub>2</sub> in N<sub>2</sub> was carried out. A thermodynamic assessment of the water splitting reaction, Figure S3.3, shows that metallic Cu cannot be oxidized to a sensible extent by steam and does therefore not contribute to the production of H<sub>2</sub> at 700 °C. This is in line with the XRD analysis of Fe<sub>30</sub>Cu<sub>10</sub>Zr<sub>60</sub> collected after steam oxidation (Figure S3.4). In contrast, metallic Fe can be oxidized

to Fe<sub>3</sub>O<sub>4</sub> with steam yielding H<sub>2</sub>. Oxidation of Fe<sub>3</sub>O<sub>4</sub> and Cu with O<sub>2</sub> yields Fe<sub>2</sub>O<sub>3</sub>, CuO and CuFe<sub>2</sub>O<sub>4</sub>, respectively. The H<sub>2</sub> production was calculated for each cycle as:

$$N_{H_2} = \dot{N}_{N_2} \times \int \frac{y_{H_2}}{1 - y_{H_2}} dt$$

where,  $N_{H_2}$  is the number of moles of H<sub>2</sub> produced,  $\dot{N}_{N_2}$  is the molar flow rate of N<sub>2</sub>, and  $y_{H_2}$  is the mole fraction of hydrogen in the gas leaving the fixed bed and t is the time. The average molar flow rate of N<sub>2</sub>, and  $y_{H_2}$  is the mole fraction of hydrogen in the gas leaving the fixed bed and t is the time. The average H<sub>2</sub> production capacity of Fe<sub>30</sub>Zr<sub>70</sub> was found to be 3.5 mmol H<sub>2</sub> per g oxygen carrier that is lower than the theoretically expected value (5 mmol H<sub>2</sub> per g oxygen carrier).

In contrast to Fe<sub>30</sub>Zr<sub>70</sub>, Fe<sub>30</sub>Cu<sub>10</sub>Zr<sub>60</sub> showed high and very stable H<sub>2</sub> yields, e.g. 5 mmol H<sub>2</sub> per g oxygen carrier over 15 cycles. The difference in the H<sub>2</sub> yields can be correlated with their redox reactivity. Specifically, Fe<sub>30</sub>Zr<sub>70</sub> could not be reduced fully during the reduction time of 6 min owing to the slower reduction kinetics (in spite of possessing a smaller crystallite size than Fe<sub>30</sub>Cu<sub>10</sub>Zr<sub>60</sub>). In the following, we applied H<sub>2</sub>-TPR and *in situ* XANES spectroscopy to probe in more detail the reduction characteristics of the oxygen carriers.

### 3.4.3 Reduction behaviour of the oxygen carriers

Temperature programmed reduction combined with *ex situ* XRD – Cu K-edge XAS analysis. H<sub>2</sub>-temperature programmed reduction (H<sub>2</sub>-TPR) experiments were carried out to compare the reducibility of the two oxygen carriers (Figure 3.2a). The H<sub>2</sub>-TPR profile of Fe<sub>30</sub>Zr<sub>70</sub> had a broad peak centred at 600 °C with two shoulders at 475 °C and 700 °C. Deconvolution revealed the presence of three reduction steps at around 460, 600 and 690 °C. For Fe<sub>30</sub>Cu<sub>10</sub>Zr<sub>60</sub>, the first peak was centred at 391 °C followed by a broad peak at ~550 °C. Importantly, from Figure 3.2a it is clear that in Fe<sub>30</sub>Cu<sub>10</sub>Zr<sub>60</sub> the reduction of the iron oxide phases was completed at appreciably lower temperatures compared to Fe<sub>30</sub>Zr<sub>70</sub>. The deconvolution of the TPR profile of Fe<sub>30</sub>Cu<sub>10</sub>Zr<sub>60</sub> was performed considering three main peaks based on the XRD data discussed below.

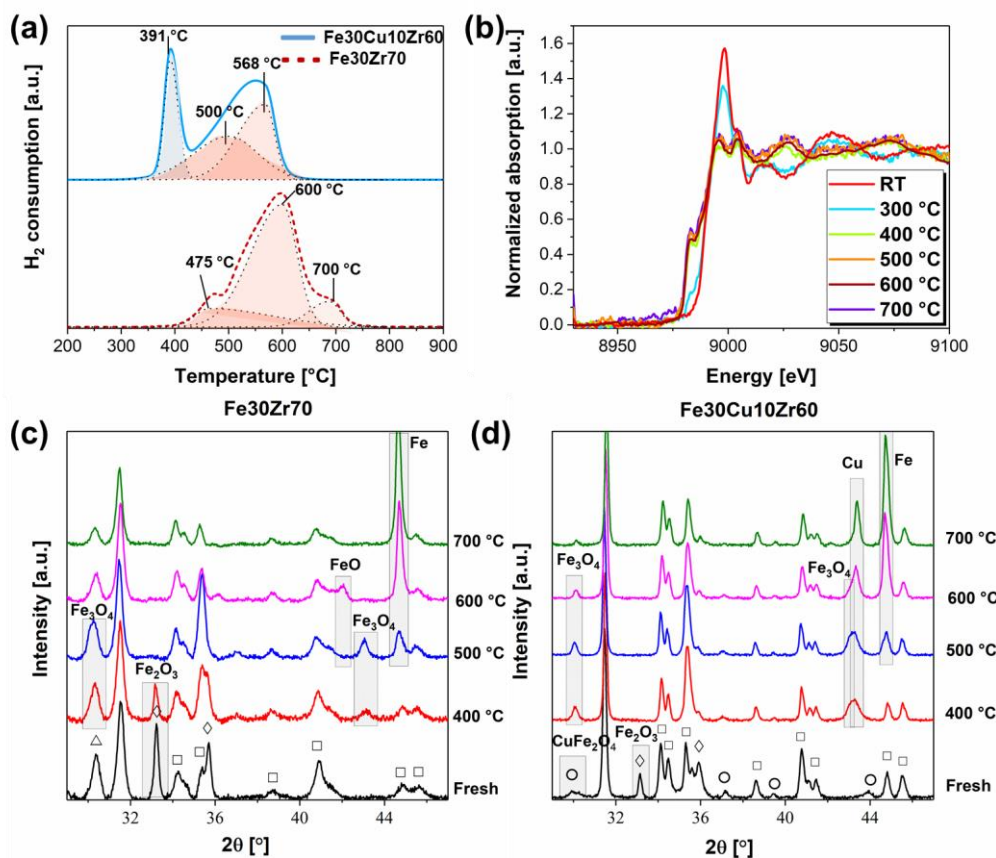


**Figure 3.2:** (a) H<sub>2</sub> consumption during TPR of Fe<sub>30</sub>Zr<sub>70</sub> (----) and Fe<sub>30</sub>Cu<sub>10</sub>Zr<sub>60</sub> (—), (b) Cu K-edge XANES spectra of Fe<sub>30</sub>Cu<sub>10</sub>Zr<sub>60</sub> collected at the temperatures marked (during a TPR program); series of XRD patterns of (c) Fe<sub>30</sub>Zr<sub>70</sub> and (d) Fe<sub>30</sub>Cu<sub>10</sub>Zr<sub>60</sub> after H<sub>2</sub> reduction at various temperatures. The following compounds were identified in the fresh samples: (◇) Fe<sub>2</sub>O<sub>3</sub>, (□) m-ZrO<sub>2</sub>, (Δ) t-ZrO<sub>2</sub>, (○) t-CuFe<sub>2</sub>O<sub>4</sub>.

To identify the phases formed during TPR, a series of Cu Kedge XANES (Figure 3.2b) and XRD (Figure 3.2c, d and Figure S3.5) data were collected after certain steps of the TPR program. The XRD patterns of Fe<sub>30</sub>Zr<sub>70</sub> show that Fe<sub>2</sub>O<sub>3</sub> started to reduce at 400 °C. With increasing temperature, diffraction peaks of intermediate iron oxide phases, Fe<sub>3</sub>O<sub>4</sub> (at 500 °C) and FeO (at 600 °C), were detected (Figure 3.2c).

In Fe<sub>30</sub>Cu<sub>10</sub>Zr<sub>60</sub>, two Bragg peaks due to CuFe<sub>2</sub>O<sub>4</sub> can be observed in the 2θ range of 29°–31° (freshly calcined material, Figure 3.2d) which correspond to the 011 and 110 Bragg reflections of the t-CuFe<sub>2</sub>O<sub>4</sub> spinel (I41/amd space group). Increasing the reduction temperature (400 °C), the two peaks evolved to a single peak (220 peak, Fd3m space group, Fe<sub>3</sub>O<sub>4</sub>) owing to the reduction of CuFe<sub>2</sub>O<sub>4</sub> and the formation of Fe<sub>3</sub>O<sub>4</sub>. At 400 °C, the peaks due to Fe<sub>2</sub>O<sub>3</sub> have disappeared completely and a fcc-Cu

phase was identified (Figure S3.6). To complement the XRD analysis, Cu K-edge XAS was utilized to identify the stage at which metallic  $\text{Cu}^0$  is formed (Figure 3.2b and Figure S3.7). The Cu K-edge XANES spectrum of  $\text{Fe}_{30}\text{Cu}_{10}\text{Zr}_{60}$  confirms the presence of  $\text{Cu}^0$  at temperatures  $\sim 400$  °C. Hence, combining our XRD and Cu K-edge XANES analyses, we can conclude that the reduction of  $\text{CuFe}_2\text{O}_4$  follows  $\text{CuFe}_2\text{O}_4 \rightarrow \text{Cu}^0 + \text{Fe}_3\text{O}_4$  whereby  $\text{Cu}^0$  segregates out of the  $\text{CuFe}_2\text{O}_4$  spinel at 400 °C. This is in line with previous interpretations of (albeit indirect) TGA measurements <sup>26</sup>. With increasing reduction temperature, from 400 °C to 700 °C, the formation of  $\text{Fe}_3\text{O}_4$  and Fe is revealed by XRD. On the other hand, we did not detect a FeO phase by XRD in  $\text{Fe}_{30}\text{Cu}_{10}\text{Zr}_{60}$ , possibly because FeO is unstable below 570 °C and instead a direct  $\text{Fe}_3\text{O}_4$  - Fe transition occurs in  $\text{Fe}_{30}\text{Cu}_{10}\text{Zr}_{60}$  below this temperature <sup>27</sup>. Therefore, the determination of the reduction pathways under CLC relevant conditions is needed. To this end, *in situ* XANES studies at the Fe K-edge during isothermal reduction (700 °C) were carried out, as described in the following section.

#### 3.4.4 Reduction pathways probed by *in situ* XANES

*In situ* (pulsed- $\text{H}_2$ ) Fe K-edge XANES experiments allowed us to determine the reduction pathways of the oxygen carriers and to quantify the intermediate states as a function of Cu promotion. Three redox cycles were performed at 700 °C using 5 vol. %  $\text{H}_2$  in He and 5 vol. %  $\text{O}_2$  in He, for reduction and oxidation, respectively. To probe the reduction steps, each Fe K-edge XANES spectrum was collected in He after a short pulse of  $\text{H}_2$  had been released into the bed.

In the first cycle, 145  $\text{H}_2$ -pulses were used to track the reduction pathways. The XANES spectra are represented as 2D contour plots of  $\text{Fe}_{30}\text{Zr}_{70}$  and  $\text{Fe}_{30}\text{Cu}_{10}\text{Zr}_{60}$  in Figure 3.3a and b, respectively. Here, the normalized absorption is plotted as a function of pulse number and photon energy (red represents high intensity and blue represents low intensity). Together with the 2D contour plots, the first (bottom: initial state) and the last (top: final state after reduction) XANES spectra recorded for  $\text{Fe}_{30}\text{Zr}_{70}$  and  $\text{Fe}_{30}\text{Cu}_{10}\text{Zr}_{60}$  in the first reduction cycle are displayed (all the collected individual spectra are shown in Figure S3.8). From Figure S3.8 we observe in both oxygen carriers a shift in the edge position of the XANES spectra to lower energies, which indicates the reduction of  $\text{Fe}_2\text{O}_3$ , since the binding energies of 1s electrons decrease <sup>28</sup>. The qualitative comparison of the *in situ* collected spectra of

Fe<sub>30</sub>Zr<sub>70</sub> with reference spectra (Figure S3.9) suggests a reduction to metallic Fe that involves the formation of the intermediate states, Fe<sub>3</sub>O<sub>4</sub> and FeO. Notably, the reduction of Fe<sub>30</sub>Cu<sub>10</sub>Zr<sub>60</sub> was considerably faster than that of Fe<sub>30</sub>Zr<sub>70</sub>, as observed by XANES in Figure 3.3a. Fe<sub>30</sub>Zr<sub>70</sub> and Fe<sub>30</sub>Cu<sub>10</sub>Zr<sub>60</sub> were fully reduced after 140 and 60 H<sub>2</sub>-pulses (first cycle, 700 °C), respectively. A quantitative assessment of the reduction pathways was obtained through linear combination fitting (LCF) using Fe<sub>2</sub>O<sub>3</sub>, Fe<sub>3</sub>O<sub>4</sub>, FeO, Fe and CuFe<sub>2</sub>O<sub>4</sub> as standards, Figure 3.3c and d. In addition, Figure S3.11 plots the loss of oxygen in mol O/mol Fe in the oxygen carriers during reduction. The fitting quality of the linear combination is demonstrated in Figure S3.10 for selected Fe K-edge XANES data. The main observations obtained from the LCF analyses are described below:

**Reduction of Fe<sub>30</sub>Zr<sub>70</sub>.** The reduction of Fe<sub>2</sub>O<sub>3</sub> to metallic Fe<sup>0</sup> proceeds through two intermediate states *i.e.* Fe<sub>3</sub>O<sub>4</sub> and FeO (Fe<sub>2</sub>O<sub>3</sub>-Fe<sub>3</sub>O<sub>4</sub>-FeO-Fe<sup>0</sup>) in a simultaneous manner. The reduction of Fe<sub>2</sub>O<sub>3</sub> and Fe<sub>3</sub>O<sub>4</sub> was completed within a reaction time of 1000 s and 1500 s, respectively. When the weight fractions of Fe<sub>2</sub>O<sub>3</sub> and Fe<sub>3</sub>O<sub>4</sub> reached ~20 wt. %, the rate of reduction decreases appreciably. The final reduction step, *i.e.* FeO - Fe<sup>0</sup> was the slowest transition (Figure 3.3c), in line with previous reports<sup>29,30</sup>. The rate of formation of Fe shows two regions: an initial period in which the rate of formation of Fe increases (first 1000 s), followed by a reaction stage in which the rate of formation of Fe decreases (after 1000 s). The increasing rate of formation of Fe is possibly associated with the growth of Fe<sup>0</sup> nuclei at the surface of FeO<sub>x</sub>. These nuclei promote the dissociative adsorption of H<sub>2</sub>, as suggested in previous studies<sup>29,30</sup>. The reduced rate of Fe formation after 1000 s might be due to the coverage of iron oxide with a layer of Fe which limits the diffusion of the reactants<sup>30,31</sup>.

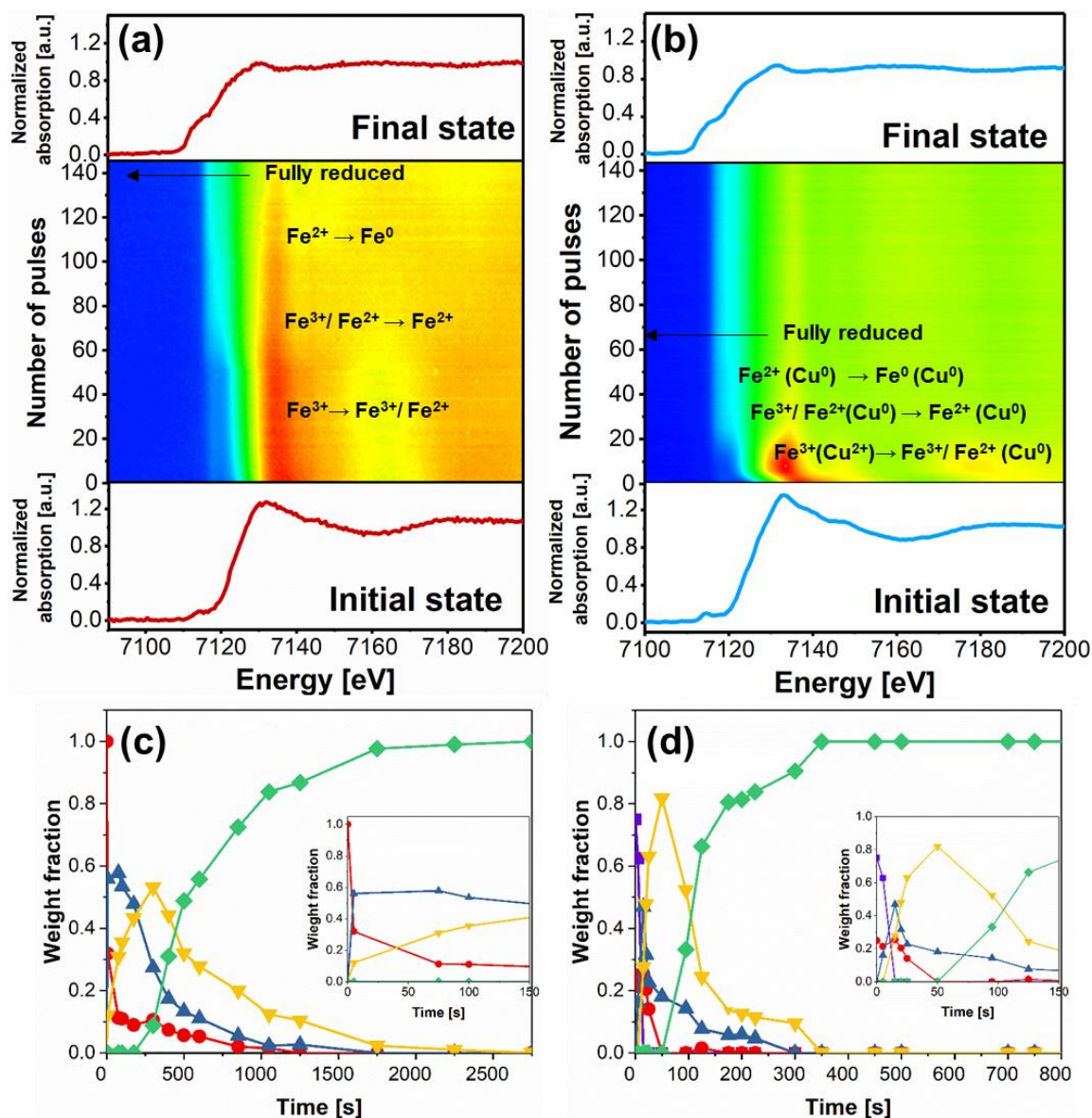


**Figure 3.3:** 2D contour plots of the XANES spectra of (a) Fe<sub>30</sub>Zr<sub>70</sub> and (b) Fe<sub>30</sub>Cu<sub>10</sub>Zr<sub>70</sub> in the first cycle during reduction at 700 °C using 5 vol. % H<sub>2</sub> in He. Weight fractions of Fe<sub>2</sub>O<sub>3</sub> (—●—), CuFe<sub>2</sub>O<sub>4</sub> (—■—), Fe<sub>3</sub>O<sub>4</sub> (—▲—), FeO (—▼—) and Fe (—◆—) determined by linear combination fitting of the Fe K-edge XANES spectra for the reduction of (c) Fe<sub>30</sub>Zr<sub>70</sub> and (d) Fe<sub>30</sub>Cu<sub>10</sub>Zr<sub>60</sub> in the 1<sup>st</sup> cycle. For Fe<sub>30</sub>Zr<sub>70</sub> and Fe<sub>30</sub>Cu<sub>10</sub>Zr<sub>60</sub> LCF results are plotted over 2750 s and 800 s, respectively, due to different reduction times.

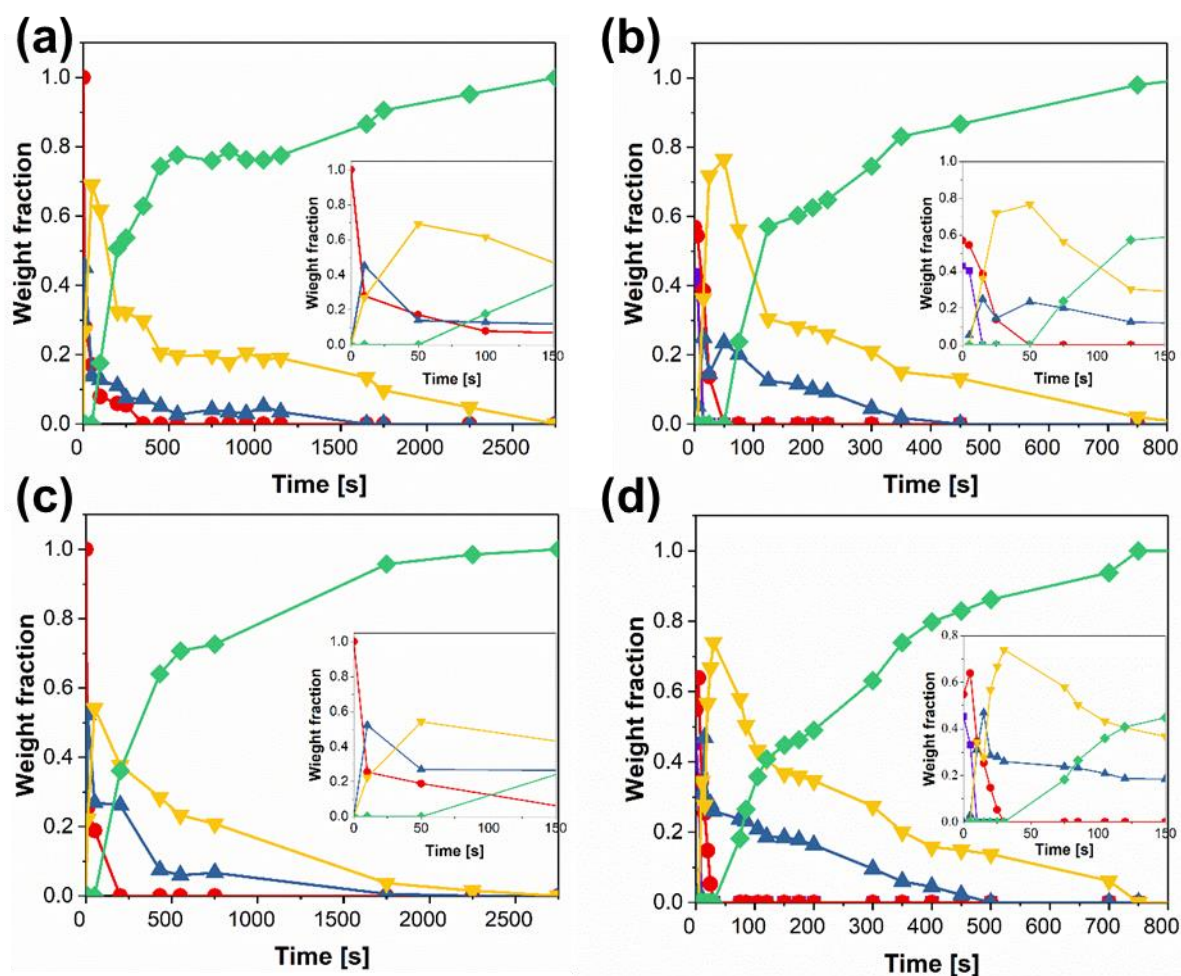
**Reduction of Fe<sub>30</sub>Cu<sub>10</sub>Zr<sub>60</sub>.** The reduction pathway of Fe<sub>30</sub>Cu<sub>10</sub>Zr<sub>60</sub> is plotted in Figure 3.3b and d. The reduction of Fe<sub>2</sub>O<sub>3</sub> - Fe<sub>3</sub>O<sub>4</sub> was considerably faster when compared to Fe<sub>30</sub>Zr<sub>70</sub> and occurred simultaneously with the reduction of CuFe<sub>2</sub>O<sub>4</sub> to Fe<sub>3</sub>O<sub>4</sub> and metallic Cu<sup>0</sup> (according to *ex situ* XRD and Cu K-edge XANES given in

Figure 3.2). Also for Fe<sub>30</sub>Cu<sub>10</sub>Zr<sub>60</sub> the reduction of Fe<sub>2</sub>O<sub>3</sub> proceeded in the following sequence Fe<sub>3</sub>O<sub>4</sub> - FeO - Fe<sup>0</sup>. The overlap of the two intermediates, Fe<sub>3</sub>O<sub>4</sub> and FeO, is smaller compared to Fe<sub>30</sub>Zr<sub>70</sub> indicative of a faster reduction of Fe<sub>3</sub>O<sub>4</sub> to FeO in Fe<sub>30</sub>Cu<sub>10</sub>Zr<sub>60</sub>. Fe<sub>30</sub>Cu<sub>10</sub>Zr<sub>60</sub> was reduced fully after 60 H<sub>2</sub>-pulses (350 s) (1/6th of the total reduction time required for Fe<sub>30</sub>Zr<sub>70</sub>). These results are in line with the observation that the presence of Cu<sup>0</sup> enhances the reducibility of iron oxide for all oxidation phases. The most remarkable effect of the presence of Cu<sup>0</sup> on the rates of reduction was observed for the final reduction step, *i.e.* FeO - Fe<sup>0</sup> (which is the slowest reduction step).

In the following, the effect of cycle number on (i) the rate of reduction (time for total reduction) and (ii) the reduction pathway (*i.e.* the intermediate states) was studied. Figure 3.4 shows the second and third reduction cycle for both oxygen carriers. For Fe<sub>30</sub>Zr<sub>70</sub>, the cycle number had only a small effect on the reaction rate and no effect on the reduction pathway, in line with the results of the fixed bed experiments. Similar to the first cycle, the reduction of Fe<sub>30</sub>Cu<sub>10</sub>Zr<sub>60</sub> followed the pathway Fe<sub>2</sub>O<sub>3</sub>/CuFe<sub>2</sub>O<sub>4</sub> - Fe<sub>3</sub>O<sub>4</sub> (Cu<sup>0</sup>) - FeO (Cu<sup>0</sup>) - Fe<sup>0</sup> (Cu<sup>0</sup>) also in the second and third cycle. However, for Fe<sub>30</sub>Cu<sub>10</sub>Zr<sub>60</sub> the time required to achieve full reduction was increased for the second cycle when compared to the first cycle. In spite of this decrease in the reduction rate, the reduction of Fe<sub>30</sub>Cu<sub>10</sub>Zr<sub>60</sub> was still considerably faster than for Fe<sub>30</sub>Zr<sub>70</sub> in the respective cycles. On the other hand, for Fe<sub>30</sub>Cu<sub>10</sub>Zr<sub>60</sub> we did not observe any differences between the reduction time for the second and third cycle. Moreover, when compared to the original oxygen carrier, the CuFe<sub>2</sub>O<sub>4</sub> weight fraction in the re-oxidized oxygen carrier decreases to 0.4 in the second and third cycle (compared to 0.8 in the freshly calcined material, Figure S3.12). A possible explanation for this reduced quantity of CuFe<sub>2</sub>O<sub>4</sub> might be that the oxidation time was too short to form the spinel structure. The reduced fraction of CuFe<sub>2</sub>O<sub>4</sub> has been observed also by XRD of cycled and re-oxidized Fe<sub>30</sub>Cu<sub>10</sub>Zr<sub>60</sub> in the fixed bed experiments (Figure S3.13) shows the presence of CuO after re-oxidation for 5 min in 5 vol. % O<sub>2</sub> in N<sub>2</sub>, the CuO peaks disappeared when the oxidation time was increased to 20 min). We speculate that the dispersion of Cu<sup>0</sup> is increased when obtained through a reductive segregation from CuFe<sub>2</sub>O<sub>4</sub> compared to CuO derived Cu. Nonetheless, the lack of a complete spinel formation seems to have little effect on the reduction rate and did not translate to a reduced hydrogen yield with cycle number. The effect of the formation of Cu<sup>0</sup> in



Fe<sub>30</sub>Cu<sub>10</sub>Zr<sub>60</sub> is examined further in the next section using H<sub>2</sub>-temperature programmed desorption (TPD).



**Figure 3.4:** Weight fractions of Fe<sub>2</sub>O<sub>3</sub> (—●—), CuFe<sub>2</sub>O<sub>4</sub> (—■—), Fe<sub>3</sub>O<sub>4</sub> (—▲—), FeO (—▼—) and Fe (—◆—) determined by linear combination fitting of the Fe K-edge XANES spectra during the reduction of Fe<sub>30</sub>Zr<sub>70</sub> in (a) the 2<sup>nd</sup> cycle and (c) the 3<sup>rd</sup> cycle and of Fe<sub>30</sub>Cu<sub>10</sub>Zr<sub>60</sub> in (b) the 2<sup>nd</sup> cycle and (d) the 3<sup>rd</sup> cycle.

### 3.4.5 H<sub>2</sub>-temperature programmed desorption (TPD)

The *in situ* (pulsed-H<sub>2</sub>) Fe K-edge XANES experiments together with *ex situ* Cu K-edge analysis indicates that metallic copper might promote the rate of reduction of Fe<sub>30</sub>Cu<sub>10</sub>Zr<sub>60</sub> compared to Fe<sub>30</sub>Zr<sub>70</sub>. To provide some further insight into the role of copper additional H<sub>2</sub>-temperature programmed desorption (TPD) experiments were performed. Specifically, TPD measurements were carried out on calcined and pre-reduced oxygen carriers at 250 °C, 400 °C and 800 °C. The corresponding TPD



profiles, Figure 3.5, complemented by XRD of the pre-reduced material, reveal no H<sub>2</sub> adsorption on the calcined oxygen carriers. On the other hand, TPD profiles of Fe<sub>30</sub>Cu<sub>10</sub>Zr<sub>60</sub>, pre-reduced at 200 °C and 250 °C, indicate that the quantity of adsorbed H<sub>2</sub> increases significantly with the presence of metallic Cu (which is fully formed at 400 °C, Figure S3.7), in agreement with literature<sup>28,32–34</sup>. However, for pre-reduced Fe<sub>30</sub>Zr<sub>70</sub>, there is only a slight increase in the quantity of H<sub>2</sub> adsorbed. When the pre-reduction temperature was increased to 800 °C a high quantity of H<sub>2</sub> adsorbed (due to the presence of both metallic Fe and Cu)<sup>30,31,35,36</sup>.

These experimental results suggest that the rapid formation of Cu<sup>0</sup> (segregated from the spinel structure in the first stage of the reduction) promotes the reduction of FeO<sub>x</sub> by dissociatively adsorbing H<sub>2</sub> that subsequently spills over to FeO<sub>x</sub>. This explanation would be in line with the proposed mechanism for the enhanced reduction of iron oxide in the presence of copper for Fischer–Tropsch catalysis at low temperatures (200–350 °C)<sup>28,34,37</sup>.

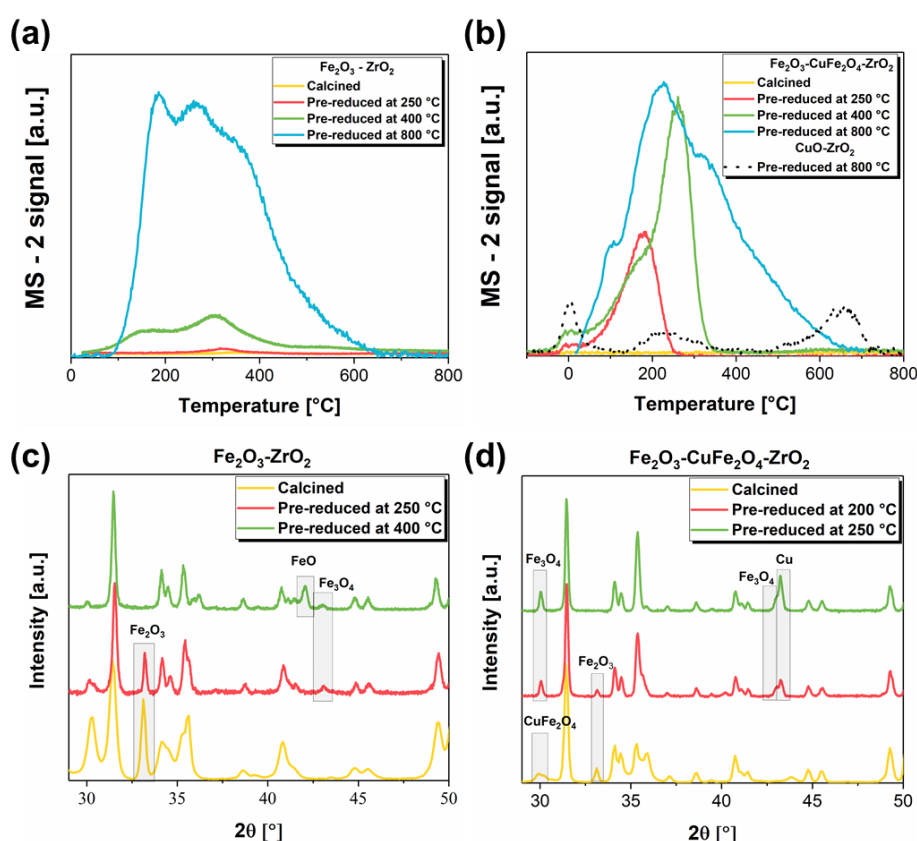


**Figure 3.5:** H<sub>2</sub>-TPD-MS profile of (a) Fe<sub>30</sub>Zr<sub>70</sub> and (b) Fe<sub>30</sub>Cu<sub>10</sub>Zr<sub>60</sub> pre-reduced at different temperatures, XRD of (c) Fe<sub>30</sub>Zr<sub>70</sub> and (d) Fe<sub>30</sub>Cu<sub>10</sub>Zr<sub>60</sub> after TPD tests.

### 3.5 Conclusions

In this work we probe in detail the effect of copper on the cyclic redox characteristics of Fe<sub>2</sub>O<sub>3</sub>-based, ZrO<sub>2</sub>-supported oxygen carriers for the production of H<sub>2</sub> via a chemical looping cycle. Cu containing oxygen carriers possessed a high H<sub>2</sub> yield (close to the theoretically expected value) while maintaining a high stability over 15 redox cycles at 700 °C. On the other hand, unpromoted Fe<sub>2</sub>O<sub>3</sub>-ZrO<sub>2</sub> showed a low H<sub>2</sub> yield (30% below the theoretically expected value), due to the incomplete reduction of Fe<sub>2</sub>O<sub>3</sub> at the given conditions (700 °C in 2.5 vol. % H<sub>2</sub> in N<sub>2</sub>). The iron was present as Fe<sub>2</sub>O<sub>3</sub> and spinel CuFe<sub>2</sub>O<sub>4</sub> + Fe<sub>2</sub>O<sub>3</sub> in the as-synthesized Fe<sub>30</sub>Zr<sub>70</sub> and Fe<sub>30</sub>Cu<sub>10</sub>Zr<sub>60</sub>, respectively, together with ZrO<sub>2</sub> phases. *In situ* XANES provided insight into the reduction pathways of the promoted and unpromoted oxygen carriers and the rate of formation of the different oxidation states of iron. It was found that at 700 °C in both oxygen carriers the reduction of Fe<sub>2</sub>O<sub>3</sub> to metallic Fe<sup>0</sup> proceeded via Fe<sub>3</sub>O<sub>4</sub> and FeO intermediate phases, whereby the transition FeO - Fe<sup>0</sup> was the slowest reduction step in both oxygen carriers. The promotion of iron oxide with copper resulted in a six times faster reduction of FeO to metallic Fe<sup>0</sup>. It is proposed that metallic Cu, which readily segregates from the spinel structure under reductive conditions, promotes the reduction of FeO<sub>x</sub> through the dissociative adsorption of H<sub>2</sub> and its spill-over to FeO<sub>x</sub>. Overall, the bimetallic Fe-Cu oxygen carrier developed in this study demonstrated a significant enhancement in its reactivity and redox stability, making the new material an interesting candidate for the H<sub>2</sub> production through chemical looping cycles.

### 3.6 Supporting Information

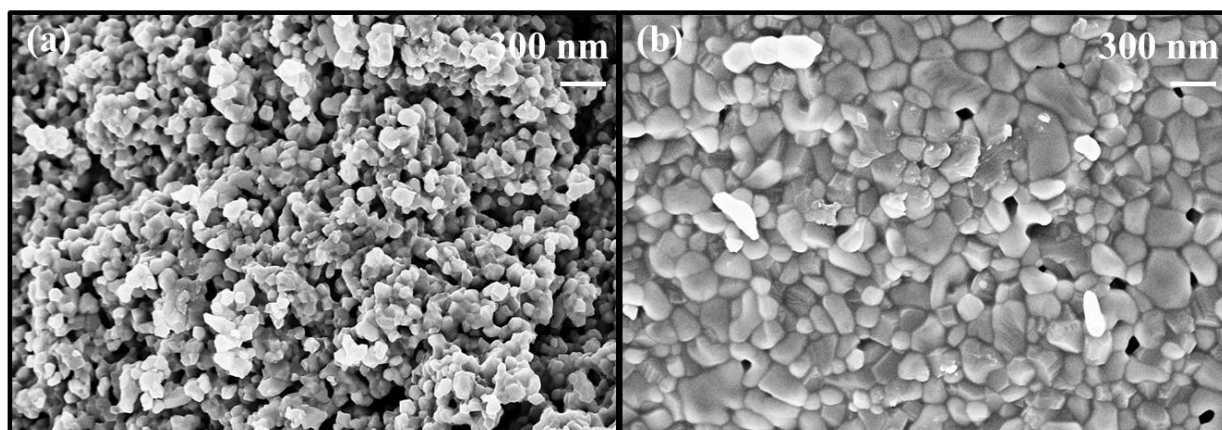


**Figure S3.1:** Scanning electron micrographs of the calcined oxygen carriers (a)  $\text{Fe}_{30}\text{Zr}_{70}$  and (b)  $\text{Fe}_{30}\text{Cu}_{10}\text{Zr}_{60}$ .

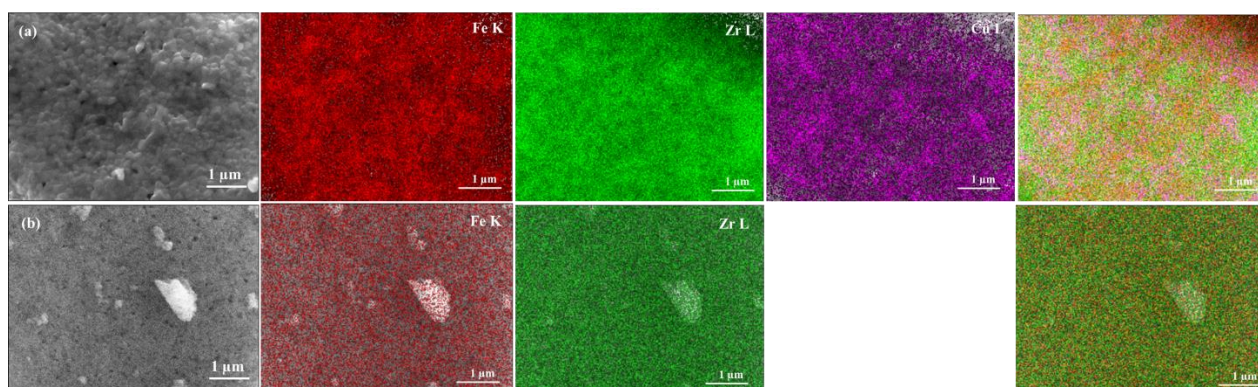


**Figure S3.2:** EDX maps of calcined (a)  $\text{Fe}_{30}\text{Zr}_{70}$  and (b)  $\text{Fe}_{30}\text{Cu}_{10}\text{Zr}_{60}$ , Copper, zirconium and iron are represented with the colours pink, green and red, respectively.

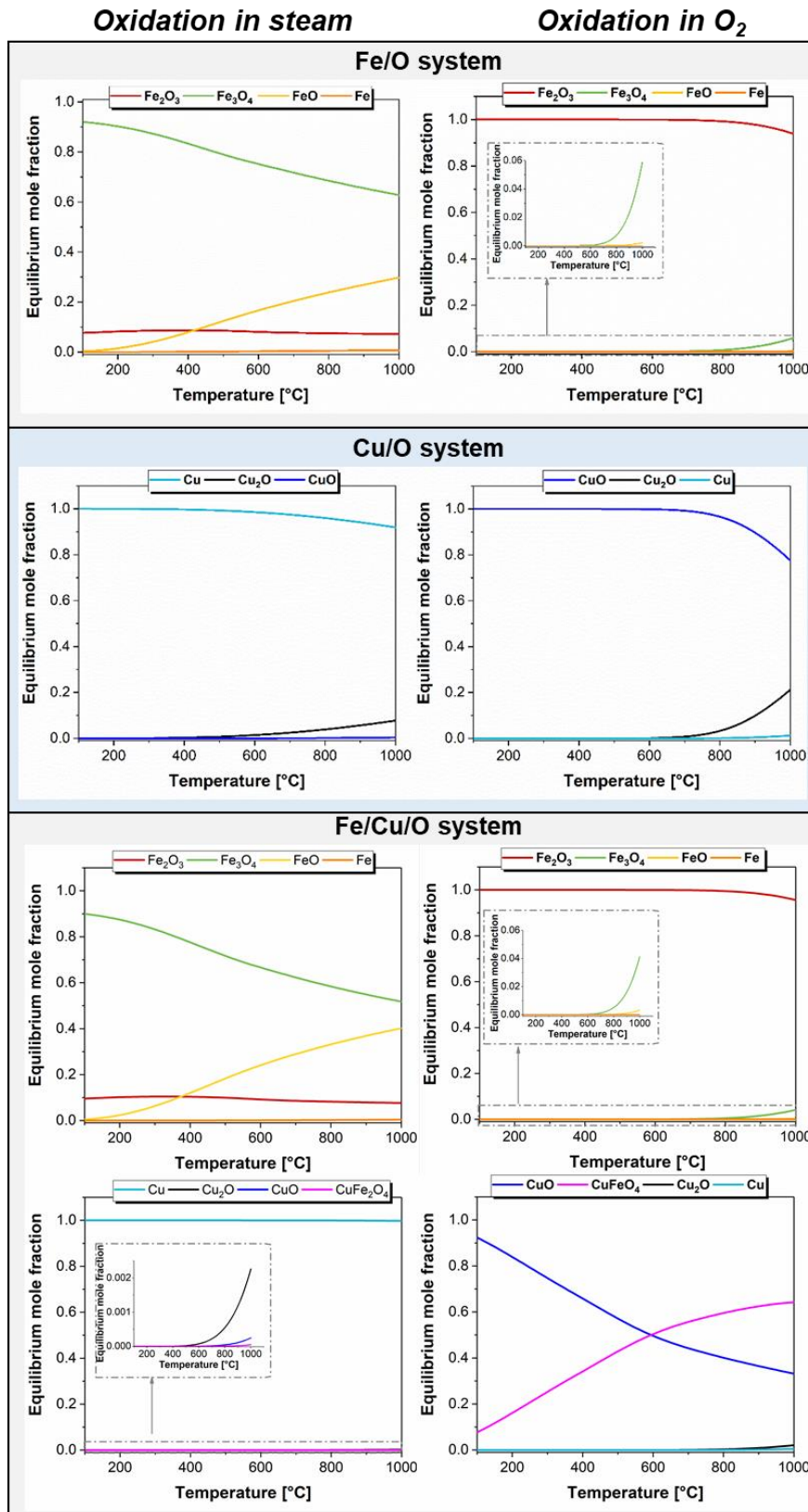


**Figure S3.3:** Equilibrium thermodynamics calculations for the Fe/O, Cu/O and Fe/Cu/O systems during oxidative (steam and oxygen) conditions (molar ratio Fe:Cu = 3:1).

A thermodynamic evaluation of the materials is given in Figure S3. The equilibrium mole fractions of the different phases considered (Cu, Cu<sub>2</sub>O, CuO, CuFe<sub>2</sub>O<sub>4</sub>, Fe<sub>2</sub>O<sub>3</sub>, Fe<sub>3</sub>O<sub>4</sub>, FeO and Fe) were calculated by Gibbs free energy minimization using the HSC chemistry software 6.0 and the thermochemical data of Barin and Platzki <sup>1</sup>. The equilibrium thermodynamics calculations were performed for the i) Fe/O, ii) Cu/O and iii) Fe/Cu/O systems under steam oxidation (molar ratio of Fe:Cu:H<sub>2</sub>O = 3:1:100) and oxygen oxidation (molar ratio of Fe:Cu:O<sub>2</sub> = 3:1:100) conditions, as a function temperature.

- i. **Oxidation in steam:** In the metallic state, there is no alloy formation between Cu and Fe, in line with experimental evidence (XRD and XANES) and literature.<sup>2</sup> A thermodynamic assessment of the steam oxidation of metallic Fe indicates that Fe can be oxidized up to Fe<sub>3</sub>O<sub>4</sub>. The steam oxidation of metallic Cu gives only a small quantity of Cu<sub>2</sub>O (3 %), with the majority being Cu (97 %), indicating that Cu cannot be oxidized to a sensible extent with steam (*i.e.* no water splitting reaction using Cu according to equilibrium thermodynamic calculations). In the bimetallic Fe-Cu system, the mole fraction of Cu is not affected by the presence of steam (100 %) and Cu<sub>2</sub>O does not form (in line with XRD of Fe<sub>30</sub>Cu<sub>10</sub>Zr<sub>60</sub> after steam oxidation, Figure S4). Fe is oxidized up to Fe<sub>3</sub>O<sub>4</sub>, while the formation of CuFe<sub>2</sub>O<sub>4</sub> or Fe<sub>2</sub>O<sub>3</sub> is thermodynamically not favoured under steam oxidation conditions.
- ii. **Oxidation in O<sub>2</sub>:** For the thermodynamic assessment of the oxidation in O<sub>2</sub>, the reactants were Fe<sub>3</sub>O<sub>4</sub> and Cu. At 700 °C, Fe<sub>3</sub>O<sub>4</sub> is oxidized to Fe<sub>2</sub>O<sub>3</sub> (complete oxidation) in the Fe/O system while Cu was oxidized to CuO in the Cu/O system. The formation of Fe<sub>2</sub>O<sub>3</sub>, CuO and CuFe<sub>2</sub>O<sub>4</sub> is predicted in the Cu/Fe system.

<sup>1</sup> I. Barin, G. Platzki, *Thermochemical data of pure substances*. Wiley Online Library, **1989**; Vol. 304.

<sup>2</sup> A. Bachmaier, M. Kerberb, D. Setman, R. Pippan, *Acta Materialia*, **60**, **2012**, 860-871.

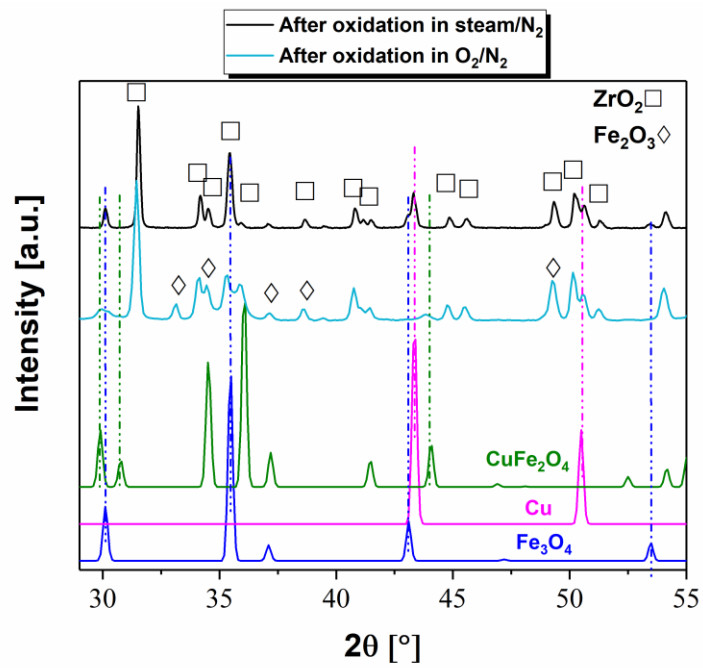


**Figure S3.4:** XRD patterns of Fe<sub>30</sub>Cu<sub>10</sub>Zr<sub>60</sub> (previously reduced in 2.5 % H<sub>2</sub> in N<sub>2</sub>) subjected to oxidation in steam/N<sub>2</sub> and followed by O<sub>2</sub>/N<sub>2</sub>. Cu is in its metallic state after steam oxidation and CuFe<sub>2</sub>O<sub>4</sub> is formed after oxidation in O<sub>2</sub>/N<sub>2</sub> for 20 min.



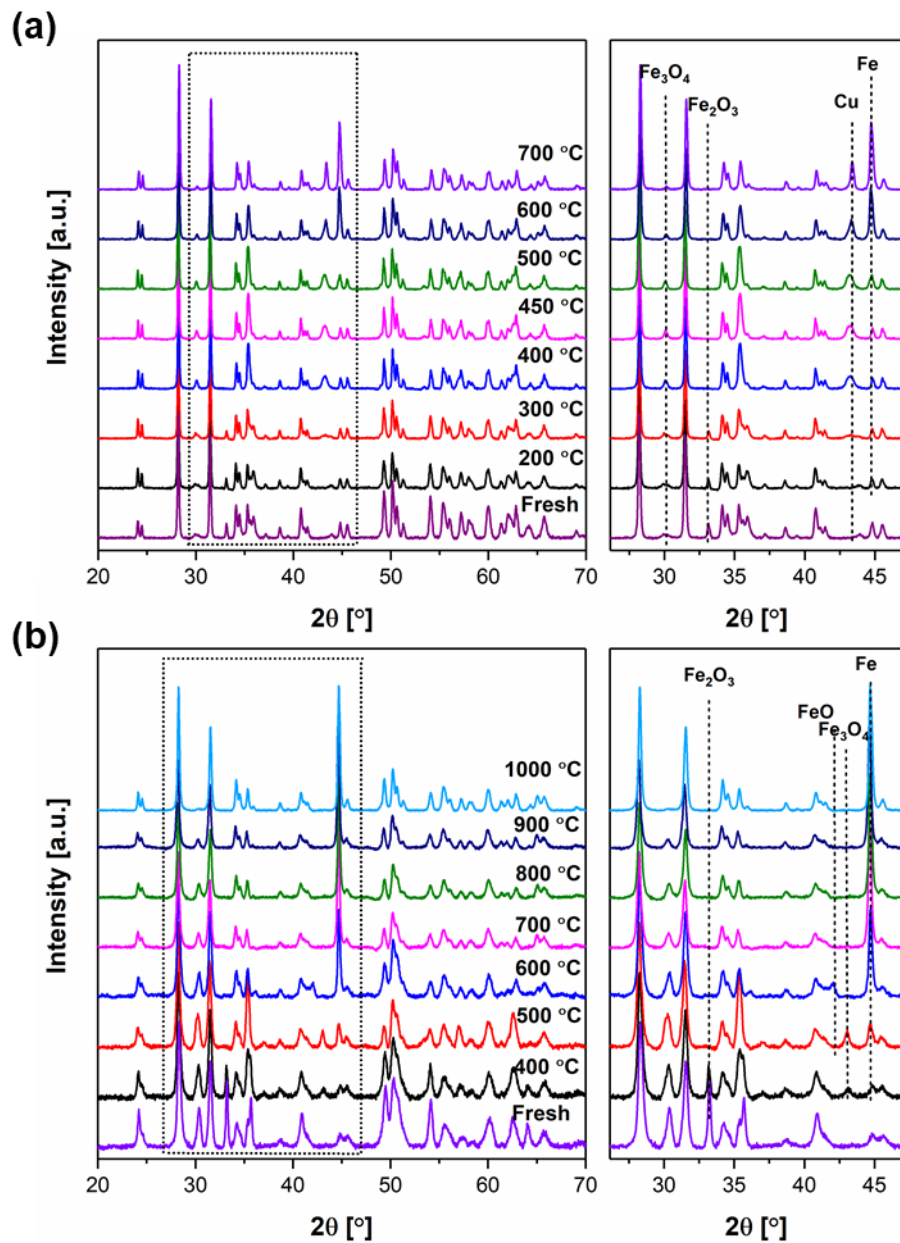


**Figure S3.5:** Overall XRD series (a) Fe<sub>30</sub>Zr<sub>70</sub> and (b) Fe<sub>30</sub>Cu<sub>10</sub>Zr<sub>60</sub> 30 at room temperature after H<sub>2</sub> reduction at various temperatures in the temperature range from 25 - 1050 °C.

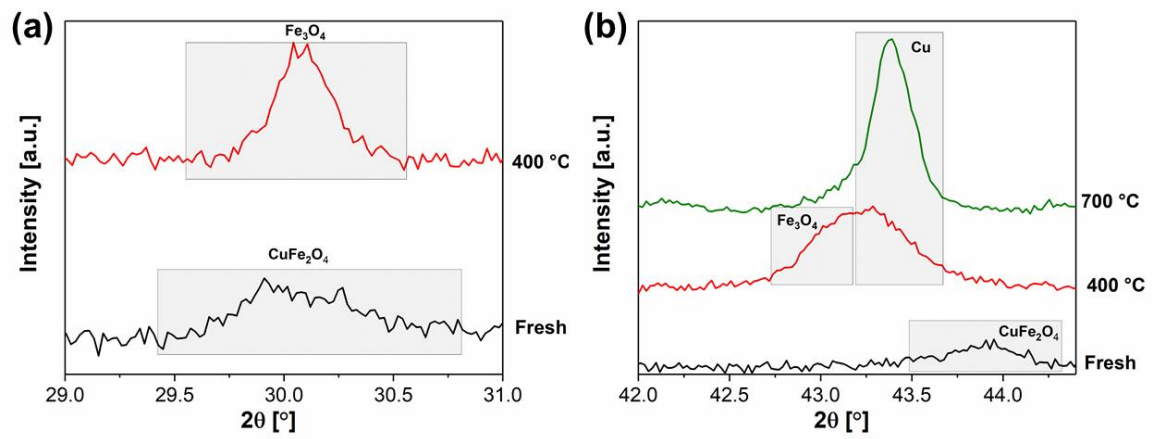


**Figure S3.6:** XRD series Fe<sub>30</sub>Cu<sub>10</sub>Zr<sub>60</sub> at room temperature after H<sub>2</sub> reduction 400 °C representing CuFe<sub>2</sub>O<sub>4</sub> to Fe<sub>3</sub>O<sub>4</sub> and Cu transition.

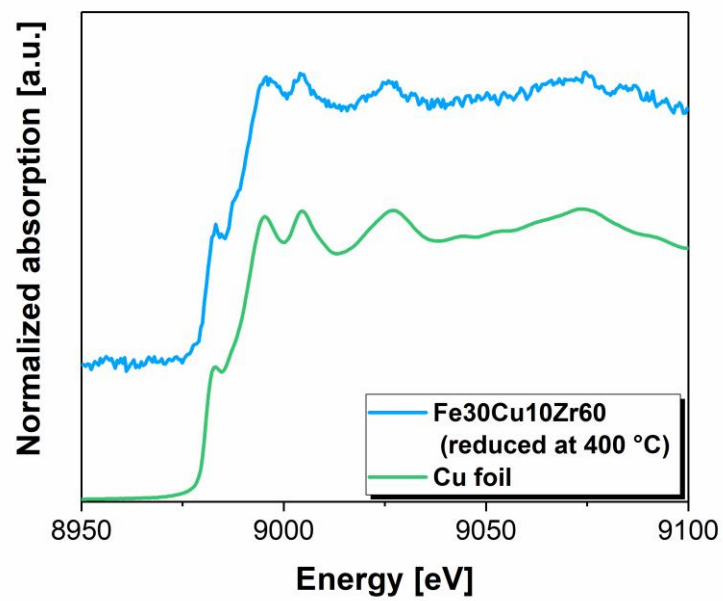


**Figure S3.7:** Cu-edge XANES spectra of Fe<sub>30</sub>Cu<sub>10</sub>Zr<sub>60</sub> together with Cu foil.



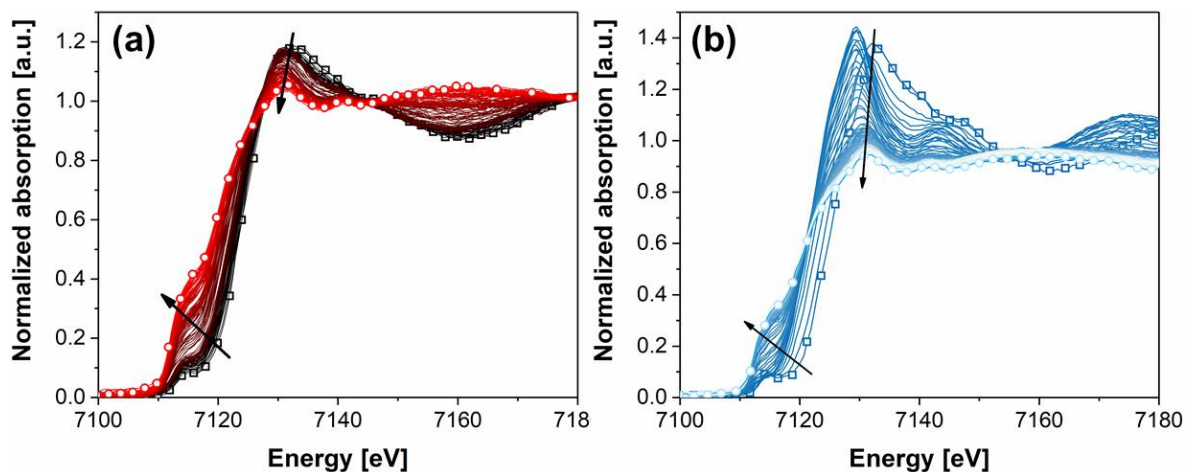


**Figure S3.8:** Time-resolved Fe K-edge XANES spectra during reduction of (a) Fe<sub>30</sub>Zr<sub>70</sub> and (b) Fe<sub>30</sub>Cu<sub>10</sub>Zr<sub>70</sub> at 750 °C using 5 vol. % H<sub>2</sub> in He. The square (□) and circle (○) symbols correspond to the initial and final states, respectively. The arrows indicate the direction of the changes with time.

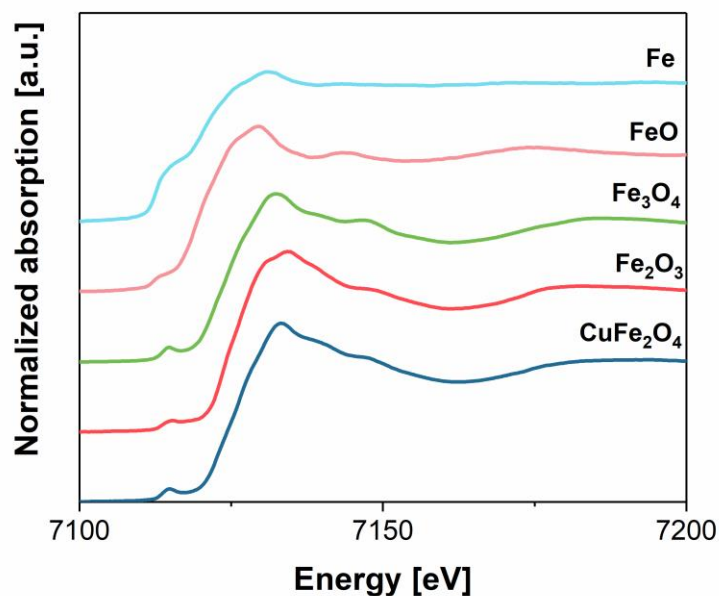


**Figure S3.9:** (a) Fe K-edge XANES spectra of (—) CuFe<sub>2</sub>O<sub>4</sub> reference, (—) α-Fe<sub>2</sub>O<sub>3</sub> reference, (—) Fe<sub>3</sub>O<sub>4</sub> reference, (—) FeO reference and (—) Fe reference.

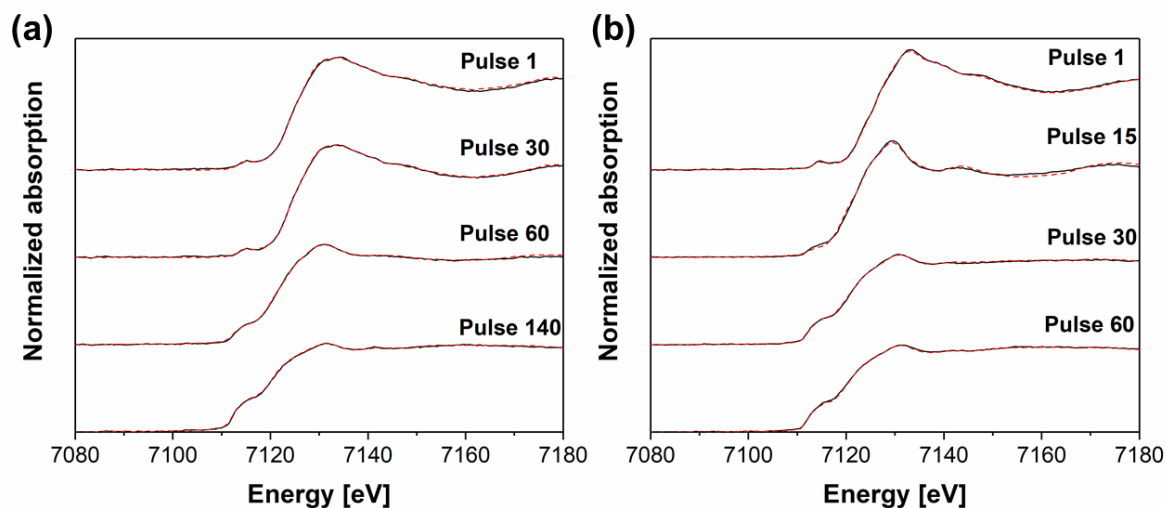


**Figure S3.10:** Fe K-edge XANES experimental data (solid black) and corresponding fitting using the least-squares linear combination of standard samples (red dash).

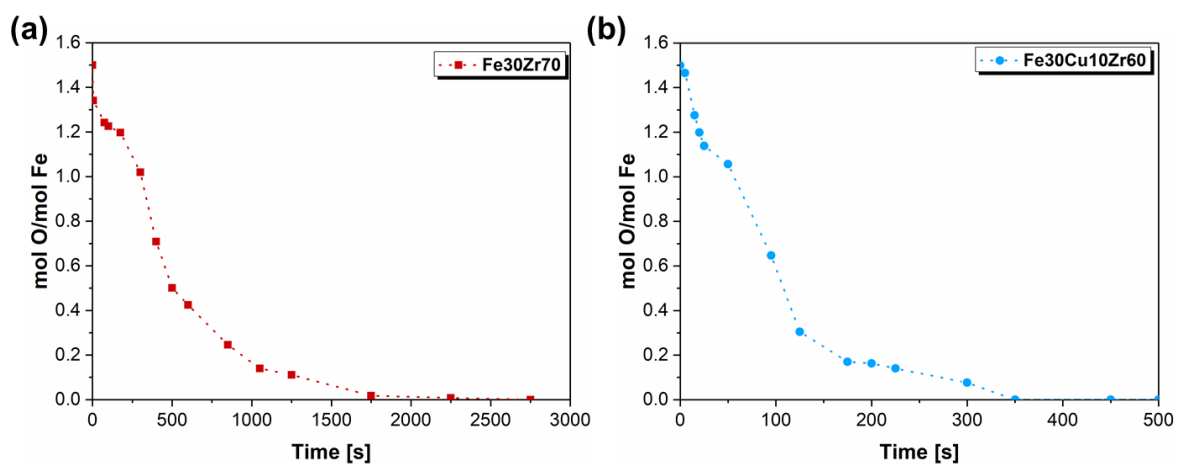


**Figure S3.11:** The loss of oxygen in (a) Fe<sub>30</sub>Zr<sub>70</sub> and (b) Fe<sub>30</sub>Cu<sub>10</sub>Zr<sub>60</sub> as a function of time.

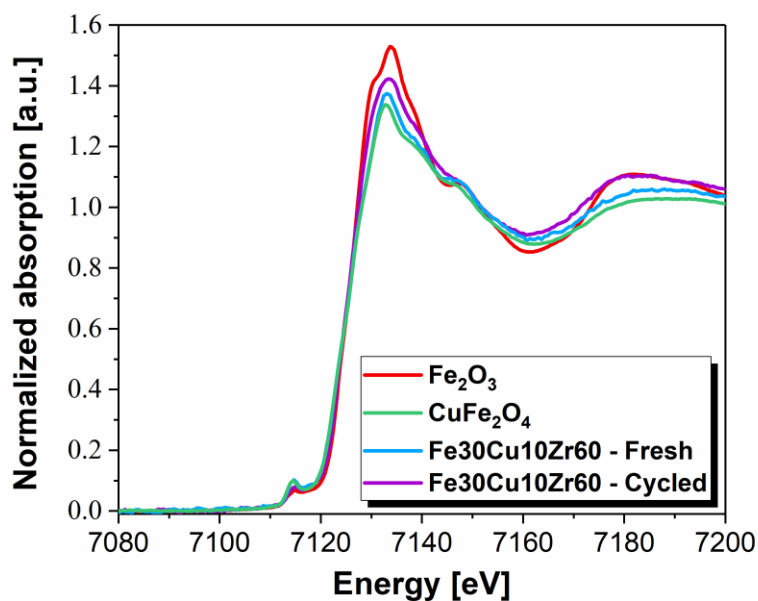


**Figure S3.12:** Fe-edge XANES spectra of fresh and cycled Fe30Cu10Zr60 together with  $\alpha\text{-Fe}_2\text{O}_3$  reference and  $\text{CuFe}_2\text{O}_4$  reference.

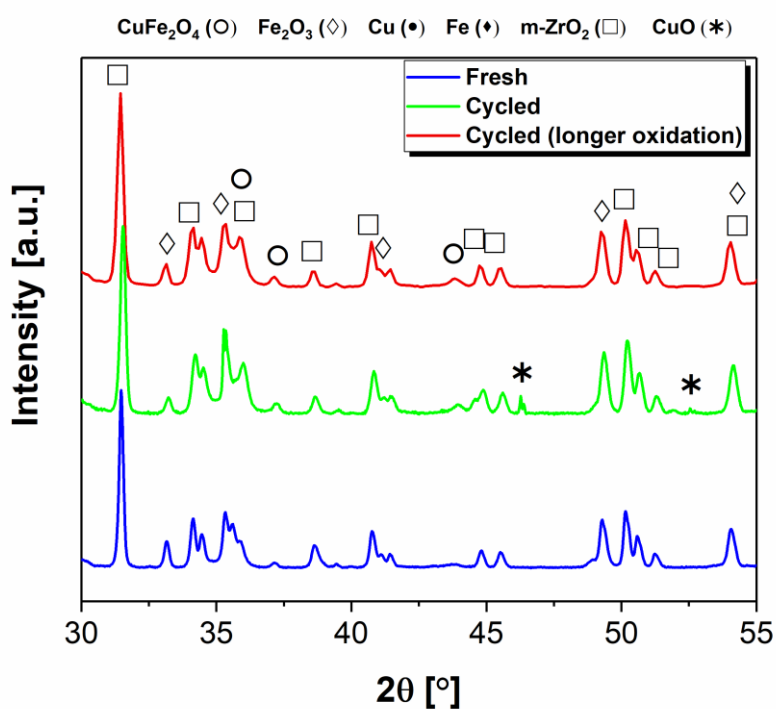


**Figure S3.13:** XRD of (—) fresh and cycled and oxidized Fe30Cu10Zr60. The oxygen carrier was oxidized for (—) 5 min. and (—) 20 min after being subjected to 15 redox cycles.

### 3.7 References

1. C. D. Bohn, C. R. Müller, J. P. Cleeton, A. N. Hayhurst, J. F. Davidson, S. A. Scott and J. S. Dennis, *Ind. Eng. Chem. Res.*, 2008, **47**, 7623-7630.
2. C. R. Müller, C. D. Bohn, Q. Song, S. A. Scott and J. S. Dennis, *Chem. Eng. J.*, 2011, **166**, 1052-1060.
3. A. Thursfield, A. Murugan, R. Franca and I. S. Metcalfe, *Energy Environ. Sci.*, 2012, **5**, 7421-7459.
4. A. M. Kierzkowska, C. D. Bohn, S. A. Scott, J. P. Cleeton, J. S. Dennis and C. R. Müller, *Ind. Eng. Chem. Res.*, 2010, **49**, 5383-5391.
5. N. S. Yüzbaşı, A. M. Kierzkowska, Q. Imtiaz, P. M. Abdala, A. Kurlov, J. L. M. Rupp and C. R. Müller, *J. Phys. Chem. C*, 2016, **120**, 18977-18985.
6. Q. Imtiaz, N. S. Yüzbaşı, P. M. Abdala, A. M. Kierzkowska, W. van Beek, M. Broda and C. R. Müller, *J. Mater. Chem. A*, 2016, **4**, 113-123.
7. P. R. Kidambi, J. P. E. Cleeton, S. A. Scott, J. S. Dennis and C. D. Bohn, *Energy Fuels*, 2012, **26**, 603-617.
8. W. Liu, J. S. Dennis and S. A. Scott, *Ind. Eng. Chem Res.*, 2012, **51**, 16597-16609.
9. C. Chung, L. Qin, V. Shah and L. S. Fan, *Energy. Environ. Sci.*, 2017, **10**, 2318-2323.
10. N. S. Yüzbaşı, A. Kierzkowska and C. Müller, *Energy Procedia*, 2017, **114**, 436-445.
11. F. He, N. Galinsky and F. Li, *Int. J. Hydrogen Energy*, 2013, **38**, 7839-7854.
12. J. A. Pena, E. Lorente, E. Romero and J. Herguido, *Catal. Today*, 2006, **116**, 439-444.
13. L. Qin, Z. Cheng, M. Guo, M. Xu, J. A. Fan and L. S. Fan, *ACS Energy Lett.*, 2017, **2**, 70-74.
14. K. S. Kang, C. H. Kim, W. C. Cho, K. K. Bae, S. W. Woo and C. S. Park, *Int. J. Hydrogen Energy*, 2008, **33**, 4560-4568.
15. R. Siriwardane, H. J. Tian, T. Simonyi and J. Poston, *Fuel*, 2013, **108**, 319-333.
16. B. W. Wang, R. Yan, H. B. Zhao, Y. Zheng, Z. H. Liu and C. G. Zheng, *Energy Fuels*, 2011, **25**, 3344-3354.
17. B. W. Wang, H. B. Zhao, Y. Zheng, Z. H. Liu, R. Yan and C. G. Zheng, *Fuel Process. Technol.*, 2012, **96**, 104-115.
18. S. Z. Wang, G. X. Wang, F. Jiang, M. Luo and H. Y. Li, *Energy Environ. Sci.*, 2010, **3**, 1353-1360.
19. L. M. Martínez T, C. Montes de Correa, J. A. Odriozola and M. A. Centeno, *Catal. Today*, 2005, **107-108**, 800-808.
20. S. Brunauer, P. H. Emmett and E. Teller, *J. Am. Chem. Soc.*, 1938, **60**, 309-319.
21. E. P. Barrett, L. G. Joyner and P. P. Halenda, *J. Am. Chem. Soc.*, 1951, **73**, 373-380.

22. Q. Imtiaz, P. M. Abdala, A. M. Kierzkowska, W. Van Beek, S. Schweiger, J. L. Rupp and C. R. Müller, *Phys. Chem. Chem. Phys.*, 2016, **18**, 12278-12288.
23. B. Ravel and M. Newville, *J. Synchrotron Radiat.*, 2005, **12**, 537-541.
24. A. L. Patterson, *Physical Review*, 1939, **56**, 978-982.
25. D. Hosseini, Q. Imtiaz, P. M. Abdala, S. Yoon, A. M. Kierzkowska, A. Weidenkaff and C. R. Müller, *J. Mater. Chem. A*, 2015, **3**, 10545-10550.
26. H. C. Shin, S.-C. Choi, K.-D. Jung and S.-H. Han, *Chem. Mater.*, 2001, **13**, 1238-1242.
27. W. Jozwiak, E. Kaczmarek, T. Maniecki, W. Ignaczak, W. Maniukiewicz, *Appl. Catal.*, **2007**, 326, 17-27.
28. S. Li, G. D. Meitzner and E. Iglesia, *J. Phys. Chem. B*, 2001, **105**, 5743-5750.
29. Y. Wang, X. Hua, C. Zhao, T. Fu, W. Li and W. Wang, *Int. J. Hydrogen Energy*, 2017, **42**, 5667-5675.
30. W. Liu, J. Y. Lim, M. A. Saucedo, A. N. Hayhurst, S. A. Scott and J. S. Dennis, *Chem. Eng. Sci.*, 2014, **120**, 149-166.
31. N. W. Hurst, S. J. Gentry, A. Jones and B. D. McNicol, *Catal. Rev.: Sci. Eng.*, 1982, **24**, 233-309.
32. S. Li, A. Li, S. Krishnamoorthy and E. Iglesia, *Catal. Lett.*, 2001, **77**, 197-205.
33. S. Li, S. Krishnamoorthy, A. Li, G. D. Meitzner and E. Iglesia, *J. Catal.*, 2002, **206**, 202-217.
34. E. de Smit, F. M. de Groot, R. Blume, M. Hävecker, A. Knop-Gericke and B. M. Weckhuysen, *Phys. Chem. Chem. Phys.*, 2010, **12**, 667-680.
35. G. P. Van Der Laan and A. A. C. M. Beenackers, *Catal. Rev.*, 1999, **41**, 255-318.
36. J. W. Geus, *Appl. Catal.*, 1986, **25**, 313-333.
37. E. de Smit, A. M. Beale, S. Nikitenko and B. M. Weckhuysen, *J. Catal.*, 2009, **262**, 244-256.

## Chapter 4: Sodium Promotion of Fe<sub>2</sub>O<sub>3</sub>-Al<sub>2</sub>O<sub>3</sub>: Effect on Phase and Redox Stability

---

This section contains a manuscript that is still in preparation: Yüzbaşı, N.S., Abdala, P.M., Hosseini D., Armutlulu, A., Huthwelker T., and Müller, C.R., 2018. Sodium promotion of Fe<sub>2</sub>O<sub>3</sub>-Al<sub>2</sub>O<sub>3</sub>: Effect on phase and redox stability, *In preparation*.

The author of this thesis carried out the synthesis of the oxygen carriers, XRD, BET and cyclic performance tests. Dr. A. Armutlulu performed SEM and SEM/EDX. Davood Hosseini carried out STEM/EDX. Dr. T. Huthwelker assisted in *ex situ* XAS measurements at the Swiss Light Source Synchrotron Facility in PSI. Dr. P. M. Abdala provided guidance in *ex situ* XRD and XAS analyses. Additionally, Dr. P. M. Abdala and Prof. C. R. Müller assisted with overall discussion and proof-reading of the paper.

## 4.1 Abstract

Chemical looping offers the possibility to produce high purity hydrogen ( $H_2$ ) from fossil fuels or biomass with the simultaneous capture of the  $CO_2$  produced at the distributed scale. Such a process relies on  $Fe_2O_3$ -based oxygen carriers that undergo repeated redox cycles. To prevent the sintering of  $Fe_2O_3$  it has to be stabilized by high Tammann temperature materials, e.g.  $Al_2O_3$ . However,  $Fe_2O_3-Al_2O_3$  possesses a poor cyclic redox performance exhibiting a decay in its  $H_2$  yield with cycle number due to the (gradual) formation of  $FeAl_2O_4$  that cannot be re-oxidized with steam. In this study, the addition of sodium was assessed as a means to prevent the formation of  $FeAl_2O_4$ . Detailed structural insight into the effect of sodium on the material's structure was gained by combined X-ray powder diffraction (XRD), X-ray absorption spectroscopy (XAS) at the Al, Na and Fe K-edges and scanning transmission electron microscopy/energy-dispersive X-ray spectroscopy (STEM/EDX) analyses. XRD and Fe K-edge XAS confirmed that the addition of sodium (with a molar ratio of  $Na:(Fe+Al) = 0.07$ ) prevented the formation of  $FeAl_2O_4$ . Na and Al K-edge XAS complemented by XRD revealed the formation of a sodium aluminate ( $Na-\beta-Al_2O_3$ ,  $NaAl_{11}O_{17}$  structure). It is hypothesized that the formation of sodium aluminate is the main reason for the suppression of the  $FeAl_2O_4$  formation. Na K-edge XAS showed that the local Na environment is preserved during redox cycling, explaining the excellent redox stability and high  $H_2$  yield of the sodium modified  $Fe_2O_3-Al_2O_3$  system.

## 4.2 Introduction

Hydrogen (H<sub>2</sub>) is an emerging energy carrier with potential applications in the transport, industry and power sectors <sup>1-3</sup>. H<sub>2</sub> is a clean-burning fuel yielding water vapour as the only combustion product. If produced sustainably, H<sub>2</sub> has the potential to become a near-zero emission energy carrier, hence reducing energy-related CO<sub>2</sub> emissions <sup>1-3</sup>. Currently, the majority of H<sub>2</sub> is produced from natural gas via steam methane reforming (SMR) without carbon capture, which is an energy intensive process and emits a significant amount of CO<sub>2</sub> <sup>3,4</sup>. Hence, for H<sub>2</sub> to become an energy carrier in a sustainable framework, it must be produced in an efficient and sustainable manner (*i.e.* from renewable sources or with CO<sub>2</sub> capture) and with high purity <sup>5,6</sup>.

Chemical looping offers the possibility to produce high purity H<sub>2</sub> with inherent CO<sub>2</sub> capture, utilizing *e.g.* the cyclic redox reactions of Fe<sub>2</sub>O<sub>3</sub> <sup>5-12</sup>. In this scheme, a carbonaceous fuel is gasified first yielding a synthesis gas which is mostly composed of CO and H<sub>2</sub>. The synthesis gas is used subsequently to reduce Fe<sub>2</sub>O<sub>3</sub> to lower oxidation states (ideally metallic Fe) following reactions 1-6 in Figure 4.1. During reduction, a pure stream of CO<sub>2</sub> is obtained readily by condensing H<sub>2</sub>O. The oxidation of metallic Fe with steam produces H<sub>2</sub> (reactions 7 and 8 in Figure 4.1). To fully re-oxidize Fe<sub>3</sub>O<sub>4</sub> back to Fe<sub>2</sub>O<sub>3</sub> to close the cycle, oxidation with O<sub>2</sub> is required (reaction 9).

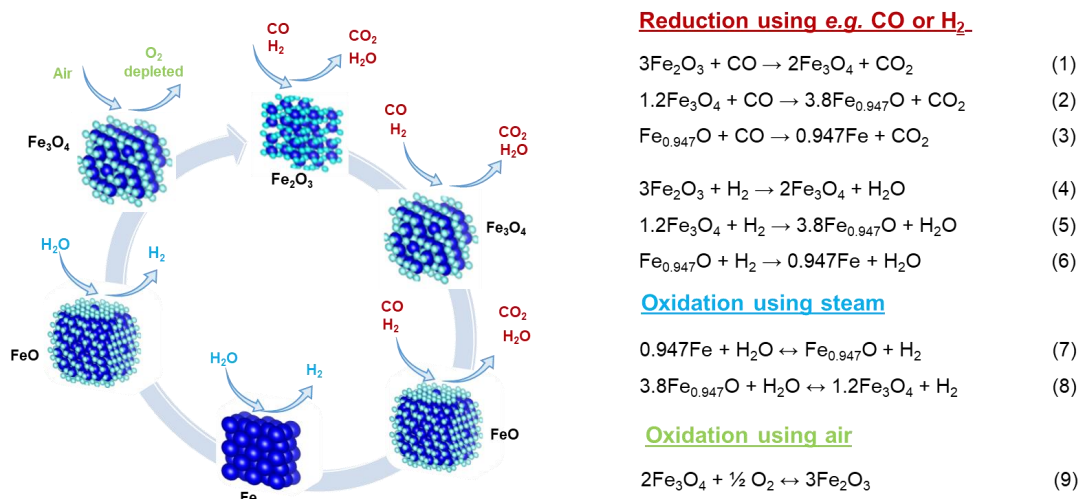


**Figure 4.1:** Schematic of the chemical looping-based process for the production of H<sub>2</sub> using synthesis gas (H<sub>2</sub> and CO) as the fuel.



Owing to its favourable thermodynamics iron oxide is one of the most attractive oxygen carriers for the chemical-looping based production of hydrogen<sup>5-9, 11, 13-23</sup>. However, pure (*i.e.* unsupported) Fe<sub>2</sub>O<sub>3</sub> shows a dramatic decay in its H<sub>2</sub> yield with number of redox cycles owing to sintering. To mitigate sintering Fe<sub>2</sub>O<sub>3</sub> is often stabilized by a second oxide, *e.g.* Al<sub>2</sub>O<sub>3</sub><sup>5, 8, 18, 22, 24</sup>, SiO<sub>2</sub><sup>5, 7</sup>, TiO<sub>2</sub><sup>25</sup>, CeO<sub>2</sub><sup>12</sup>, MgAl<sub>2</sub>O<sub>4</sub><sup>17, 26</sup> and ZrO<sub>2</sub><sup>11, 19, 23</sup>. A requirement for such stabilizer is chemical inertness *i.e.* to not react with iron (oxide) to form an inactive solid solution<sup>19</sup>.

Al<sub>2</sub>O<sub>3</sub> is one of the most studied stabilizers for Fe<sub>2</sub>O<sub>3</sub><sup>27-29</sup>. However, Al<sub>2</sub>O<sub>3</sub> is not chemically inert when mixed with Fe<sub>2</sub>O<sub>3</sub>, under CL-relevant conditions<sup>8, 18, 22</sup>. Ishida *et al.* reported the formation of a solid solution of hematite-(ss) and corundum-(ss), in Fe<sub>2</sub>O<sub>3</sub>-Al<sub>2</sub>O<sub>3</sub> composite particles (75-25 wt. %) when calcined at temperatures exceeding 1000 °C<sup>24</sup>. The formation of a spinel mixed oxide phase (hercynite, FeAl<sub>2</sub>O<sub>4</sub>) leads to a decay in the H<sub>2</sub> yield of the material as it cannot be re-oxidized with steam. Similar observations were made by Kierzkowska *et al.*<sup>18</sup> who developed a cyclically stable, Al<sub>2</sub>O<sub>3</sub>-supported Fe<sub>2</sub>O<sub>3</sub> (containing 40 wt. % Al<sub>2</sub>O<sub>3</sub>) that, however, exhibited a H<sub>2</sub> yield that was 25 % less than the theoretically expected value due to the formation of hercynite.

Recently, it has been reported that the formation of a spinel *e.g.* CuAl<sub>2</sub>O<sub>4</sub> or FeAl<sub>2</sub>O<sub>4</sub> can be inhibited by the addition of an alkali metal<sup>19, 29, 30</sup>. For example, the addition of Na<sup>+</sup> (with a molar ratio of Na:(Fe+Al) = 0.33 or Na:Fe:Al = 0.4:0.8:0) yielded a Fe<sub>2</sub>O<sub>3</sub>-Al<sub>2</sub>O<sub>3</sub> material (65 wt. % Fe<sub>2</sub>O<sub>3</sub>) that exhibited a high hydrogen yield<sup>26</sup>. It was reported that the addition of Na inhibited the formation of FeAl<sub>2</sub>O<sub>4</sub> through the formation of NaAlO<sub>2</sub>. However, oxygen carriers that were not exposed to a second oxidation step in air showed a gradual replacement of Al<sup>3+</sup> by Fe<sup>3+</sup> in NaAlO<sub>2</sub> with number of redox cycles leading to the formation of Al<sub>2</sub>O<sub>3</sub>. Subsequently, Al<sub>2</sub>O<sub>3</sub> reacted with FeO to form again unreactive FeAl<sub>2</sub>O<sub>4</sub>. On the other hand Huang *et al.*<sup>16</sup> (with a molar ratio of Na:(Fe+Al) = 0.11 or Na:Fe:Al = 0.16:0.75:0.78) identified the formation of Na<sub>2</sub>(Al,Fe)<sub>12</sub>O<sub>19</sub> and Na(Al,Fe)O<sub>2</sub> and linked their presence to poor kinetics and attrition resistance. However, reducing the sodium loading (molar ratio of Na:(Fe+Al) = 0.02 or Na:Fe:Al = 0.03:0.75:0.78) increased the reduction kinetics and the sintering resistance of the material. In a recent work Liu *et al.*<sup>31</sup> attributed the improved redox stability of a Na promoted Fe<sub>2</sub>O<sub>3</sub>-Al<sub>2</sub>O<sub>3</sub> system (with a molar ratio of Na:(Fe+Al) = 0.01

or Na:Fe:Al = 0.03:0.98:0.98) due to the improved oxygen transport characteristics in the material.

Although several studies agree that the addition of Na can prevent the solid-solid interaction between Fe<sub>2</sub>O<sub>3</sub> and Al<sub>2</sub>O<sub>3</sub> during reduction, the underlying mechanism (*i.e.* at the atomic scale) is currently under debate. Hence, this work aims at shedding some light on the interaction of Na-Fe-Al oxides under redox conditions by applying simultaneously X-ray diffraction (XRD) and X-ray absorption spectroscopy (XAS) at the Fe, Al and Na K-edges to probe the structural properties of sodium modified Fe<sub>2</sub>O<sub>3</sub>-Al<sub>2</sub>O<sub>3</sub> and to address the following questions: (i) how does the addition of a small quantity of sodium hinder FeAl<sub>2</sub>O<sub>4</sub> formation? (ii) does sodium interact with Al<sub>2</sub>O<sub>3</sub>, Fe<sub>2</sub>O<sub>3</sub>, or both? and in connection with this, does the addition of sodium modify the local structures of Fe and Al and (iii) are sodium containing phases stable under cyclic redox conditions?

## 4.3 Experimental

### 4.3.1 Synthesis of the oxygen carriers

Fe<sub>2</sub>O<sub>3</sub>-based oxygen carriers, supported on aluminium oxide, with and without sodium promotion, were synthesized using a sol-gel method<sup>18</sup>. In a typical synthesis, aluminum isopropoxide was mixed with water and the mixture was hydrolysed for two hours at 75 °C under constant stirring. Nitric acid was used to peptize the slurry. The required amount of the iron (and sodium) precursor was mixed with water to obtain a 1 M solution that was added subsequently to the slurry and refluxed for 12 h at 90 °C. Iron nitrate (Fe(NO<sub>3</sub>)<sub>3</sub>·9H<sub>2</sub>O) and sodium nitrate (NaNO<sub>3</sub>) was used as the iron and sodium precursor, respectively. The molar ratio of Al<sup>3+</sup>:H<sub>2</sub>O:H<sup>+</sup> was fixed to 0.5:50:0.07. The resulting gel was dried at 100 °C overnight to remove the encapsulated solvents. A xerogel was obtained after calcination at 900 °C for 2 hours. The molar Fe:Al ratio is 0.95:0.42 (the weight ratio of Fe<sub>2</sub>O<sub>3</sub> to Al<sub>2</sub>O<sub>3</sub> 75:25) in the reference material (referred to as FeAl in the following). Two additional samples were made by promoting FeAl with sodium with a molar ratio of Na:Fe:Al of 0.03:0.95:0.45 (Na:(Fe+Al) = 0.02) and 0.10:0.92:0.47 (Na:(Fe+Al) = 0.07) (referred to as FeAlNa1 and FeAlNa5, respectively). The nominal molar compositions of the materials synthesized are listed in Table 1:

**Table 4.1:** Molar composition (on metal basis), surface area, pore volume, average grain size and average crystallite size of Fe<sub>2</sub>O<sub>3</sub> (calculated using Scherrer equation) of the materials calcined at 900 °C for 2h.

		FeAl	FeAlNa1	FeAlNa5
<b>Nominal molar ratio</b>	<b>Fe</b>	0.94	0.95	0.92
	<b>Al</b>	0.49	0.45	0.47
	<b>Na</b>	-	0.03	0.10
	<b>Al:Fe ratio</b>	0.52	0.47	0.51
	<b>Na:(Fe+Al)</b>	-	0.02	0.07
<b>Molar ratio calculated from EDX</b>	<b>Fe</b>	0.96	0.95	0.94
	<b>Al</b>	0.44	0.42	0.42
	<b>Na</b>	-	0.03	0.14
	<b>Al:Fe ratio</b>	0.46	0.44	0.45
	<b>Na:(Fe+Al)</b>	-	0.02	0.10
<b>Surface Area [m<sup>2</sup>/g]</b>		9	17	11
<b>Pore Volume [cm<sup>3</sup>/g]</b>		0.1	0.19	0.13
<b>Average grain size [nm]</b>		110 ± 20	90 ± 20	110 ± 30
<b>Average crystallite size of Fe<sub>2</sub>O<sub>3</sub> [nm]</b>		90	58	90

An additional reference material, viz. Al<sub>2</sub>O<sub>3</sub> modified with sodium (molar Na:Al ratio=1:12) was synthesized using sol-gel, using the synthesis protocol described above. This material is referred to as AlNa5. The calcined materials were crushed and sieved to a particle size range 300 – 425 µm for further characterization.

### 4.3.2 Characterization of the oxygen carriers

The crystalline phases of the calcined and cycled oxygen carriers were probed by X-ray diffraction (XRD), using a PANalytical Empyrean X-ray Powder Diffractometer, equipped with a X'Celerator Scientific ultra-fast line detector and Bragg–Brentano HD incident beam optics using Cu K<sub>α</sub> radiation (45 kV and 40 mA). A monochromator was employed to suppress unwanted fluorescence originating from iron. Patterns were collected in the range of 2θ = 5-90 °, with a step size of 0.016 °/s and a scanning speed of 0.0056 s<sup>-1</sup>. On selected samples synchrotron (wavelength, λ=0.258 Å) XRD data were collected at the Swiss-Norwegian beamline (BM01B) at the European Synchrotron Radiation Facility (ESRF), Grenoble, France. Rietveld refinements were performed using FullProf <sup>32</sup>.

The local structure of the materials was characterized by X-ray absorption spectroscopy (XAS) at the Fe, Na and Al K-edges. The Na K-edge and Al K-edge XAS measurements were carried out at the Phoenix II, elliptical undulator beamline at the Swiss Light Source (SLS) at the Paul Scherrer Institute (PSI), Switzerland. In a typical experiment a small quantity of material was pressed on an indium foil and fixed to a copper plate<sup>33</sup>. XAS measurements were performed in fluorescence mode. The X-ray fluorescence signal was detected using a 4-element Si-drift diode detector (Vortex). The current of the incoming beam ( $I_0$ ) was measured using the total electron yield signal from a 0.5  $\mu\text{s}$  thin polyester foil that was coated with a 50 nm thick layer of nickel. The beam passed through this foil approximately 1 m upstream of the sample in a vacuum chamber held at  $\sim 10^{-6}$  mbar. The Fe K-edge XAS spectra were collected at the BM01B beamline at the ESRF, Grenoble, France. The samples were ground, mixed with cellulose to optimize the X-ray absorption in the samples and pelletized. The data were collected in transmission mode using a Si (111) double crystal monochromator. Post-processing and analysis of the XAS data were performed using the Athena and Artemis software package (Demeter 0.9.20)<sup>34</sup>.

High-resolution field emission scanning electron microscopy (Zeiss ULTRA 55 plus) was employed to visualize the surface morphology of the oxygen carriers before and after cyclic redox tests. Furthermore, elemental mapping of the synthesized materials was achieved via a Leo Gemini 1530 SEM equipped with an energy dispersive X-ray spectrometer (EDX). A FEI Talos F200X operated at 200 kV was used in both transmission electron microscopy (TEM) and scanning TEM (STEM) modes, with a probe size of approximately 0.8 nm. The instrument is equipped with SuperX EDX comprising four SDD detectors. The STEM/EDX analyses were complemented with atomic number sensitive, high angle annular dark field (HAADF) STEM.

The surface area as well as the pore size distribution of the calcined oxygen carriers were determined using a Quantochrome NOVA 4000e  $\text{N}_2$  adsorption analyzer. The samples were degassed at 300 °C for two hours prior to the acquisition of the  $\text{N}_2$  isotherms. The BET<sup>35</sup> and BJH<sup>36</sup> models were used to calculate, respectively, the surface area and the pore size distribution of the materials.

### 4.3.3 Cycling redox tests

Cyclic redox experiments were performed in a packed bed reactor made of recrystallized  $\text{Al}_2\text{O}_3$ , with an internal diameter of 20 mm (length 590 mm). A frit (5 holes with diameter 1.5 mm) was located 200 mm above the bottom of the reactor. The bed was initially loaded with 3.5 g of coarse  $\text{Al}_2\text{O}_3$  (1400-1700  $\mu\text{m}$ ), followed by an approximately 10 mm long plug of quartz wool. This was followed by 0.5 g of the oxygen carrier mixed with 5 g of  $\text{Al}_2\text{O}_3$  (300-425  $\mu\text{m}$ ). Finally, 10 g of coarse alumina (1400-1700  $\mu\text{m}$ ) were added. The coarse alumina layer and the quartz wool plug at the bottom section of the bed prevented oxygen carriers from falling through the holes of the frit, whereas the top layer of coarse alumina effectively preheated the gas entering the bed. The reactor was placed in a tubular furnace and the temperature of the bed was controlled *via* an N-type thermocouple placed inside the layer of the oxygen carrier. The flow rate of CO was recorded with a calibrated rotameter, while the flowrates of  $\text{CO}_2$ ,  $\text{N}_2$  and air were recorded via calibrated mass flow meters (AWM5101VN, Honeywell). A computer-controlled setup comprising six solenoid valves were utilized for switching between different gas atmospheres. Water was fed by a syringe pump (0.3 ml/min) to an electrically heated vaporizer maintained at 210 °C. A typical redox cycle consists of the following steps: (i) reduction in CO (10 vol. % CO in  $\text{N}_2$ ) for 15 minutes (1.5 L/min), (ii) purging with  $\text{N}_2$  (1.5 L/min) for 1 minute, (iii) oxidation of the reduced oxygen carrier with steam (23 vol. %  $\text{H}_2\text{O}$  in  $\text{N}_2$ ) for 7 minutes (1.94 L/min), (iv) purging with  $\text{N}_2$  (1.5 L/min) for 1 minute, and (v) oxidation with 5 vol. %  $\text{O}_2$  in  $\text{N}_2$  (2 L/min) for 5 minutes. The gas stream leaving the packed bed reactor was first passed through three impinger tubes, immersed in an ice bath, followed by a  $\text{CaCl}_2$  drying tube, to remove unreacted steam. The gas stream composition was determined using the following analyzers: (i) non-dispersive infrared analyzer for CO,  $\text{CH}_4$  and  $\text{CO}_2$  (ABB, Uras 26), (ii) non-dispersive infrared analyzer for CO in the range 0 – 5000 ppmv (ABB, Uras 26), (iii) paramagnetic analyzer for  $\text{O}_2$  (ABB, Magnos 206) and (iv) thermal conductivity analyzer for  $\text{H}_2$  (ABB, Caldos 27). Gas analysers are calibrated after each experiment using appropriate calibration gas cylinders.

## 4.4 Results and Discussion

### 4.4.1 Structure and microstructure of the calcined materials

#### *Texture*

The BET surface area and BJH pore volume of the calcined oxygen carriers are summarized in Table 4.1. The BET surface areas of the calcined materials were determined as 9, 17 and 11 m<sup>2</sup>/g for FeAl, FeAlNa1 and FeAlNa5. The addition of sodium did not affect significantly the surface area and pore volume of the calcined oxygen carriers.

The surface morphology of freshly calcined Al<sub>2</sub>O<sub>3</sub>-stabilized Fe<sub>2</sub>O<sub>3</sub>, as probed by electron microscopy, is affected only marginally by the addition of sodium. The calcined oxygen carriers were composed of nano-sized particles (Figure S4.1) with an average size of ~ 100 ± 20 nm (calculated based on the analysis of 20 particles; 110 ± 20 nm, 90 ± 20 nm and 110 ± 30 nm for FeAl, FeAlNa1 and FeAlNa5, respectively). SEM/EDX mapping of the oxygen carriers revealed that the sol-gel synthesis led to a homogenous distribution of the different atoms in the materials (Figure S4.2). The compositions of the materials calculated from elemental mapping are in good agreement with the nominal compositions of the oxygen carriers and are reported in Table 4.1.

#### *Crystalline and local atomic structure*

The main crystalline component in the calcined materials is hematite ( $\alpha$ -Fe<sub>2</sub>O<sub>3</sub>, ICSD: 88418), as determined by XRD analysis (Figure 4.2). Corundum ( $\alpha$ -Al<sub>2</sub>O<sub>3</sub>, ICSD: 160606) was also identified in all of the materials. However, with the addition of sodium, the relative intensity of the  $\alpha$ -Al<sub>2</sub>O<sub>3</sub> peaks decreases (data normalized by the Fe<sub>2</sub>O<sub>3</sub> (104) peak). In the case of FeAlNa5, sodium aluminate Na- $\beta$ -alumina (NaAl<sub>11</sub>O<sub>17</sub>, ICSD: 067545) was detected (main peak at 2 $\theta$  = 7.7°). It is important to note that we did not detect the iron aluminate phase FeAl<sub>2</sub>O<sub>4</sub> in any of the calcined oxygen carriers. On the other hand, we did not observe the presence of Na- $\beta$ -alumina in FeAlNa1.

Rietveld, whole-pattern refinement of the XRD data (Figure 4.2, Figure S4.3 and Table S4.1) revealed that the unit cell parameters of  $\alpha$ -Fe<sub>2</sub>O<sub>3</sub> and  $\alpha$ -Al<sub>2</sub>O<sub>3</sub> did not

change (within the experimental error) by the addition of sodium. This implies that sodium is not incorporated into the crystal structures of  $\alpha$ -Fe<sub>2</sub>O<sub>3</sub> or  $\alpha$ -Al<sub>2</sub>O<sub>3</sub>. In the case of FeAlNa5, the cell parameters,  $a = b$  and  $c$ , of Na- $\beta$ -alumina, are 5.64(1) Å and 22.778(6) Å, respectively, using a P63/mmc space group. These values are in a good agreement with previous studies<sup>37-39</sup>.

The weight percentages of  $\alpha$ -Fe<sub>2</sub>O<sub>3</sub> and  $\alpha$ -Al<sub>2</sub>O<sub>3</sub> in the calcined materials, as determined by Rietveld refinement are 75 and 25 wt. % for FeAl, and 84 and 16 wt. % for FeAlNa1, respectively, *i.e.* the content of  $\alpha$ -Al<sub>2</sub>O<sub>3</sub> is reduced in FeAlNa1 compared to FeAl. Comparing Rietveld results with the chemical composition obtained by EDX (assuming all of Fe, Al and Na are in the form of Fe<sub>2</sub>O<sub>3</sub>, Al<sub>2</sub>O<sub>3</sub> and Na<sub>2</sub>O, respectively, Table S2), a good agreement can be observed for FeAl (from Rietveld analysis the calculated molar ratio of Al: Fe=0.52, EDX analysis gives Al:Fe=0.46). On the other hand, for FeAlNa1 the molar ratio of Al:Fe as determined by Rietveld is 0.31, which is considerably lower than the ratio of Al:Fe=0.44 as determined by EDX analysis. Rietveld refinement takes into account only crystalline phases, therefore, this difference may indicate that in FeAlNa1 aluminium is not only present as  $\alpha$ -Al<sub>2</sub>O<sub>3</sub> but also in an amorphous phase. In the case of FeAlNa5, the phase composition estimated by Rietveld analysis is 80 wt. %  $\alpha$ -Fe<sub>2</sub>O<sub>3</sub>, 5 wt. % Al<sub>2</sub>O<sub>3</sub> and 15 wt. % Na- $\beta$ -alumina.

A disadvantage of XRD analysis is that it is sensitive to crystalline phases only and does not provide information on phases with a short coherence length, in particular when these phases are present in relatively small quantities. Therefore, to obtain further insight into the effect of sodium on phase formation and stability, X-ray absorption spectroscopy (XAS) at the Fe, Na and Al K-edges was performed.

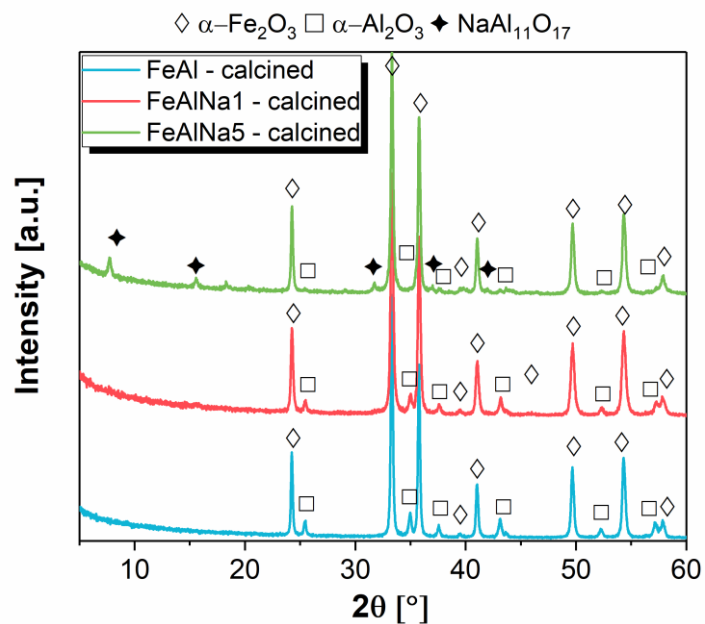


**Figure 4.2:** XRD patterns of the materials calcined at 900 °C for 2 hours (normalized by the intensity of the  $\text{Fe}_2\text{O}_3$  (104) peak).

Fe K-edge XANES (X-ray absorption near edge structure) spectra of the calcined oxygen carriers are provided in Figure 4.3a. The spectra of all of the oxygen carriers contain essentially the same features as the  $\alpha\text{-Fe}_2\text{O}_3$  reference. The EXAFS (extended X-ray absorption fine structure) functions and the corresponding Fourier transform (FT) are given in Figure S4.4. The peaks located in the range 1–2 Å correspond to Fe–O bonds, and those in the range 2–4 Å are dominated by Fe–Fe distances, in agreement with the local environmental of Fe in  $\alpha\text{-Fe}_2\text{O}_3$ . Hence, XAS confirms our previous XRD observation that the local environment of Fe is not affected by the addition of sodium. Hence, there is no formation of a solid solution or mixed oxide (such as  $\text{FeAl}_2\text{O}_4$ ) between  $\text{Fe}_2\text{O}_3$  and  $\text{Al}_2\text{O}_3$  upon calcination at 900 °C.



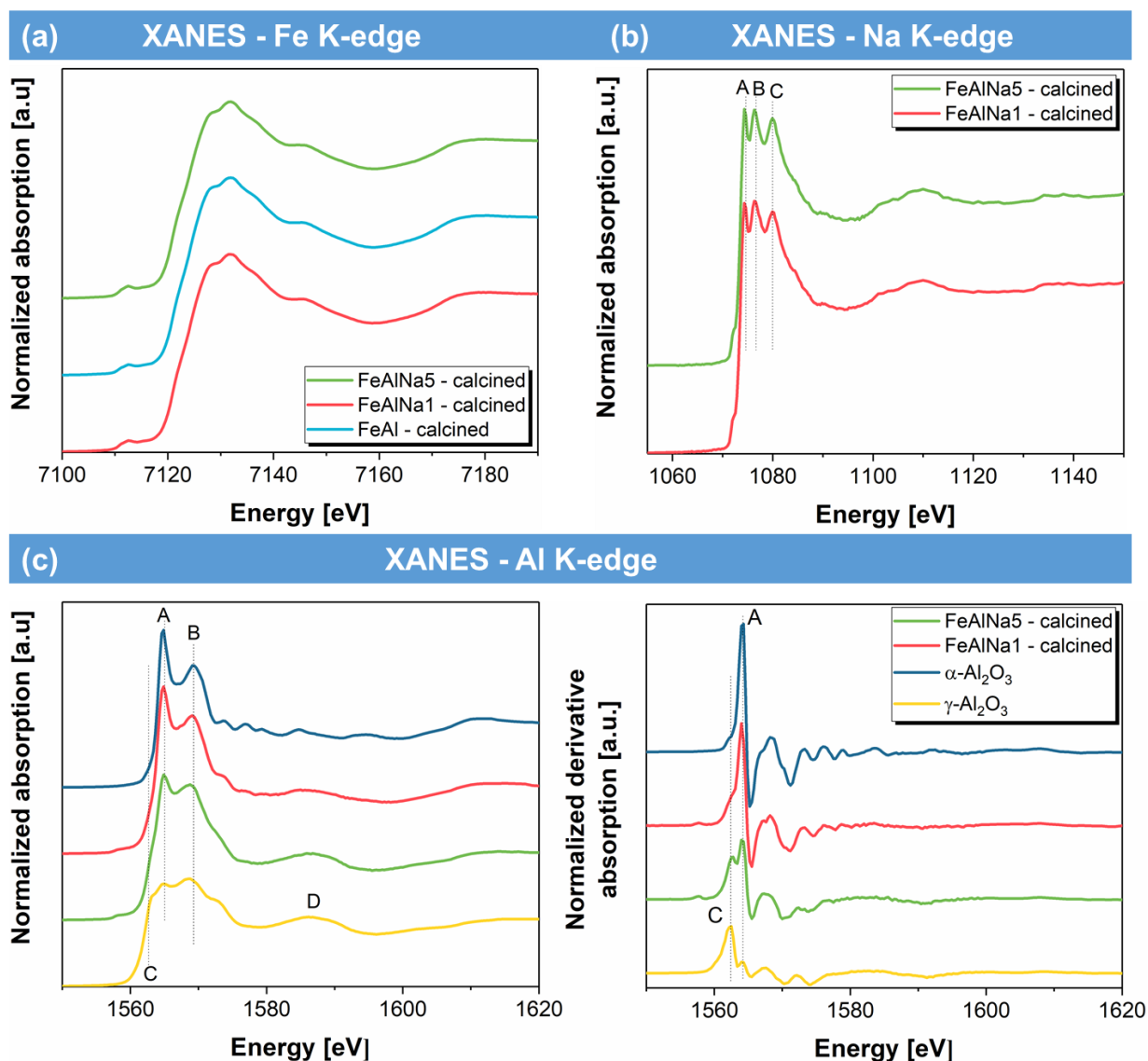


**Figure 4.3:** XANES spectra at (a) Fe K-edge, (b) Na K-edge and (c) Al K-edge of the materials calcined at 900 °C for 2 hours.

Figure 4.3c and Figure S4.5 display the Al K-edge XANES spectra of the calcined materials and the reference materials  $\alpha$ - $\text{Al}_2\text{O}_3$  and  $\gamma$ - $\text{Al}_2\text{O}_3$ . The reference  $\alpha$ - $\text{Al}_2\text{O}_3$  can be described as a hexagonal cell containing 12 Al and 18 O. Al is in an octahedral coordination, with three short Al–O bonds (1.86 Å) and three longer Al–O bonds (1.97 Å). The XANES spectrum obtained for the  $\alpha$ - $\text{Al}_2\text{O}_3$  reference (Figure 4.3c) exhibits a doublet peak in the white-line region, with an intense peak at 1565 eV (labelled as A), and a less intense one at 1568 eV (labelled as B), typical for an octahedral coordination and is agreement with previously published data<sup>40, 41</sup>. The second reference,  $\gamma$ - $\text{Al}_2\text{O}_3$  is of a cubic defect spinel type structure, in which the O atoms are arranged in a cubic close packing and the Al atoms occupy the octahedral and

tetrahedral sites. In the XANES spectrum of  $\gamma$ - $\text{Al}_2\text{O}_3$  two features (labelled as A and B) are observed (at 1565 and 1568 eV, respectively). Feature A is considerably less intense than in the case of  $\alpha$ - $\text{Al}_2\text{O}_3$ . Additionally, the spectrum of  $\gamma$ - $\text{Al}_2\text{O}_3$  exhibits a lower energy feature (C) at 1562 eV and a broad peak at 1586 eV (D) which are attributed to tetrahedrally coordinated Al, in agreement with previous studies<sup>42, 43</sup>. We did not have the reference Na- $\beta$ -alumina, but as it is composed of a layered structure containing layers of  $\gamma$ - $\text{Al}_2\text{O}_3$  that are linked together by sodium and oxygen (Figure 4.4)<sup>44, 45</sup>, it is expected that the Al K-edge XANES spectrum of Na- $\beta$ -alumina would exhibit similar features as  $\gamma$ - $\text{Al}_2\text{O}_3$ .

Turning now to the XANES spectra of FeAlNa1 and FeAlNa5, we observe in both materials feature (A) that is attributed to  $\alpha$ - $\text{Al}_2\text{O}_3$ . However, the relative intensity of feature A with respect to feature B is lower than for the reference  $\alpha$ - $\text{Al}_2\text{O}_3$  and the intensity decreases with increasing sodium content. This implies that the fraction of  $\alpha$ - $\text{Al}_2\text{O}_3$  in the material decreases with increasing sodium content. The fact that we also observe features C and D indicates the presence of an additional spinel-type  $\gamma$ - $\text{Al}_2\text{O}_3$  environment in both FeAlNa1 and FeAlNa5. Hence, our XANES results confirm that FeAlNa1 and FeAlNa5 contain a mixture of  $\alpha$ - $\text{Al}_2\text{O}_3$  and a spinel-type  $\gamma$ - $\text{Al}_2\text{O}_3$  phase, with a decreasing quantity of  $\alpha$ - $\text{Al}_2\text{O}_3$  with increasing sodium content. In line with our XRD findings, the XAS results suggest that the addition of sodium stabilizes the spinel-type  $\gamma$ - $\text{Al}_2\text{O}_3$  environment (as found in Na- $\beta$ -alumina).

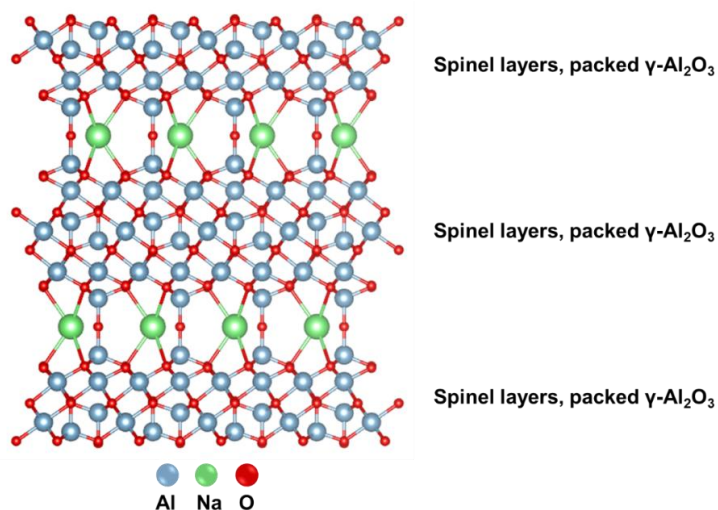


**Figure 4.4:** Representation of the layered structure of Na- $\beta$ - $\text{Al}_2\text{O}_3$  containing layers of  $\gamma$ -alumina (defect spinel structure) that are connected by a layer of bridging oxygen and sodium ions<sup>45-49</sup>.

Additional information on the phases formed in the presence of sodium was provided by Na K-edge XANES (Figure 4.3). The Na K-edge XANES spectra of FeAlNa1 and FeAlNa5 exhibit three main features at 1074.4 eV (A), 1076.4 eV (B) and 1080.2 eV (C), suggesting a similar Na local environment in both calcined, sodium-containing samples, independent of the sodium content. Since XRD and Al K-edge XAS analysis indicated the presence of Na- $\beta$ -alumina in FeAlNa5, this may suggest that Na is also in a Na- $\beta$ -alumina environment in FeAlNa1. The absence of diffraction peaks corresponding to Na- $\beta$ -alumina in FeAlNa1, may suggest that this phase lacks long-range coherence in FeAlNa1. Further insight into the Na local environment of FeAlNa1 and FeAlNa5 was obtained from EXAFS analysis. Figure 4.5 plots the Fourier transformed (FT) EXAFS functions and the fitting results are presented in Table S4.3. Two main peaks can be observed in the FT-EXAFS functions of FeAlNa1 and FeAlNa5. The first peak is attributed to a Na-O coordination whereas the second peak is attributed to a Na-cation (*i.e.* Na-Al, Na-Na) sphere. The fitting of the first shell in FeAlNa5 shows two Na-O distances at 2.2 Å and 2.8 Å; and a Na-Al (or Na-Na) distance of 3.6 Å. A similar observation can be extracted from the fitting of the EXAFS function of FeAlNa1 (Table S4.3). The expected crystallographic Na-O distance in Na- $\beta$ -Al<sub>2</sub>O<sub>3</sub> (with Na<sup>+</sup> in 2d site) is 2.8 Å (and 3.6 Å for Na-Al), in line with the longest Na-O and the Na-Al distances<sup>39</sup>. The existence of a shorter Na-O distance at 2.2 Å suggests that Na<sup>+</sup> is not only in a Na- $\beta$ -Al<sub>2</sub>O<sub>3</sub> environment. One possible explanation is the dispersion of some Na on the surface of the spinel-type  $\gamma$ -Al<sub>2</sub>O<sub>3</sub>, as hypothesized by others previously<sup>50</sup>.

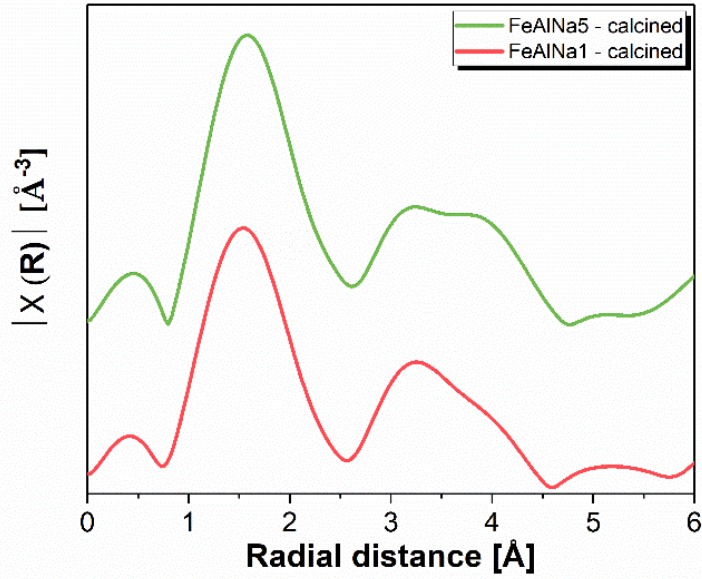


**Figure 4.5:** FT-EXAFS functions ( $k^3$ -weighted) of the calcined oxygen carriers measured at the Na K-edge.

#### 4.4.2 Cyclic redox performance

The cyclic redox performance of the oxygen carriers was assessed over 15 redox cycles in a packed bed reactor at 800 °C. The oxygen carriers were reduced in CO (10 vol. % CO in  $N_2$ ) and oxidized first in  $H_2O$  (23 vol. %  $H_2O$  in  $N_2$ ) and in a second step in  $O_2$  (5 vol. %  $O_2$  in  $N_2$ ). For each cycle, the  $H_2$  yield was calculated according to:

$$N_{H_2} = \dot{N}_{N_2} \times \int \frac{y_{H_2}}{1 - y_{H_2}} dt$$

where  $N_{H_2}$  is the number of moles of  $H_2$  produced,  $\dot{N}_{N_2}$  is the molar flow rate of  $N_2$ , and  $y_{H_2}$  is mole fraction of  $H_2$  in the gas leaving the packed bed. The  $H_2$  yield expressed as mmol  $H_2$ /g of oxygen carriers as a function of cycle number is given in Figure 4.6. The  $H_2$  yield of FeAl decreased rapidly over 15 cycles, *i.e.* from 12.1 mmol  $H_2$ /g oxygen carrier in the first cycle to 6 mmol  $H_2$ /g oxygen carrier in the 15<sup>th</sup> redox cycle. The addition of sodium enhanced the redox stability of FeAlNa1 and increased the  $H_2$  yield compared to FeAl; however, from the 8<sup>th</sup> redox cycle onwards also for this material the  $H_2$  yield started to decrease. On the other hand, the  $H_2$  yield of FeAlNa5

was stable over 15 redox cycles and was close to the theoretically expected value of 13.3 mmol/g oxygen carrier.

Previous studies have attributed the deactivation of Al<sub>2</sub>O<sub>3</sub> stabilized Fe<sub>2</sub>O<sub>3</sub> to the formation of hercynite (FeAl<sub>2</sub>O<sub>4</sub>) during reduction.<sup>8, 18, 22, 23, 26</sup> The formation of FeAl<sub>2</sub>O<sub>4</sub> is thermodynamically favoured for  $8 \times 10^{-2} < p_{CO_2}/p_{CO} < 1.8 \times 10^5$  and  $1 \times 10^{-2} < p_{H_2O}/p_{H_2} < 2.1 \times 10^5$ .<sup>8</sup> The formation of FeAl<sub>2</sub>O<sub>4</sub> is disadvantageous as the re-oxidation of FeAl<sub>2</sub>O<sub>4</sub> with steam is thermodynamically limited, explaining the lower than expected H<sub>2</sub> yield of FeAl and FeAlNa1. To obtain further insight into the origin of the enhanced cyclic redox stability of FeAlNa5 and the effect of the addition of sodium to the Fe<sub>2</sub>O<sub>3</sub>-Al<sub>2</sub>O<sub>3</sub> system on the structural and morphological characteristics of the material during redox cycling, the cycled materials were probed by XRD, XAS and STEM/EDX.

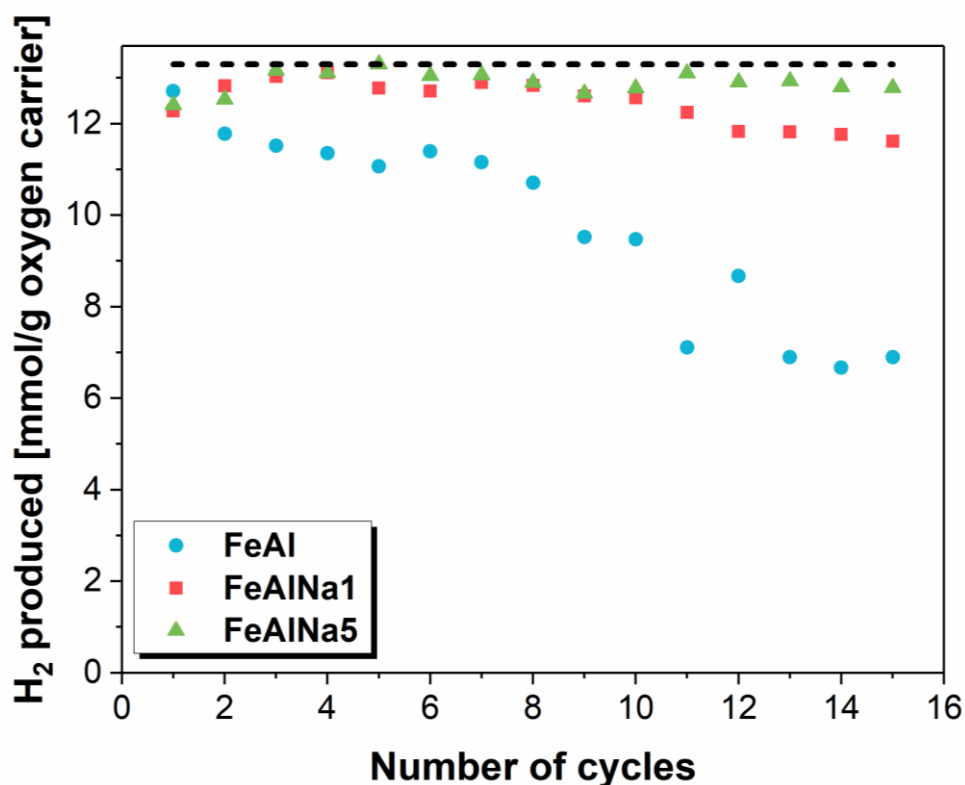


**Figure 4.6:** H<sub>2</sub> yield as a function of cycle number. The redox experiments were performed at 800 °C in a packed-bed reactor using 10 vol. % CO in N<sub>2</sub> for reduction and 23 vol. % H<sub>2</sub>O in N<sub>2</sub> followed by 5 vol. % O<sub>2</sub> in N<sub>2</sub> for re-oxidation. The dashed horizontal line represents the theoretically expected H<sub>2</sub> yield (13.3 mmol/g) for an oxygen carrier that contains 80 wt. % Fe<sub>2</sub>O<sub>3</sub>.

### 4.4.3 Structural evolution over multiple redox cycles

#### *Crystalline and local atomic structure*

To understand better the effect of sodium on the redox stability of the  $\text{Fe}_2\text{O}_3\text{-Al}_2\text{O}_3$  system the structures of the oxygen carriers that have undergone 15 redox cycles were characterized by XRD and XAS. The cycled oxygen carriers were analysed in their reduced state as it has been hypothesized that the presence of sodium hinders the formation of hercynite in the reduction step<sup>8, 18, 22</sup>.

All of the materials that have been exposed to 15 cycles (reduced state) exhibit strong reflections due to f.c.c. Fe (Figure 4.7a). However, in FeAl and FeAlNa1 the presence of magnetite ( $\text{Fe}_3\text{O}_4$ , ICSD code: 30860), wuestite (FeO, detected only in FeAl) and hercynite ( $\text{FeAl}_2\text{O}_4$ , ICSD: 86562) points to an incomplete reduction under the conditions applied here. It is worth noting that the quantity of  $\text{Fe}_3\text{O}_4$  and  $\text{FeAl}_2\text{O}_4$  is considerably lower in FeAlNa1 and FeAlNa5 compared to FeAl. In addition, the XRD pattern of FeAlNa5 does not show any peaks due to  $\text{FeAl}_2\text{O}_4$ .

Fitting of the Fe K-edge XANES spectra (Figure 4.8a) yielded the following quantities of metallic iron: 48 and 79 and 94 wt. % for FeAl, FeAlNa1 and FeAlNa5, respectively. These results confirm that in FeAlNa5 the formation of  $\text{FeAl}_2\text{O}_4$  is hindered during reduction (and to some extent in FeAlNa1). Moreover, the X-ray diffractogram of FeAlNa5 shows the presence of Na- $\beta\text{-Al}_2\text{O}_3$  as a minor phase after reduction (Figure S4.6). Using Rietveld refinement of the diffractogram of FeAlNa5 predicts a composition of 67 wt. % Fe, 27 wt. % Na- $\beta\text{-Al}_2\text{O}_3$  and 6%  $\text{Fe}_3\text{O}_4$  after reduction in CO for 15 min.

Turning to the analysis of the Al K-edge XANES data of the cycled and reduced oxygen carriers, we could not observe signatures due to  $\alpha\text{-Al}_2\text{O}_3$  in FeAlNa5 (A and B in Figure 4.3), instead showing a spectrum with similar features as the  $\gamma\text{-Al}_2\text{O}_3$  reference (Figure 4.8c). This indicates that with redox cycling  $\alpha\text{-Al}_2\text{O}_3$  transforms into a spinel-type  $\gamma\text{-Al}_2\text{O}_3$  phase stabilized by sodium (*i.e.* Na- $\beta\text{-Al}_2\text{O}_3$ ). Similarly, cycled FeAl and FeAlNa1 (reduced state) exhibit changes in the Al environment with respect to the calcined state (Figure S4.7). However, for these two materials the changes in the spectra can be related to the formation of an iron aluminate spinel ( $\text{FeAl}_2\text{O}_4$ ) owing

to the presence of three characteristic peaks <sup>42, 51</sup> (in line with XRD and Fe K-edge XAS analysis).

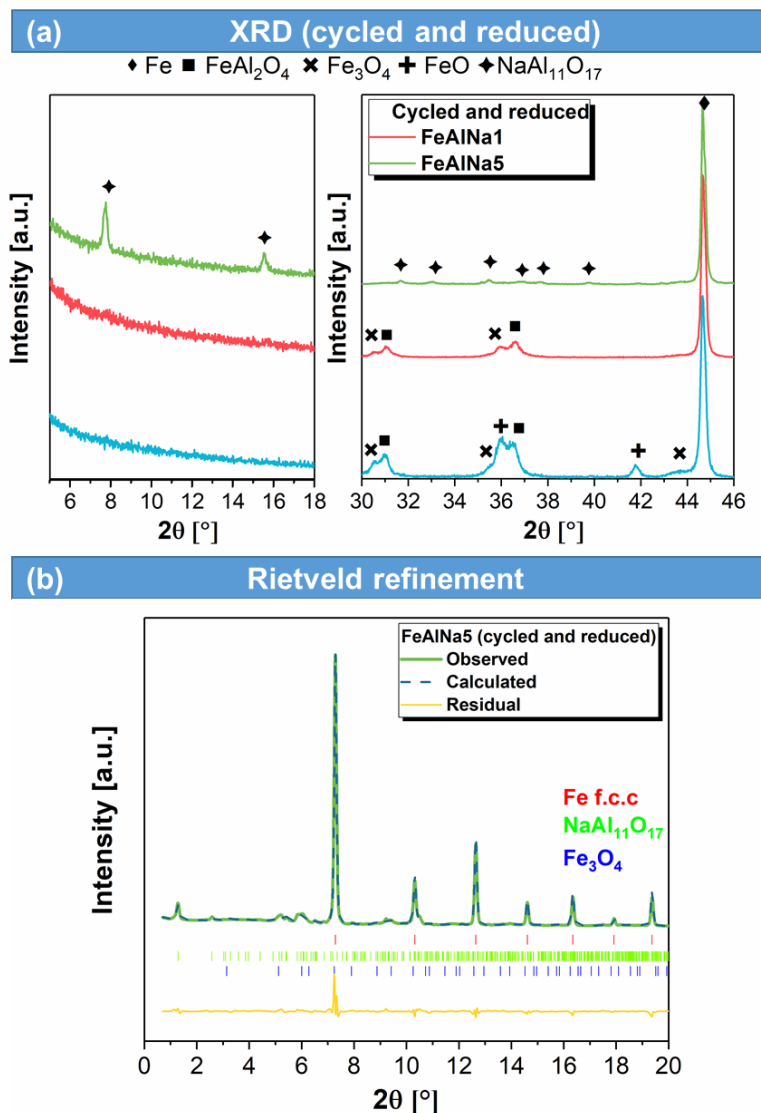


**Figure 4.7:** (a) XRD patterns of the cycled materials (15 redox cycles, reduced state) and (b) Rietveld refinement of the diffractogram of cycled FeAl5Na (reduced state, wavelength,  $\lambda=0.258$  Å).

To address whether the local environment of Na changes with redox cycling, Na K-edge spectra of the cycled materials (reduced state) were acquired (Figure 4.8b, showing also the spectrum of freshly-calcined FeAlNa5 for comparison). Our data suggests that in FeAlNa5 the local environment of Na is preserved largely during redox cycling, as evidenced by the presence of the three sharp peaks labelled as A, B and C (previously also observed in the spectra of calcined FeAlNa1 and FeAlNa5 in Figure 4.3b). On the other hand, the Na-edge XANES spectrum of cycled FeAlNa1 exhibits

a change in the Na environment when compared to the freshly-calcined state. The three sharp peaks found in calcined FeAlNa1 (A, B and C) merged into a doublet at 1075 and 1080.5 eV after redox cycling. The Na K-edge XANES spectrum of FeAlNa1 (reduced state), Figure 8b, indicates that FeAlNa1 closely resembles the spectrum of the AlNa5 reference material (AlNa5 is a material in which sodium is dispersed on  $\gamma$ - $\text{Al}_2\text{O}_3$  without the formation of a crystalline Na- $\beta$ - $\text{Al}_2\text{O}_3$  structure). These results suggest that Na initially found in an amorphous Na- $\beta$ -alumina environment in freshly-calcined FeAlNa1 becomes dispersed on a  $\text{Al}_2\text{O}_3$  spinel with redox cycling (without the formation of a crystalline structure as previously evidenced by XRD of AlNa5 in Figure S4.9).

Combing the results of the cyclic redox tests, XRD and XAS measurements we can conclude that a cyclically stable presence of Na- $\beta$ - $\text{Al}_2\text{O}_3$  (FeAlNa5) hinders the formation of  $\text{FeAl}_2\text{O}_4$  leading in turn to stable hydrogen yield. However, for the case that the amorphous Na- $\beta$ - $\text{Al}_2\text{O}_3$  phase is not stable during redox cycles (FeAlNa1),  $\alpha$ -alumina and amorphous Na- $\beta$ - $\text{Al}_2\text{O}_3$  transforms to hercynite while sodium is dispersed on the surface of spinel  $\text{Al}_2\text{O}_3$ , leading in turn to material deactivation.



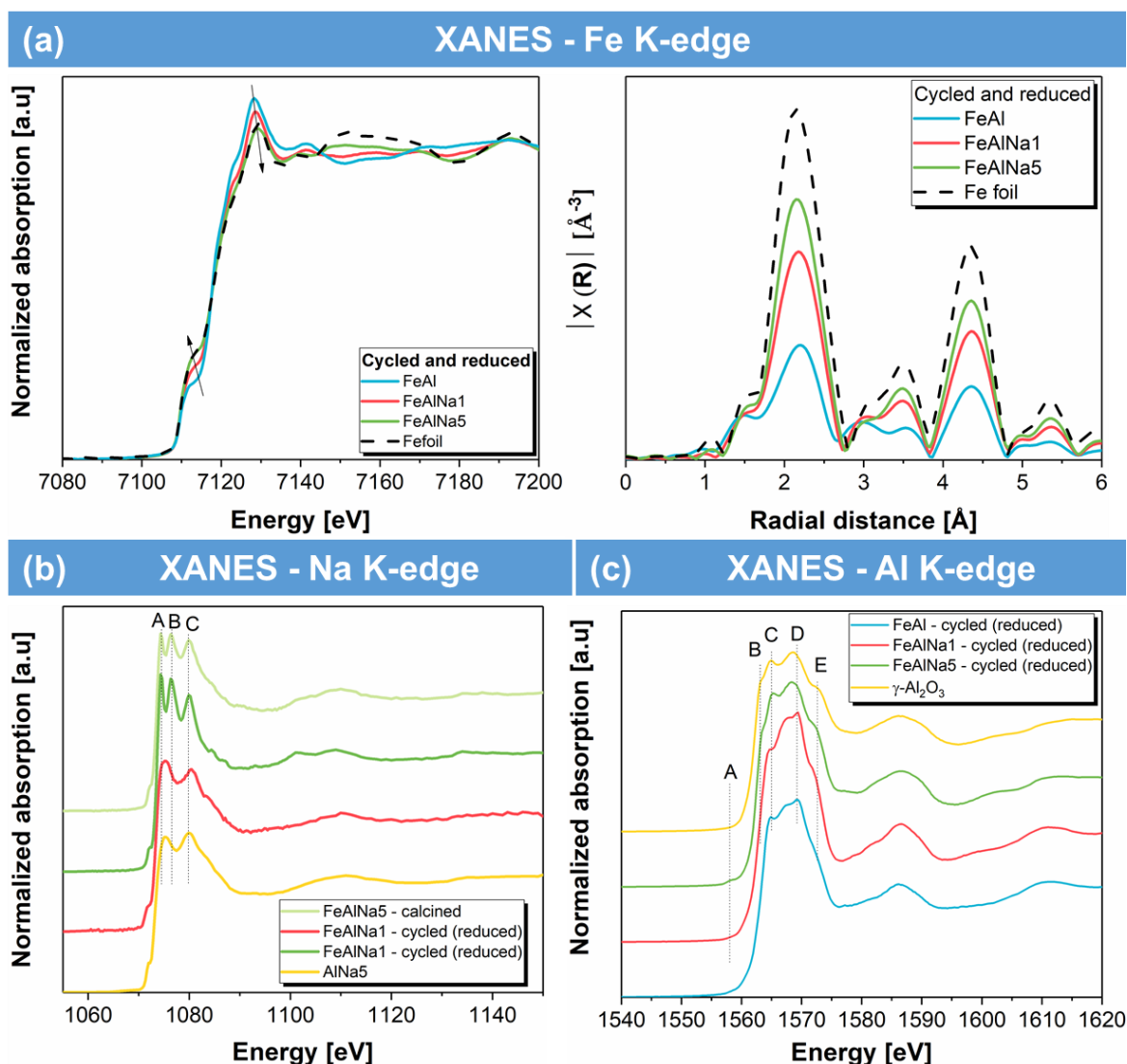


**Figure 4.8:** XANES spectra at the (a) Fe K-edge, (b) Na K-edge and (c) Al K-edge of the materials that have undergone 15 redox cycles (reduced state).

#### 4.4.4 Microstructural changes on redox cycles

HAADF-STEM images and the corresponding EDX maps of Fe, Al and Na are given in Figure 4.9. The freshly-calcined materials (*i.e.* FeAl, FeAlNa1 and FeAlNa5) show the formation of discrete phases of Fe<sub>2</sub>O<sub>3</sub> and Al<sub>2</sub>O<sub>3</sub>, whereas Na seems to be distributed homogeneously in FeAlNa1. For FeAlNa5 Al and Na seem to be present in the same particles, in line with the XRD analysis pointing to the formation of a Na- $\beta$ -Al<sub>2</sub>O<sub>3</sub> phase (Figure 4.2). The EDX maps of redox-cycled FeAl and FeAlNa1 (reduced state) show mostly overlapping maps of Fe and Al, which agrees with the formation of hercynite as determined by XRD (Figure 4.6). On the other hand, no clear overlap of the maps of Fe and Al could be observed in cycled FeAlNa5 owing to the stable interaction of

Na with Al. Cycled FeAlNa5 (oxidized state) shows only a partial overlap of the Al and Fe maps (Figure S4.10), indicative of separate phases of Fe<sub>2</sub>O<sub>3</sub> and Al<sub>2</sub>O<sub>3</sub> after re-oxidation.

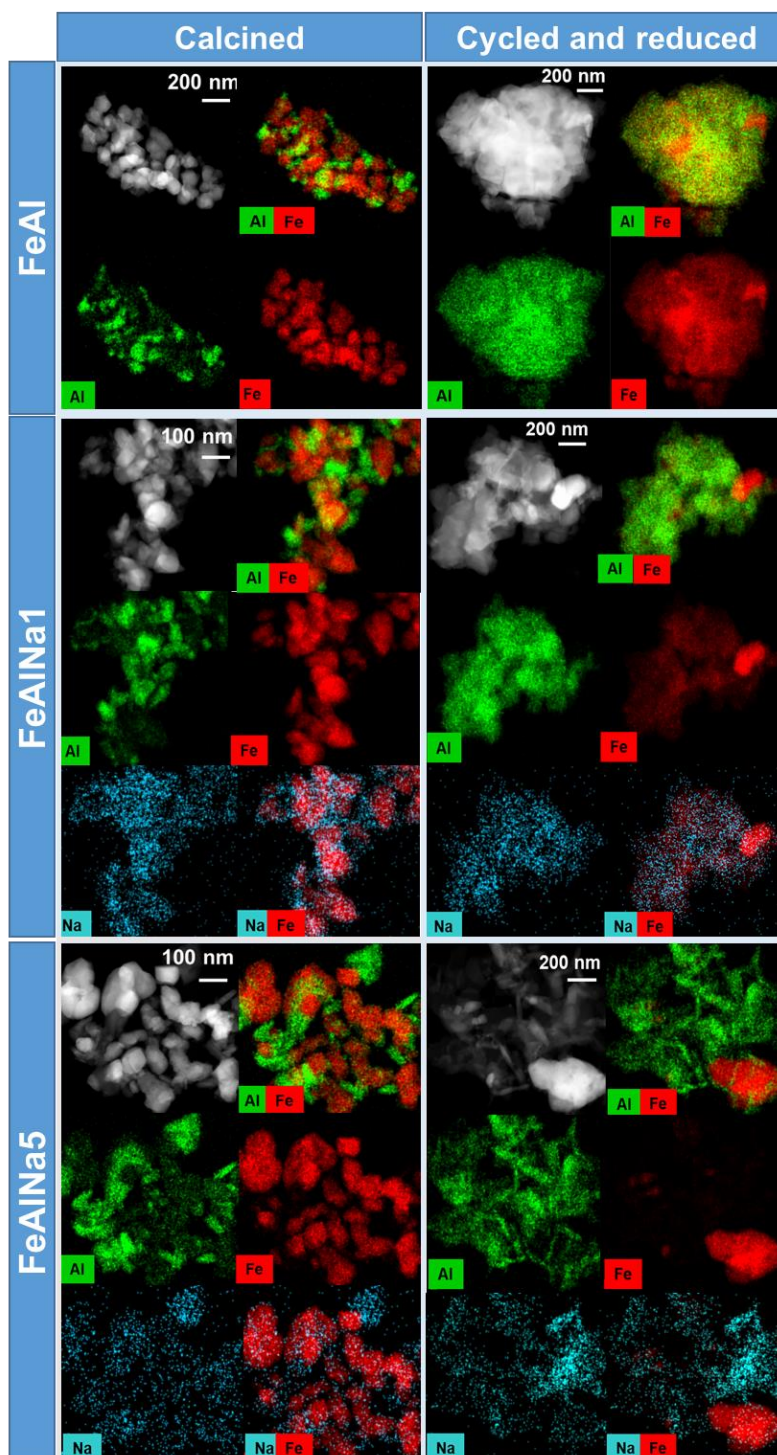


**Figure 4.9:** HAADF images and elemental mapping of the synthesized oxygen carriers after calcination and cycling experiments (in reduced state).

## 4.5 Conclusions

In this work we probe the effect of sodium on the phase formation and stability in the  $\text{Fe}_2\text{O}_3\text{-Al}_2\text{O}_3$  system and its consequences for the hydrogen yield. Overall, the addition of sodium stabilizes the hydrogen yield and the addition of sodium (with a molar ratio of  $\text{Na}:(\text{Fe}+\text{Al}) = 0.07$ ) yields a stable redox performance over 15 redox cycles.

Applying X-ray powder diffraction (XRD), X-ray absorption spectroscopy (XAS) at the Al, Na and Fe K-edges and scanning transmission electron microscopy/energy-dispersive X-ray spectroscopy (STEM/EDX) to the freshly-calcined and cycled materials allowed us to draw the following conclusions:

- (i) sodium does not affect the structure of  $\text{Fe}_2\text{O}_3$
- (ii) sodium (partially) hinders the formation of  $\alpha\text{-Al}_2\text{O}_3$  upon calcination at  $900\text{ }^\circ\text{C}$  (up to what extent depends on the amount of sodium added) and
- (iii) sodium stabilizes a crystalline  $\text{Na-}\beta\text{-Al}_2\text{O}_3$  or an amorphous Na-spinel environment, depending on the amount of sodium in the material.

In addition, we could draw the following conclusions concerning the interplay between the structure of the materials and their cyclic redox stability: The hydrogen yield of unpromoted decays due to the formation of  $\text{FeAl}_2\text{O}_4$  during reduction. Promoting  $\text{Fe}_2\text{O}_3\text{-Al}_2\text{O}_3$  with a sufficiently high quantity of sodium ( $\text{FeAlNa}_5$ ) leads to the formation of a cyclically stable  $\text{Na-}\beta\text{-Al}_2\text{O}_3$  ( $\text{NaAl}_{11}\text{O}_{17}$ ) phase that hinders the formation of  $\text{FeAl}_2\text{O}_4$  and yields in turn cyclically stable  $\text{H}_2$  yields. Insufficient sodium promotion ( $\text{FeAlNa}_1$ ) yields an amorphous  $\text{Na-}\beta\text{-Al}_2\text{O}_3$  phase that is not stable upon cycling, leading to the formation of some  $\text{FeAl}_2\text{O}_4$ . The gradual formation of  $\text{FeAl}_2\text{O}_4$  is most likely the reason for some deactivation observed from the 8<sup>th</sup> cycle onwards.

## 4.6 References

1. BP Energy Outlook 2017 edition.
2. IEA Technology Roadmap: Hydrogen and Fuel Cells, 2015.
3. J. A. Turner, *Science*, 2004, **305**, 972-974.
4. M. Zerta, P. R. Schmidt, C. Stiller and H. Lindinger, *International journal of hydrogen energy*, 2008, **33**, 3021-3025.
5. C. Bohn, J. Cleeton, C. Müller, S. Chuang, S. Scott and J. Dennis, *Energy & Fuels*, 2010, **24**, 4025-4033.
6. A. Thursfield, A. Murugan, R. Franca and I. S. Metcalfe, *Energy & Environmental Science*, 2012, **5**, 7421-7459.
7. Q. Zafar, T. Mattisson and B. Gevert, *Industrial & Engineering Chemistry Research*, 2005, **44**, 3485-3496.
8. P. R. Kidambi, J. P. E. Cleeton, S. A. Scott, J. S. Dennis and C. D. Bohn, *Energy & Fuels*, 2012, **26**, 603-617.
9. J. R. Scheffe, M. D. Allendorf, E. N. Coker, B. W. Jacobs, A. H. McDaniel and A. W. Weimer, *Chemistry of Materials*, 2011, **23**, 2030-2038.
10. R. D. Solunke and G. Veser, *Industrial & Engineering Chemistry Research*, 2010, **49**, 11037-11044.
11. N. S. Yüzbaşı, P. M. Abdala, Q. Imtiaz, S. M. Kim, A. M. Kierzkowska, A. Armutlulu, W. van Beek and C. R. Müller, *Physical Chemistry Chemical Physics*, 2018, **20**, 12736-12745.
12. L.-S. Fan and F. Li, *Industrial & Engineering Chemistry Research*, 2010, **49**, 10200-10211.
13. C. D. Bohn, C. R. Müller, J. P. Cleeton, A. N. Hayhurst, J. F. Davidson, S. A. Scott and J. S. Dennis, *Industrial & Engineering Chemistry Research*, 2008, **47**, 7623-7630.
14. J. P. E. Cleeton, C. D. Bohn, C. R. Müller, J. S. Dennis and S. A. Scott, *International Journal of Hydrogen Energy*, 2009, **34**, 1-12.
15. D. Hosseini, F. Donat, S. M. Kim, L. Bernard, A. M. Kierzkowska and C. R. Müller, *ACS Applied Energy Materials*, 2018.
16. W.-C. Huang, Y.-L. Kuo, P.-C. Su, Y.-H. Tseng, H.-Y. Lee and Y. Ku, *Chemical Engineering Journal*, 2018, **334**, 2079-2087.
17. Q. Imtiaz, N. S. Yüzbaşı, P. M. Abdala, A. M. Kierzkowska, W. van Beek, M. Broda and C. R. Müller, *Journal of Materials Chemistry A*, 2016, **4**, 113-123.
18. A. Kierzkowska, C. Bohn, S. Scott, J. Cleeton, J. Dennis and C. Müller, *Industrial & Engineering Chemistry Research*, 2010, **49**, 5383-5391.
19. W. Liu, J. S. Dennis and S. A. Scott, *Industrial & Engineering Chemistry Research*, 2012, **51**, 16597-16609.
20. C. Müller, C. Bohn, Q. Song, S. Scott and J. Dennis, *Chemical engineering journal*, 2011, **166**, 1052-1060.
21. J.-b. Yang, N.-s. Cai and Z.-s. Li, *Energy & Fuels*, 2008, **22**, 2570-2579.

22. N. S. Yüzbaşı, A. Kierzkowska and C. Müller, *Energy Procedia*, 2017, **114**, 436-445.
23. N. S. Yüzbaşı, A. M. Kierzkowska, Q. Imtiaz, P. M. Abdala, A. Kurlov, J. L. M. Rupp and C. R. Müller, *The Journal of Physical Chemistry C*, 2016, **120**, 18977-18985.
24. M. Ishida, K. Takeshita, K. Suzuki and T. Ohba, *Energy & Fuels*, 2005, **19**, 2514-2518.
25. C. Chung, L. Qin, V. Shah and L.-S. Fan, *Energy & Environmental Science*, 2017.
26. W. Liu, M. Ismail, M. T. Dunstan, W. Hu, Z. Zhang, P. S. Fennell, S. A. Scott and J. S. Dennis, *RSC Advances*, 2015, **5**, 1759-1771.
27. M. Arjmand, A.-M. Azad, H. Leion, T. Mattisson and A. Lyngfelt, *Industrial & Engineering Chemistry Research*, 2012, **51**, 13924-13934.
28. J. Adanez, A. Abad, F. Garcia-Labiano, P. Gayan and L. F. de Diego, *Progress in Energy and Combustion Science*, 2012, **38**, 215-282.
29. Q. Imtiaz, P. M. Abdala, A. M. Kierzkowska, W. Van Beek, S. Schweiger, J. L. Rupp and C. R. Müller, *Physical Chemistry Chemical Physics*, 2016, **18**, 12278-12288.
30. Q. Song, W. Liu, C. D. Bohn, R. N. Harper, E. Sivaniah, S. A. Scott and J. S. Dennis, *Energy & Environmental Science*, 2013, **6**, 288-298.
31. L. Liu and M. R. Zachariah, *Energy & Fuels*, 2013, **27**, 4977-4983.
32. J. Rodriguez-Carvajal, *Physica B*, 1993, **192**, 55.
33. M. Galib, M. Baer, L. Skinner, C. Mundy, T. Huthwelker, G. Schenter, C. Benmore, N. Govind and J. L. Fulton, *The Journal of Chemical Physics*, 2017, **146**, 084504.
34. B. Ravel and M. Newville, *J Synchrotron Radiat*, 2005, **12**, 537-541.
35. S. Brunauer, P. H. Emmett and E. Teller, *J Am Chem Soc*, 1938, **60**, 309-319.
36. E. P. Barrett, L. G. Joyner and P. P. Halenda, *J Am Chem Soc*, 1951, **73**, 373-380.
37. W. A. England, A. J. Jacobson and B. C. Tofield, *Solid State Ionics*, 1982, **6**, 21-27.
38. C. Peters, M. Bettman, J. t. Moore and M. Glick, *Acta Crystallographica Section B: Structural Crystallography and Crystal Chemistry*, 1971, **27**, 1826-1834.
39. N. Zhu, F. Guo, S. Yan, L. Chen and A. Li, *Acta Chimica Sinica*, 1992, **50**, 527-532.
40. A. Omegna, R. Prins and J. A. van Bokhoven, *The Journal of Physical Chemistry B*, 2005, **109**, 9280-9283.
41. D. R. Neuville, L. Cormier, A.-M. Flank, V. Briois and D. Massiot, *Chemical Geology*, 2004, **213**, 153-163.
42. D. R. Neuville, D. De Ligny, L. Cormier, G. S. Henderson, J. Roux, A.-M. Flank and P. Lagarde, *Geochimica et Cosmochimica Acta*, 2009, **73**, 3410-3422.
43. Y. Kato, K.-i. Shimizu, N. Matsushita, T. Yoshida, H. Yoshida, A. Satsuma and T. Hattori, *Physical Chemistry Chemical Physics*, 2001, **3**, 1925-1929.

44. N. Iyi, S. Takekawa and S. Kimura, *Journal of Solid State Chemistry*, 1989, **83**, 8-19.
45. Y. Yung-Fang Yu and J. T. Kummer, *Journal of Inorganic and Nuclear Chemistry*, 1967, **29**, 2453-2475.
46. U. Strom and P. Taylor, *Journal of Applied Physics*, 1979, **50**, 5761-5763.
47. M. S. Whittingham and R. A. Huggins, *The Journal of Chemical Physics*, 1971, **54**, 414-416.
48. B. N. Pal, B. M. Dhar, K. C. See and H. E. Katz, *Nature materials*, 2009, **8**, 898.
49. G. A. El-Shobaky, T. El-Nabarawy, G. A. Fagal and N. H. Amin, *Thermochimica Acta*, 1989, **141**, 195-203.
50. M. Digne, P. Raybaud, P. Sautet, D. Guillaume and H. Toulhoat, *Physical Chemistry Chemical Physics*, 2007, **9**, 2577-2582.
51. C. M. B. Henderson, C. I. Pearce, J. M. Charnock, R. J. Harrison and K. M. Rosso, *American Mineralogist*, 2016, **101**, 1373-1388.

## 4.7 Supporting Information

**Table S4.1:** Phase composition and cell volumes determined by Rietveld refinement of the XRD data of the calcined oxygen carriers. <sup>a</sup>

		a [Å]	b [Å]	c [Å]	Cell volume [Å <sup>3</sup> ]	Phase content [wt %]	Rp	Rwp	Rexp
<b>FeAl</b>	<b>Fe<sub>2</sub>O<sub>3</sub></b>	5.0170(2)	5.0170(2)	13.6853(6)	298.30(2)	75.1(8)	7.32	10	6.69
	<b>Al<sub>2</sub>O<sub>3</sub></b>	4.7854(4)	4.7854(4)	13.051(2)	258.83(5)	24.9(7)			
<b>FeAlNa1</b>	<b>Fe<sub>2</sub>O<sub>3</sub></b>	5.0179(2)	5.0179(2)	13.6921(7)	298.56(2)	83.3(9)	7.02	9.4	4.57
	<b>Al<sub>2</sub>O<sub>3</sub></b>	4.7811(5)	4.7811(5)	13.050(2)	258.34(6)	16.7(6)			
<b>FeAlNa5</b>	<b>Fe<sub>2</sub>O<sub>3</sub></b>	5.0161(1)	5.0161(1)	13.6802(6)	298.09(2)	79(1)	7.07	9.69	4.25
	<b>Al<sub>2</sub>O<sub>3</sub></b>	4.7813 (9)	4.7813(9)	13.046(4)	258.3(1)	5.2(5)			
	<b>NaAl<sub>11</sub>O<sub>17</sub></b>	5.64(1)	5.64(1)	22.778(6)	626.8(2)	15.0(7)			

<sup>a</sup> Fe<sub>2</sub>O<sub>3</sub> phase: *R*-3 *c* space group <sup>1</sup>, Al<sub>2</sub>O<sub>3</sub> phase: *R*-3 *c* space group <sup>2</sup> and NaAl<sub>11</sub>O<sub>17</sub> phase: *P63/mmc* space group <sup>3</sup>

1. P. Schouwink, L. Dubrovinsky, K. Glazyrin, M. Merlini, M. Hanfland, T. Pippinger and R. Miletich, *American Mineralogist*, 2011, **96**, 1781-1786.
2. S. Kondo, K. Tateishi and N. Ishizawa, *Japanese Journal of Applied Physics*, 2008, **47**, 616.
3. N. Zhu, F. Guo, S. Yan, L. Chen and A. Li, *Acta Chimica Sinica*, 1992, **50**, 527-532.

**Table S4.2:** Weight compositions of the materials calcined at 900 °C.

		FeAl	FeAlNa1	FeAlNa5
<b>Nominal weight compositions</b>	<b>Fe<sub>2</sub>O<sub>3</sub> (wt. %)</b>	75	76	73
	<b>Al<sub>2</sub>O<sub>3</sub> (wt. %)</b>	25	23	24
	<b>Na<sub>2</sub>O (wt. %)</b>	-	1	3
	<b>Al<sub>2</sub>O<sub>3</sub>:Fe<sub>2</sub>O<sub>3</sub> ratio</b>	0.33	0.30	0.33
<b>Weight compositions calculated from EDX</b>	<b>Fe<sub>2</sub>O<sub>3</sub> (wt. %)</b>	77	76.4	73.8
	<b>Al<sub>2</sub>O<sub>3</sub> (wt. %)</b>	23	22.5	21.9
	<b>Na<sub>2</sub>O (wt. %)</b>		1.1	4.3
	<b>Al<sub>2</sub>O<sub>3</sub>:Fe<sub>2</sub>O<sub>3</sub> ratio</b>	0.30	0.30	0.33

**Table S4.3:** EXAFS fitting results of the Na K edge XAS data of the calcined and cycled materials.

		d [Å]	$\sigma^2$ [Å <sup>2</sup> ]	CN	R-factor
<b>FeAlNa1</b> <b>calcined</b>	Na-O	2.2(1)	0.004	2.7 (0.8)	0.02
	Na-O	2.8(1)	0.004	1.7 (0.8)	
	Na-Al	3.6(1)	0.01(1)	4 (2)	
<b>FeAlNa5</b> <b>calcined</b>	Na-O	2.2(1)	0.004	2.7 (0.7)	0.03
	Na-O	2.8(1)	0.004	2 (1)	
	Na-Al	3.6(1)	0.009	3 (1)	
<b>FeAlNa1</b> <b>cycled</b>	Na-O	2.2	0.004	3.5 (0.8)	0.018
	Na-O	2.8	0.004	1 (1)	
	Na-Al	3.6 (1)	0.009	4 (1)	
<b>FeAlNa5</b> <b>cycled</b>	Na-O	2.2(1)	0.004	2.2(0.5)	0.034
	Na-O	2.8(1)	0.004	2.3(1)	
	Na-Al	3.6 (1)	0.009	4 (1)	

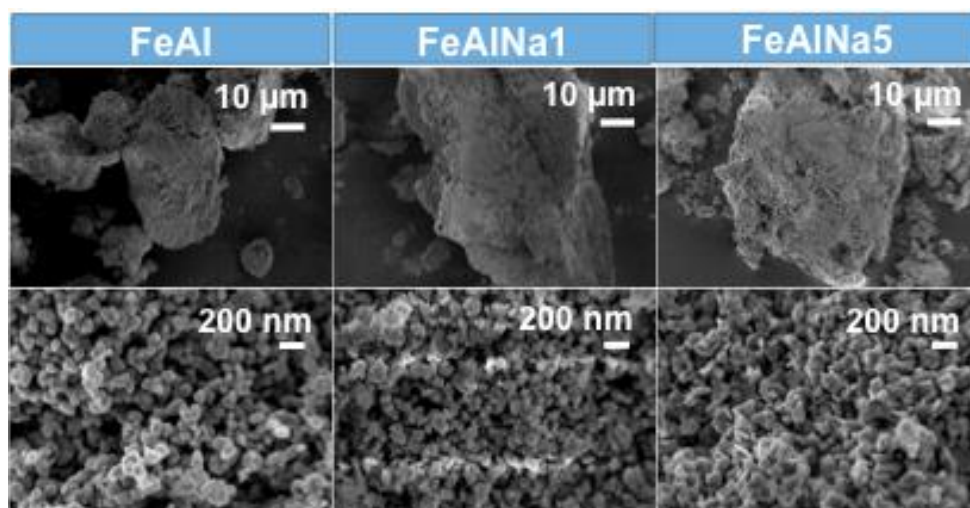


**Figure S4.1:** Electron micrographs of the calcined oxygen carriers.



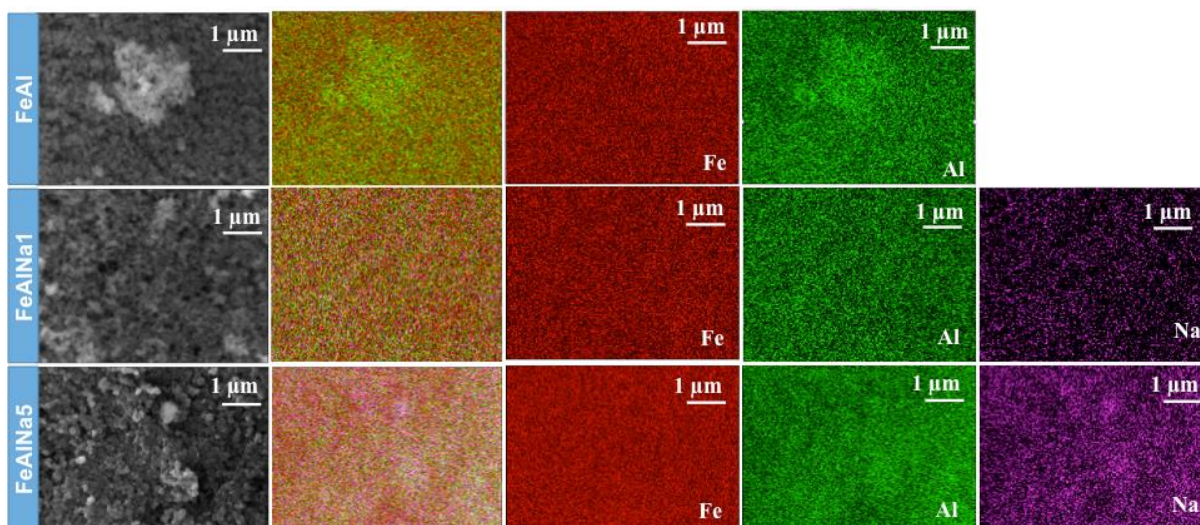


Figure S4.2: SEM/EDX maps of the calcined materials.

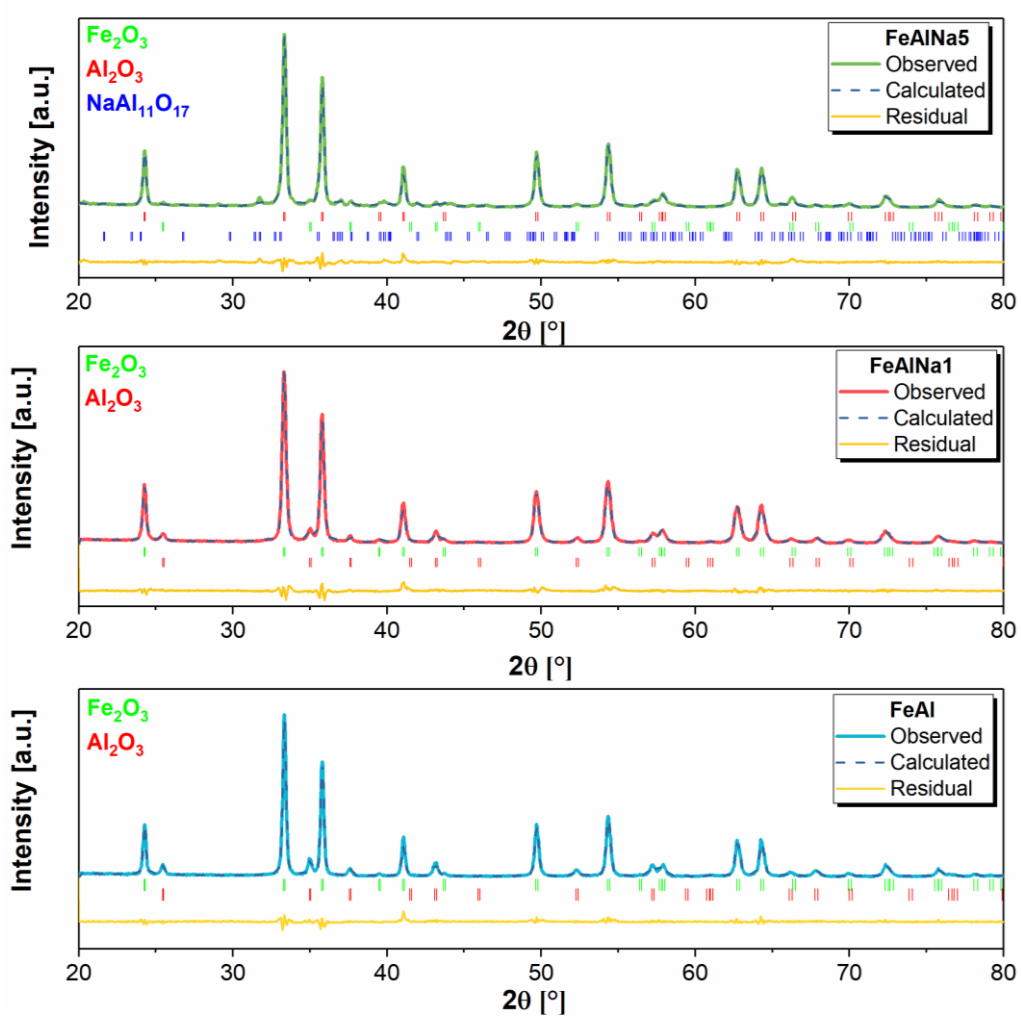
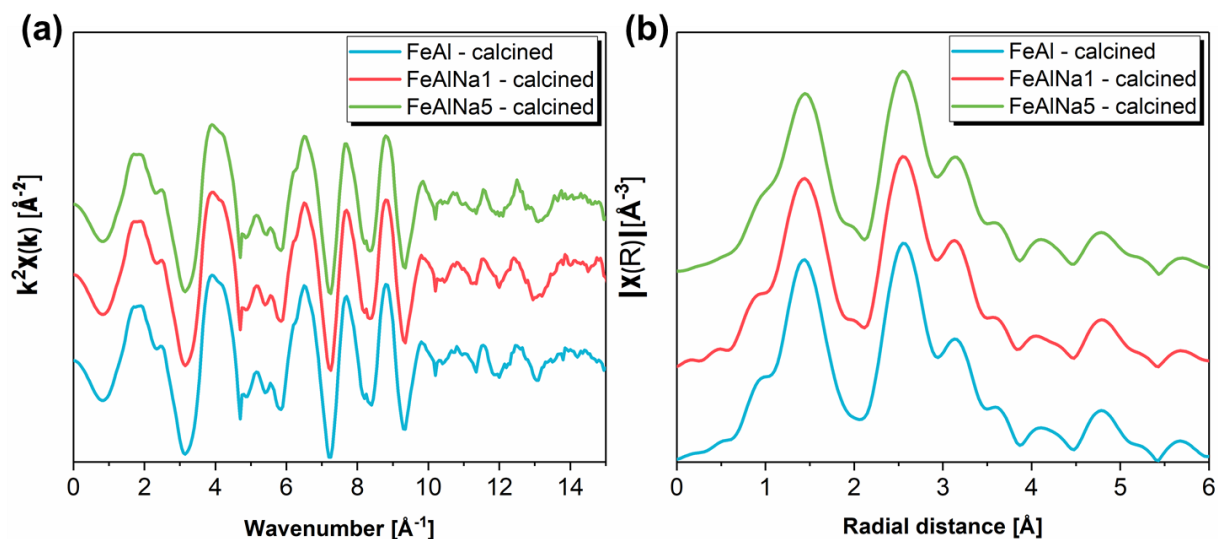
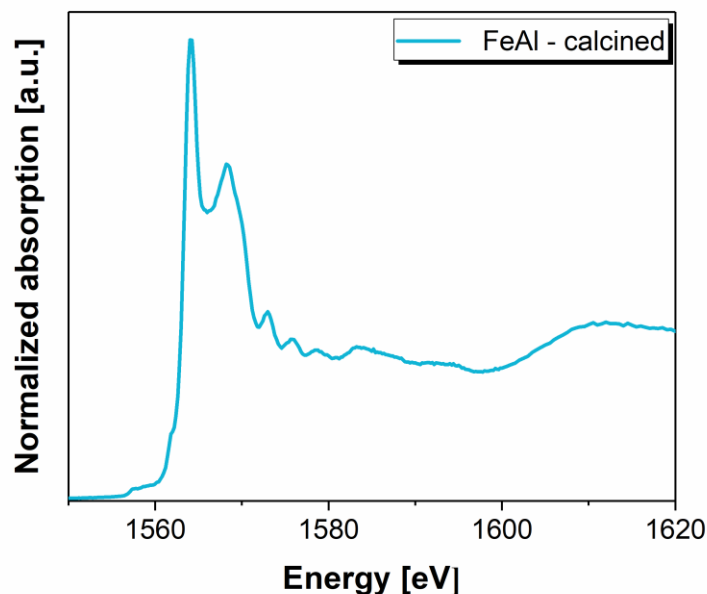


Figure S4.3: Rietveld refinement profiles of the calcined oxygen carriers.



**Figure S4.4:** (a)  $k^2$ -weighted EXAFS spectra and (b) Fourier transformed EXAFS functions ( $k^2$ -weighted) of the calcined oxygen carriers measured at the Fe K-edge.



**Figure S4.5:** Al K-edge XANES spectra of FeAl calcined at 900 °C for 2 hours. The spectrum of FeAl shows a white-line at 1566 eV with a shoulder at 1570 eV and a broad peak at 20 eV above the absorption edge, indicative of an Al environment in an octahedral coordination as in  $\alpha$ - $\text{Al}_2\text{O}_3$  <sup>4</sup>.

4. A. Omega, R. Prins and J. A. van Bokhoven, *The Journal of Physical Chemistry B*, 2005, **109**, 9280-9283.

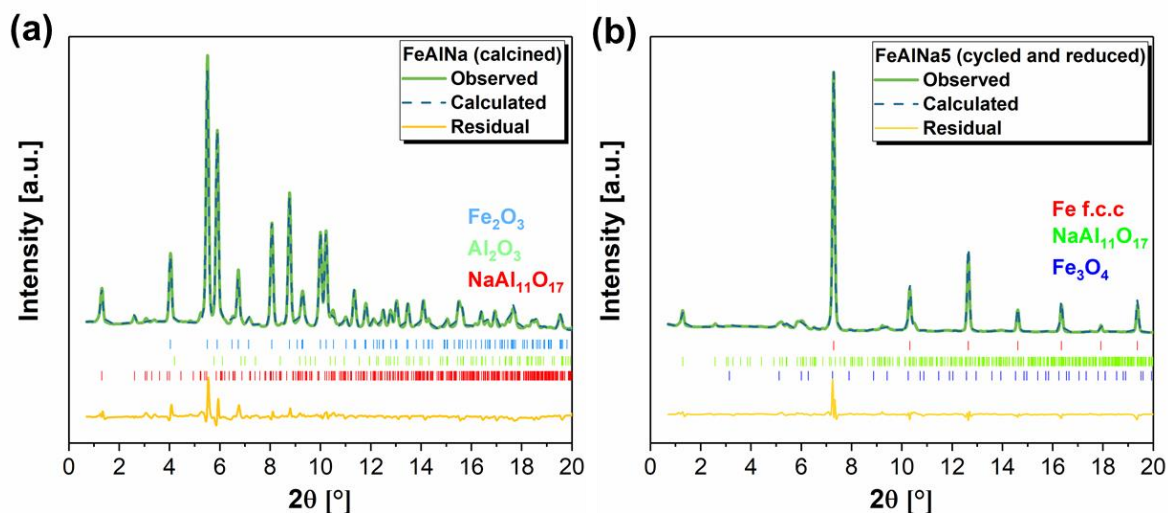


**Figure S4.6:** Rietveld refinement profiles of calcined and cycled (reduced state) FeAlNa5 (wavelength,  $\lambda=0.258 \text{ \AA}$ ).

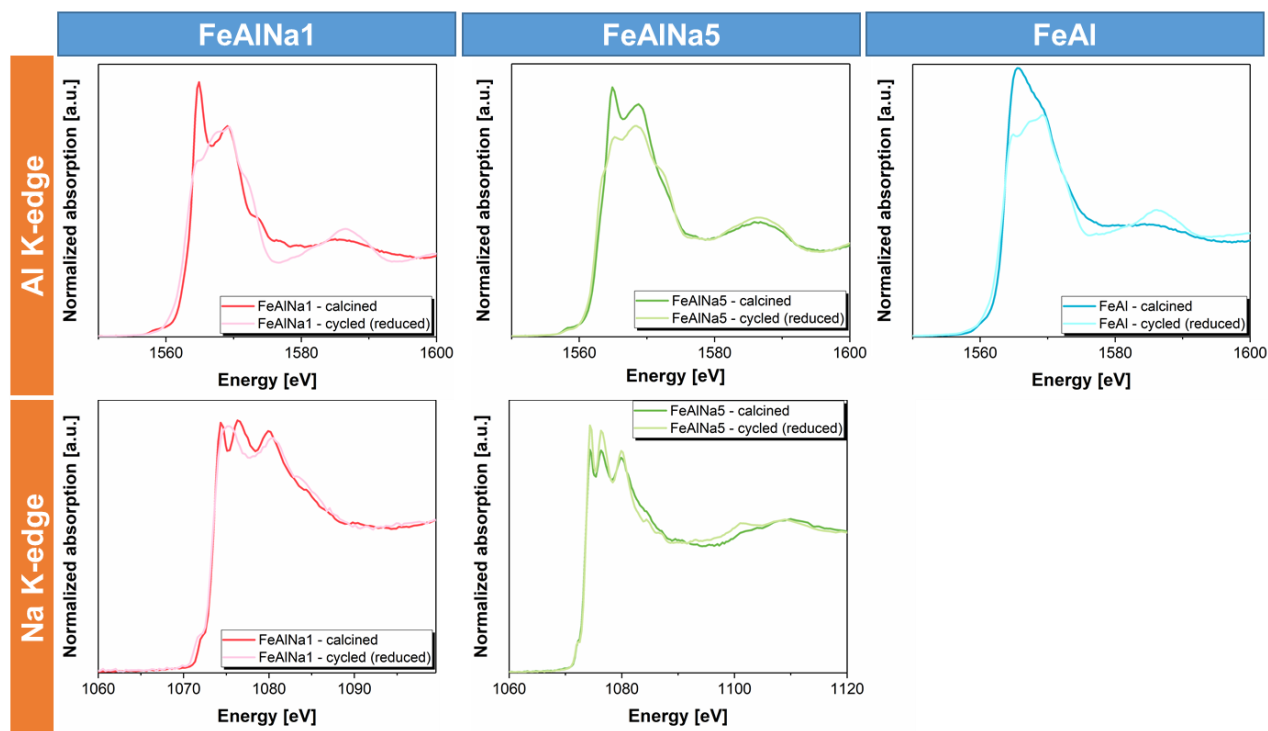


**Figure S4.7:** Comparison of the XANES spectra at the Fe K-edge, Na K-edge and Al K-edge of the materials before and after cyclic redox tests (reduced state).

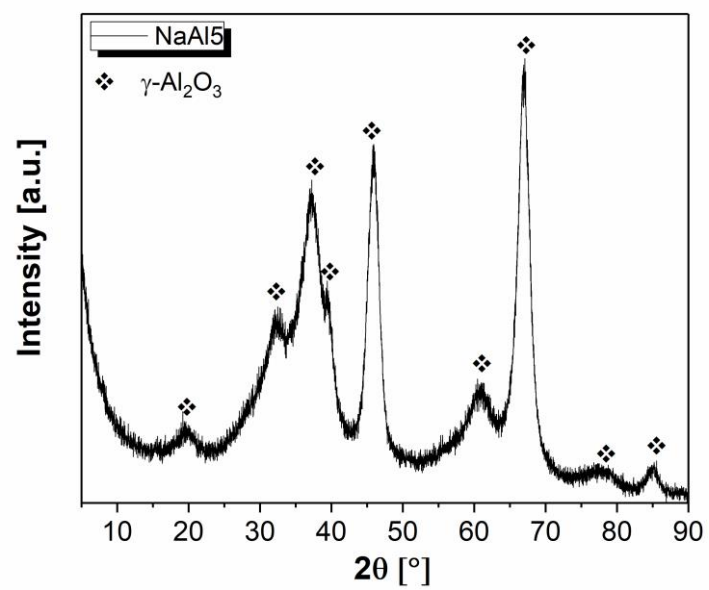


**Figure S4.8:** XRD pattern of AlNa5.



SEM images of the cycled materials after reduction (in 10 vol. % CO in N<sub>2</sub>) and subsequent re-oxidation (in 23 vol. % H<sub>2</sub>O in N<sub>2</sub> followed by 5 vol. % O<sub>2</sub> in N<sub>2</sub>) are given in Figure S4.9. SEM images indicate that the oxygen carriers that showed very poor cyclic redox performance (FeAl and FeAlNa1) were sintered after being exposed to 15 redox cycles. Interestingly, the degree of sintering in FeAlNa5 was relatively lower than FeAl and FeAlNa1 during cyclic redox reactions.

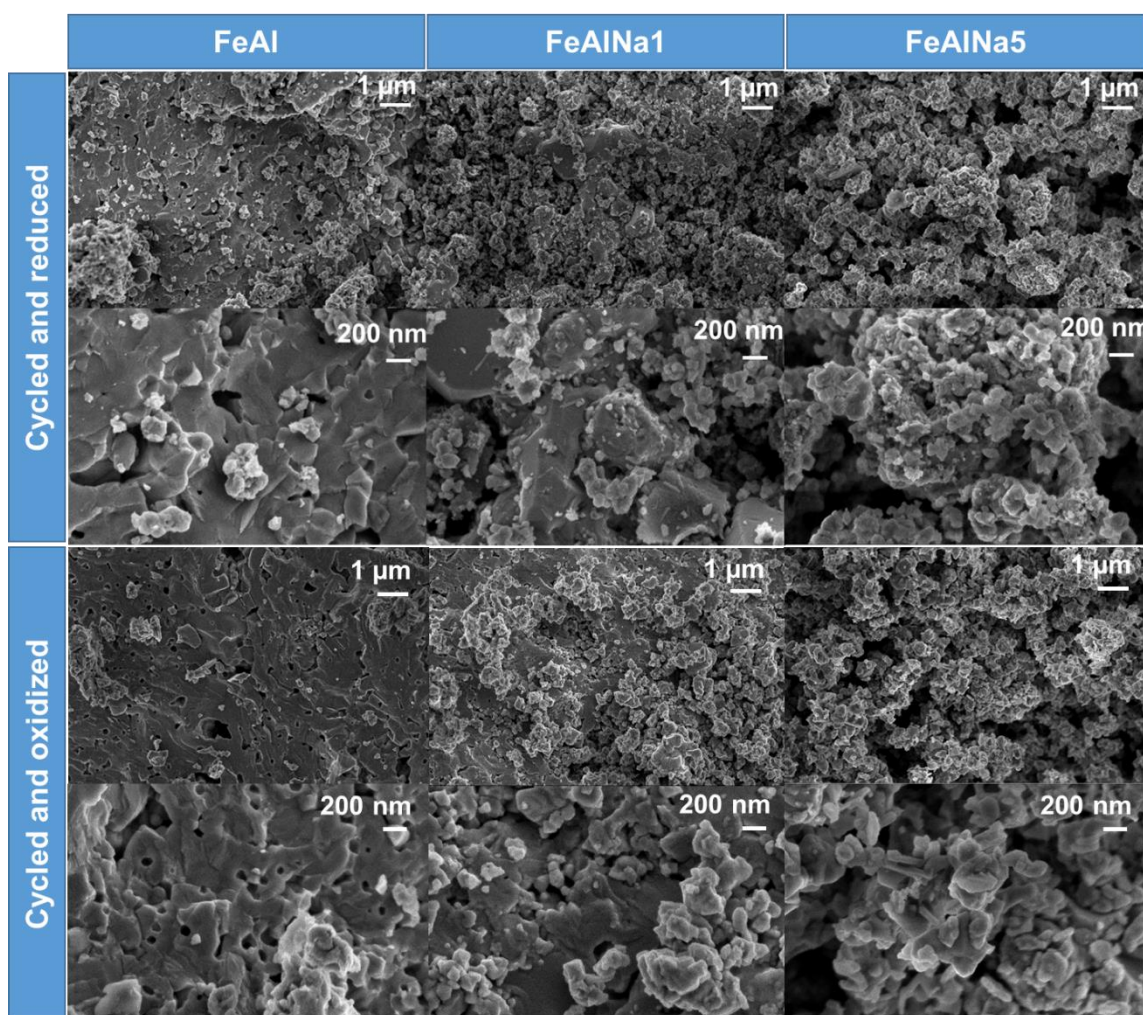


**Figure S4.9:** Electron micrographs of the cycled (in reduced and oxidized state) oxygen carriers after being subjected to 15 redox cycles in a fixed bed.

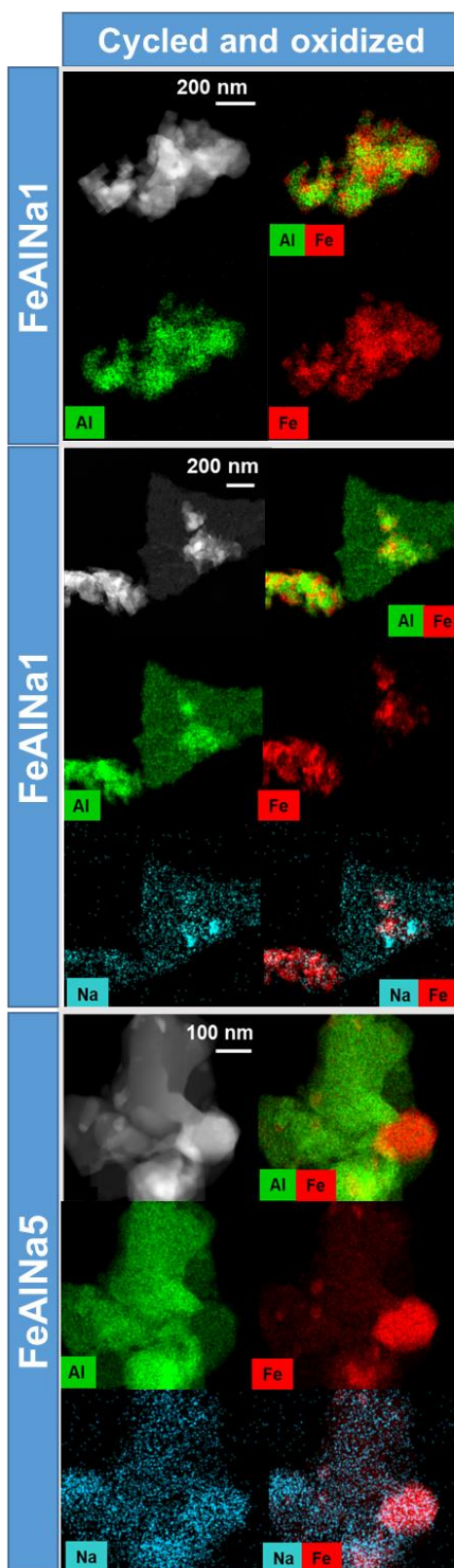


**Figure S4.10:** HAADF images and elemental mapping of the cycled oxygen carriers (15 redox cycles, oxidized state  $\text{H}_2\text{O}/\text{N}_2$  followed by  $\text{O}_2/\text{N}_2$ ).

## Chapter 5: Atomic Layer Deposition of a Film of Al<sub>2</sub>O<sub>3</sub> on Electrodeposited Copper Foams to Yield Highly Effective Oxygen Carriers for Chemical Looping Combustion-Based CO<sub>2</sub> Capture

---

This section contains a reprint of the submitted article: Yüzbaşı, N.S., Armutlulu, A., Abdala, P.M., and Müller, C.R., 2018. Atomic layer deposition of a film of Al<sub>2</sub>O<sub>3</sub> on electrodeposited copper foams to yield highly effective oxygen carriers for chemical looping combustion-based CO<sub>2</sub> capture. ACS Applied Materials & Interfaces, *Under revision*.

The author of this thesis carried out the synthesis of the oxygen carriers, TGA, XRD, BET and cyclic performance tests. Dr. A. Armutlulu performed ALD, SEM, TEM, SEM/EDX, STEM/EDX, FIB/SEM and sputtering of the model thin films. Dr. P. M. Abdala provided guidance in *ex situ* XRD and *in situ* XRD data analysis. Additionally, Dr. A. Armutlulu, Dr. P. M. Abdala and Prof. C. R. Müller assisted with overall discussion and proof-reading of the paper.

## 5.1 Abstract

We report a rapid electrochemical deposition protocol to synthesize highly porous Cu foams serving as oxygen carriers for chemical looping, a promising technology to reduce anthropogenic CO<sub>2</sub> emissions. To overcome the sintering-induced decay in the oxygen carrying capacity of unsupported Cu foams, Al<sub>2</sub>O<sub>3</sub> films of different thicknesses (0.1-25 nm) were deposited onto the Cu foams via atomic layer deposition (ALD). An ALD-grown Al<sub>2</sub>O<sub>3</sub> overcoat of 20 nm thickness (~4 wt. % Al<sub>2</sub>O<sub>3</sub>) was shown to be sufficient to ensure excellent redox cyclic stability. Al<sub>2</sub>O<sub>3</sub>-coated Cu foams exhibited a capacity retention of 96 % over 10 redox cycles, outperforming their co-precipitated counterpart (equal Al<sub>2</sub>O<sub>3</sub> content). The structural evolution of the stabilized foams was probed in detail and compared to benchmark materials to elucidate the stabilizing role of the Al<sub>2</sub>O<sub>3</sub> overcoat. Upon heat treatment, the initially conformal Al<sub>2</sub>O<sub>3</sub> overcoat induces a fragmentation of large Cu(O) branches into small particles. After multiple redox cycles, the Al<sub>2</sub>O<sub>3</sub> overcoat transformed into sub-micrometer-sized grains of aluminium containing phases ( $\delta$ -Al<sub>2</sub>O<sub>3</sub>, CuAl<sub>2</sub>O<sub>4</sub>, and CuAlO<sub>2</sub>) that are dispersed homogeneously within the CuO matrix. Finally, the diffusion of Cu through an Al<sub>2</sub>O<sub>3</sub> layer upon heat treatment in an oxidizing atmosphere is probed in model thin films.

## 5.2 Introduction

Mitigating climate change and meeting the ever-growing energy demand due to population growth and economic development are one of the biggest challenges of the current century. When relying on fossil fuels as energy carriers, a rise in the energy demand translates directly to an increase in the emission of anthropogenic greenhouse gases, in particular CO<sub>2</sub><sup>1,2</sup>. Since the pre-industrial era, the CO<sub>2</sub> level in the atmosphere has increased from ~ 280 ppm to ~ 407 ppm<sup>3</sup>. The continuing (and even accelerating) increase in anthropogenic CO<sub>2</sub> emissions and their adverse impact on our planet's climate necessitates the near-term implementation of strategies pertaining to the reduction of CO<sub>2</sub> emissions. To this end, chemical looping combustion (CLC) is a promising technique to capture CO<sub>2</sub> at reduced costs when compared to conventional amine scrubbing<sup>2</sup>. In CLC, instead of air, a solid oxygen carrier, typically a transition metal oxide, provides the oxygen to oxidize a carbonaceous fuel (e.g., natural gas, coal or syngas) yielding a mixture of CO<sub>2</sub> and



steam. A pure stream of CO<sub>2</sub> is readily obtained after the condensation of steam. The reduced oxygen carrier is regenerated (*i.e.*, oxidized back to its original oxidation state) by air<sup>4-7</sup>.

One of the key factors affecting the efficiency of a CLC process is the performance (activity, stability, kinetics, etc.) of the oxygen carrier. A particularly attractive oxygen carrier is CuO owing to its (i) high oxygen carrying capacity of 0.2 g O<sub>2</sub> per g CuO, (ii) low tendency for carbon deposition, and (iii) high reactivity for the reduction and oxidation reactions<sup>8-10</sup>. In practice, however, the redox stability of pure, *i.e.* unsupported CuO decreases very quickly over repeated reduction and oxidation (redox) cycles. It has been argued that sintering is the key deactivation mechanism<sup>8, 11</sup>. The Tammann temperature of CuO (526 °C), an indicator for the onset of sintering, is significantly below the typical operating temperatures of the CLC process (850 – 1000 °C), hence, leading inevitably to substantial, irreversible morphological alterations of the oxygen carriers<sup>10</sup>. To alleviate the sintering-induced destabilization of CuO, incorporation of high-Tammann-temperature materials (*e.g.*, SiO<sub>2</sub><sup>12, 13</sup>, Al<sub>2</sub>O<sub>3</sub><sup>5, 13-15</sup>, MgAl<sub>2</sub>O<sub>4</sub><sup>8, 16</sup>, ZrO<sub>2</sub><sup>17, 18</sup> and TiO<sub>2</sub><sup>15, 19, 20</sup>) into the CuO matrix has been proposed. Such stabilized oxygen carriers have been synthesized typically via “conventional” methods including mechanical mixing, freeze granulation, wet impregnation, and co-precipitation<sup>4, 9, 11, 21-23</sup>. Although well-established and relatively straightforward, the majority of the aforementioned synthesis techniques lead to structures that feature a low surface area limiting intra-particle diffusivity and leading, in turn, to slow reaction kinetics<sup>7, 10, 11</sup>. Moreover, Al<sub>2</sub>O<sub>3</sub>-stabilized CuO prepared via impregnation<sup>21, 24, 25</sup> required typically a large fraction of inactive stabilizer (*i.e.*, 70-85 wt. % Al<sub>2</sub>O<sub>3</sub>) in order to achieve a considerable degree of stability during repeated redox cycles, which results in a reduced overall oxygen carrying capacity of the material (expressed in g O<sub>2</sub>/g oxygen carrier). On the other hand, more recent studies demonstrated that CuO-based oxygen carriers synthesized via co-precipitation featured both a stable redox performance and a relatively high oxygen carrying capacity, despite their reduced Al<sub>2</sub>O<sub>3</sub> content of 17.5 wt. %<sup>9, 10</sup>. These latter studies suggest that it is possible to effectively stabilize CuO with a comparatively small quantity of Al<sub>2</sub>O<sub>3</sub> if the mixing between the active component (Cu) and the inactive stabilizer (Al<sub>2</sub>O<sub>3</sub>) occurs on the microscopic (as opposed to macroscopic) level.

Considering the importance of the level of mixing between the active component (Cu) and the stabilizer, we study here approaches to stabilize effectively Cu-based macroporous foams with  $\text{Al}_2\text{O}_3$  and the stability of the level of mixing when exposed to repeated redox cycles under CLC conditions. Following the electrodeposition of Cu foams, an  $\text{Al}_2\text{O}_3$  layer was introduced as a stabilizer via atomic layer deposition (ALD), as shown schematically in Figure 5.1. ALD enables the deposition of films with atom level control of their thickness and high conformity<sup>26, 27</sup>. Such characteristics are difficult to achieve with other deposition techniques, in particular for non-planar, three-dimensional structures.

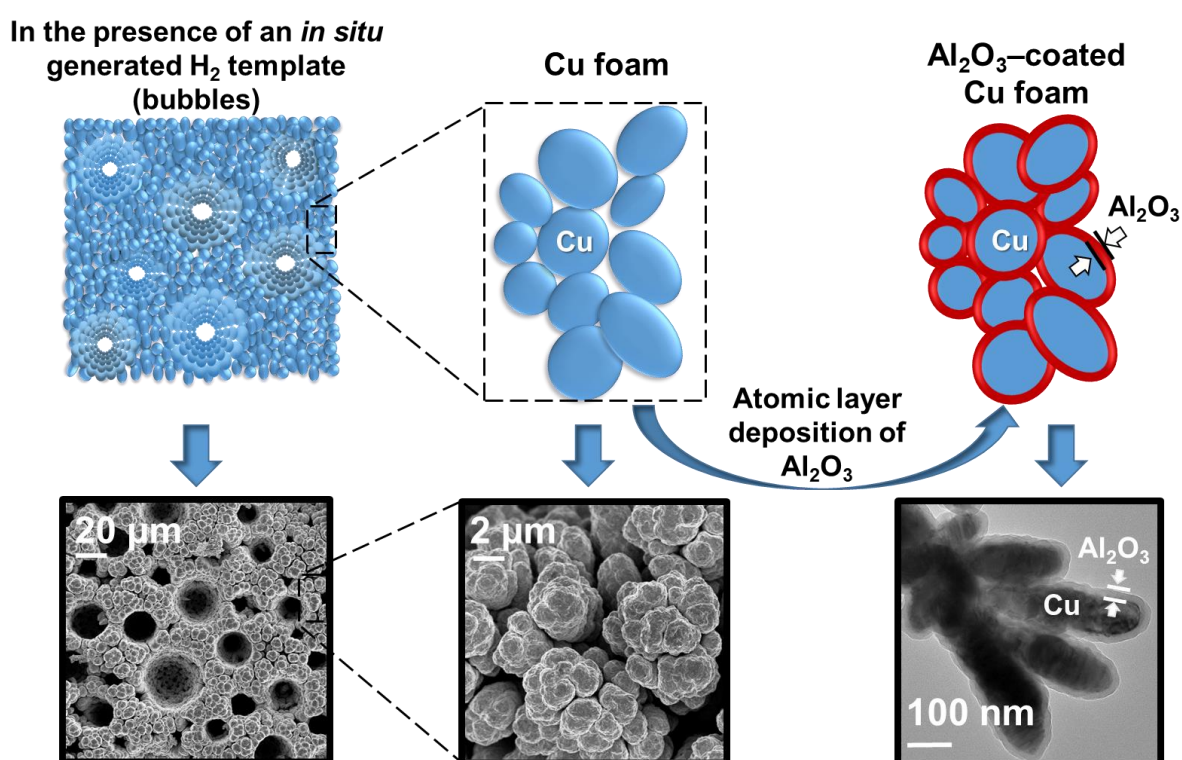


**Figure 5.1:** Schematic illustration of the fabrication process of  $\text{Al}_2\text{O}_3$ -stabilized Cu foams supplemented with electron microscopy.

### 5.3 Experimental

**Material synthesis:** A 2-electrode-cell configuration was adapted to yield Cu foams. Specifically, 50- $\mu\text{m}$ -thick transparent base PET films (Kimoto) metallized *via* sputtering of Cu (<100 nm) were used as the sacrificial substrate (cathode). A Pt mesh was used as the counter electrode (anode). In a typical synthesis, an aqueous

electrolyte containing 0.4 M CuSO<sub>4</sub> and 1.5 M H<sub>2</sub>SO<sub>4</sub> was used. Deposition of the Cu foams was performed by applying a constant current density of 1.5 A/cm<sup>2</sup> using a VoltaLab 40 potentiostat at room temperature for 60 s. In addition, the effect of HCl as a catalyst for the Cu deposition process was assessed by introducing 0.5 mM HCl into the base electrolyte solution. The deposition parameters, *i.e.*, current density, deposition time, and inter-electrode distance, were kept constant.

As benchmark materials, commercial CuO (Nanopowder, <50 nm particle size, Sigma Aldrich), and CuO-Al<sub>2</sub>O<sub>3</sub> synthesized via co-precipitation were used. For the materials synthesized by co-precipitation, a 2 M aqueous solution of Cu(NO<sub>3</sub>)<sub>2</sub>·2.5H<sub>2</sub>O and Al(NO<sub>3</sub>)<sub>3</sub>·9H<sub>2</sub>O was prepared using the appropriate quantities of the precursors to yield 96 wt. % of CuO in the final material. A 2 M NaOH solution was used for titration and added dropwise to the solution under magnetic stirring until a pH of 10 was reached. The resulting slurry was aged for 2 h at room temperature. To remove excess nitrate and alkali ions, the precipitate was washed thoroughly with DI water until the conductivity of the filtrate was less than 100 μS/cm. The washed precipitate was dried at 100 °C overnight.

**Atomic layer deposition (ALD):** A commercial ALD system (Sunale R-150B, Picosun) was used for the deposition of the Al<sub>2</sub>O<sub>3</sub> films. Multiple layers of Al<sub>2</sub>O<sub>3</sub> were formed on Cu foams by alternating pulse injections of trimethylaluminum (TMA) and water, whereby nitrogen was used as both the carrier and purge gas. The pulse and purge times for the precursors were set to 0.1 s and 5 s, respectively. The sample chamber was purged three times with nitrogen before deposition, and the deposition was performed at 150 °C. Cu foams were coated by ALD-grown Al<sub>2</sub>O<sub>3</sub> films with different thicknesses (*i.e.*, cycle numbers): 1, 10, 30, 60, 120, 150, 200, and 250 cycles. Ellipsometry studies showed that 1 ALD cycle refers to an Al<sub>2</sub>O<sub>3</sub> layer thickness of ~0.1 nm.

All of the synthesized oxygen carriers were calcined in a muffle furnace at 800 °C for 1 h (2 °C/min ramp) to remove the sacrificial PET substrate. The oxygen carriers are described using the following nomenclature: CuAl\_ALD(x), CuAl\_(HCl)\_ALD(x) and CuAl\_CP, whereby the following abbreviations of the synthesis technique are used: CP (co-precipitation) and ALD. The thickness of the deposited Al<sub>2</sub>O<sub>3</sub> layer (in

nm) is denoted in brackets with x. HCl is added for the case that HCl was used during the electrodeposition of the Cu foam.

**Characterization of the materials:** A PANalytical Empyrean X-ray powder diffractometer was used for the characterization of the crystalline phases. The diffractometer was equipped with a X'Celerator Scientific ultra-fast line detector and Bragg-Brentano HD incident beam optics using Cu K $\alpha$  radiation (45 kV and 40 mA). The scans were collected in the  $2\theta$  range of  $10^\circ$ - $90^\circ$  with a step size of  $0.016^\circ$  and scanning speed of  $0.022^\circ/\text{s}$ . Rietveld refinement of the XRD data was done using the FullProf suite <sup>28</sup>.

*In situ* XRD measurements were performed in the same equipment using an Anton Paar XRK 900 reactor chamber (Macor sample holder) allowing *in situ* XRD studies in a reflection geometry, with uniform temperature control and gas flow through the sample. In these experiments, 20 mg of an oxygen carrier was loaded into the *in situ* cell and heated up to  $900^\circ\text{C}$  under a flow of 5 vol. % O $_2$ /N $_2$  (total flow: 200 mL/min). Subsequently, ten redox cycles were performed: Reduction in 5 vol. % H $_2$ /N $_2$  (total flow rate of 200 mL/min) followed by oxidation in 5 vol. % O $_2$ /N $_2$  (total flow rate of 200 mL/min). XRD patterns were recorded continuously in the  $2\theta$  range of  $33^\circ$ - $45^\circ$  with a step size of  $0.03^\circ$  and a scan speed of  $0.2^\circ/\text{s}$  during redox cycling. The total scan time of one diffractogram was 1 min. The total number of scans collected during the reduction and oxidation steps were 10 and 15, respectively (isothermal mode). The oxidation characteristics of the as-synthesized materials were also analysed in a dynamic fashion, in the temperature range of  $150$ – $500^\circ\text{C}$  (heating rate of  $5^\circ\text{C}/\text{min}$ ) using 2 vol. % O $_2$ /N $_2$  (total flow of 200 mL/min). After reaching  $500^\circ\text{C}$ , the oxygen carriers were oxidized until complete oxidation was achieved. A semi-quantitative assessment of the phases detected during reduction and oxidation was performed by integration of the respective diffraction peaks and calculating their fraction with regards to the overall area <sup>29, 30</sup>.

The surface morphology of the oxygen carriers was visualized using high-resolution field emission scanning electron microscopy (Zeiss ULTRA 55 plus). Additionally, a Leo Gemini 1530 SEM equipped with an energy dispersive X-ray spectrometer (EDX) was utilized for elemental mapping of the synthesized materials. The cross sectional area of the oxygen carriers was characterized by focused ion

beam scanning electron microscopy (FIB-SEM, NVision 40, Zeiss). Transmission electron microscopy (TEM) was performed on a FEI Talos F200X operated at 200 kV in both TEM and scanning TEM (STEM) modes. The probe size used in the STEM mode was approximately 0.8 nm. The instrument is equipped with SuperX EDX comprising four SDD detectors. Atomic number sensitive, high angle annular dark field (HAADF) STEM was utilized to complement the STEM EDX analyses.

A Quantachrome NOVA 4000e N<sub>2</sub> adsorption analyser was utilized to determine the surface area and pore size distribution of the dried materials. Initially, the materials were degassed at 300 °C for two hours. The surface area and the pore size distribution of the materials were calculated using the Brunauer–Emmett–Teller (BET) and Barrett-Joyner-Halenda (BJH) models, respectively<sup>31, 32</sup>.

Temperature programmed oxidation (TPO) was performed in a thermogravimetric analyser (TGA, Mettler Toledo TGA/DSC 1). In a typical experiment, ~4 mg of the oxygen carrier was placed in an alumina crucible. The flow rate of O<sub>2</sub> (5 vol. % O<sub>2</sub> in N<sub>2</sub>) was set to 25 ml/min. The sample was heated from 25 to 500 °C using a temperature ramp of 5 °C/min in 5 vol. % O<sub>2</sub>/N<sub>2</sub> (total flow of 100 ml/min). Subsequently, the sample was held at 500 °C for 30 minutes. There was a continuous flow of a N<sub>2</sub> purge stream over the micro-balance (flowrate of 25 ml/min).

**Performance tests:** The cyclic redox performance of the oxygen carriers was tested in a TGA. In a typical experiment, 5 mg of an oxygen carrier was placed in an alumina crucible and subjected to 10 redox cycles at 900 °C. The oxygen carrier was heated from room temperature to 900 °C under air. Subsequently, a reduction step was conducted in 5 vol. % CH<sub>4</sub> in N<sub>2</sub> for 10 min. Re-oxidation was carried out in 10 vol. % O<sub>2</sub>/N<sub>2</sub> for 10 min. In between the reduction and oxidation steps, the reaction chamber was purged with N<sub>2</sub>. The total flowrate in all of the reaction stages was 50 ml/min. The cyclic redox performance of the oxygen carriers was also tested at 650 °C. In this case, the reduction and oxidation times were extended to 30 min.

**Preparation and characterization of thin films:** Cu thin films were prepared on 3-in., p-type Si (100) wafers (thickness of 381 μm, Si-Mat Silicon Materials, Germany) using a magnetron sputtering system (PVD Products Inc., USA). The base pressure of the chamber was  $3.1 \times 10^{-7}$  Torr. The deposition of the Cu film was achieved by sputtering from a Cu target in a 3 mTorr, 20 sccm Ar flow. The Al<sub>2</sub>O<sub>3</sub> film was deposited

via reactive sputtering from an Al target (5 mTorr, 300 W, 50 sccm Ar flow, and 5 sccm O<sub>2</sub> flow). For a uniform film deposition, the substrate was rotated continuously at 30 rpm during sputtering. The thin films were oxidized (400 °C, 800 °C and 900 °C in a flow of air) and cycled (reduction in 10 vol. % CH<sub>4</sub> in N<sub>2</sub> followed by oxidation in air at 900 °C) in a TGA. Reacted thin films were analyzed further by FIB-SEM and EDX.

## 5.4 Results and Discussion

### 5.4.1 Structural and morphological characterization of the as-synthesized and calcined materials

The morphology of the Cu foams obtained by the single-step electrodeposition of Cu for 60 s and applying a high current density (1.5 A/cm<sup>2</sup>) are visualized by SEM (at different magnification levels, Figure 5.2a). Figure 5.2a shows 3D foam structures featuring ramified porous walls, with sub-micrometer-sized particles/branches (500 ± 90 nm). The formation of pores and branch-like structures is due to the evolution of hydrogen bubbles during the electrodeposition of Cu at high current densities<sup>26</sup>. These bubbles act as a dynamic template and determine critically the morphology of the foam. By introducing a small quantity of HCl into the electrolyte, the morphology of the Cu foams is altered (Figure 5.2b), yielding a more porous structure, smaller particle (branches) sizes (120 ± 20 nm) and a higher surface area, as confirmed by N<sub>2</sub> physisorption experiments (Table S1). The presence of chloride ions during the electrodeposition process led to an increase in the deposition rate, yielding a vigorous H<sub>2</sub> evolution around the Cu deposits, which disrupts their continuous growth<sup>26, 33</sup>.

The electrodeposited foams were subsequently stabilized by ALD-grown films of Al<sub>2</sub>O<sub>3</sub>. The porous structure of the Cu foams ensured full access of the organometallic precursor of Al<sub>2</sub>O<sub>3</sub> (*i.e.*, TMA) and water, leading in turn to a homogeneous distribution of Al<sub>2</sub>O<sub>3</sub> on the entire surface of the Cu foam. TEM along with HAADF-STEM supported by EDX (Figure 5.2c and 2d) reveal the formation of a dense and conformal film of Al<sub>2</sub>O<sub>3</sub> onto the Cu grains of the foam. The thickness of the Al<sub>2</sub>O<sub>3</sub> film obtained by 200 ALD cycles was determined as 20 nm, indicating an Al<sub>2</sub>O<sub>3</sub> growth rate of ~ 0.1 nm per cycle which is in good agreement with the film thickness grown simultaneously on a Si wafer and measured via ellipsometry.

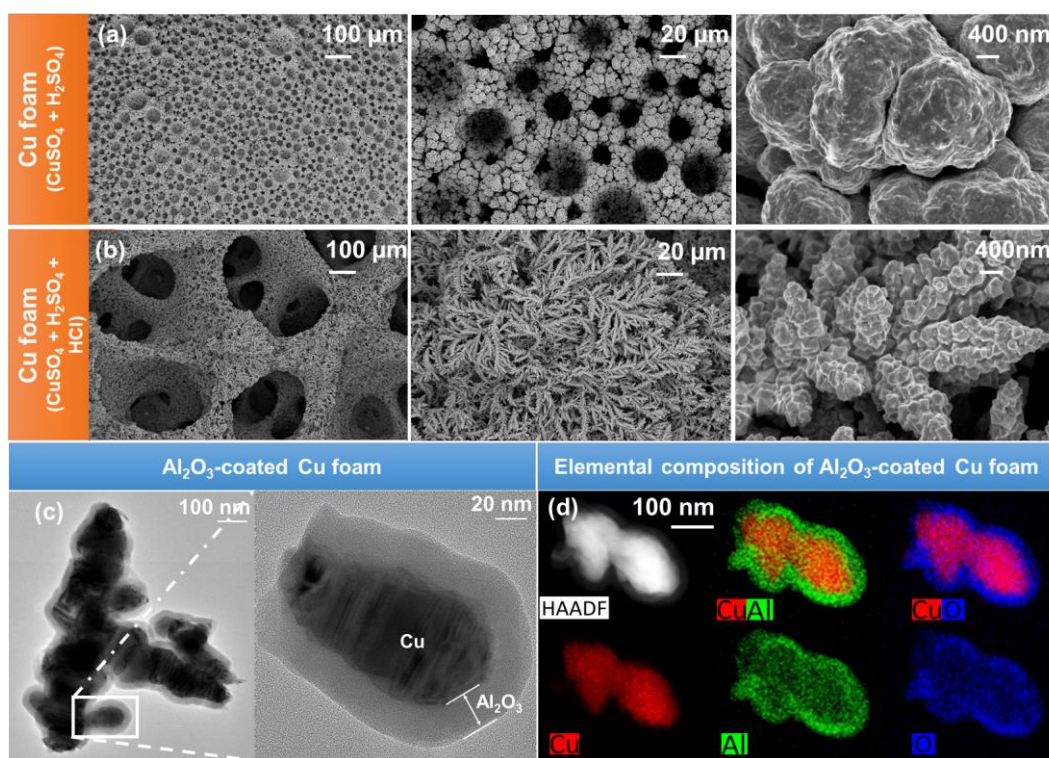


**Figure 5.2:** SEM images of Cu foams electrodeposited in the (a) absence and (b) presence of HCl, (c) TEM and (d) STEM images along with EDX mapping of as-synthesized CuAl\_ALD(20) prior to calcination.

XRD analysis of the Cu foams (as prepared and after drying at 100 °C, Figure 5.3a, reveals the dominant presence of metallic Cu (fcc-Cu) along with traces of the  $\text{CuSO}_4 \cdot \text{H}_2\text{O}$  precursor and  $\text{Cu}_2\text{O}$  (inset Figure 5.3a). CuAl\_ALD(20) exhibits diffraction peaks due to metallic Cu. We could not observe any peaks due to  $\text{Al}_2\text{O}_3$ , pointing to an amorphous nature of the as-deposited films. After calcination at 800°C, Cu transformed to CuO and the formation of a small quantity of the spinel  $\text{CuAl}_2\text{O}_4$  was observed, in agreement with equilibrium thermodynamics of the Cu–O–Al system<sup>34, 35</sup>. The CuO crystal structure in the calcined material was determined by Rietveld refinement using a C2/c space group (Table S5.2 and Figure S5.1). The following CuO cell parameters were determined for the calcined Cu foam:  $a=4.6871(2)$  Å,  $b=3.4236(2)$  Å,  $c=5.1322(1)$  Å and  $\beta=99.417(1)$  °. The structural parameters obtained for CuAl\_ALD(20) are:  $a=4.6868(2)$  Å,  $b=3.4236(2)$  Å,  $c=5.1329(2)$  Å and  $\beta=99.370(2)$  °. The small differences in the parameters are within the experimental error, indicating that the presence of an  $\text{Al}_2\text{O}_3$  overcoat did not modify the crystal structure of CuO. However, a certain fraction of CuO reacted with  $\text{Al}_2\text{O}_3$  to form  $\text{CuAl}_2\text{O}_4$ . The weight fraction of  $\text{CuAl}_2\text{O}_4$  and its unit cell volume were determined as 3.4(2) wt. % and



526.0(1) Å<sup>3</sup>, respectively. The cell volume determined is in good agreement with the values reported for the spinel CuAl<sub>2</sub>O<sub>4</sub> in the literature<sup>36-38</sup>.

To probe the influence of the Al<sub>2</sub>O<sub>3</sub> overcoat on the microstructure of the foams upon calcination (800°C), the calcined materials were also characterized by electron microscopy (Figure 5.3b). We observed that the uncoated material underwent a notable increase in particle size (average grain sizes of 1.2 ± 0.4 μm). On the other hand, the presence of an Al<sub>2</sub>O<sub>3</sub> overcoat seems to suppress appreciably grain growth. In fact, grains of sub-micrometer size were observed in calcined CuAl\_ALD(12). The average grain size was 400 ± 80 nm. Importantly, the STEM-EDX maps of the Al<sub>2</sub>O<sub>3</sub>-coated Cu foams reveal, that even after calcination the integrity of the ALD-grown Al<sub>2</sub>O<sub>3</sub> film was preserved largely, suggesting that the Al<sub>2</sub>O<sub>3</sub> overcoat prevented the sintering of the CuO foam during calcination (Figure 5.3c).

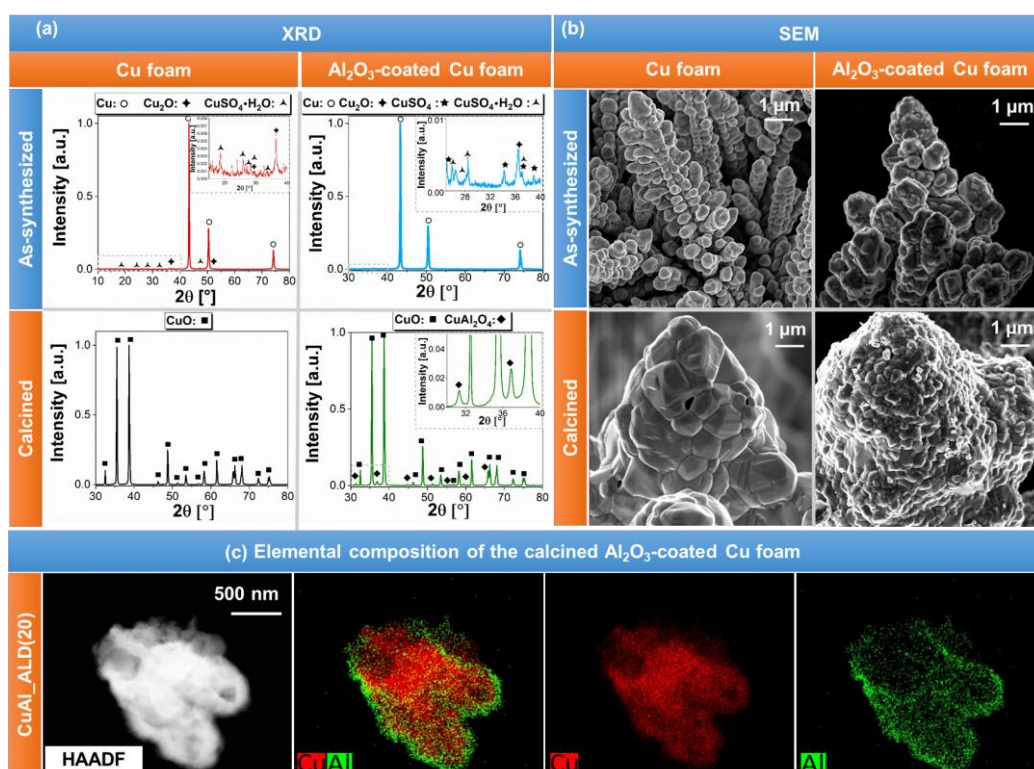


**Figure 5.3:** (a) X-ray diffractogram and (b) SEM micrographs of Cu foams with and without Al<sub>2</sub>O<sub>3</sub> overcoats prior to and after calcination (800 °C in air), and (c) STEM-EDX maps of CuAl\_ALD(20) after calcination at 800 °C in air.

The mass fraction of Al<sub>2</sub>O<sub>3</sub> in the oxygen carriers was calculated by temperature-programmed reduction (TPR) of the calcined samples. The mass fraction of Al<sub>2</sub>O<sub>3</sub> obtained from the TPR experiments is plotted as a function of the film thickness in



Figure S5.3a. The maximal Al<sub>2</sub>O<sub>3</sub> content was determined as 4.2 wt. % (sample exposed to 250 ALD cycles, *i.e.*, CuAl\_ALD(25)). It is noteworthy that for Cu foams that have been synthesized in the presence of HCl a given thickness of the Al<sub>2</sub>O<sub>3</sub> film translates to a larger mass fraction of Al<sub>2</sub>O<sub>3</sub> in the material (compared to a material that was synthesized in the absence of HCl, Figure S5.3b). For example, we determined an Al<sub>2</sub>O<sub>3</sub> content of 9.8 wt. % in CuAl\_(HCl)\_ALD(12) and 3.2 wt. % in CuAl\_ALD(12). This confirms that Cu foams synthesized in the presence of HCl feature a smaller particle size and a larger surface area (as ALD is a surface-controlled deposition process).

#### 5.4.2 Cyclic redox performance of the oxygen carriers

The cyclic redox performance of the Cu foams was assessed as a function of the thickness of the Al<sub>2</sub>O<sub>3</sub> overcoat in a TGA at 900 °C. Here, CH<sub>4</sub> was used for the reduction and air for its re-oxidation. A commercial CuO powder and co-precipitated CuO-Al<sub>2</sub>O<sub>3</sub> were used for benchmarking. Figure 5.4a reveals a gradual decrease in the oxygen capacity with number of redox cycles for the unstabilized Cu foam and commercial CuO. The loss in the oxygen capacity is due to a reduction in the apparent oxidation kinetics stemming mainly from the sintering of the material (as shown and discussed in the following sections). Conversely, the sintering of the oxygen carriers did not have a notable effect on the rate of reduction, as observed in the temporally resolved TGA profiles of the samples during reduction and oxidation (Figure S5.4). It is worth noting that in the first three redox cycles, Figure 5.4a, the unstabilized Cu foam possessed a higher oxygen carrying capacity when compared to commercial CuO. The improved performance of the Cu foam may be attributed to its initially, favourable macroporous structure leading to improved mass transfer characteristics

33.

The retention of the cyclic oxygen capacity was improved appreciably when an Al<sub>2</sub>O<sub>3</sub> overcoat was introduced onto the Cu foam. Already a single ALD cycle of Al<sub>2</sub>O<sub>3</sub>, corresponding to a ~0.1-nm-thick Al<sub>2</sub>O<sub>3</sub> film, resulted in an increase in the oxygen capacity by 20 % over 10 redox cycles when compared to the pristine Cu foam (Figure 5.4b). Increasing the thickness of the Al<sub>2</sub>O<sub>3</sub> overcoat improved further the cyclic stability. A 20-nm-thick Al<sub>2</sub>O<sub>3</sub> overcoat, corresponding to an Al<sub>2</sub>O<sub>3</sub> content of 4 wt. %,

was found to provide a remarkable degree of stabilization over 10 redox cycles (*i.e.*, 96 % capacity retention).

Turning to the Cu foams that were synthesized in the presence of HCl during electrodeposition (leading to a smaller grain size), it was found that a smaller number of ALD cycles provided a sufficient redox stability compared to their Al<sub>2</sub>O<sub>3</sub>-coated, larger-grain counterparts (absence of HCl, Figure 5.4c vs. 5.4d). For example, while 200 ALD cycles were required to achieve a stable redox performance for Cu foams synthesized in the absence of HCl, a similar degree of stability was achieved with only 120 ALD cycles when the Cu foams were realized via a HCl-assisted electrodeposition. However, for materials synthesized in the presence of HCl a slightly lower oxygen carrying capacity was obtained, owing to the presence of nearly twice as much of Al<sub>2</sub>O<sub>3</sub> (Figure S5.3b). This observation implies that the initial microstructure of the Al<sub>2</sub>O<sub>3</sub>-stabilized Cu foam is an important parameter to achieve a high cyclic stability.

Similarly, when sintering was reduced by lowering the operating temperature of the redox cycle experiments to 650 °C, a smaller number of ALD cycles (*i.e.*, 120 ALD cycles) were sufficient for material stabilization (compared to 200 ALD cycles for 900 °C). Figure S5.5 shows that CuAl\_ALD(12) and CuAl\_ALD(20) yield a nearly identical performance when operated at 650 °C. However, in contrast to an operation temperature of 900 °C, at 650 °C, the reduction kinetics become the limiting step during cyclic operations (Figure S5.6).

To investigate the influence of the synthesis approach on the redox stability of the material, co-precipitated CuO-Al<sub>2</sub>O<sub>3</sub> with an Al<sub>2</sub>O<sub>3</sub> content of 4 wt. % was studied as a benchmark material (CuAl\_CP). Compared to unstabilized CuO, also CuAl\_CP showed some improved redox stability. Its oxygen capacity retention was 80 % over 10 redox cycles, a value that is, however, significantly lower than that of CuAl\_ALD(20). This observation implies that apart from the mass fraction of the stabilizer introduced, also the synthesis technique (and hence the level of mixing between the active phase and the stabilizer) affects the performance of the oxygen carriers.

From the observation described above the following questions arise: (i) what is the underlying reason why the same quantity of Al<sub>2</sub>O<sub>3</sub> when introduced by ALD shows a

superior performance compared to its introduction by co-precipitation, (ii) what are the performance limiting steps in a redox cycle and does the incorporation of a stabilizer affect the reduction and oxidation pathways/kinetics and (iii) what structural features of the ALD-coated, Cu foams are key to obtain materials with an improved redox stability?

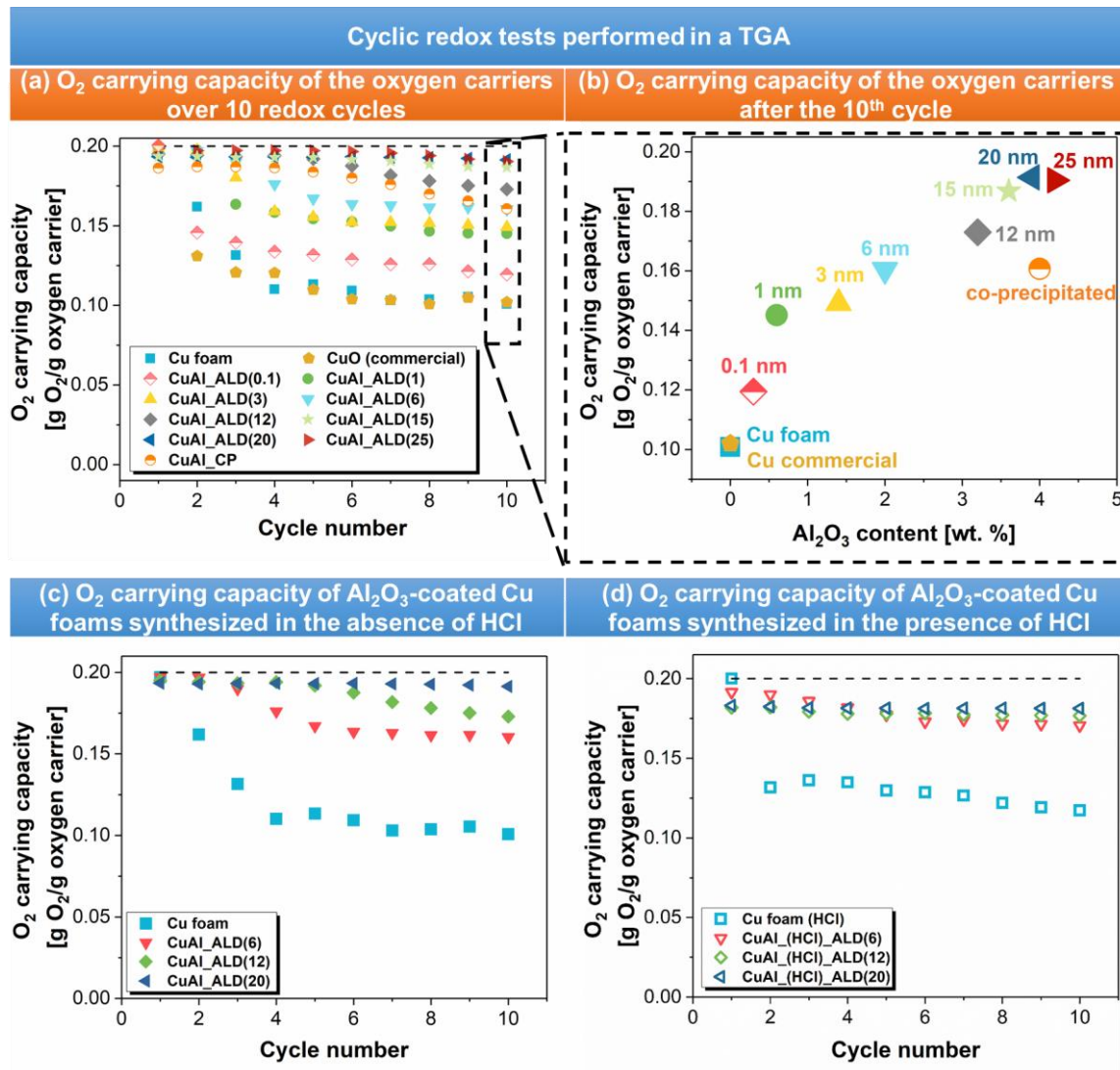


**Figure 5.4:** (a) Cyclic redox performance of Al<sub>2</sub>O<sub>3</sub>-coated Cu foams as a function of the thickness of the Al<sub>2</sub>O<sub>3</sub> overcoat and compared to benchmark materials, (b) oxygen carrying capacity after 10 redox cycles as a function of the Al<sub>2</sub>O<sub>3</sub> content, cyclic redox performance of Al<sub>2</sub>O<sub>3</sub>-coated Cu foams synthesized in the (c) absence and (d) presence of HCl.

### 5.4.3 Redox pathways as determined by *in situ* XRD

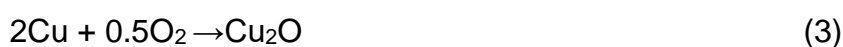
To obtain further insight into the redox mechanism of the materials synthesized, the reduction and oxidation pathways of the Cu foam, CuAl\_ALD(20) and CuAl\_CP were probed by *in situ* XRD. The evolution of the different phases identified is given in the contour plots of Figure 5.5a (measurements during the first cycle). The X-ray diffractograms recorded in the 1<sup>st</sup>, 5<sup>th</sup> and 10<sup>th</sup> cycle (CuAl\_ALD(20)) are plotted in Figure S5.7. Additionally, the weight fraction of the different phases (Cu, Cu<sub>2</sub>O and CuO) as determined by integration of the diffraction peaks during reduction and oxidation (1<sup>st</sup> and 10<sup>th</sup> cycle) are reported in Figure S5.8 and S9 (Cu foam, CuAl\_ALD(20) and CuAl\_CP).

In all of the oxygen carriers studied, the reduction proceeded via an “indirect” route (Cu → Cu<sub>2</sub>O → Cu), *i.e.*, the intermediate Cu<sub>2</sub>O was formed independent of the synthesis approach or the presence of a stabilizer. It is conceivable that the reaction conditions affect whether there is a direct transition from CuO to metallic Cu or whether the reduction proceeds via intermediates (Cu<sub>3</sub>O<sub>4</sub> and/or Cu<sub>2</sub>O). High reaction temperatures and a low concentration of the reducing gas seem to favour a reduction pathway processing through an intermediate phase<sup>39, 40</sup>. Under the reaction conditions studied here (*i.e.*, 900 °C in 5 vol. % H<sub>2</sub> in N<sub>2</sub>), the following reactions occur sequentially during reduction:



Figure 5.5a shows that reaction (1) proceeds faster than reaction (2), hence the latter one is the rate-limiting step for the formation of Cu from CuO. The presence of Al<sub>2</sub>O<sub>3</sub> affects the kinetics of reaction (2), as the reduction of Cu<sub>2</sub>O to Cu was 1.5 times faster for CuAl\_ALD(20) and CuAl\_CP when compared to unstabilized Cu.

Moreover, *in situ* XRD reveals that also the oxidation of metallic Cu to CuO proceeded through the Cu<sub>2</sub>O intermediate:



This observation is consistent with previous reports<sup>39, 41, 42</sup>. Although all of the oxygen carriers studied here follow similar reduction pathways, they do differ appreciably in the apparent rate of Cu<sub>2</sub>O oxidation (Figure S5.9 and S5.10). Specifically, in deactivating oxygen carriers (*i.e.*, Cu foam and CuAl\_CP) an oxidation time of 15 min was not sufficient to oxidize Cu<sub>2</sub>O fully back to CuO (16 wt. % residual Cu<sub>2</sub>O in the Cu foam and 7 wt. % in CuAl\_CP), whereas a nearly complete oxidation to CuO was achieved for CuAl\_ALD(20) in the first cycle. In the 10<sup>th</sup> oxidation cycle, the Cu<sub>2</sub>O content was determined as 33, 14, and 7 wt. % for pure Cu foam, CuAl\_CP, and CuAl\_ALD(20), respectively, indicating a decrease in the rate of oxidation with cycle number.

Concerning the Al-containing phases, the peaks due to CuAl<sub>2</sub>O<sub>4</sub> are rather weak owing to its small weight fraction and the relatively low signal to noise ratio obtained in the *in situ* experiments; yet, the weak reflections recorded at  $2\theta = 36.4^\circ$  and  $44.4^\circ$  in CuAl\_ALD(20) indicate that the CuAl<sub>2</sub>O<sub>4</sub> and CuO phases appear and disappear simultaneously during, respectively, oxidation and reduction (Figure S5.11).

The reaction pathways as a function of the number of redox cycles are provided in Figure S5.12. The number of redox cycles did not affect the reaction pathways and the “indirect” route (Cu → Cu<sub>2</sub>O → CuO) was observed for all cycles. The apparent rate of reduction of the oxygen carriers was stable over the 10 redox cycles tested. However, the apparent rate of the second oxidation step (*i.e.*, Cu<sub>2</sub>O → CuO) decreased with number of redox cycles, whereas the apparent rate of the first oxidation step (*i.e.*, Cu → Cu<sub>2</sub>O) was stable with cycle number. Hence, we can conclude that the apparent rate of the Cu<sub>2</sub>O → CuO transition (i) is the rate-limiting step and (ii) decreases with an increasing number of redox cycles.

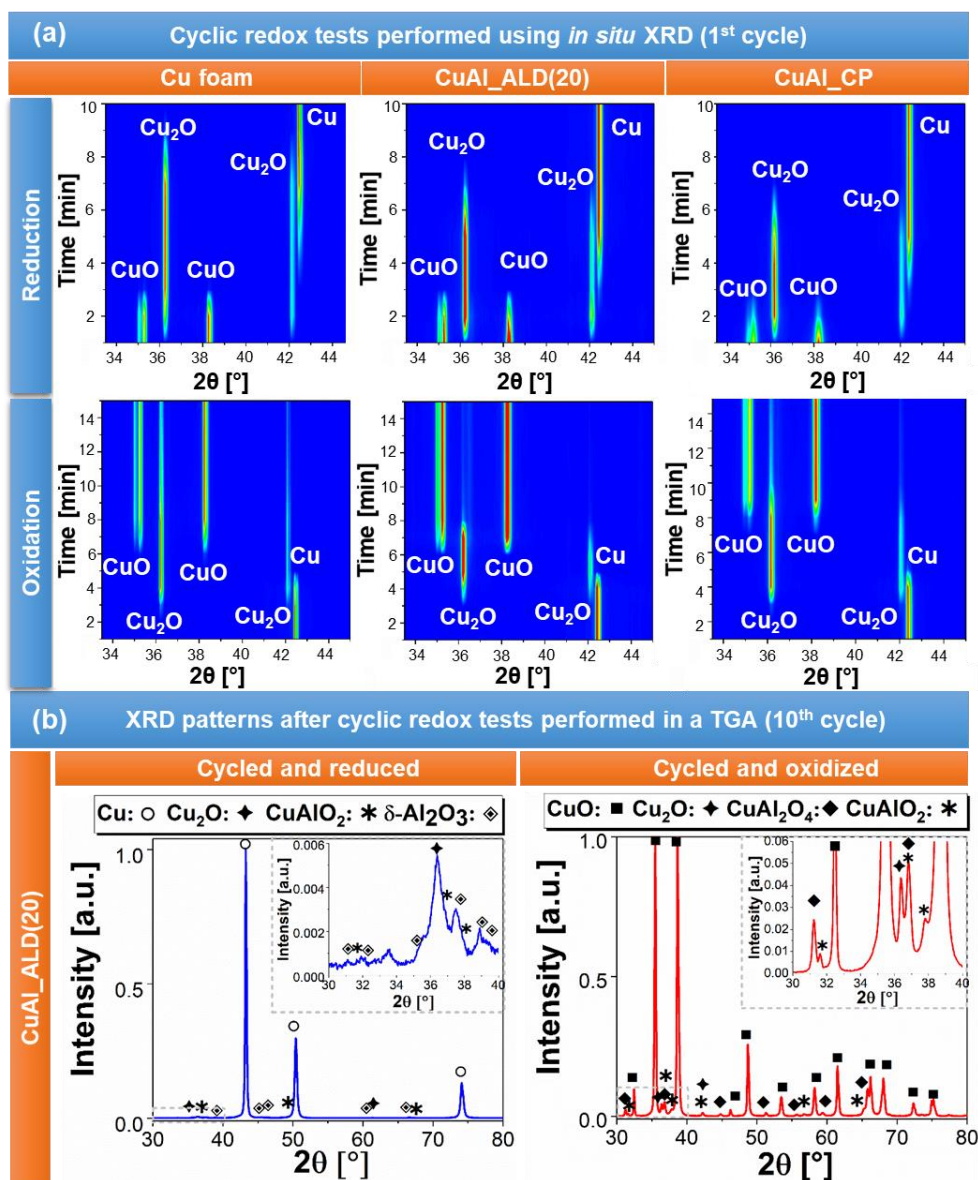


**Figure 5.5:** (a) Contour plots presenting *in situ* XRD measurements of Cu foam, CuAl\_ALD(20) and CuAl\_CP during the first cycle of a cyclic redox experiment. Normalized intensity plotted as a function of time (scan number with each scan lasting 1 min) and  $2\theta$  (red represents a high intensity and blue represents a low intensity) and (b) X-ray diffractograms (normalized by the highest peak) of CuAl\_ALD(20) in its reduced and oxidized state after being subjected to 10 redox cycles in a TGA at 900 °C (extended  $2\theta$  range of the inset figure is given in Figure S5.13).

#### 5.4.4 Structural and morphological evolution of the oxygen carriers during redox cycles

To obtain further insight into the origin of the enhanced cyclic redox performance of Al<sub>2</sub>O<sub>3</sub>-coated Cu foams, their structural and morphological evolution with number of redox cycles was evaluated.

##### ***Phase composition of the cycled materials***

We complement *in situ* XRD experiment with an *ex situ* XRD characterization of the cycled materials that have been subjected to 10 redox cycles at 900 °C in TGA (both reduced and oxidized states). Owing to the longer acquisition time during *ex situ* XRD a higher signal to noise ratio is obtained. Figure 5.5b shows that the oxygen carrier that features a stable oxygen capacity over 10 redox cycles at 900 °C, *i.e.*, CuAl\_ALD(20) was reduced almost completely to metallic Cu in a methane atmosphere and was also oxidized fully back to CuO in air. In addition to metallic Cu, cycled CuAl\_ALD(20) (after the 10<sup>th</sup> reduction step) shows the presence of  $\delta$ -Al<sub>2</sub>O<sub>3</sub> and a small quantity of delafossite (CuAlO<sub>2</sub>). After re-oxidation in air, the spinel CuAl<sub>2</sub>O<sub>4</sub> was regenerated, and only a minor quantity of CuAlO<sub>2</sub> remained in the material.

On the other hand, the deactivating oxygen carriers revealed an incomplete oxidation, exhibiting a mixture of CuO and Cu<sub>2</sub>O (Figure S5.14) after oxidation. For instance, CuAl\_ALD(6) showed a ~20 % decrease in its O<sub>2</sub> capacity between the 2<sup>nd</sup> and 8<sup>th</sup> cycle (XRD data after cyclic performance shown in Figure S5.15). At the same time the mass fraction (determined by Rietveld analysis) of Cu<sub>2</sub>O (oxygen carrier in oxidized state) increased from 21 wt. % in the 2<sup>nd</sup> cycle to 35 wt. % in the 8<sup>th</sup> cycle. These results confirm that material deactivation is linked to an insufficient oxidation of Cu<sub>2</sub>O, in line with the *in situ* XRD experiments.

##### ***Microstructural changes and oxidation behaviour of Cu foams with and without Al<sub>2</sub>O<sub>3</sub>-coating***

To correlate the morphological changes a material experiences with its oxidation characteristics, Cu foam and CuAl\_ALD(20) were investigated in more detail by additional temperature programmed oxidation (TPO) experiments combined with STEM/EDX characterization. The TPO experiments used Cu foam and CuAl\_ALD(20)

in the following stages: (i) as-synthesized (before calcination), (ii) calcined (at 800 °C) and reduced (CH<sub>4</sub>), and (iii) cycled (5 redox cycles) and reduced (CH<sub>4</sub>). The change of sample weight and the evolution of the different phases during TPO are given in Figure 5.6a and 5.6b, respectively. Figure 5.6a shows that as-synthesized CuAl\_ALD(20) starts to oxidize at a higher temperature when compared to the pristine Cu-foam. For both materials, the oxidation proceeds via the intermediate Cu<sub>2</sub>O, whereby the presence of an Al<sub>2</sub>O<sub>3</sub> film retards the formation of oxides (Cu → Cu<sub>2</sub>O and Cu<sub>2</sub>O → CuO), as revealed by *in situ* XRD (Figure 5.6b). This reduction in the apparent rate of oxidation is possibly related to the non-porous nature of the as-synthesized Al<sub>2</sub>O<sub>3</sub> overcoat reducing its diffusivity<sup>43</sup>. On the other hand, the TPO experiments also showed that the oxidation of calcined (and reduced) and cycled (and reduced) CuAl\_ALD(20) was faster than that of the as-synthesized CuAl\_ALD(20). This observation points to a restructuring of the materials during calcination, leading to higher rates of oxidation and in turn a stable redox performance. Exposing ALD-grown Al<sub>2</sub>O<sub>3</sub> films to temperatures exceeding 650 °C is known to introduce micro- and meso-porosity to the overcoat, increasing its permeability<sup>44</sup>. This will be discussed in more detail in the subsequent section.

STEM/EDX analysis of the calcined oxygen carriers (Figure 5.6c) revealed that the Al<sub>2</sub>O<sub>3</sub> overcoat is preserved largely after TPO. Furthermore, Figure 5.6c shows the fragmentation of the bulk Cu(O) foam after exposure to high temperatures. The fragmentation of the Cu(O) foam, *i.e.* the re-structuring of Cu(O) branches into sub-micrometric particles during calcination is linked to the presence of an Al<sub>2</sub>O<sub>3</sub> overcoat, as previously observed by Qin *et al.*<sup>43</sup>. The formation of such smaller particles yields an oxygen carrier with improved oxidation kinetics owing to reduced diffusion lengths.



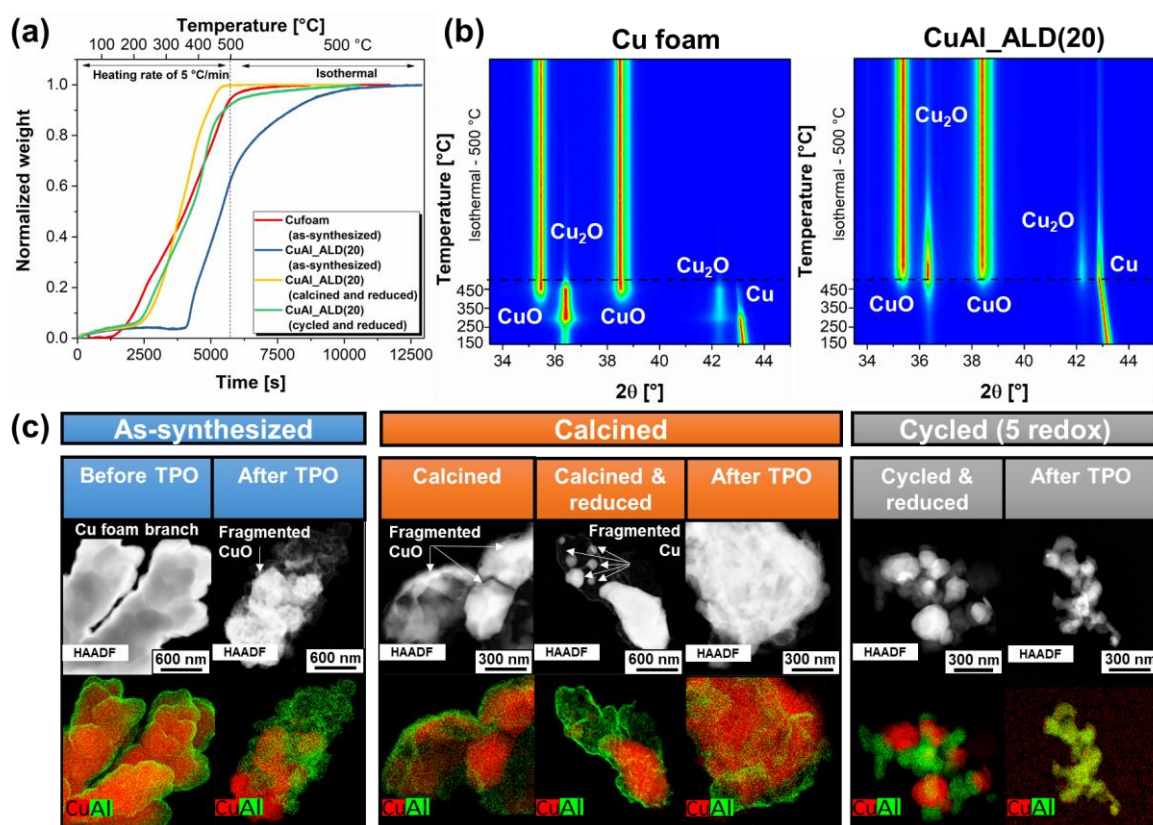


**Figure 5.6:** (a) TPO of different oxygen carriers: as-synthesized Cu\_Foam, as-synthesized CuAl\_ALD(20), calcined (and reduced) CuAl\_ALD(20), and cycled (and reduced) CuAl\_ALD(20), (b) contour plots of *in situ* XRD measurements of Cu-foam and CuAl\_ALD(20), and (c) STEM-EDX maps of as-synthesized, calcined (at 800 °C) and reduced (CH<sub>4</sub>, first cycle) and cycled and reduced (CH<sub>4</sub>, fifth cycle) CuAl\_ALD(20) before (reduced form) and after TPO experiments, *i.e.* oxidized form).

### ***Morphology of the cycled oxygen carriers***

The structural evolution of the oxygen carriers upon cycling was assessed further by electron microscopy. As shown in Figure S5.16, the initially highly porous structure of the pristine Cu foam could not be preserved under high temperatures (*i.e.*, 900 °C). Coating the foam with a film of Al<sub>2</sub>O<sub>3</sub> alleviated the sintering of the Cu foam allowing the material to maintain a notable degree of porosity. A more in-depth characterization of the compositional homogeneity was obtained via STEM/EDX analysis, showing the elemental (Cu, Al, O) distribution in the materials on a nanometer scale after cyclic operation (Figure 5.7). Figure 5.7a confirms that the conformal Al<sub>2</sub>O<sub>3</sub> overcoat was not preserved during cycling; however, the cycled material featured a homogenous distribution of Cu and Al. On the other hand, the co-precipitated sample reveals a more

heterogeneous distribution of Cu and Al (Figure 5.7b). Therefore, the superior cyclic stability of the Al<sub>2</sub>O<sub>3</sub> coated Cu foam, *i.e.* CuAl\_ALD(20), can be related to its compositional homogeneity.

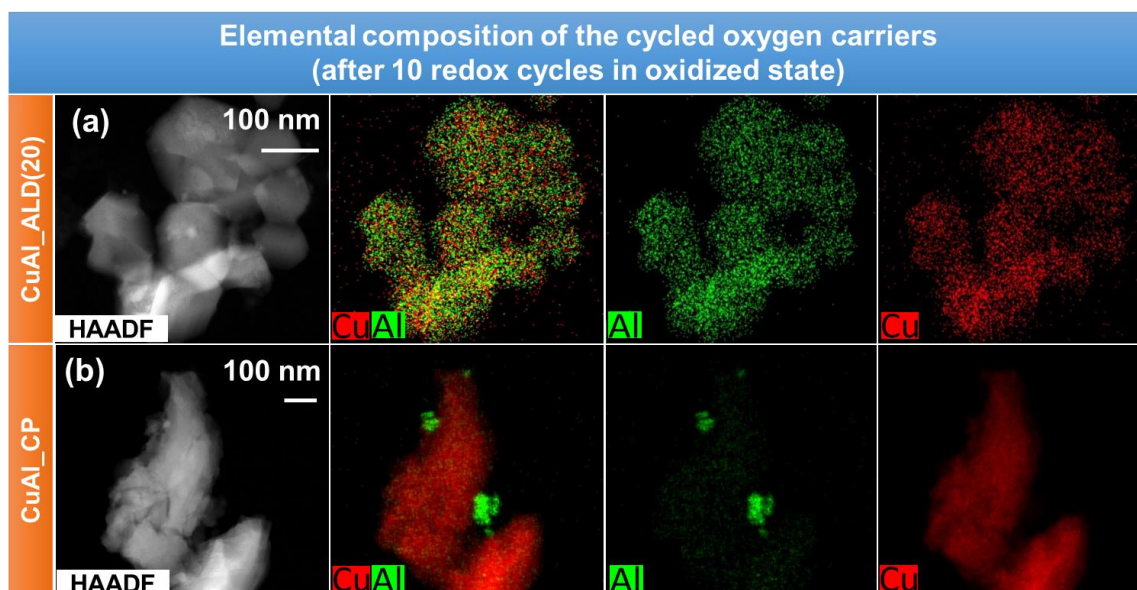


**Figure 5.7:** STEM-EDX maps of cycled (a) CuAl\_ALD(20), and (b) CuAl\_CP (10 redox cycles at 900 °C, oxidized form).

To visualize sub-surface changes of the material over cyclic redox tests, cross-sections of calcined and cycled CuAl\_ALD(20) were imaged by FIB-assisted electron microscopy and EDX (Figure 5.8). SEM images of FIB-cut cross-sections reveal a transformation of the Al<sub>2</sub>O<sub>3</sub> overcoat to sub-micrometer sized grains that are distributed throughout the CuO matrix. The formation of Al-containing particles seems to be initiated at the Cu(CuO)/Al<sub>2</sub>O<sub>3</sub> interface during the first oxidation step. After 10 redox cycles the average size of the Al-rich particles is 200 ± 50 nm. Probing the cuts of cycled Cu foams by EDX (Figure 5.8b) revealed that the grains are composed of Al-containing phases, most likely CuAl<sub>2</sub>O<sub>4</sub> and/or CuAlO<sub>2</sub> after oxidation and δ-Al<sub>2</sub>O<sub>3</sub> and/or CuAlO<sub>2</sub> after reduction (based on the XRD analysis described above).

The formation of granular (Al-rich) phases within the CuO matrix was observed in all of the Al<sub>2</sub>O<sub>3</sub>-stabilized oxygen carriers independent of the synthesis technique utilized. For example, sub-micrometer Al-rich grains with an average grain size of 350 ± 80 nm were observed also in CuAl\_CP (Figure S5.17a-b). However, the distribution of these grains within the Cu matrix was more heterogeneous when compared to CuAl\_ALD(20). In addition, SEM images of FIB cross-sections (Figure S5.17g-h) of a

material with a poor cyclic stability, *i.e.* CuAl\_ALD(6), revealed a considerable growth of the granular features with cycle number (increase in particle size from  $100 \pm 30$  nm in the 2<sup>nd</sup> cycle to  $200 \pm 70$  nm in the 8<sup>th</sup> cycle) in combination with a rather heterogeneous distribution of those granular features (similar to CuAl\_CP). The information obtained from FIB-SEM cross sections combined with STEM/EDX mapping suggests that the distribution (and dispersion) of the stabilizer, Al<sub>2</sub>O<sub>3</sub>, in the material plays an important role for its redox performance.

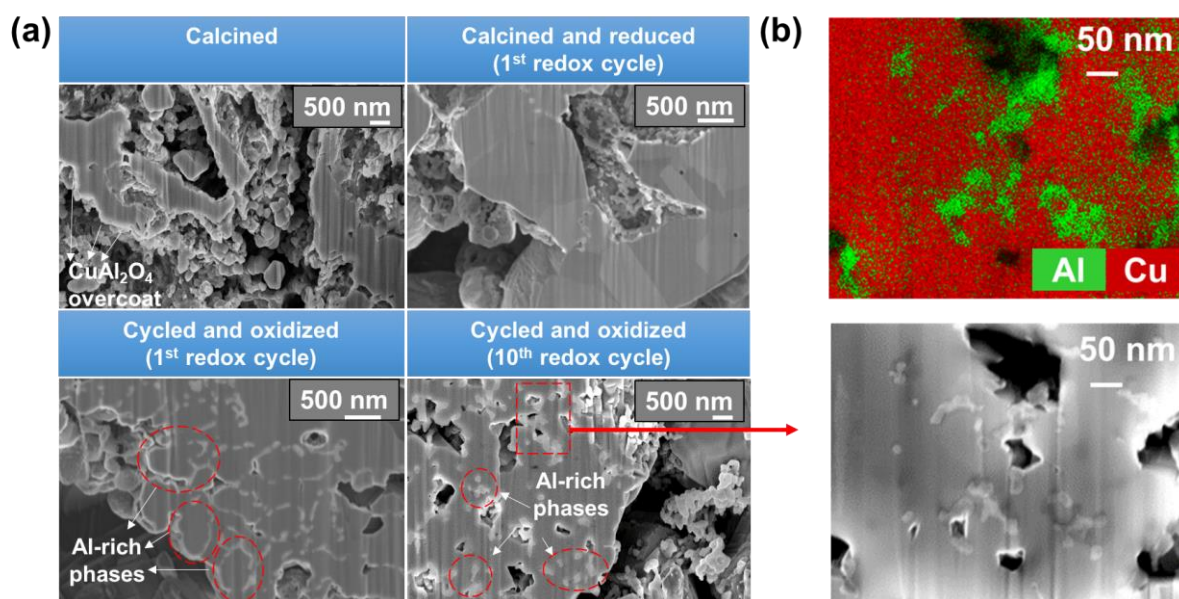


**Figure 5.8:** (a) SEM images of FIB cross-sections of CuAl\_ALD(20) at different states of a redox cycle (900 °C), and (b) EDX maps of Cu and Al in a cross-section of CuAl\_ALD(20) that has undergone 10 redox cycles (oxidized state).

#### 5.4.5 Probing solid-state diffusion and phase interaction in model films

It has been argued that solid state ionic diffusion has an important effect on both the kinetics and the redox stability of oxygen carriers<sup>41, 45</sup>. Indeed, the incomplete re-oxidation of Cu<sub>2</sub>O to CuO might indicate that differences and changes in the diffusion of Cu (and/or oxygen) are responsible for the poor cyclability of a material. In order to shed light on the diffusion characteristics of Cu during oxidation, a thin film of Cu (with a Pt marker layer on top) was sputter-coated. This model system was exposed to air at elevated temperatures (400 and 800 °C). EDX mapping of FIB cross-sections of the

Cu film, Figure 5.9a, clearly confirm the outward diffusion of Cu through the Pt marker during oxidation. This observation is in agreement with previous reports<sup>6, 43, 46</sup>. For example, Qin *et al.*<sup>43</sup> demonstrated the formation of hollow Cu oxide nano-spheres due to the outward diffusion of Cu through an copper oxide layer that formed on top of copper at the onset of oxidation. This phenomenon was explained by differences in the diffusion rates of Cu and O (Kirkendall effect<sup>47</sup>).

To monitor the interaction of the Al<sub>2</sub>O<sub>3</sub>-overcoat and the Cu matrix, further model structures were prepared by sputtering a film of Al<sub>2</sub>O<sub>3</sub> on the Cu film. These films were exposed to the same redox conditions as the Cu foams. EDX maps of FIB cross-sections of these model structures at different stages of the experimental protocol are shown in Figure 5.9b. Calcination at 900 °C resulted in the outward diffusion of Cu through the Al<sub>2</sub>O<sub>3</sub> film (Figure 5.9b). After exposure to 10 redox cycles at 900 °C, the Cu film was found to be distorted to a large extent (Figure 5.9b). These observations can be extended to Cu foams coated by an ALD-grown film of Al<sub>2</sub>O<sub>3</sub>. Upon heat treatment (calcination or cycling), Cu diffuses outward through the Al<sub>2</sub>O<sub>3</sub>-overcoat, resulting in a re-structuring (fragmentation) of Cu(O) branches as demonstrated earlier in Figure 5.6c and the transformation of the initially conformal Al<sub>2</sub>O<sub>3</sub> overcoat into Al-containing grains that are distributed within the CuO matrix. Hence, the mobility of Cu, the volumetric changes it undergoes during redox cycling, and its chemical interaction with Al<sub>2</sub>O<sub>3</sub> play a key role in the morphological transformation of the originally conformal film of Al<sub>2</sub>O<sub>3</sub>.



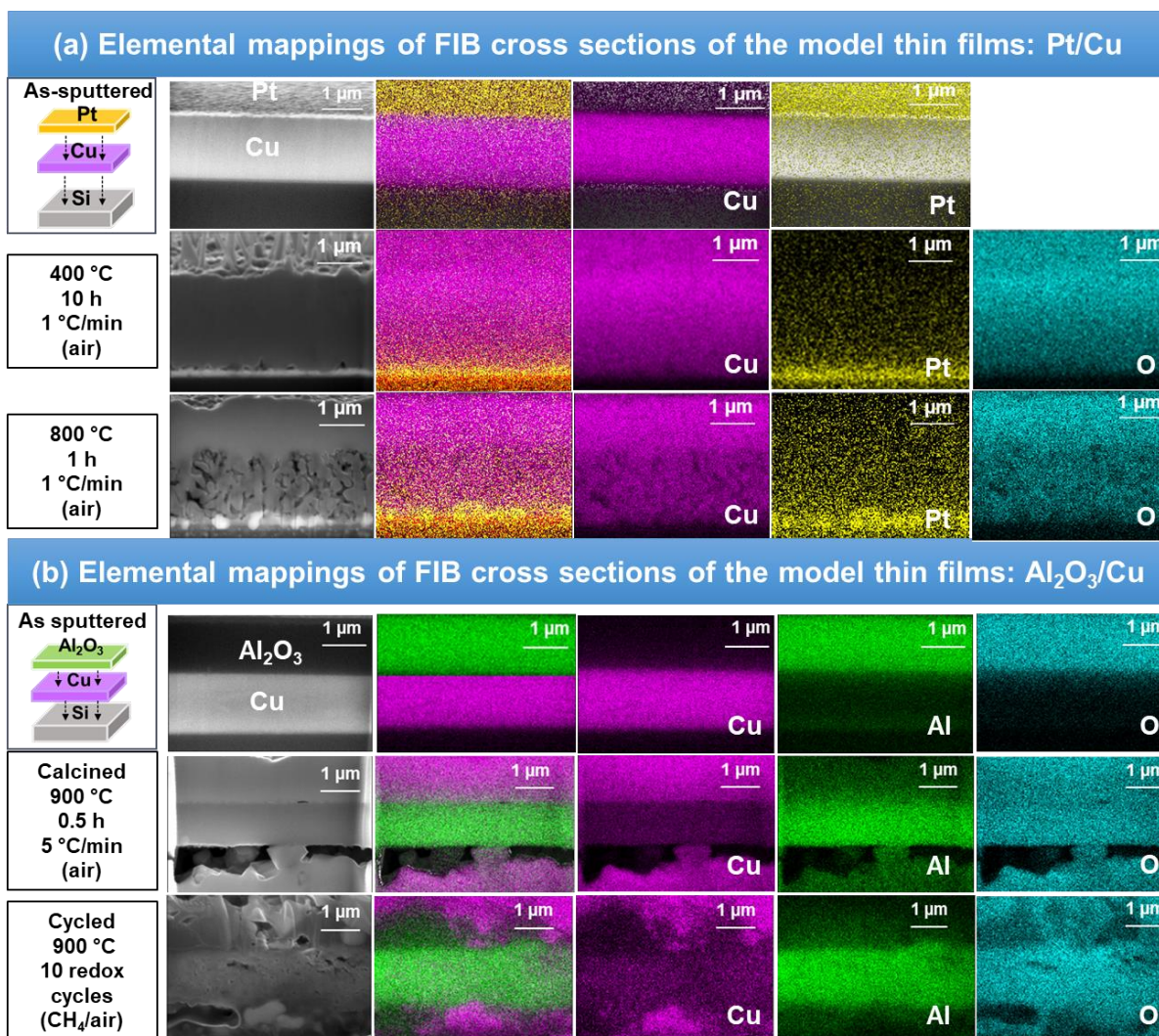


**Figure 5.9:** SEM images showing FIB cross sections along with EDX mapping of (a) Cu thin films with a Pt cap sputtered onto a Si substrate after oxidation in air at 400 °C and 800 °C, and (b) films of Cu and Al<sub>2</sub>O<sub>3</sub> on a Si substrate; as prepared, after calcination in air at 900°C and after 10 redox cycles at 900 °C (oxidized state).

## 5.5 Conclusions

In this work, we report on the development of Cu-based oxygen carriers with stable redox characteristics that were realized via the rapid electrodeposition of highly porous Cu foams followed by their coating with a thin film of Al<sub>2</sub>O<sub>3</sub> using ALD. The presence of a conformal Al<sub>2</sub>O<sub>3</sub> overcoat offers an effective means to stabilize the oxygen carriers against sintering-induced deactivation during repeated redox cycles. A 20-nm-thick Al<sub>2</sub>O<sub>3</sub> layer corresponding to an Al<sub>2</sub>O<sub>3</sub> content of 4 wt. % was sufficient to yield a capacity retention of 96 % over 10 redox cycles, exceeding the performance of a co-precipitated reference material that contains the same quantity of Al<sub>2</sub>O<sub>3</sub>. Deactivation of the oxygen carriers was found to be linked to their incomplete re-oxidation. *In situ* XRD experiments show that both the reduction and oxidation proceeds via the Cu<sub>2</sub>O intermediate, whereby the oxidation of Cu<sub>2</sub>O to CuO is the rate-limiting step. The rate of this reaction step was found to decrease with redox cycle number. Electron microscopy revealed that the presence of an Al<sub>2</sub>O<sub>3</sub> overcoat induces fragmentation of the Cu(O) foam breaking up large Cu(O) branches into smaller particles under high temperature conditions. Such a phenomenon was not observed for materials derived via co-precipitation. The formation of fragmented Cu(O) structures led to faster apparent oxidation kinetics. With number of redox cycles, the Al<sub>2</sub>O<sub>3</sub> film evolves from an amorphous overcoat in the as-synthesized materials to a highly dispersed Cu<sub>x</sub>Al<sub>y</sub>O<sub>z</sub> phase within the Cu(O) matrix. The particle size is in the sub-micrometer range. The evolution of the Al<sub>2</sub>O<sub>3</sub> overcoat to a well-dispersed phase is most likely triggered by the diffusion of Cu through the Al<sub>2</sub>O<sub>3</sub> layer during oxidation. The outward diffusion of Cu was demonstrated experimentally on model films.

## 5.6 References

1. N. Mac Dowell, P. S. Fennell, N. Shah and G. C. Maitland, *Nat. Clim. Change*, 2017, 7, 243.
2. M. E. Boot-Handford, J. C. Abanades, E. J. Anthony, M. J. Blunt, S. Brandani, N. Mac Dowell, J. R. Fernández, M.-C. Ferrari, R. Gross, J. P. Hallett, S. R. Haszeldine, P. Heptonstall, A. Lyngfelt, Z. Makuch, E. Mangano, R. T. J. Porter, M. Pourkashanian, G. T. Rochelle, N. Shah, J. G. Yao and P. S. Fennell, *Energy Environ. Sci.*, 2014, 7, 130-189.
3. EIA, U.S. Energy Information Administration, *International Energy Outlook 2017*.
4. J. Adanez, A. Abad, F. Garcia-Labiano, P. Gayan and L. F. de Diego, *Prog. Energy Combust. Sci.*, 2012, 38, 215-282.
5. M. Arjmand, A.-M. Azad, H. Leion, T. Mattisson and A. Lyngfelt, *Ind. Eng. Chem. Res.*, 2012, 51, 13924-13934.
6. S. Y. Chuang, J. S. Dennis, A. N. Hayhurst and S. A. Scott, *Energy Fuels*, 2010, 24, 3917-3927.
7. Q. Imtiaz, D. Hosseini and C. R. Müller, *Energy Technol-Ger*, 2013, 1, 633-647.
8. M. Arjmand, A.-M. Azad, H. Leion, A. Lyngfelt and T. Mattisson, *Energy Fuels*, 2011, 25, 5493-5502.
9. S. Y. Chuang, J. S. Dennis, A. N. Hayhurst and S. A. Scott, *Combust. Flame*, 2008, 154, 109-121.
10. Q. Imtiaz, A. M. Kierzkowska, M. Broda and C. R. Müller, *Environ. Sci. Technol.*, 2012, 46, 3561-3566.
11. D. Hosseini, Q. Imtiaz, P. M. Abdala, S. Yoon, A. M. Kierzkowska, A. Weidenkaff and C. R. Müller, *J. Mater. Chem. A*, 2015, 3, 10545-10550.
12. B. M. Corbella, L. de Diego, F. García-Labiano, J. Adánez and J. M. Palacios, *Energy Fuels*, 2006, 20, 148-154.
13. M. A. San Pio, M. Martini, F. Gallucci, I. Roghair and M. van Sint Annaland, *Chem. Eng. Sci.*, 2018, 175, 56-71.
14. M. A. San Pio, F. Sabatino, F. Gallucci and M. van Sint Annaland, *Chem. Eng. J.*, 2018, 334, 1905-1916.
15. X. Tian, Y. Wei and H. Zhao, *Chem. Eng. J.*, 2018, 334, 611-618.
16. J. Y. Do, N. Son, N.-K. Park, B. S. Kwak, J.-I. Baek, H.-J. Ryu and M. Kang, *Appl. Energ.*, 2018, 219, 138-150.
17. P. Gayán, I. Adánez-Rubio, A. Abad, L. F. de Diego, F. García-Labiano and J. Adánez, *Fuel*, 2012, 96, 226-238.
18. L. Díez-Martín, G. Grasa, R. Murillo, A. Scullard and G. Williams, *Ind. Eng. Chem. Res.*, 2018, 57, 2890-2904.
19. Z. Xu, H. Zhao, Y. Wei and C. Zheng, *Combust. Flame*, 2015, 162, 3030-3045.
20. B. M. Corbella, L. De Diego, F. García, J. Adánez and J. M. Palacios, *Energy Fuels*, 2005, 19, 433-441.

21. L. F. de Diego, F. García-Labiano, J. Adánez, P. Gayán, A. Abad, B. M. Corbella and J. María Palacios, *Fuel*, 2004, 83, 1749-1757.
22. M. M. Hossain and H. I. de Lasa, *Chem. Eng. Sci.*, 2008, 63, 4433-4451.
23. N. S. Yüzbaşı, A. M. Kierzkowska, Q. Imtiaz, P. M. Abdala, A. Kurlov, J. L. Rupp and C. R. Müller, *J. Phys. Chem. C*, 2016, 120, 18977-18985.
24. J. Adánez, P. Gayán, J. Celaya, L. F. de Diego, F. García-Labiano and A. Abad, *Ind. Eng. Chem. Res.*, 2006, 45, 6075-6080.
25. T. Mattisson, A. Järnäs and A. Lyngfelt, *Energy Fuels*, 2003, 17, 643-651.
26. H. C. Shin, J. Dong and M. Liu, *Adv. Mater.*, 2003, 15, 1610-1614.
27. A. Armutlulu, M. A. Naeem, H. J. Liu, S. M. Kim, A. Kierzkowska, A. Fedorov and C. R. Müller, *Adv. Mater.*, 2017, 29, 1702896.
28. J. Rodríguez-Carvajal, *Physica B*, 1993, 192, 55.
29. P. Pietsch, M. Hess, W. Ludwig, J. Eller and V. Wood, *Sci Rep.*, 2016, 6, 27994.
30. J. Elmer, T. Palmer, S. Babu, W. Zhang and T. DebRoy, *Weld J.*, 2004, 83.
31. E. P. Barrett, L. G. Joyner and P. P. Halenda, *J. Am. Chem. Soc.*, 1951, 73, 373-380.
32. S. Brunauer, P. H. Emmett and E. Teller, *J. Am. Chem. Soc.*, 1938, 60, 309-319.
33. H.-C. Shin and M. Liu, *Chem. Mater.*, 2004, 16, 5460-5464.
34. W. Hu, F. Donat, S. Scott and J. Dennis, *RSC Adv.*, 2016, 6, 113016-113024.
35. K. Jacob and C. Alcock, *J. Am. Ceram. Soc.*, 1975, 58, 192-195.
36. R. F. Cooley and J. S. Reed, *J. Am. Ceram. Soc.*, 1972, 55, 395-398.
37. J. S. D. Viñuela, C. O. Areán and F. S. Stone, *J. Chem. Soc., Faraday Trans. 1*, 1983, 79, 1191-1198.
38. R. A. Fregola, F. Bosi, H. Skogby and U. Hålenius, *Am. Mineral.*, 2012, 97, 1821-1827.
39. J. Y. Kim, J. A. Rodríguez, J. C. Hanson, A. I. Frenkel and P. L. Lee, *J. Am. Chem. Soc.*, 2003, 125, 10684-10692.
40. J. Pike, S.-W. Chan, F. Zhang, X. Wang and J. Hanson, *Appl. Catal.*, 2006, 303, 273-277.
41. Q. Imtiaz, P. M. Abdala, A. M. Kierzkowska, W. van Beek, S. Schweiger, J. L. M. Rupp and C. R. Müller, *Phys. Chem. Chem. Phys.*, 2016, 18, 12278-12288.
42. J. A. Rodríguez, J. Y. Kim, J. C. Hanson, M. Pérez and A. I. Frenkel, *Catal. Lett.*, 2003, 85, 247-254.
43. Y. Qin, Y. Yang, R. Scholz, E. Pippel, X. Lu and M. Knez, *Nano Lett.*, 2011, 11, 2503-2509.
44. J. Lu, B. Fu, M. C. Kung, G. Xiao, J. W. Elam, H. H. Kung and P. C. Stair, *Science*, 2012, 335, 1205-1208.
45. F. Li, S. Luo, Z. Sun, X. Bao and L.-S. Fan, *Energy Environ. Sci.*, 2011, 4, 3661-3667.
46. K. Mimura, J.-W. Lim, M. Isshiki, Y. Zhu and Q. Jiang, *Metall. Mater. Trans. A*, 2006, 37, 1231-1237.
47. Y. Yin, R. M. Rioux, C. K. Erdonmez, S. Hughes, G. A. Somorjai and A. P. Alivisatos, *Science*, 2004, 304, 711-714.



## 5.7 Supporting Information

**Table S5.1:** BET surface area, BJH pore radii and pore volumes of the pristine materials.

	<b>BET surface area</b> <b>[m<sup>2</sup>/g]</b>	<b>BJH pore size</b> <b>[nm]</b>	<b>BJH pore volume</b> <b>[cm<sup>3</sup>/g]</b>
<b>Cu foam</b>	3.7	0.87	0.02
<b>Cu foam (HCl)</b>	10.2	0.81	0.04
<b>Cu reference (commercial)</b>	< 1	0.81	< 0.01

**Table S5.2:** Summary of unit-cell data obtained from Rietveld refinement for the calcined materials (standard deviations reported in parentheses). CuO phase: C2/c space group, Cu atomic coordinates  $x = y = 0.25$ ,  $z = 0$  and O atomic coordinates  $x = 0$ ,  $y = 0.417(1)$ ,  $z = 0.25$ <sup>1</sup>. CuAl<sub>2</sub>O<sub>4</sub> phase: Fd-3m space group, Cu(1) atomic coordinates  $x = y = z = 0.125$ , Cu(2) atomic coordinates  $x = y = z = 0.5$ , Al(1) atomic coordinates  $x = y = z = 0.125$ , Al(2) atomic coordinates  $x = y = z = 0.5$ , O atomic coordinates  $x = y = z = 0.261(2)$ <sup>2</sup>.

		Lattice parameters				Cell	Phase				
		a [Å]	b [Å]	c [Å]	$\beta$ [°]	volume	content	R <sub>p</sub>	R <sub>wp</sub>	R <sub>exp</sub>	
							[Å <sup>3</sup> ]	[%]			
<b>Cu foam</b>		4.6871(2)	3.4236(2)	5.1322(2)	99.417(1)	81.246(8)	100	8.04	11.1	1.73	
<b>Cu foam - Al<sub>2</sub>O<sub>3</sub> (200 ALD)</b>	CuO	4.6868(2)	3.4235(2)	5.1328(2)	99.370 (1)	81.277(8)	97(1)	8.69	12.5	1.2	
	CuAl <sub>2</sub> O <sub>4</sub>	8.0721(8)	a=b=c	a=b=c	90	526.1 (2)	3.0(1)				
<b>CuO - Al<sub>2</sub>O<sub>3</sub> (CP)</b>	CuO	4.6879(2)	3.4244(2)	5.1328(2)	99.462(2)	81.278(8)	99 (1)	8.22	11.9	1.19	
	CuAl <sub>2</sub> O <sub>4</sub>	8.076(2)	a=b=c	a=b=c	90	526.9(3)	1.0 (1)				
<b>CuO (Precip.)</b>		4.6851(4)	3.4253(4)	5.1311(5)	99.482(2)	81.23(2)	100	14.1	19.0	1.42	

For comparison, Rietveld refinement was also performed on the benchmark materials, *i.e.*, precipitated CuO and co-precipitated CuO-Al<sub>2</sub>O<sub>3</sub> (Figure S5.2). Only small variations in the structural parameters (< 0.04%) was observed.

<sup>1</sup> Cooley, R. F.; Reed, J. S., Equilibrium cation distribution in NiAl<sub>2</sub>O<sub>4</sub>, CuAl<sub>2</sub>O<sub>4</sub>, and ZnAl<sub>2</sub>O<sub>4</sub> spinels. *Journal of the American Ceramic Society* **1972**, 55 (8), 395-398.

<sup>2</sup> Massarotti, V., X-ray powder diffraction ab initio structure solution of materials from solid state synthesis: the copper oxide case. *Z. Kristallogr* **1998**, 213, 259-265.

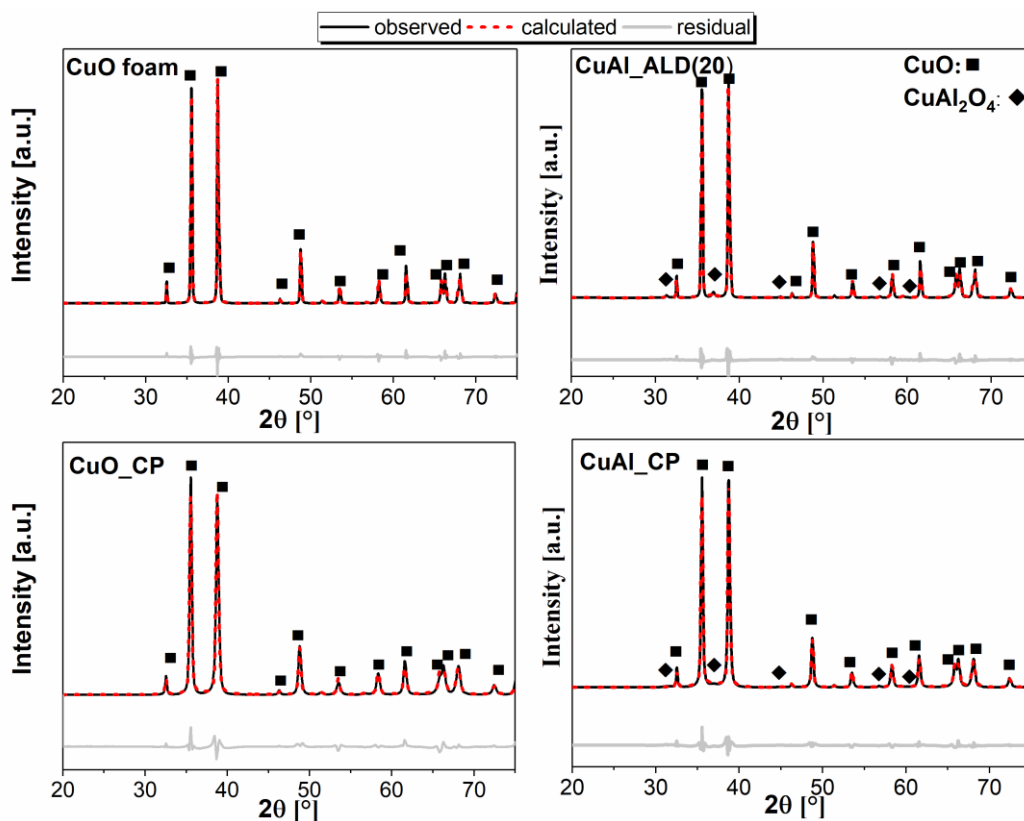


**Figure S5.2:** Rietveld refinement profiles of calcined CuO foam, CuO\_CP, CuAl\_CP and CuAl\_ALD(20).

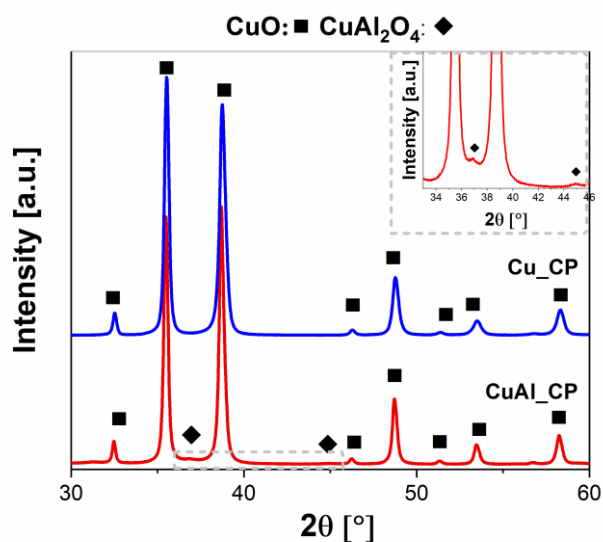


**Figure S5.3:** XRD patterns of CuO\_CP and CuAl\_CP after calcination at 800 °C for 1h.

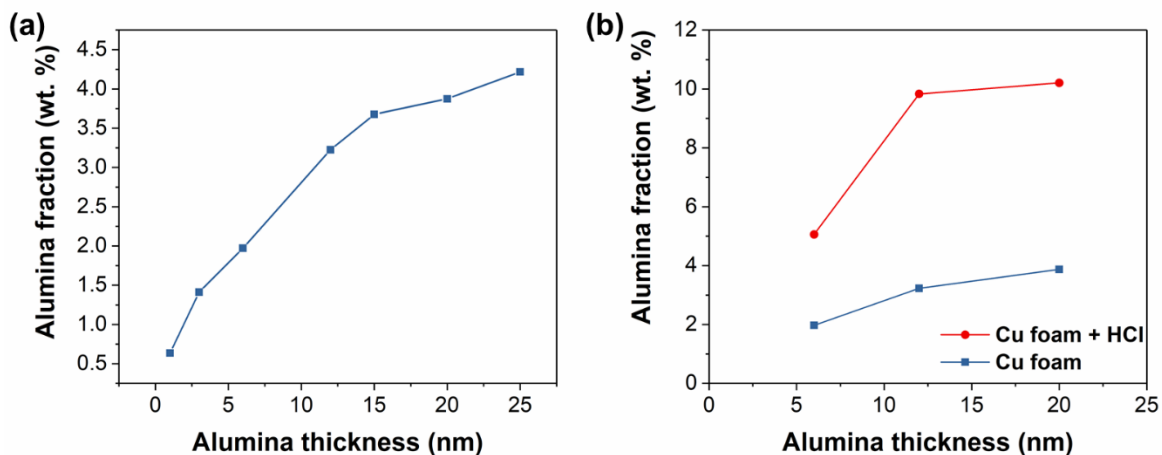


**Figure S5.4:** (a)  $\text{Al}_2\text{O}_3$  content in ALD-coated Cu foams as determined by TPR experiments, (b)  $\text{Al}_2\text{O}_3$  content in ALD-coated Cu foams synthesized in the presence and absence of HCl.

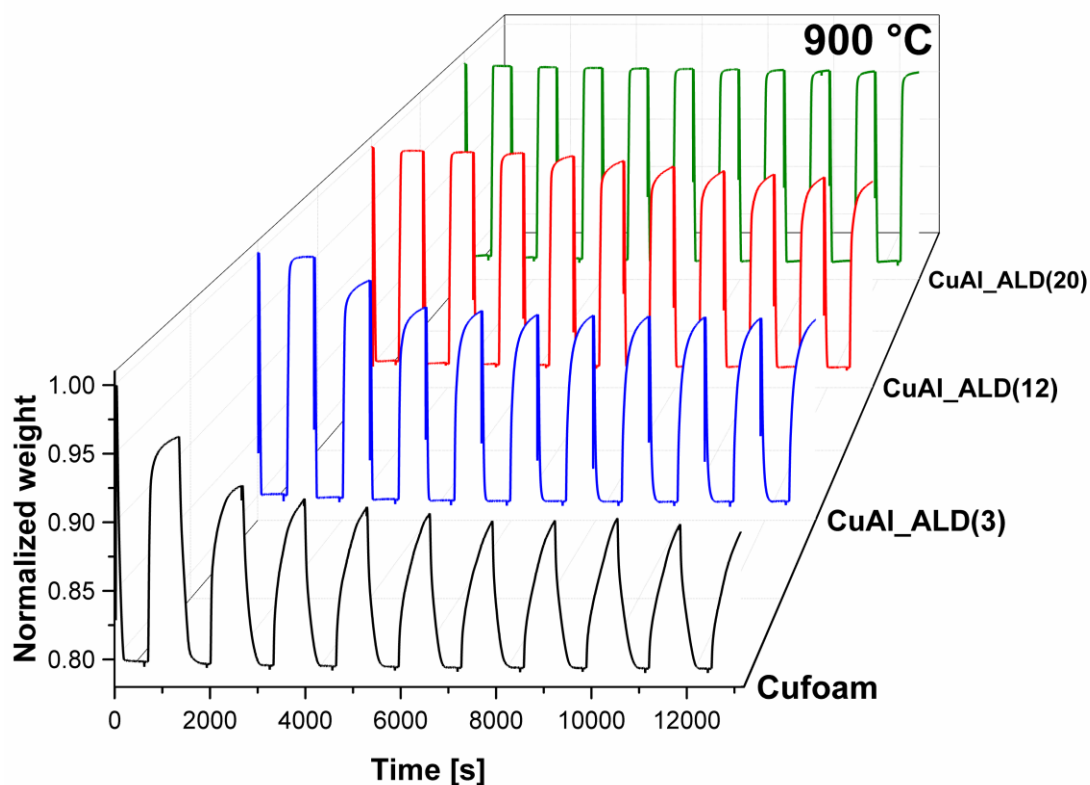


**Figure S5.5:** Redox TGA profiles of the oxygen carriers synthesized (900 °C).

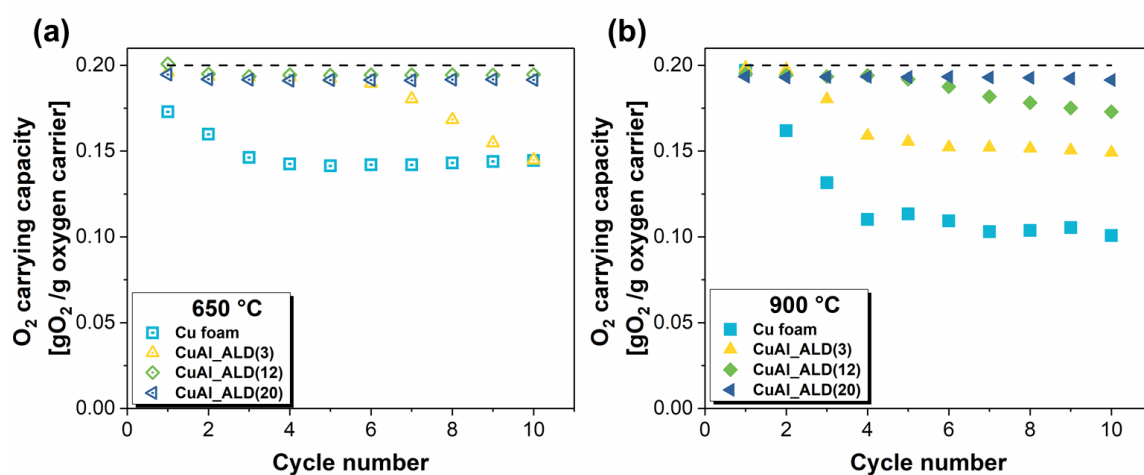


**Figure S5.6:** Cyclic redox performance of Al<sub>2</sub>O<sub>3</sub>-coated Cu foams: **(a)** 650 °C and **(b)** 900 °C.

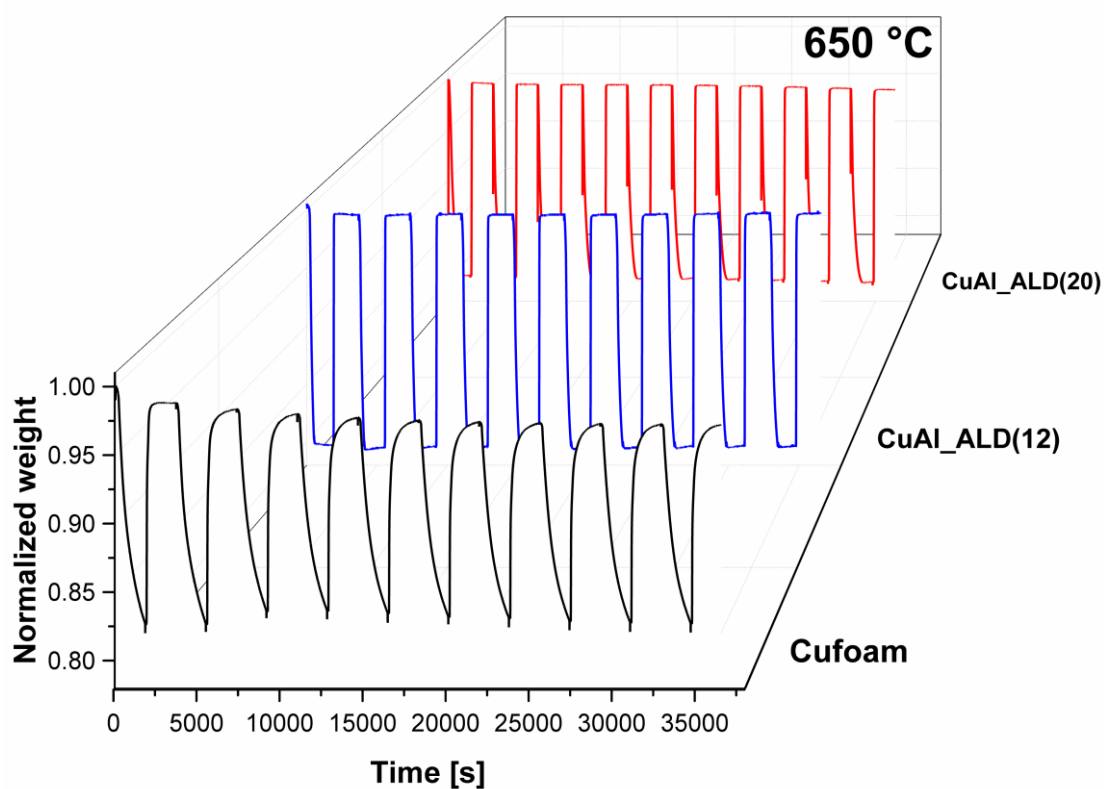


**Figure S5.7:** Redox TGA profiles of the oxygen carriers (650 °C).

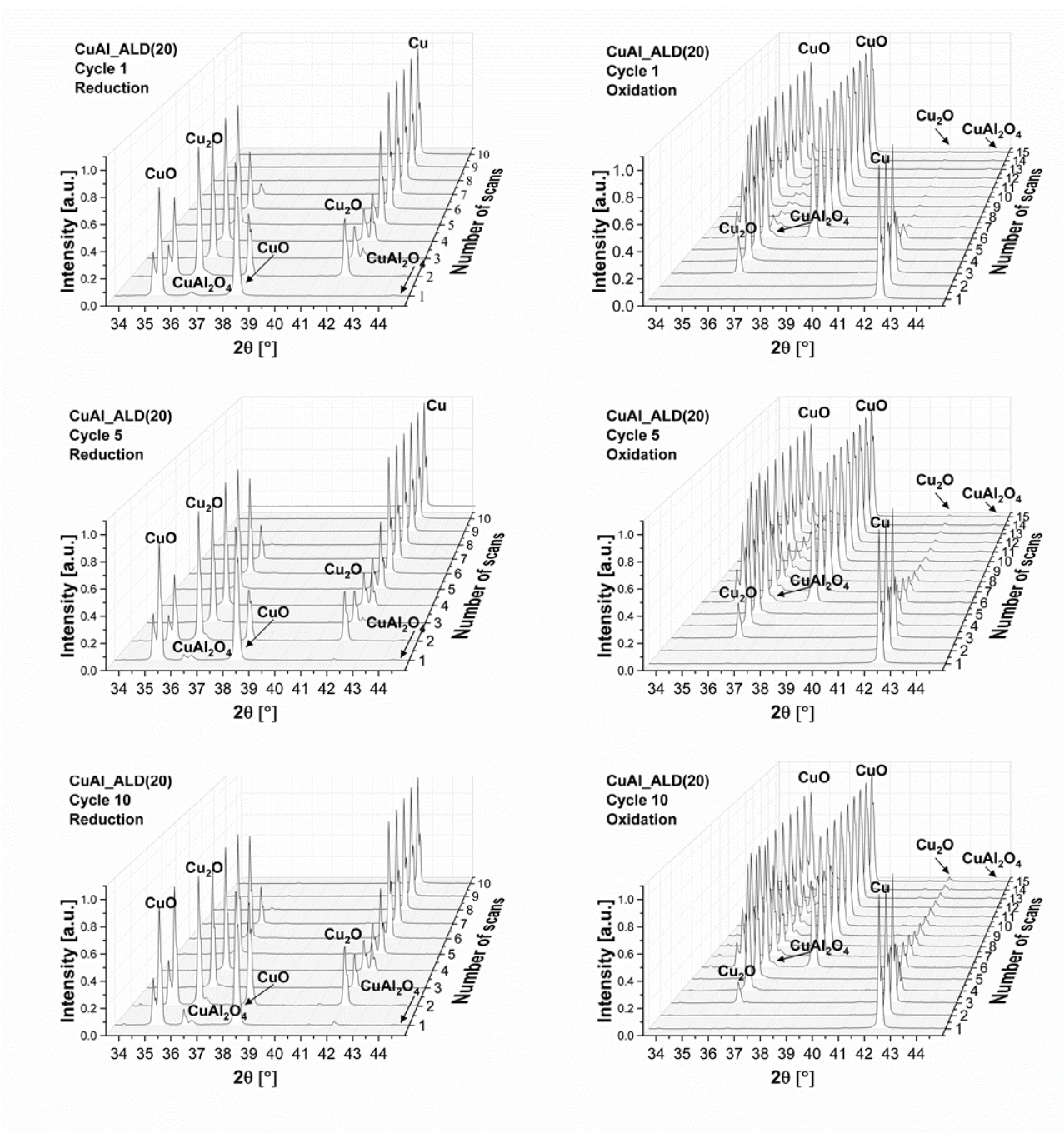


**Figure S5.8:** *In situ* XRD of CuAl\_ALD(20) over multiple redox cycles.

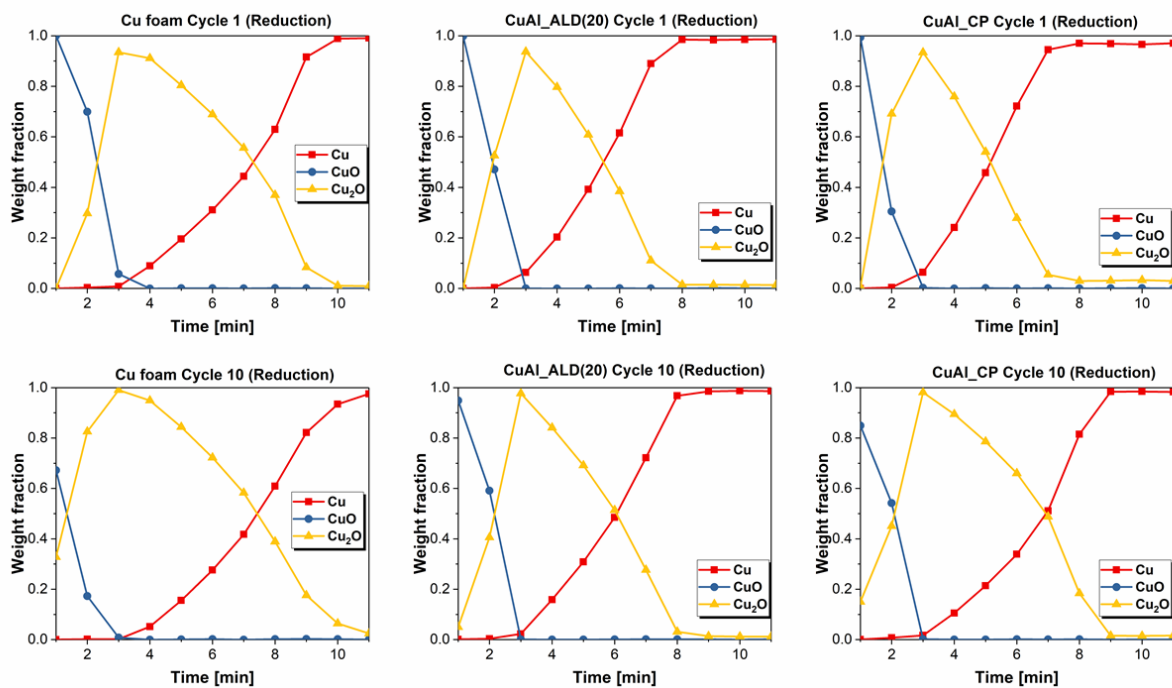


**Figure S5.9:** Temporally resolved reduction profiles obtained by integrating the diffraction peaks (1<sup>st</sup> and 10<sup>th</sup> cycle).

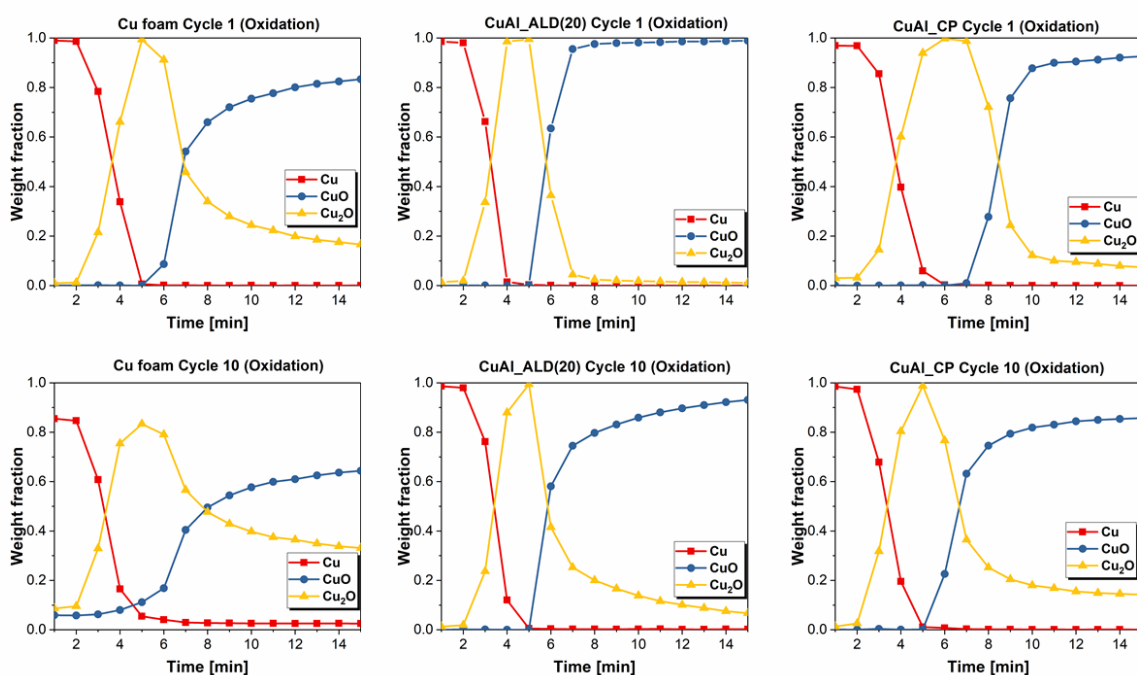


**Figure S5.10:** Temporally resolved oxidation profiles obtained by integrating the diffraction peaks (1<sup>st</sup> and 10<sup>th</sup> cycle).



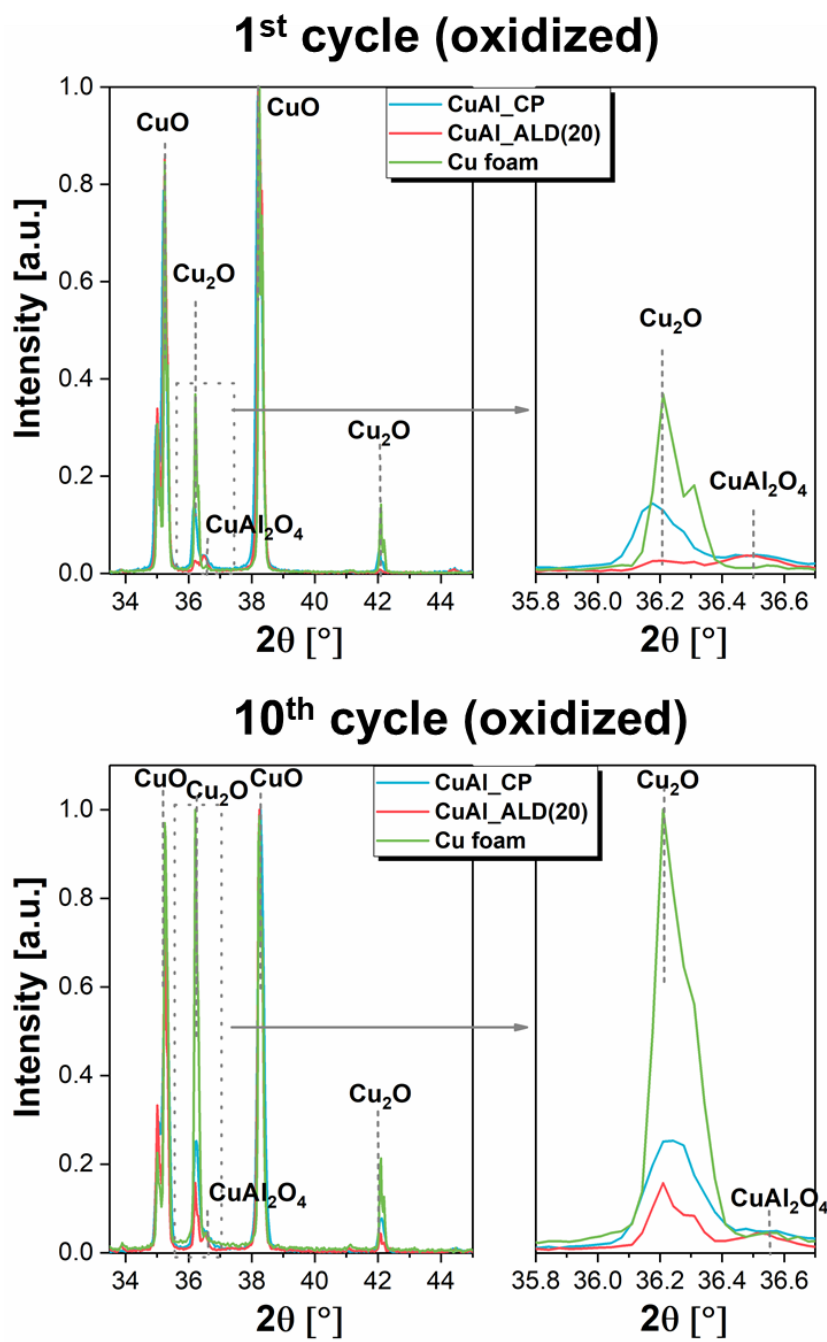


**Figure S5.11:** Comparison of *in situ* X-ray diffractograms (normalized individually by CuO (111)) of the 1<sup>st</sup> and 10<sup>th</sup> cycle (oxidized state).



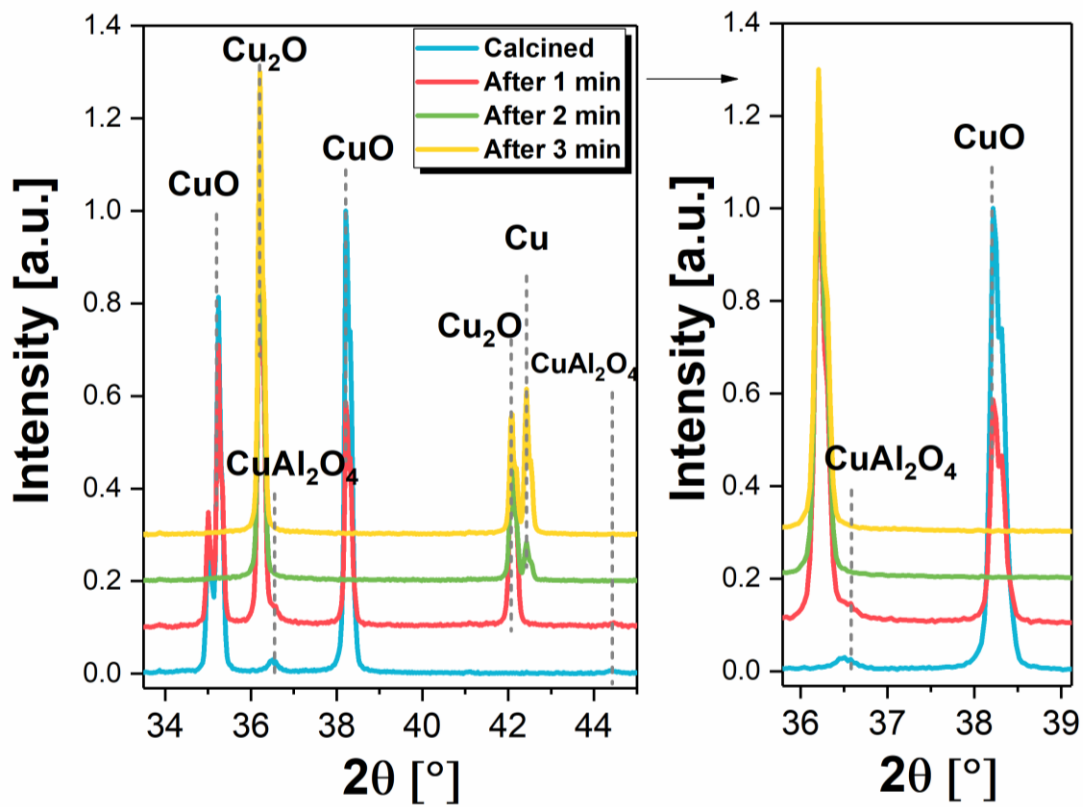


**Figure S5.12:** Comparison of the in situ XRD patterns for CuAl\_ALD(20) during the 1<sup>st</sup> redox cycle in cyclic redox tests.

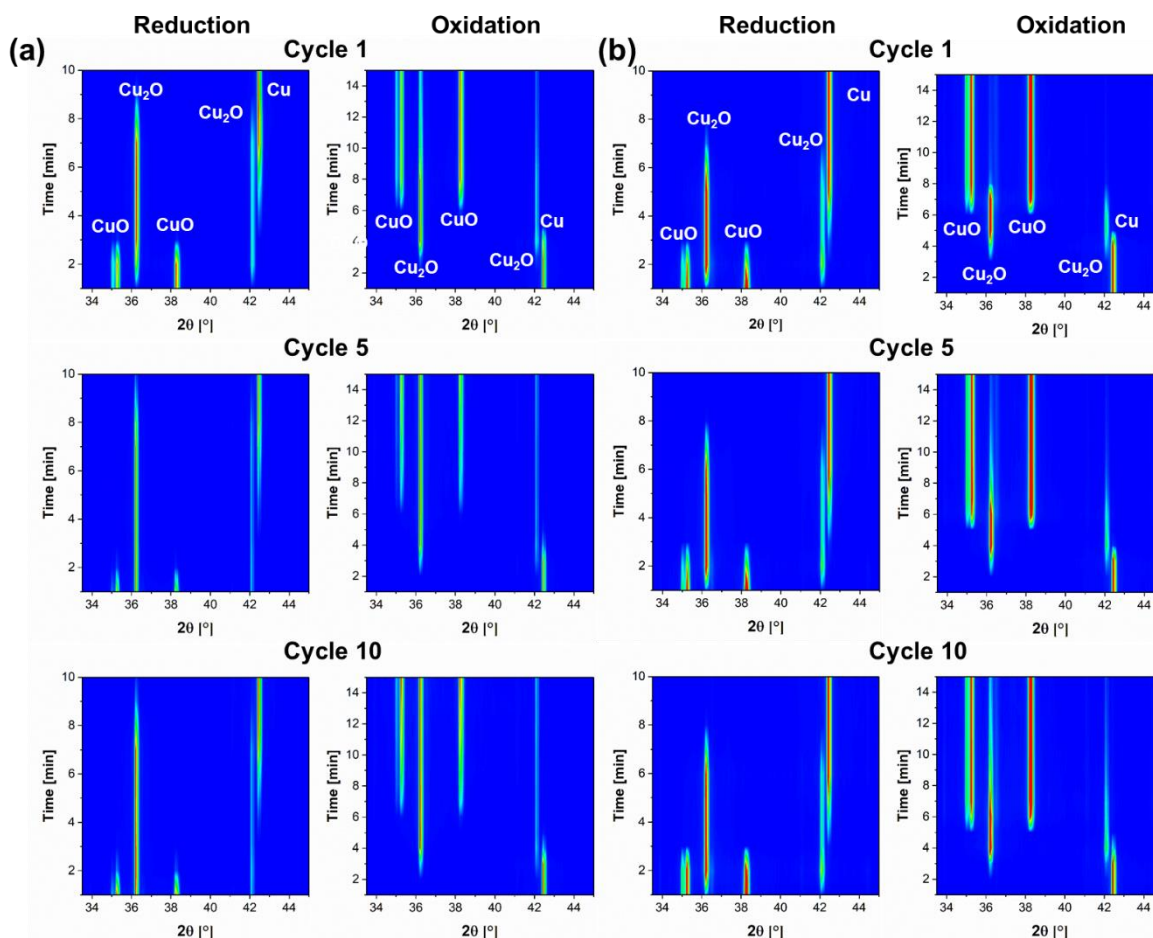


**Figure S5.13:** Contour plots of the *in situ* XRD measurements: (a) Cu foam, (b) CuAl\_ALD(20) for the 1<sup>st</sup>, 5<sup>th</sup> and 10<sup>th</sup> cycle.

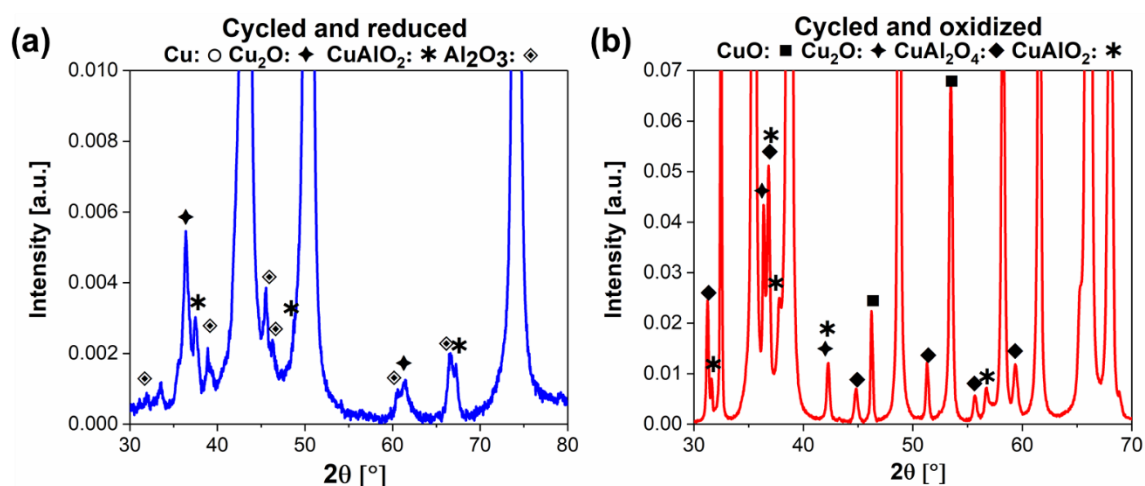


**Figure S5.14:** Magnification of minor peaks in the XRD patterns (normalized by the most intense peak) of cyclized CuAl\_ALD(20) in its reduced and oxidized state after being subjected to 10 redox cycles in TGA at 900 °C.

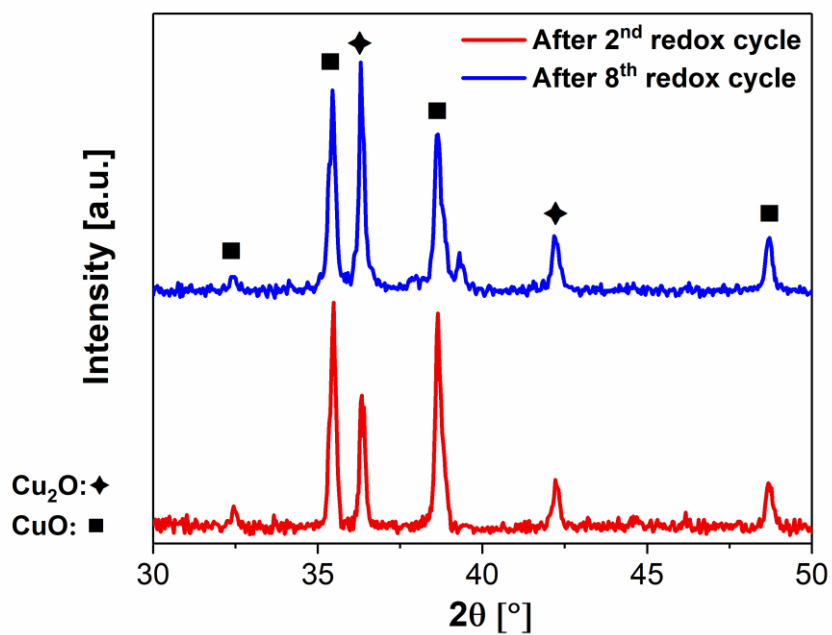


**Figure S5.15:** XRD patterns of CuAl\_ALD(6) after being subjected to 2 and 8 redox cycles at 900 °C (oxidized state).

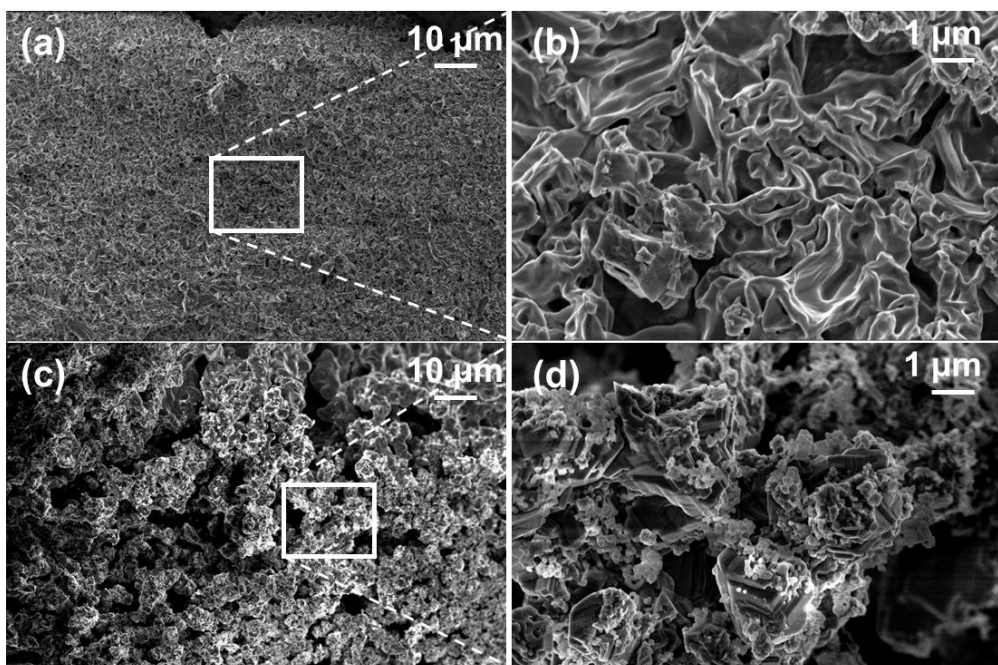


**Figure S5.16:** SEM micrographs of Cu foams: (a-b) without an  $\text{Al}_2\text{O}_3$  overcoat and (c-d) with a 20-nm-thick  $\text{Al}_2\text{O}_3$  overcoat after being subjected to 10 redox cycles at 900 °C.

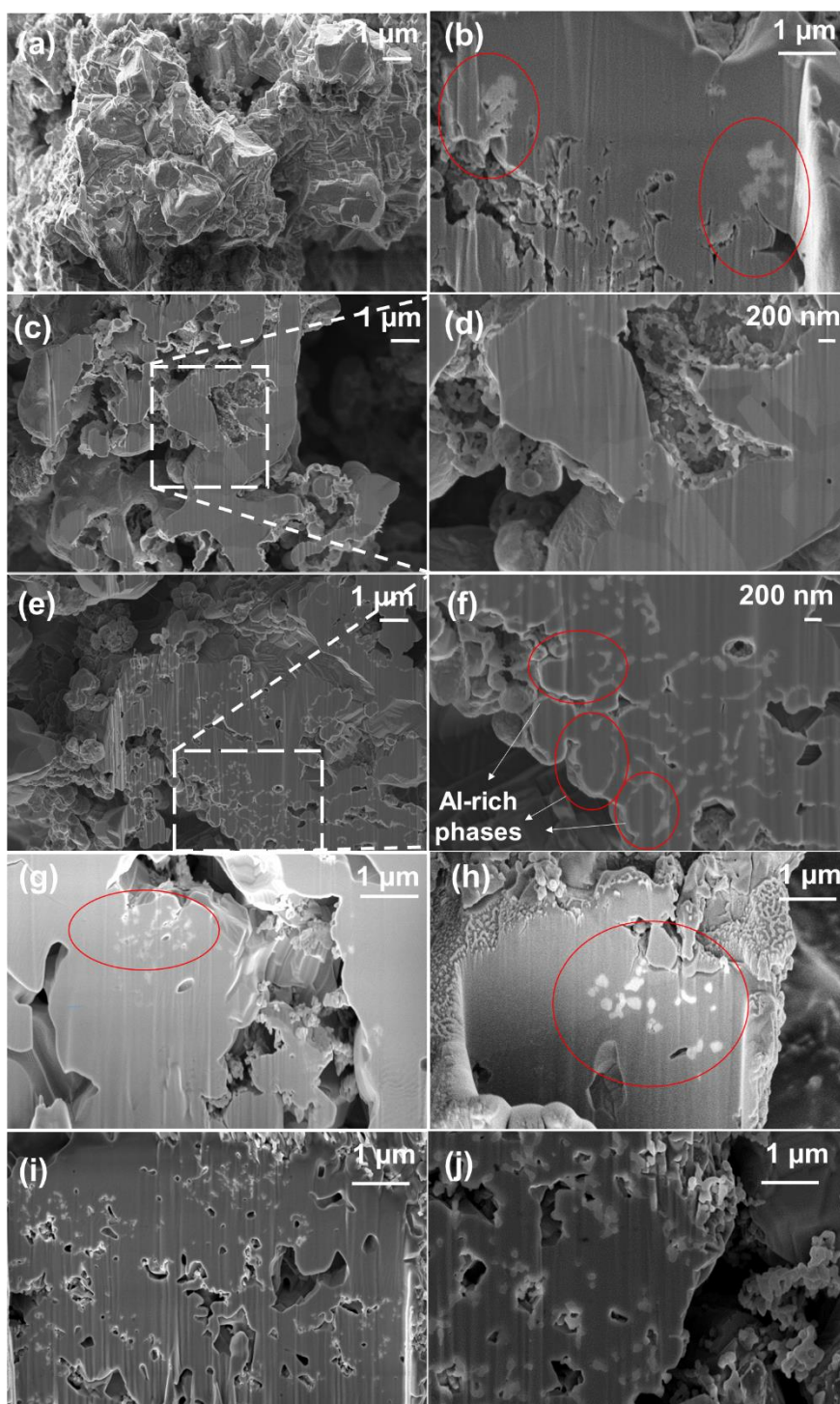


**Figure S5.17:** (a) SEM image and (b) FIB cross-section of CuAl\_CP; FIB-SEM cross sections of CuAl\_ALD(20) after the 1<sup>st</sup> redox cycle (c-d) reduced state and (e-f) oxidized state; FIB-SEM cross sections of CuAl\_ALD(6) after (g) the 2<sup>nd</sup> redox cycle oxidized state and (h) 8<sup>th</sup> redox cycle in oxidized state; SEM/FIB cross sections of CuAl\_ALD(20) after being subjected to 10 redox cycles (oxidized state) at (i) 650 °C and (j) 900 °C.



## 6. Conclusions and Future Work

---

### 6.1 Conclusions

This Dissertation is concerned with the development of effective  $\text{Fe}_2\text{O}_3$  and CuO-based oxygen carriers and the formulation of structure-performance relationships in such materials. For the chemical looping-based  $\text{H}_2$  production,  $\text{Fe}_2\text{O}_3$ -based oxygen carriers require structural stabilization to avoid deactivation over multiple redox cycles as previously reported in the studies summarized in Chapter 1. Ideally, stabilizers should be inert, *i.e.*, not react with iron (oxide) under CL-relevant reaction conditions, to optimize the quantity of the looping active phase. In Chapter 2, the effect of the type of stabilizer ( $\text{ZrO}_2$  or  $\text{Al}_2\text{O}_3$ ) on the redox characteristics of  $\text{Fe}_2\text{O}_3$  was investigated. Supporting  $\text{Fe}_2\text{O}_3$  with  $\text{Al}_2\text{O}_3$  resulted in poor redox properties due to the interaction between the active component ( $\text{Fe}_2\text{O}_3$ ) and the stabilizing material leading to the formation of unreactive hercynite ( $\text{FeAl}_2\text{O}_4$ ). On the other hand,  $\text{ZrO}_2$  was found to be an attractive stabilizer for the CL-based production of  $\text{H}_2$  since  $\text{ZrO}_2$  did not only provide sintering resistance without the formation of a mixed oxide with iron oxide, but also enhanced the solid-state ionic diffusion of the material, as probed by conductivity measurements. The pH value at which the precipitation was performed, was identified as a key synthesis parameter affecting critically the local structure of Fe in  $\text{Fe}_2\text{O}_3$  (possibly as a result of the substitution of  $\text{Zr}^{4+}$  by  $\text{Fe}^{3+}$ ) and the cyclic redox stability of the oxygen carrier, yet to link disorder to redox characteristics requires further work.  $\text{ZrO}_2$ -supported oxygen carriers displayed a very high and stable  $\text{H}_2$  yield over 15 redox cycles when precipitation was performed at  $\text{pH} > 5$ .

In Chapter 3, a metal promoter (Cu) was added to increase the reduction kinetics of the  $\text{Fe}_2\text{O}_3$ - $\text{ZrO}_2$  system.  $\text{ZrO}_2$ -supported, bimetallic Fe–Cu oxygen carriers were developed using a sol-gel technique to achieve a homogenous mixing between the active phases and the stabilizer. Cu-containing oxygen carriers demonstrated a significant enhancement in their reactivity and possessed a high  $\text{H}_2$  yield and redox stability at  $700\text{ }^\circ\text{C}$ . *In situ* pulsed- $\text{H}_2$  XANES (Fe K-edge) experiments were utilized to resolve the reduction pathways of the promoted and unpromoted oxygen carriers and the rate of formation of the different oxidation states of iron. The reduction of both materials proceeded via a  $\text{Fe}^{2+}$  intermediate. It was found that Cu, which was initially

incorporated in the spinel  $\text{CuFe}_2\text{O}_4$ , segregated from the spinel structure under reducing conditions and promoted the reduction of iron oxides ( $\text{FeO}_x$ ) through the dissociative adsorption of  $\text{H}_2$  and its spill-over to  $\text{FeO}_x$ .

To avoid the formation of unreactive  $\text{FeAl}_2\text{O}_4$ , Chapter 4 investigates a  $\text{Na}^+$  doping strategy to improve the hydrogen yield of the  $\text{Fe}_2\text{O}_3$ - $\text{Al}_2\text{O}_3$  system. A series of Na-containing  $\text{Fe}_2\text{O}_3$ - $\text{Al}_2\text{O}_3$  oxygen carriers were prepared by sol-gel. Sodium addition proved to be effective to avoid the formation of  $\text{FeAl}_2\text{O}_4$ , as confirmed by XRD and Fe K-edge XAS. STEM/EDX complemented with *ex situ* XRD demonstrated that  $\text{Al}_2\text{O}_3$  forms a mixed oxide with  $\text{Na}_2\text{O}$ , *i.e.*,  $\text{NaAl}_{11}\text{O}_{17}$ . Na K-edge XANES indicated that the local Na environment was preserved during cycling tests.

As demonstrated in the previous chapters, the presence of a stabilizer is crucial for the stability of an oxygen carrier during repeated redox cycles. To obtain highly effective oxygen carriers, the active component and the inactive stabilizer ought to be mixed at the atomic scale. In Chapter 5, an atomic layer deposition (ALD) approach was utilized to improve the compositional homogeneity of a CuO-based oxygen carriers. Highly porous electrodeposited Cu foams coated with an ALD-grown, 20 nm thin film of  $\text{Al}_2\text{O}_3$ , corresponding to an  $\text{Al}_2\text{O}_3$  content of 4 wt. %, were found to yield a capacity retention of 96 % over 10 redox cycles, exceeding the performance of a co-precipitated benchmark material that contained the same quantity of  $\text{Al}_2\text{O}_3$ . The presence of a conformal  $\text{Al}_2\text{O}_3$  overcoat modified the morphology of the material upon heat treatment and induced a fragmentation of large Cu(O) branches into small particles, which led to faster apparent oxidation kinetics. With number of redox cycles, the  $\text{Al}_2\text{O}_3$  film evolved from an amorphous overcoat in the as-synthesized materials to a highly dispersed  $\text{Cu}_x\text{Al}_y\text{O}_z$  phase within the Cu(O) matrix as probed in FIB/SEM cross sections of the materials.

## 6.2 Future Work

Chemical looping based schemes for the production of  $\text{H}_2$  could be of interest for large-scale implementation. Using a synthesis gas for reduction,  $\text{Fe}_2\text{O}_3$  stabilized by  $\text{ZrO}_2$  possessed an excellent redox stability and high  $\text{H}_2$  production capacity, as discussed in Chapters 2 and 3.

An important aspect that requires further investigation is the performance of the oxygen carriers developed here when alternative fuels such as CH<sub>4</sub> or other higher hydrocarbons are used. Fe<sub>2</sub>O<sub>3</sub>-based oxygen carriers are known to have a reactivity with hydrocarbons (in particular methane) and are prone to carbon deposition. In this context, the reactivity of Fe<sub>2</sub>O<sub>3</sub>-based oxygen carriers could be enhanced through the addition of promoters such as Ru, Cu and K since such promoters can lower the rate of carbon deposition. Hence, it is worth assessing how the addition of a small amount of metal promoters to the Fe<sub>2</sub>O<sub>3</sub>-ZrO<sub>2</sub> system could affect its reducibility, redox stability and rate of carbon deposition. A further approach to increase the reactivity of Fe<sub>2</sub>O<sub>3</sub> with hydrocarbons is to integrate a dry reforming step into chemical looping. Here, a dry reforming catalyst (for example nickel) would allow the conversion of CH<sub>4</sub> (and some recycled CO<sub>2</sub>) into a synthesis gas 1-4 ( $\text{CO}_2 + \text{CH}_4 \rightarrow 2\text{H}_2 + 2\text{CO}$ ), which has a high reactivity with iron oxide. This concept could be investigated using the Fe<sub>2</sub>O<sub>3</sub>-ZrO<sub>2</sub> oxygen carriers developed in Chapters 2 and 3.

In the work reported here it was found that the formation of FeAl<sub>2</sub>O<sub>4</sub> could be avoided through the addition of Na<sup>+</sup>. The local structure of Fe, Na and Al in the Na-modified Fe<sub>2</sub>O<sub>3</sub>-Al<sub>2</sub>O<sub>3</sub> system was probed using XAS with the aim to understand the mechanism through which Na<sup>+</sup> inhibits the reaction between Fe<sub>2</sub>O<sub>3</sub> and Al<sub>2</sub>O<sub>3</sub>. Na and Al K-edge XAS analysis of a series of reference compounds is planned and will be performed in collaboration with Thomas Huthwelker (PHOENIX beamline at PSI). These reference materials include: pure Na-β-Al<sub>2</sub>O<sub>3</sub> phases and sodium modified γ-Al<sub>2</sub>O<sub>3</sub> with different loadings of Na. It is hoped that these measurements will help us to model our XAS data collected on Na promoted Fe<sub>2</sub>O<sub>3</sub>-Al<sub>2</sub>O<sub>3</sub> systems. For example, access to reference data will help to understand better the XANES features attributed to crystalline Na-β-Al<sub>2</sub>O<sub>3</sub> and the sodium surface species on Al<sub>2</sub>O<sub>3</sub> improve the simulation of the XANES data.

The electrodeposition of Cu foams is a practical approach to produce highly effective CuO-based oxygen carriers, as discussed in Chapter 5. This study can be extended further to the production of Fe or bimetallic systems for the CL-based H<sub>2</sub>-production. Furthermore, a facile synthesis route that relies solely on electrochemical deposition can be adapted to stabilize foam structures with various support materials such as Al<sub>2</sub>O<sub>3</sub>, ZrO<sub>2</sub>, CeO<sub>2</sub> or MgO, as observed from preliminary tests in our laboratory. Hence, the cumbersome ALD process could be avoided.

In addition, future research is also required to probe the effect of minor constituents in a real gasifier gas, *e.g.*, sulphurous components, tarry substances and ash (traces of alkali), on the stability of the oxygen carriers and the purity of the H<sub>2</sub> produced. For instance, H<sub>2</sub>S formed during the (partial) gasification of the biomass may react with Fe<sub>2</sub>O<sub>3</sub> according to  $\text{Fe}_3\text{O}_4 + 3\text{H}_2\text{S} + \text{H}_2 \rightarrow 3\text{FeS} + 4\text{H}_2\text{O}$ . However, the presence of FeS would lead to the formation and release of SO<sub>2</sub> during steam oxidation and thus would contaminate the H<sub>2</sub> produced. Moreover, alkali traces can affect negatively the reactivity of the oxygen carriers or promote agglomeration. For this reason, testing of the oxygen carriers under realistic gas composition is a key aspect for future research.

## References

1. L. C. Buelens, V. V. Galvita, H. Poelman, C. Detavernier and G. B. Marin, *Science*, 2016, DOI: 10.1126/science.aah7161.
2. V. V. Galvita, H. Poelman, C. Detavernier and G. B. Marin, *Applied Catalysis B: Environmental*, 2015, 164, 184-191.
3. D. Kang, M. Lee, H. S. Lim and J. W. Lee, *Fuel*, 2018, 215, 787-798.
4. M. Tang, L. Xu and M. Fan, *Applied Energy*, 2015, 151, 143-156.



## Curriculum Vitae

### Nur Sena YÜZBASI

---

**Date of birth:** 14.12.1987  
**Nationality:** Turkish  
**E-mail:** [senayuzbasi@gmail.com](mailto:senayuzbasi@gmail.com)

#### EDUCATION

---

- 2012 – 2018** Swiss Federal Institute of Technology (ETHZ), Zürich, Switzerland  
Doctor of Science (Dr.Sc.) in Mechanical & Process Engineering
- 2008 – 2011** METU Ankara, Turkey  
Master of Science (M.Sc.) in Chemical Engineering (GPA: 3.43/4.00)
- 2006 – 2007** Universitat Politècnica de Valencia, Valencia, Spain  
Bachelor of Science (B.Sc.), Chemical and Nuclear Engineering  
Socrates/Erasmus Exchange Program
- 2004 – 2008** Gazi University, Ankara, Turkey  
Bachelor of Science (B.Sc.), Chemical Engineering (GPA: 3.24/4.00)

#### RESEARCH & EXPERIENCE

---

**2012 – 2018 Research assistant – Laboratory of Energy Science and Engineering (LESE), ETH Zürich, Switzerland**

- Development, characterization and performance assessment of Fe<sub>2</sub>O<sub>3</sub>-based materials utilized in chemical looping based H<sub>2</sub> production
- CuO-based materials utilized in chemical looping combustion for CO<sub>2</sub> capture
- NiO-based materials utilized for dry reforming of CH<sub>4</sub> for syngas production
- Obtaining a detailed understanding of the structural changes in the synthesized materials during cyclic redox operations
- Authoring and co-authoring multiple peer-reviewed papers
- Supervision of master students (2016)

**2009 – 2011 Teaching assistant – METU Ankara, Turkey**

- Teaching ChE 420 Chemical Engineering Laboratory III, Thermal Conductivity, Size Reduction and Fluidization experiments
- Preparation prior to the experiments and supervision to B.Sc. students

**2008 – 2011 Research assistant – METU Ankara, Turkey**

- General and fundamental understanding on pyrolysis and combustion behaviour of various fuels in oxygen enriched air and CO<sub>2</sub> atmospheres
- Authoring and co-authoring multiple peer-reviewed papers

**2007 Summer internship - Petkim Petrochemical Holding A.S. İzmir, Turkey**

- Trainings on production process flow and control in ethylene production plant

**2006 Summer internship - Turkish Aerospace Industries Inc., Ankara, Turkey**

- Trainings on process flow and control in water and chemical treatment facilities and composite material production units

## SKILLS

---

### Scientific Skills

#### Synthesis

- Experienced in various material development techniques: impregnation, co-precipitation, sol-gel, pechini, atomic layer deposition (ALD) and electrodeposition

#### Characterization

- Experienced in microscopy techniques: scanning electron microscope (SEM), transmission electron microscope (TEM), focused ion beam/scanning electron microscope (FIB/SEM), and optical microscope
- Experienced in spectroscopic characterization: X-ray diffraction (XRD), X-ray absorption (XAS), Energy-dispersive X-ray spectroscopy (EDX), Fourier-transform infrared (FTIR)
- Experienced in N<sub>2</sub> adsorption-desorption isotherm

#### Processing

- Thermogravimetric analysis (TGA)
- Fixed and fluidized bed reactors

### IT Skills

- Proficient in Microsoft Office and Windows operating systems
- Knowledge of MATLAB, Origin Lab, Endnote, and ImageJ

### Languages

- **English:** Full professional proficiency \*
- **German:** Elementary proficiency \*
- **Spanish:** Elementary proficiency \*
- **Turkish:** Native

\* Based on the interagency language roundtable (ILR) scale

## REFERENCES

---

**Prof. Dr. Christoph R. Müller** - [muelchri@ethz.ch](mailto:muelchri@ethz.ch)

Associate professor (tenured), Department of Mechanical and Process Engineering, ETH Zürich

**Dr. Paula M. Abdala** - [abdalap@ethz.ch](mailto:abdalap@ethz.ch)

Research fellow, Department of Mechanical and Process Engineering, ETH Zürich

A detailed list of my journal publications and conference presentations can be found on the following page.

## PUBLICATIONS & PRESENTATIONS

ORCID: <https://orcid.org/0000-0002-7304-4552>

Google Scholar: Nur Sena Yuzbasi, total citations: 186, h-index: 5

### Journal Papers

- **Yüzbaşı, N. S.**, Abdala, P. M., Hosseini, D., Armutlulu, A., Huthwelker, T., and Müller, C.R., 2018. Effect of sodium addition on phase evolution of Fe<sub>2</sub>O<sub>3</sub>-Al<sub>2</sub>O<sub>3</sub> oxygen carriers during chemical looping combustion, in preparation.
- **Yüzbaşı, N. S.**, Abdala, P. M., Armutlulu, A., and Müller, C.R., 2018. Atomic layer deposition of a film of Al<sub>2</sub>O<sub>3</sub> on electrodeposited copper foams to yield highly effective oxygen carriers for chemical looping combustion-based CO<sub>2</sub> capture. ACS Applied Materials & Interfaces, submitted.
- **Yüzbaşı, N. S.**, Abdala, P. M., Imtiaz, Q., Kim, S.M., Kierzkowska, A.M., Armutlulu, A., van Beek, W. and Müller, C.R., 2018. The effect of copper on the redox behaviour of iron oxide for chemical-looping hydrogen production probed by in situ X-ray absorption spectroscopy. Physical Chemistry Chemical Physics, pp.12736-12745.
- **Yüzbaşı, N. S.**, Kierzkowska, A.M. and Müller, C.R., 2017. Development of Fe<sub>2</sub>O<sub>3</sub>-based, Al<sub>2</sub>O<sub>3</sub>-stabilized oxygen carriers using sol-gel technique for H<sub>2</sub> production via chemical looping. Energy Procedia, 114, pp.436-445.
- **Yüzbaşı, N. S.**, Kierzkowska, A.M., Imtiaz, Q., Abdala, P. M., Kurlov, A., Rupp, J.L. and Müller, C.R., 2016. ZrO<sub>2</sub>-supported Fe<sub>2</sub>O<sub>3</sub> for chemical-looping-based hydrogen production: Effect of pH on its structure and performance as probed by X-ray absorption spectroscopy and electrical conductivity measurements. The journal of physical chemistry C, 120(34), pp.18977-18985.
- Imtiaz, Q., **Yüzbaşı, N. S.**, Abdala, P. M., Kierzkowska, A.M., van Beek, W., Broda, M. and Müller, C.R., 2016. Development of MgAl<sub>2</sub>O<sub>4</sub>-stabilized, Cu-doped, Fe<sub>2</sub>O<sub>3</sub>-based oxygen carriers for thermochemical water-splitting. Journal of Materials Chemistry A, 4(1), pp.113-123.
- **Yüzbaşı, N. S.** and Selçuk, N., 2012. Pyrolysis and combustion behaviour of ternary fuel blends in air and oxy-fuel conditions by using TGA-FTIR. Combustion Science and Technology, 184(7-8), pp.1152-1163.
- **Yüzbaşı, N. S.** and Selçuk, N., 2012. Air and oxy-fuel combustion behaviour of petcoke/lignite blends. Fuel, 92(1), pp.137-144.
- **Yüzbaşı, N. S.** and Selçuk, N., 2011. Air and oxy-fuel combustion characteristics of biomass/lignite blends in tga-ftir. Fuel processing technology, 92(5), pp.1101-1108.
- Selçuk, N. and **Yüzbaşı, N. S.**, 2011. Combustion behaviour of Turkish lignite in O<sub>2</sub>/N<sub>2</sub> and O<sub>2</sub>/CO<sub>2</sub> mixtures by using TGA-FTIR. Journal of Analytical and Applied Pyrolysis, 90(2), pp.133-139.

### Scientific talks & Conference proceedings

- **Yüzbaşı, N. S.**, Abdala, P.M., Imtiaz, Q., Kim, S.M., Kierzkowska, A.M., Armutlulu, A., van Beek, W. and Müller, C.R., Sol-gel-derived, ZrO<sub>2</sub>-supported, CuO-promoted, Fe<sub>2</sub>O<sub>3</sub>-based materials for chemical-looping based hydrogen production, Oral presentation, 7<sup>th</sup> High temperature solid looping cycles network meeting, Luleå, Sweden, September 4-5, 2017.
- **Yüzbaşı, N. S.**, Kierzkowska, A. and Müller, C.R., Development of Fe<sub>2</sub>O<sub>3</sub>-based, Al<sub>2</sub>O<sub>3</sub>-stabilized oxygen carriers using sol-gel technique for H<sub>2</sub> production via chemical looping. 13<sup>th</sup> International conference on greenhouse gas control technologies, Poster presentation, GHGT-13, Lausanne, Switzerland, November 14-18, 2016.
- **Yüzbaşı, N. S.**, Imtiaz, Q., Kierzkowska, A.M. and Müller, C.R., Synthesis and performance of Fe<sub>2</sub>O<sub>3</sub>-based oxygen carriers for hydrogen production via chemical looping, 3<sup>rd</sup> International Conference on Chemical Looping, Oral presentation, Gothenburg, Sweden, September 9-11, 2014.
- **Yüzbaşı, N. S.**, Imtiaz, Q., and Müller, C.R., Sol-gel derived Fe<sub>2</sub>O<sub>3</sub>-based, Al<sub>2</sub>O<sub>3</sub> supported oxygen carriers for hydrogen production via a chemical looping cycle, Oral presentation, AIChE 2013 Annual Meeting, San Francisco, CA, USA, November 3-8, 2013.
- **Yüzbaşı, N. S.**; Selçuk, N., Air and oxy-fuel combustion characteristics of indigenous lignite in TGA-FTIR, Oral presentation, 5<sup>th</sup> International Exergy, Energy and Environmental Symposium IEEES-5, Luxor, EGYPT.
- Aktaş, Ö.; Yerlikaya, G.; **Yüzbaşı, N. S.**; Yaşyerli, S.; Doğu, G., Production of Propylene by Oxidative Dehydrogenation of Propane Using Mo-Ce Incorporated MCM-41 Supported Catalysts, Poster presentation, 23. National Chemistry Congress, June 2009, Sivas, TURKEY.